İSTANBUL TECHNICAL UNIVERSITY ★ INFORMATICS INSTITUTE

MATHEMATICAL MODELING AND STRESS ANALYSIS OF WIRE ROPES UNDER CERTAIN LOADING CONDITIONS

Ph.D. Thesis by
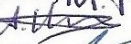**Cengiz ERDÖNMEZ**

Department : Computational Science & Engineering

Programme : Computational Science & Engineering

MAY 2010

MATHEMATICAL MODELING AND STRESS ANALYSIS OF WIRE ROPES UNDER CERTAIN LOADING CONDITIONS

Ph.D. Thesis by
Cengiz ERDÖNMEZ
(702012002)

Date of submission :	**20 January 2010**
Date of defence examination:	**17 May 2010**

Supervisor (Chairman) :	**Prof.Dr. C.Erdem İMRAK (ITU)**
Members of the Examining Committee :	**Prof.Dr. M.Serdar ÇELEBİ (ITU)**
	Prof.Dr. Ata MUĞAN (ITU)
	Prof.Dr. M.Orhan KAYA (ITU)
	Assoc.Prof.Dr. Ö.Ümit ÇOLAK (YTU)

MAY 2010

İSTANBUL TEKNİK ÜNİVERSİTESİ ★ BİLİŞİM ENSTİTÜSÜ

BELİRLİ KOŞULLAR ALTINDA TEL HALATLARIN MATEMATİK MODELLENMESİ VE GERİLİM ANALİZİ

DOKTORA TEZİ
Cengiz ERDÖNMEZ
(702012002)

Tezin Enstitüye Verildiği Tarih : 20 Ocak 2010
Tezin Savunulduğu Tarih : 17 Mayıs 2010

Tez Danışmanı : Prof.Dr. C.Erdem İMRAK (İTÜ)
Diğer Jüri Üyeleri : Prof.Dr. M.Serdar ÇELEBİ (İTÜ)
Prof.Dr. Ata MUĞAN (İTÜ)
Prof.Dr. M.Orhan KAYA (İTÜ)
Doç.Dr. Ö.Ümit ÇOLAK (YTÜ)

MAYIS 2010

FOREWORD

First of all, I would like to thank my supervisor, Prof.Dr. C. Erdem İmrak, for his support and guidance during the all period of my Ph.D. study. His encouragements always supported and lead me forward during this difficult period. When I am in trouble, he gave me power to struggle with the difficulties and pass over the problems. He took me out of a big dust storm when I lost drowning down at the beginning of my Ph.D. thesis. For this reason, I am so lucky to have such a supervisor.

I would like to thank to my thesis committee members one by one for their invaluable supports and helps. I would like to thank Prof.Dr. M. Serdar Çelebi for his supports and grateful inspiration during this period. I would like to thank Prof.Dr. Ata Muğan for his support about guidance and knowledge sharing during the analysis period. Their invaluable discussions helped me to improve myself and served me in the right way when I lost my direction sometimes. In addition, I am grateful to Prof.Dr. M. Orhan Kaya and Doç.Dr. Ö. Ümit Çolak for their valuable reviews and comments on my thesis.

I would like to thank to academic members starting from Prof.Dr. Metin Demiralp, Prof.Dr. M. Serdar Çelebi, Prof.Dr. Hasan Dağ, Doç.Dr. Lale Tükenmez Ergene and the others for their supports, also I would like to thank to the unbelievable stuffs of the Institute starting from Ayhan Tokuri, Elife Karakoç, Tomris Yaman, and the others. In addition, I would like to thank all my friends studying with me at the Informatics Institute.

At the end, I would like to thank to my colleagues whom I worked at the different times and places for their belief, support, and helps to me during these long and difficult period.

Finally, I would like to thank to my little family members A.Tolga, O.Tuna and my wife Dilek for their endless patience, support and love. In addition, I would like to thank and remember my deceased mother Şerife, for her unimaginable support and love during my life.

January 2010   Cengiz ERDÖNMEZ

                                            Informatics Institute
                                            Computational Science&Engineering

TABLE OF CONTENTS

LIST OF TABLES

LIST OF FIGURES

LIST OF SYMBOLS

N	:	Component of the shearing force on a wire cross section in x direction
N'	:	Component of the shearing force on a wire cross section in y direction
T	:	Axial tension in the wire in z direction
G	:	Component of the bending moment on a wire cross section in x direction
G'	:	Component of the bending moment on a wire cross section in y direction
H	:	Twisting moment in z direction
X, Y and Z	:	The external line load per unit length for x, y and z directions respectively
K, K' and Θ	:	The external moment per unit length for x, y and z directions respectively
κ and κ'	:	The components of the curvature in the x and y directions respectively
τ_i	:	The twist per unit length of the wire
τ_s	:	The twist per unit length of the wire strand
s	:	Arc length over the thin wire
R	:	Radius of the wire rope
v	:	Poisson's ratio
E	:	Young's Modulus
ξ	:	Axial wire strain
R_1	:	Radius of center wire
R_2	:	Radius of outer wire
m	:	Number of helical wires
α_2	:	Helix angle of an outside strand
p_2	:	Pitch of an outside wire
F_i	:	Total axial force
M_t	:	Total twisting moment
M	:	Twisting moment
ε	:	Strain
i	:	Indices declares the notation; $i=1$ for center wire, $i=2$ for outer wire
u_x, u_y, u_z	:	Translations in x, y and z directions
u_{xx}, u_{yy}, u_{zz}	:	Rotations in x, y and z directions

MATHEMATICAL MODELING AND STRESS ANALYSIS OF WIRE ROPES UNDER CERTAIN LOADING CONDITIONS

SUMMARY

Wire ropes found wide application area in the industry and daily life for ages. Analytical solutions in the literature are only available for simplified geometrical and physical considerations using the cross-section of a rope due to complex geometrical and physical constraints.

The aim of this thesis is to develop mathematical model of the complex geometry of wire ropes, solid modeling of the real 3-D geometry without length limitation, and solve the model numerically under certain loading conditions. For the sake of this aim, mathematical model of wire rope theory is investigated to find analytical solutions for comparisons with numerical results. Analytical results are obtained for axially loaded straight wire strand and independent wire rope cores (IWRC). Generated numerical models are solved by using finite element analysis and numerical results are compared to both analytical results and available test results.

One of the well-known classical treatise of Love is used as the starting point of the theory of wire ropes. Analytical solutions derived by Costello are proved in a different sense and numerical results are compared to the analytical solutions. As a result, it has been concluded that numerical and analytical results are in good agreement.

Throughout the literature search, it has been observed that most of the researchers intended not to take into account properties such as contact, friction, sliding, and length of wire strand/rope because of the difficulties arising from mathematical and geometrical complexities. In addition, most of the analytical studies and results rely on the cross-sectional part of a wire strand/rope and there is a lack of real 3-D analysis present at the literature for the complex wire ropes such as IWRC or Seale IWRC. Therefore, an exact 3-D solid model of wire strand/rope is constructed by using parametric formulations of single and nested helical wires. Mathematical formulations of the both single and nested helical wires are analyzed and a code is generated to create these helical geometries by using control points. The code is generated to find the location of a helical path where the centerline of the single and nested helical wires lies. Then helical wires are created in 3-D sense and wrapped around a straight wire to construct a simple straight strand, and strands generated before by using nested helical geometry are wrapped around a straight strand to build a solid wire rope model.

Numerical analyses are conducted over a simple straight strand at first. The numerical models are considered both by frictionless and frictional behaviors. Comparisons of both frictionless and frictional numerical results of the simple straight strand showed good agreement to the analytical and available test results. Then 3-D solid model of an IWRC for different lay types are analyzed under axial loading conditions. The results are in good agreement with the theory. Another

complicated analysis is conducted on an IWRC, which is under forced rotation. Under a constant strain, IWRCs are rotated and the obtained results are presented. In addition, a numerical model of a wire strand bent over a sheave problem is proposed. The results show the general behavior of a wire strand in the real application area. Parallelization of the numerical solution is conducted over the bending problem and results are argued. Then solid modeling of a Seale IWRC is developed using the proposed modeling technique. A wire-by-wire analysis result for Seale IWRC is presented as a consequence of the proposed modeling and analysis scheme. At the end, contact interactions over a wire strand are defined. Line of contact between core wire and outer helical wires are plotted in 3-D model by using the obtained numerical results. Deformations occurred due to contact between wires are investigated and wire radius contraction is shown by using contact interactions. One of the important benefits of the proposed method is to create solid wire rope model without length limitation. This issue is shown by generating $1m$-$5m$ wire strands and their numerical analysis. Numerically obtained analysis results are presented in wire-by-wire basis. The benefits of the proposed numerical model enable one to probe over the intended parts of a 3-D numerical model. As an industrial inquiry, length of wires necessary to compose a 6x19 Seale IWRC is computed using the parametric equations of single and nested helical wires.

In this thesis, solid wire rope modeling procedure is clearly developed for such complicated geometry. A wire rope code named Wire Rope Skeleton (WRS) is developed which is able to create both basic single helical and complicated nested (double) helical wire geometry. Then it is developed to run as a stand-alone code and named as Wire Rope Model and Mesh Generator (WRMMG). A meshed wire rope model is created by using the proposed method ready and error free to analyze using the finite element codes. The proposed scheme is applied successifully to wide range of wire ropes such as; simple straight wire strands, IWRCs and Seale IWRCs. It has been shown that with the proposed modeling methodology, wire ropes can be build without length limitation. This is also examined over a $1m$-$5m$ wire strand models. Analyses over long wire ropes are conducted using supercomputers and accurate results are obtained. From the analysis results of $1m$-$5m$ wire strands, it can be concluded that to obtain correct stress distribution over a long wire rope, model mesh plays an important role and should be increased to obtain accurate results. Contact interactions over wire ropes are included and a very fine mesh is build over a wire strand to show the interactions between core-outer wires and between individual outer wires. Deformations of the wires over the cross section of a wire strand are shown. As a result, a deep analysis model for wire rope geometries are developed, and wire-by-wire analysis results are found using the proposed method. The results are compared both with theory and available test results and shows good aggreement. Finally this modeling scheme and numerical method could be applied to wide range of complicated application areas of wire ropes such as, damage analysis, cycling loading, life expectancy, bird caging and reverse bending problems.

BELİRLİ KOŞULLAR ALTINDA TEL HALATLARIN MATEMATİK MODELLENMESİ VE GERİLİM ANALİZİ

ÖZET

Tel halatlar endüstri ve günlük yaşamda asırlardır geniş kullanım alanı bulmaktadır. Literatürde yer alan analitik çözümler sadece basitleştirilmiş geometrik ve fiziksel kabuller göz önünde bulundurularak, ara kesit yüzeyleri üzerinde karmaşık geometrik ve fizikler sınırlandırmaları öngörecek biçimde gerçekleştirilmiştir.

Bu tezin amacı; tel halatların kompleks geometrisinin matematiksel modelinin geliştirilmesi, gerçek 3-D geometrik katı modelinin uzunluk sınırlaması olmadan oluşturulması ve belirli yükleme koşulları altında modelin nümerik çözümlerinin bulunmasıdır. Bu maksatla, tel halat teorisinin matematiksel modeli araştırılarak karşılaştırma yapmak maksadıyla analitik sonuçlar türetilmiştir. Analitik sonuçlar eksenel yüklü düz tel demet ve bağımsız tel halat çekirdeği (BTHÇ) için hesaplanmıştır. Oluşturulan nümerik modeller sonlu eleman analizi ile çözülmüş ve nümerik sonuçlar analitik ve mevcut test sonuçları ile karşılaştırılmıştır.

Love'nin yazmış olduğu iyi bilinen bir bilimsel incelemesi tel halatlar teorisi için başlangıç noktası olarak kullanılmıştır. Costello tarafından türetilen analitik sonuçlar farklı bir yorumla kanıtlanmış ve nümerik sonuçlar ile analitik sonuçların karşılaştırılması yapılmıştır. Sonuç olarak nümerik ve analitik sonuçların iyi uyum gösterdikleri görülmüştür.

Literatür incelemesi boyunca araştırmacıların bir çoğunun temas, sürtünme, kayma, tel demet/halat boyu gibi özellikleri matematiksel ve geometrik karmaşıklıklarından ötürü dikkate almadıkları görülmektedir. Aynı zamanda analitik çalışmaların ve sonuçların çoğu bu sebeple tel demet/halat arakesiti üzerine dayandırılmaktadır ve literatürde BTHÇ ve Seale tipi BTHÇ için gerçek bir 3-D analize rastlanmamaktadır. Bu nedenle gerçek bir 3-D tel demet ve tel halat katı modeli tek ve çift helisel telin parametrik formülasyonu kullanılarak oluşturulmuştur. Tek ve çift helisel tellerin her ikisinin matematiksel formülasyonu analiz edilerek kontrol noktaları yardımıyla helisel yolların tespit ve çizimini yapan bir kod geliştirilmiştir. Bu kod tek ve çift helisel tellerin merkez helisel yollarının yerleşimini hesaplamaktadır. Daha sonra 3-D anlayışıyla oluşturulan teller düz bir tel üzerine sarılarak düz bir demet ve daha önce çift helisel tel geometrisini oluşturan kod yardımı ile elde edilen demetler ise düz bir demet üzerine sarılarak tel halat katı modeli oluşturulmuştur.

İlk olarak nümerik analizler basit düz bir demet üzerinde gerçekleştirilmiştir. Nümerik modeller hem sürtünmesiz hemde sürtünmeli davranışları dikkate almaktadır. Sürtünmesiz ve sürtünmeli modellerin basit düz demet için yapılan karşılaştırmalarında analitik ve test sonuçlarıyla iyi bir uyum sağlandığı gösterilmiştir. Daha sonra farklı sarım tipleri için oluşturulan üç boyutlu BTHÇ modeli eksenel yükleme koşulları altında analiz edilmiştir. Bulunan sonuçlar teori ile iyi uyum göstermiştir. Başka bir karmaşık analiz çalışması zorlanmış dönme koşulu altındaki BTHÇ üzerinde gerçekleştirilmiştir. Sabit bir uzama değerinde, BTHÇ döndürülerek hesaplanan sonuçlar sunulmuştur. Ek olarak bir tel demetinin tanbur

üzerine eğilmesi problemine ait nümerik model önerisi oluşturulmuştur. Sonuçlar bir tel demetin gerçek bir uygulama alanındaki genel davranışını göstermektedir. Nümerik çözümün paralelleştirilmesi eğilme problemi kullanılarak yapılmış ve paralelleştirmeye ilişkin elde edilen sonuçlar tartışılmıştır. Daha sonar Seale BTHÇ katı modeli önerilen modelleme tekniği kullanılarak geliştirilmiştir. Seale BTHÇ için bulunan tel bazında analiz sonuçları önerilen modelleme ve analiz şemasının bir sonucu olarak sunulmuştur. Sonunda bir tel demet üzerinde temas ilişkileri tanımlanmıştır. Merkez tel ile helisel teller arasında oluşan temas hattı elde edilen sayısal sonuçlar kullanılarak 3-D çizdirilmiştir. Teller arasındaki temas durumundan ötürü kaynaklanan deformasyon incelenmiş ve tel yarıçapındaki azalmanın değişimi temas ilişkileri kullanılarak gösterilmiştir. Önerilen metodun önemli bir faydası katı halat modelinin uzunluk sınırlaması olmadan oluşturulmasıdır. Bu sözü edilen husus $1m$-$5m$ uzunluğunda tel demetleri oluşturularak ve analizleri yapılarak gerçekleştirilmiştir. Nümerik analizler boyunca elde edilen sonuçlar tel bazında elde edilerek sunulmuştur. Önerilen nümerik modelin faydası üç boyutlu tel halat modeli üzerinde istenilen parçalar üzerinde araştırma yapmaya imkan sağlamasıdır. Endüstriyel alandan gelen bir soru üzerine 6x19 Seale BTHÇ'nin oluşturulması için her telin uzunluğu, tek ve çift helisel tellerin parametric denklemleri kullanılarak hesaplanmıştır.

Bu tezde, katı tel halat modeli yöntemi açık bir biçimde karmaşık geometriler için geliştirilmiştir. Tel Halat İskeleti (THİ) adı verilen bir tel halat kodu geliştirilmiştir. THİ kodu ile basit tek helisel tel ile karmaşık çift helisel tel geometrileri oluşturulabilmektedir. Daha sonar bu kod geliştirilerek tek başına çalışabilen bir kod olan Tel Halat Model ve Mesh Üreteci (THMMÜ) adlı kod yazılmıştır. Önerilen yöntem ile mesh yapısı kurulmuş hatasız ve analize hazır tel halat katı modelinin oluşturulması sağlanmıştır. Önerilen yöntem basit düz tel demet, BTHÇ ve Seale tipi BTHÇ gibi geniş bir alandaki katı halat modellerinin oluşturulmasında ve analizinde başarı ile kullanılmıştır. Burada önerilen metodoloji ile tel halatların uzunluk sınırlaması olmaksızın modellenebileceği gösterilmiştir. Ayrıca bu durum $1m$-$5m$ uzunluklarındaki demetlerin modellenmesi ve analizi uygulamasıyla gerçeklenmiştir. Uzun tel halatlar üzerinde yapılan analiz çalışmalarında süperbilgisayarlar kullanılarak hassas sonuçlar elde edilmiştir. $1m$ -$5m$ uzunluğundaki tel demetleri için yapılan analiz sonuçlarından uzun halat yapılarındaki gerilme dağılımlarının doğru bir biçimde elde edilebilmesinde modelin mesh büyüklüğü önemli bir role sahip olup doğru sonuçlar elde etmek için mesh büyüklüğü artırılmalıdır. Tel halatlar üzerindeki temas ilişkileri merkez tel ile dış teller arasında ve dış tellerin birbirleri arasında kurulmuş ve temas analizi için çok ince bir mesh yapısı oluşturulmuştur. Bir tel demetin arakesit bölümü üzerinde tellerin deformasyonları gösterilmiştir. Sonuç olarak tel halat geometrileri için derin bir analiz modeli geliştirilmiş ve tel bazında analiz sonuçları elde edilmiştir. Elde edilen sonuçlar teorik sonuçlar ile mevcut test sonuçları kullanılarak karşılaştırılmış ve uyumlu oldukları sonucuna varılmıştır. Son olarak, bu modelleme metodu ve nümerik çözümleme yöntemi tel halatların kullanıldığı geniş uygulama alanlarında kullanılabileceği öngörülmektedir. Bu alanlar arasında tel halatların; hasar analizi, tekrarlı yüklemeler, ömür tahmini, kuş kafesi ve ters eğilme problemleri örnek olarak sayılabilir.

1. INTRODUCTION

Theory of wire ropes relies on equilibrium equations, which are derived by Love in his well-known classical treaties. Most of the analytical solutions in the literature based on the solution of this equilibrium equations in connection with the boundary conditions and physical aspects of the present problem. Because of the complex geometry, most of the researches are based on the analytical solutions of the cross-sections of a single straight strand, and the theory is extended to the multi-lay strands and ropes. Different aspects of wire ropes are analyzed in theoretical studies. Most of them excluded frictional and contact effects. By using the solid modeling and finite element analysis, it is possible to include friction, contact, and different boundary conditions and material properties. In this thesis, more realistic 3-D solid model of a wire rope is developed by considering the mathematical models. Analysis process is conducted by considering this modeling scheme and considering the important working conditions of wire ropes.

In the second chapter, historical and structural roots of wire ropes and application areas are presented. Various components of wire ropes are described and different lay types are explained. Some of the most popular type of strands such as Seale, Filler, and Warrington are included in this chapter.

In chapter three, a survey to the literature is presented to show the researches about wire rope analysis in different aspects from the past to the present. Bases of the theory of wire ropes are explained at first. Then history of works on wire rope theory is mentioned. Four different theoretical models are presented and described. Among them helical rod model is extensively investigated and an enhanced literature survey is conducted on this theoretical model. Numbers of available test results are reported in the literature. These papers are summarized also in this chapter. At the end of this chapter, recent publications about wire ropes are investigated and presented.

In chapter four, wire rope theory using rod theory is investigated over a helical spring. The angular velocity and curvature relations acting over a thin wire is derived. Deformations over a rod and relations with a helical spring are investigated.

1

Axial loading problem over a simple straight strand is defined analytically. The general equilibrium equation, which describes the axial loads and twisting moments acting over a rope, is derived. General strain and rotation relation due to load and moments over a simple straight strand is explained. At the end of this chapter, contacts and interactions between core wire and the outer single helical wires are described.

In chapter five, equilibrium equations, for only bending moment, is defined and proved using Mapple®. Frictional effects over a strand are defined and static response of an independent wire rope core (IWRC) is investigated. The relation between the sheave and IWRC diameter is investigated for bending problem analytically. General theoretical formulation of an IWRC using the homogenization method is derived.

In chapter six, modeling of wire rope geometry, which is a complicated issue because of the complex nature of the wires, is investigated. General definition of helices and a special form of a helix is described at first. Then the nested helical system also known as double helical geometry is investigated. A moving trihedron and plane construction over a helical wire geometry is defined using Frenet-Serret frames. A single or nested helical wire solid model construction is described. Then complex wire structures are modeled. Various computer aided design (CAD) codes are used to examine a good solid wire model without length limitation and the results are compared. A new code is developed using mathematical considerations of the single helical and nested helical wire geometry. A simple straight wire strand and an IWRC modeling is investigated and different lay types of IWRCs are presented. In addition, element selection for finite element analysis (FEA) and material properties definitions are prescribed in this chapter.

In chapter seven, numerical results using FEA over a simple straight wire strand, IWRC and Seale IWRC are presented respectively. General considerations of the analysis models are defined first. Then a simple straight wire strand and an IWRC for a range of helix angles are modeled and analyzed under axial loading conditions for both elastic and plastic problems. In addition, wire radial contraction behavior over an IWRC is investigated. Complicated problems such as forced torsion and bending over a sheave are modeled and analyzed in this chapter. Bending over a sheave problem is solved using parallel computations and obtained results show the efficient

number of CPUs necessary to use with respect to CPU time. Using the proposed solid modeling scheme, a Seale IWRC is modeled and analyzed under axial loading conditions. A graphical user interface (GUI) code is developed which gathers all geometry modeling schemes of wire ropes. The code is named as Wire Rope Skeleton (WRS) and a brief explanation of the code is given. Later WRS code is developed and a new GUI code is implemented called as Wire Rope Model and Mesh Generator (WRMMG). It is designed to run as a stand-alone code and produces whole wire rope geometry automatically. At the end of this chapter, contact analysis of a simple straight strand is described and presented. Contacts interaction between wires are prescribed and included in the numerical models. Deformations takes place due to contact interactions between wires in a strand and a helical line of contact is maintained between wires. Wire radiuses are contracted due to contacts and the variation of wire radiuses with respect to strain is presented. Mesh size increament effect over a simple straight wire strand is analyzed and results are compared. One of the benefits of the proposed modeling scheme enables one to model wire ropes without length limitation. Using this modeling feature $1m$-$5m$ length wire strands are generated. Numerical analyses over these models are conducted and their discussions are presented in this chapter. Wire strand behaviors for steel and aluminum materials are compared also. During the numerical analysis, wire-by-wire basis investigations are conducted and the numerically obtained results are presented and compared with the theory and available test results. As an industrial inquery, wire lengths to manufacture a specific wire rope composition are computed by using mathematical consideration of each wire within a wire rope.

As a result, more realistic 3-D solid model of the wire ropes for different lay types is constructed without length limitation. Modeling issue is achieved by a new scheme, which is based on the generation of each wire (center straight, single helical or nested helical wires) centerline with a written code using the parametrical definition of single and nested helical wire geometry. A numerical model using the wire-by-wire based analysis method is designed and the numerical results are compared with the theory and available test results in the literature. The application of the proposed scheme is applied to the bending over a sheave problem. In addition, modeling of a Seale IWRC is achieved which is a more complex type of wire rope. At the end, contact analysis over a wire strand is achieved and wire contraction is demonstrated.

Using the proposed modeling scheme 1m-5m wire strands are modeled and analyzed. This modeling scheme with the use of finite element analysis gives opportunity to analyze mechanical behavior of long wire ropes under various application areas.

2. ROPE HISTORY AND WIRE ROPE STRUCTURE

2.1 Ancient history of ropes

Ropes made of hides, hair or plant materials from part of the earliest achievements of human civilization. The oldest illustrations of ropes are dated from approximately 12000 to 9000 BC. Remnants of ropes found in Finland are supposed to be from the Mesolithic period (9000-3000 BC); others found in Egypt and made of camel hair are more than 4000 years old. Some mural paintings in Egypt (ca. 2000 BC) show the production of ropes made of papyrus, leather or palm fibers as in Figure 2.1.
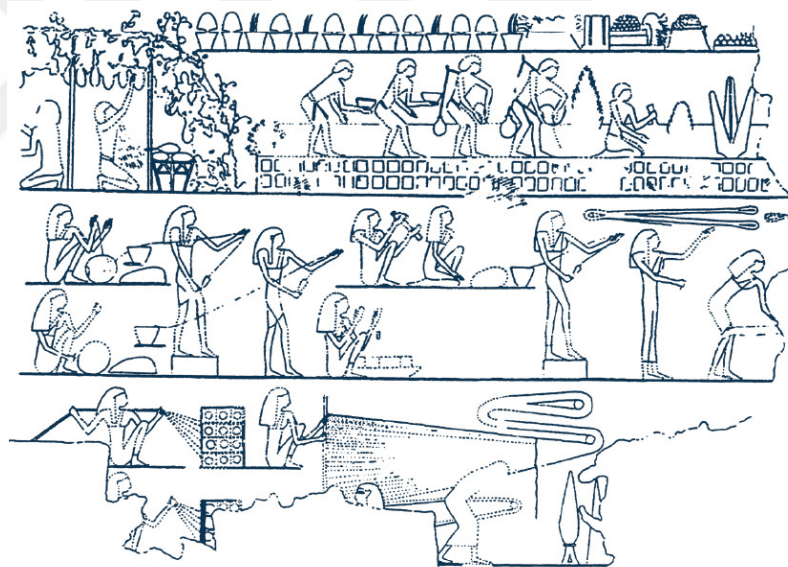
Figure 2.1: Rope production in Egypt 2000 BC.

Ropes were used for making fishing nets or traps, but also for lifting and dragging heavy loads**.** Figure 2.2 shows about 200 men dragging a colossal statue on a sledge with the help of four ropes.

Leonardo da Vinci, the technological genius of the 15th and the 16th century, made two sketches of machines for the production of ropes.
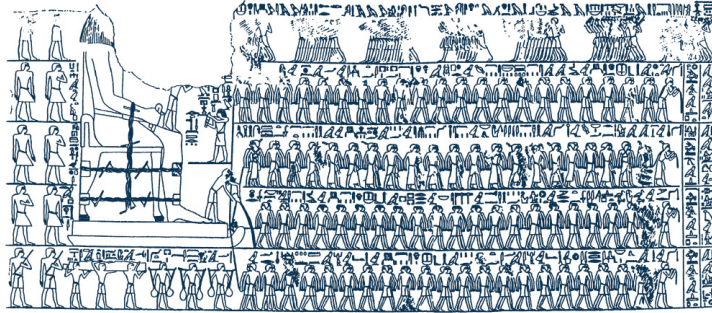
Figure 2.2: Rope application in Egypt 2000 BC.

In 1586, the papal master-builder Frederico Fontana supervises the erection of an obelisk in St.Peter's Square in Rome. After months of planning the stone weighing 327*tons* is erected by the fantastically concerted action of more than 900 men, 75 horses and with the help of a great number of reeving systems shown in Figure 2.3 [1].
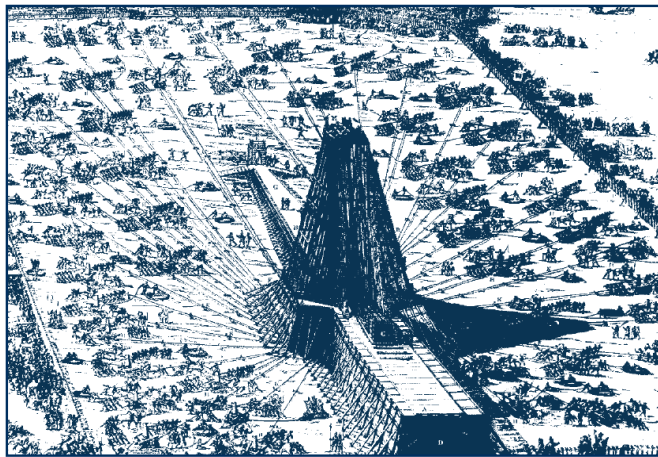
Figure 2.3: Erecting the obelisk in St.Peter's Square in 1586.

2.2   Early German and English Ropes

The first operative wire ropes of the modern era in 1834 by Wilhelm August; "Julius Albert" a 49-year-old mining engineer at Clausthal in the German silver mines Harz Mountains from 1834 to 1854. He proposed the use of ropes made from steel wires and described how to make them. The wires used were 3.5*mm* in diameter. Four wires were twisted to form a strand; three strands were twisted into the finished rope. Both strands and ropes were twisted in the same direction, i.e. they were 'lang lay' by today's terminology. The rope was dipped into a pan containing a mixture of 1/3

oil and 2/3 resin from coniferous trees. This was, as Mr. Albert stated, to protect the steel against rusting in the humid mine shafts. At the end of the production process, the ropes were formed into coils for shipment to the mine hoists. These handmade ropes, known as Albert Ropes were not very flexible because the wires were relatively large and stiff [2].

2.3   Wire Ropes and American Railroads

In Pennsylvania, a cross-country transportation system known as the Allegheny Portage RR agreed to test a handmade wire rope in 1842 as a substitute for hemp ropes.

Roebling twisted the wires together by hand, like the Albert ropes, adopted the six-strand-plus-core arrangement favored by Smith and Newall. Roebling's ropes, however, were made entirely of wire, utilizing a core that was identical to the six outer strands, each comprised of 19 wires. Roebling gave up surveying to concentrate on rope making, building a large factory in Trenton, N.J., in 1849.

In San Francisco, the dilemma of short-rope service was tackled by Thomas Seale, whose solution soon became the accepted answer to the problem of severe outerwear combined with multiple reverse bending over small-diameter sheaves. Seale's patent (#315,077 April 7, 1885) is based upon rearranging the three wire sizes into an entirely different pattern so that all the largest wire sizes are side-by-side on the exterior of the strand. James Stone's patent (#416,189 December 3, 1889) described what is now known as 6x25 filler wire construction [3].

2.4   Wire rope structure

The general geometry of a wire rope is given in Figure 2.4. Helical shaped wires are used to compose strands. Wire rope is composed by wrapping a core strand with a number of outer strands. The strands themselves have a center wire, which is the axial member around which the individual metallic wires are wrapped helically. It should be mentioned that the major portion of the load acting on a rope is carried by the strands. The main purpose of the core is to provide proper support for the strands under normal bending and loading conditions.
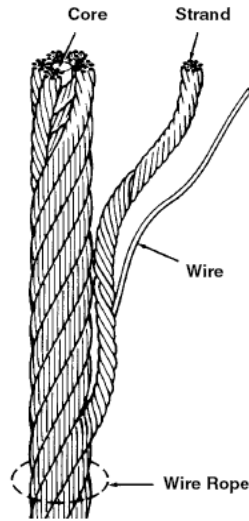
Figure 2.4: Various components of a wire rope.

Generally the wire ropes are identified by the way its strands have been laid around the core; a right regular lay, a left regular lay, a right lang lay and a left lang lay wire cores as shown in Figure 2.5.

(a) sZ   **(b)** zS   **(c)** zZ   **(d)** sS
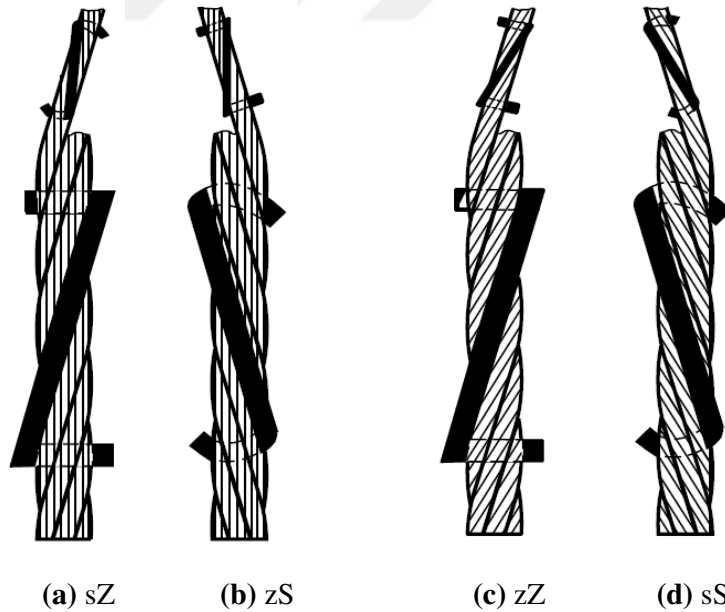
Figure 2.5: Lay types for a wire rope: (a) Right Regular Lay, (b) Left Regular Lay, (c) Right Lang Lay, (d) Left Lang Lay.

Right lang lay rope is composed by a center straight strand with right lay wrapped by a right lay outer strand. In the right regular lay rope, the lay of the wires in the outer strand is left lay, which is in opposite direction to the core strand [4]. The basic

8

element of all these cables is a simple straight strand, which is made of a core and one layer of helical wires [1]. The centre wire lay stretched in that strand whereas the other wires formed a helix. As a result, the rope elements were of different lengths and had a different shape in the rope. Moreover, it was not possible any more to inspect all the wires because the centre wire remained concealed from any angle. In Figure 2.6, a strand is composed with a straight center wire wrapped around with six helical wires as shown.
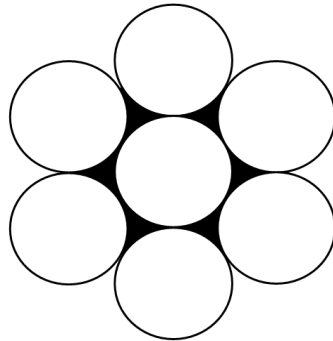
Figure 2.6: (1+6) wire strand.

Figure 2.7 shows cross sectional constructions of the basic strands: Seale, Filler, and Warrington types. In Figure 2.8 a 6x36 Warrington-Seale wire rope with steel independent wire rope core (IWRC) is presented. Figure 2.9 shows a rotation-resistant wire rope that has a steel core, which is an independent rope, closed in the opposite direction to the outer strands. Under load, the core tries to twist the rope in one direction; the outer strands try to twist it in the opposite direction.

(a) Seale 19   **(b)**   Filler strand   **(c)** Warrington strand
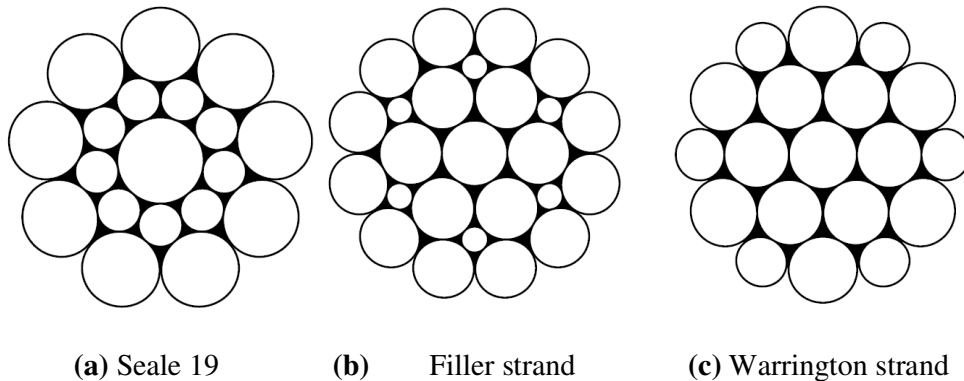
Figure 2.7: Cross sectional constructions of the basic strands.
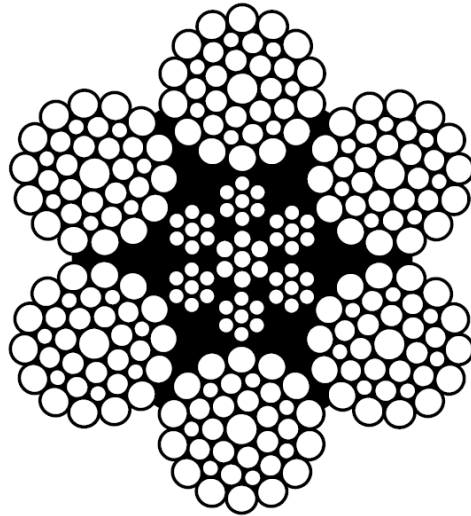
Figure 2.8: Wire rope with steel core (6x36 Warrington-Seale IWRC).
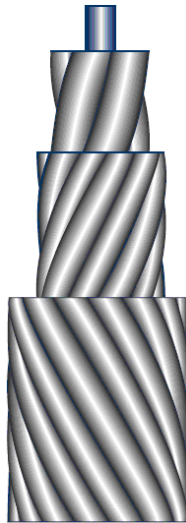
Figure 2.9: Rotation resistant rope.

3. SURVEY TO THE LITERATURE

3.1 Bases of the theory of wire ropes

Steel wire ropes have been widely employed for many different applications like, in particular, bridges and pre-stressed structures. This is why they constitute a natural field of research in civil engineering and mechanical engineering. Late 1970's wire rope theory has been widely investigated by a number of researchers because of its complex usage area.

The most analyses of wire ropes are based on the well-known classical treatise on elasticity by Love in 1944. A general theory of thin rods are included and investigated extensively by Love. General equilibrium equations of a thin rod on arc length *s* is derived and presented in [5].

The analytical and numerical solutions of wire ropes are based on the equilibrium equations as the starting point for the solutions in most of the papers included in the literature.

The mechanical behaviors of the wire ropes are investigated in a valuable reference book, which is written by Timoshenko. The reference [6] is included a chapter based on torsion and shed light to the bending analysis of the open-coiled helical springs in axial plane by bending moment and lateral load.

Green and Laws in general theory of rods [7] mentioned to a restricted and linearized form to determine stresses in helical constituent wires in cables.

Hruska's [8] pioneering study in 1951 is possibly the first paper in the literature investigating the mechanical behavior of wire ropes using the simplest constraints. However, it shed a big light to other researchers beginning from 1970's.

3.2 History of works on wire rope theory

In consequence of its complex shapes, it is a difficult task to analyze each wire in a strand to see stress and load distributions along the ropes. To cope with this difficulty

number of papers have been published which mentions the analytical solution of the wire rope theory. Pioneering works of Hruska [8-10] date back to the early fifties. He worked out a simple theory for wire ropes in tension and torsion, considering that the wires are only subjected to pure tensile forces and neglecting the clamping conditions. As a result, he did not deal with the actual contact stresses. Since then, Costello [11], and later, Utting and Jones [12,13] have followed a more fundamental approach. They treat each wire within a wire rope as a helically curved rod but make differing assumptions relative to the rope geometry or the interwire contacts. The different theories produce results, which remain close to the experimental values presented by Utting and Jones [12-13], but the question of the actual relative displacements and forces within a rope is nevertheless still open. In addition, there were numbers of theoretical studies conducted and underway.

On the other hand, at the beginning of the seventies, the finite element method used for the study of rope by Carlson and Kasper [14], who built a simplified model for armored ropes. Then, Cutchins et al. [15] dealt with the study of damping isolators. The usefulness of wire rope in shock and vibration isolation is briefly reviewed and its modeling, for the purpose of vibration analysis, is addressed in [16]. Chiang [17] modeled a small length of a single strand wire rope for geometric optimization purposes. A theoretical insight is given into the non-linear free bending characteristics of axially preloaded and large diameter sheathed spiral strands experiencing high external hydrostatic pressure in [18]. Various design methodologies of wire rope based systems are investigated in [19-22]. Analytical models of wire rope theory are compared in [23]. Finite extension of an elastic strand with a central core surrounded by a single layer of helical wires is subjected to axial forces and twisting moments. Huang uses theory of slender curved rods in his study [24]. The effect of wire rope mechanics on the material properties of cord composites, compressive loading conditions are presented in [25-28]. The bending of cord composite plates, cord composite laminate cylindrical shells, and cord composite cylindrical shells investigated respectively in [29-31]. The theoretical results are utilized to obtain analytical expressions for the maximum contact stresses induced in the multilayered strands with metallic wire core in [32]. Jiang et al. [33] proposed a concise finite element model for wire ropes using three-dimensional solid brick elements, which takes benefit from the structural and loading symmetries. The

model takes into account the combined effects of tension, shear, bending, torsion, contact, friction, and local plastic yielding in axially loaded simple straight strands nevertheless it cannot be generalized to the case of bending or more complex loadings. Nawrocki [34] et al., modeled simple straight wire rope strands using finite element method, which considers every possible interwire motion.

Mainly four theoretical models, which are important and appeared in the literatures, are presented with a brief summary.

3.3   Theoretical models

Mechanical models of helical strands are listed as follows,

- Purely tensile or fiber model,

- Semi-continuous strand model,

- Theory of thin rods model,

- Helical rod model.

Purely tensile or fiber model is due to Hruska [8], based on the most simple hypotheses; no end condition effects, contact mode is purely radial, radial contradiction is neglected, pure tensile forces are applied, there is no moments, friction can be neglected and the global strand strain is assumed small. Afterward, this theory extended to include compressible core by Knapp [35].

The analysis of fiber-core wire rope with multilayered strands developed that the rope is subjected to both an axial force and an axial twisting moment. Linear theory for helically shaped wires is used and the equations governing compliance of the fiber core are formulated in a linear fashion. The resultant linear equations are solved easily and the theory is applied to a 6x19 Seale fiber-core wire rope. A load-deformation curve for a Seale fiber-core wire rope is obtained experimentally. The theoretically predicted effective modulus of elasticity and the predicted effective Poisson's ratio of the rope compare favorably with the experimental results in [36].

Semi-continuous strand model known as orthotropic sheet model (OSM) is fist introduced by Hobbs and Raoof in 1982 [37], developed and applied in variety of problems in the literature in a number of papers [38-50]. Essentially the layers of wires in a strand are modeled as a series of cylindrical orthotropic sheets, prestressed

by the action of a mean axial load, for which the buildup of the clench forces from the outside layer inwards is obtained by solving a sequence of compatibility conditions. The properties of the orthotropic sheets can be established for the whole range between two clear limiting cases; for small load perturbations, no line-contact slip occurs, while for large enough disturbances, where fully developed slip takes place, interwire friction forces become negligible compared to force changes in the wires themselves [38].

Two semicontinuous models for wire strand analysis compared that use semicontinuous approach to predict the behavior of multilayered wire strands under axial and bending loads. Hobbs and Raoof in 1982, Jolicoeur and Cordou in 1996 develop these models. Theoretical differences and similarities between the two models are highlighted. Static stiffness results are obtained for a seven-wire steel strand and for a multilayered electric overhead conductor. In bending stiffness two discrete models referenced, Lanteigne's model [51] is accepted as an upper bound while Costello's model [11] accepted as a lower bound for bending stiffness [52].

Theory of thin rod is first introduced by Ramsey in 1988. It is based on the direct approach of Green and Laws [7], derived and applied in a restricted and linearized form to determine stresses in helical constituent wires in cables. Uniform extension, twisting, and bending of cables are considered [53].

Helical rod model is introduced by Phillips and Costello [54] based on the equilibrium equations given by Love [5]. Costello et al. investigated different aspects of wire ropes and presented them in a number of papers [54-73], and in 1990, Costello wrote a monograph summarizing these papers [11]. Recently Jiang [74] has proposed a general formulation of this theory for multi-strand ropes.

A brief survey to the literature for helical rod model is done. The literatures considered important are summarized in sorted order according to publication dates.

The solution of the problem of a helical spring subjected to an axial force and an axial twisting moment is presented in the work of Love [5].

The method of separating the cable into thin wires and solving the general nonlinear equations for the bending and twisting of a thin rod subjected to line loads. Phillips and Costello took this point of view and examined the six nonlinear equations of equilibrium for each wire. It is assumed that the cable is loaded by an axial force and

twisting moment. There are no frictional forces between the wires, and in the initial unloaded configuration of the cable, the wires are just touching each other. It is further assumed that the cable consists of a single layer of wires, and that, if the cable has a central core, the core is relatively soft in comparison to the cable wires, or it is undersized. So the radial force exerted by the core on the wires may be neglected. An exact solution for the deformed wire configuration is presented, from which all the stresses, bending, twisting, axial loading, and contact can be calculated [54].

Taking advantage of geometric considerations explicit expressions for the determination of axial force, bending and twisting moments in the helical wires, and for the axial force and twisting moment in the core of a 7-wire strand subjected to axial and torsional displacements are given. Each helical wire assumed to be in contact with the two adjacent wires, with the core, or with both core and adjacent wires. The analytical expressions for axial force, bending moment, twisting moment and contact forces between wires are presented. At the end, experimental and theoretical findings are compared. The small lay angle and consequent large helix radius of the model produces only a small contact force, and so a small friction force. This helps to explain the agreement with the theory, which neglects frictional forces [75].

In the papers [54,64], the cable is separated into thin helical wires, and the general nonlinear equations of equilibrium for each wire, including the effects of contact line loads are solved. Friction is neglected, and the wires are assumed inextensible. Costello neglected friction again, but the inextensibility assumption is removed so the wire strain becomes a new independent variable. Although the wire strain is assumed to be small, it is still possible to have large cable strains if the change in helix-angle is large. In addition, a prediction of the effective modulus of twisted wire cables by investigating the load-deflection curves at zero loads for two common types of end-condition is given in [63].

The spring which is considered curved thin rod, can suffer large deformations. The solution is exact in those six nonlinear equations of equilibrium given in [5] and satisfied. If the spring is not permitted to expand radially by some type of cylindrical constraint, the spring stiffness will increase. Costello investigated the pure bending of a helical spring with large deflections in [56].

Costello presents static behavior of wire rope with a frictionless theory. The solution shows that it is valid for complex cross sections that are usually found in practice [61].

Wires of a strand, which is wound in different directions, is considered for the static response by Costello. In the right lay-regular lay rope under tension, a tightening up of wires in the strand is produced. Numerical results for two cases presented; (i) ropes with zero end-moment and (ii) ropes restraint against rotation. The usage conditions for lang lay rope and regular lay ropes are compared. A lang lay rope should never be used where the ends of the rope are free to rotate [4].

The initial configuration of a rope, consisting of a left lay rope and a right lay outer rope, which will not rotate under axial loading, is determined in [62]. Friction is neglected and results are produced for a 1x19 rope. The theory can be applied to ropes with various other cross sections.

The static response of wire rope subjected to tension, torsion and bending which occurs frequently in ropes wrapped around sheaves is analyzed. Since the rope is generally restraint against rotation, a twisting moment is developed in the rope in addition to the tension and bending in [58].

Velinsky presents a theory that will predict the axial static response of a wire rope with complex cross sections such as a 6x19 scale IWRC. The results show that, if the rope is not allowed to rotate, the maximum tensile stress occurs in the center wire [60,76].

The mechanical behavior of ACSR (aluminum conductor steel reinforced) conductors under static-loading conditions, which may comprise any combination of tension, torsion and bending, is concerned. A stiffness matrix is developed and relations are presented for axial, torsional, and flexural rigidities and for coupling parameters. Results obtained for bending is compared with Costello [59] and found in good relation [51].

The length, measured from the fractured end of a wire, in which the wire will be able to carry its appropriate share of the load, is determined in [71]. This effective length estimation is based on the contact loads between the wires, Coulomb type friction, and Saint-Venant's principle. A simple straight strand is considered and the result indicate that a broken center wire picks up its appropriate load in less that 1.25 times

the pitch of the outer six wires. In the Seale IWRC wire rope, an outer wire picks up its share of the load in less than 1.18 times the pitch of the strands. The theory indicates that this effective length to the pitch of the outer strand is a constant for a given type cross section [71].

Stresses in the individual wires of complex wire rope are determined for rope constructions having an internal-wire-rope-core. The ropes may be pulled, twisted, and bent over a sheave or a drum. The effects of friction are neglected. Specific results for a 6x25 filler-wire IWRC rope that is prevented from twisting indicate that the maximum stresses are typically 1.5 to 3 times as large as the nominal rope stress based on rope load and total metallic area. In addition, predicted values of the "effective modulus" are slightly higher than given in the literature for the IWRC. The results may be extended by superposition to include the important case of loaded ropes pulled over a sheave or bent around a drum [73].

A general nonlinear theory has been developed to analyze complex wire ropes by Velinsky. The nonlinear equations of equilibrium for bending and twisting of thin rods are applied to a 6x19 Seale wire rope with an IWRC. The results of the nonlinear theory are compared to the recently developed linear theory and found to be nearly identical in the load range in which the most wire ropes are used. At the end, it has been concluded in [77] that the nonlinear theory for complex wire rope has no significant advantage over the linear theory.

Closed-form solutions are developed for elastic deformation characteristics of multilayered strands under tensile and torsional loads. These analytical results are applied to obtain expressions for the effective extensional and torsional moduli of rigidity for the strands. The effects of the layout of layers, number of wires in each layer, and of course, the direction and magnitude of lay angles on these important deformation characteristics are clearly described. The examples considered in the paper demonstrate the computational ease and effectiveness with which the closed-form solution can be utilized in various studies [78].

Velinsky presents a design methodology for wire strand geometry based on a detailed geometrical analysis. The nonlinear geometric equations were solved numerically and then, the solutions were curve fit such that strand design could be accomplished by merely substituting values into polynomial expressions [79].

Different types of cores; independent wire-rope-core (IWRC), fiber core (FC), and wire-strand-core (WSC) are examined and the mechanics of wire ropes described respectively. Various parameters in the design of wire ropes are examined in [80].

Jiang presents a general formulation of the nonlinear and linear analysis of wire ropes. In the formulation, wires, strands, and wire ropes are all considered as a kind of identical structure, which is characterized by seven stiffness and deformation constants, and they can be used in the same way, as component elements in some layered general structures. Based on this point, the general formulation given to analyze; wire ropes of various complex cross sections and simple wire strands as well in [74].

A symmetric linear elastic model for helical wire strand has been derived using discrete thin rod theory by Sathikh et al. A strand with a rigid core and one layer of helical wires having only core-to-wire contact (resting lay) has been analyzed taking into account the wire tension, twist and bending together, for its response under axisymmetric axial tension and torsion. The authors derive the symmetric stiffness matrix. Analysis of the derived model showed that earlier models, in spite of lacking symmetry of the stiffness matrix, do not cause any significant error over a wide range of helical angles. It has also seen that Costello's model [63] is much closer to the test measurements in spite of lack of symmetric stiffness matrix. Also a brief comparison of models given in the literature in [8,35,63,51,75,78,81] are compared [82].

Numbers of thesis are conducted over the wire rope theory and analysis. A theory is developed which is capable of analyzing the static response of wire ropes with complex cross sections. The basis of the theory is the linearization of the solution to the non-linear equations of equilibrium, which the individual wires in the rope are examined in [76].

A geometrically nonlinear formulation for forces on wire ropes is presented which includes the coupling between the axial and torsional behavior of the ropes in [83].

By analyzing the stresses of individual wires for a loaded and bent 6x19 Seale IWRC, $(D/d)\sigma_{nom}/E - \sigma_{max}/\sigma_{nom}$ diagram is plotted. When the sheave diameter, rope diameter and load are known, an estimate of the stresses of individual wires for a 6x19 Seale IWRC can be determined by using the related diagram [84].

18

The formulation of helically symmetric boundary conditions is used and a general strand model using the finite element method is presented for a basic sector of a simple straight strand in [85].

3.4   Experimental studies

Stress distribution and load transfer on wire strands subjected to various loading conditions is tested experimentally. General considerations on geometry of the strand are; ideal strand, variations from the ideal case and non-linear behavior is expressed. The four important loads considered and presented are; axial load with the ends of the strand restrained from rotation, axial load with the ends free to rotate, torsion and bending. The deviations from the theoretically predicted ideal behavior are surprisingly large, and the experimental results show non-linear elastic behavior. Those deviations may be due to initial irregularities in geometry of the strand, e.g., gaps between wires, different length of wires, etc [86].

Utting and Jones report experimental tests on wire rope strands subjected to static axial loads. The wire rope strands are held with a polyester resin and silica filler in conical end grips, which are capable of full end fixity, partial restraint, or zero torsional resistance (free ends). Strain gauge load cells monitor the tensile load and the associated twisting moment developed in a strand, which is restrained at both ends. A new instrument 'extrometer' designed to record simultaneously the extension and rotation over a predetermined gauge length. Strain gauges are used to measure the surface strains on the wires in the outer layer of the strand. Preliminary tests on seven-wire strands demonstrated that the extrometer instrument provides reliable results [87].

A series of carefully instrumented tests on straight steel strands of seven-wire construction having a range of practical lay angels are presented in [12]. Details of the tests are given in the article and a new mathematical model for the strand response is presented which takes account to friction between the individual wires, Poisson ratio effects and flattening of the individual wires in Part I [12].

Part II [13] is a companion paper to part I of [12]. Theoretical predictions with previously published analytical work and the corresponding experimental results reported for the following situations. Torque generated in a strand under axial

loading found to be larger in strands with smaller helix angles. The strand extension under a given load is greater for strands with less torsional restraint on the end terminations. The strand rotation under a given loading found to be greater with less torsional restraint on the end terminations and is larger for strands with a lower helix angle. The numerical predictions for the surface strains on the helical wires, which take account of interwire friction, are closer to the experimental results at the mid-strand. The surface strains measured on the helical wires reveal an unevenness of loading between the wires that is more pronounced for small torsional restraints on the strand ends [13].

Raoof and Hobbs reported torsional characteristics of substantial structural strands. Experimental results for an old and fully bedded-in 39mm diameter, 91-wire spiral strand and some theoretical predictions are given. The theory treats the individual layers of wires in a strand as orthotropic sheets and, via established results in contact stress theory, takes full account of the frictional interactions between wires. Static and dynamic torsional stiffness and hysteresis data are presented for axially preloaded strands [88].

3.5   Recent publications about wire ropes

A finite element model of a seven-wire strand is considered to establish the termination effects. The cyclic symmetric features of the strand are taken into account to reduce the length of the model. In addition, the fixed-end termination effects over the contact forces and the relative movements between wires along the contact line are considered using frictional effects in the spiral strands in [89].

A concise finite element model, which takes full advantage of the helical symmetry features of a strand, has been developed for a simple straight strand in [90]. Taking the advantage of the helical symmetry of a strand, a slice of 1/12 of a 7-wire strand has been considered as the basic sector for the analysis with ANSYS program. Three-dimensional solid brick elements used for structural discretization. In the implementation of the finite element analysis, precise boundary conditions were established and hence more accurate are obtained. The results are compared with elasticity theory of Costello [11] and experimental data of Utting and Jones [12,13], and shows excellent agreement in the determination of the global responses of a simple straight wire rope strand [33]. Also as a continuous study, a three-layered

20

form to show axial loadings of a simple straight strand is presented in [90]. The formulation of helically symmetric boundary conditions for finite element modeling is explained in [91].

Nawrocki has given a finite element model of a simple straight strand based on a Cartesian isoparametric formulation. Every possible interwire motion is taken into account. Interwire pivoting is shown to be the most important and rules the axial strand behavior, and interwire sliding is predominant in bending. Comparisons with experimental data showed that pivoting could be considered as free in a real strand. A variational and then a finite element formulation of the problems are given. It has been shown that bending has no influence on the core tension [34].

For simulating the mechanical response of a wire rope with an IWRC, a new model, which fully considers the double-helix configuration of individual wires within the wound strand in contrast to the previous models that, considers the effective response of wound strand. This enables directly to relate the wire level stress to the overall applied load at rope level. The model assumes a fiber response of individual wires [92].

The modeling of the axial behavior of synthetic ropes is presented. The structures considered are simple straight strand cables consisting of six helical wires wrapped around a straight core. The loading consists of an axial force and torque. The objectivity of the study is to determine the validity domain of the two analytical models developed by Costello and Labrosse for the predictions of the corresponding four stiffness matrix components. Reference results are obtained from SAMCEF finite element code. The validity of this model is limited to small helix angles but for typical synthetic rope constructions, these are within range [94].

Ghoreishi et al have developed a non-linear elastic continuum model for the analysis of the overall axial stiffness of fibrous structures with a large number of twisted components. By contrast with multilayered approaches, the structure under consideration is depicted as a set of coaxial helixes only characterized by their external lay angle and corresponding radius. The constitutive material is assumed linear. Static monotonic axial loads are considered, the inter-fiber friction effects are not taken into account. Moreover, the studied structures exhibiting small lay angles, the overall diametric contractions are neglected, which may contribute to the overestimation of stiffness. The analytical model developed leads to useful closed-

form expressions thus allowing rope constructions to be optimized. The model compared with models of the literature. The results obtained, have shown that all the models give results that agree reasonably well with each other, except with respect to the torsion stiffness, for which there is a significant difference [95].

Ghoreishi et al have developed a linear elastic model for the computation of the elastic axial stiffness terms of a fibrous structure, made of six helical strands wrapped around a straight core (1+6 wire structure). A model designed for metallic cables has been modified for synthetic fiber ropes applications. The bending moments and shear forces are neglected. The elastic tensile and torsion behavior of constituents are taken into account, with coupling which appears from the construction effect. The approach developed by the authors leads to analytical closed-form expressions. The model has first compared with Leech's model implemented in FRM software and gave to provide similar results, except with respect to the torsion term, for which there is a significant difference [96].

Throughout the literature search, Jiang et. al. investigated simple straight strands numerical models considering only basic sectors and analyzed by using the finite element method in [33,89-91]. In addition, Nawrocki-Labrosse studied all the possible interwire motions by writing a code using finite element method. Elata et.al. gave an illustration for an IWRC model using double helical parametric equations and conducted an analytical model in their study [92]. There were no realistic 3-D IWRC solid modeling scheme is available in the literature. One of the aims of this thesis is to give an insight to model a complex shaped design of wire rope such as IWRC and Seale IWRC using the advantage of the nested (double) helical geometry. In addition, different loading conditions are investigated using 3-D solid models. Various lay types of IWRCs are modeled and analyzed numerically. Through this research, modeling nested helical wires are found to be complicated via CAD software's and a new code is written to accomplish this issue. In addition, the length limitation of the current CAD tools are confronted as a problem and a solution strategy is developed for modeling complex wire ropes. An extensive literature search is given in this study. Validity of the proposed modeling approach is provided by the comparison of numerical, analytical, and available test results in literature. An application of the proposed modeling scheme is applied to wire rope bent over sheave problem. While bending problem solution process, reaction force distribution

22

over the encastre boundary is investigated. In addition, stress distribution over the IWRC is presented. Finally, a 6x19 wire Seale IWRC model is constructed and analyzed. Wire behavior under axial loading condition on a Seale IWRC is investigated. At the end a simple straight strand solid model for 1m-5m is created and an axial loading analysis is conducted to show the proposed solid modeling schemes accuracy to analyze wire ropes without lack of any length limitation. In this aspect wire rope behavior is analysed with different lay lengths using 1m-5m wire strand models. In addition, interactions between wires, which brings contact force and contact pressure is analyzed over a wire strand. Due to contact interactions, there occurs a deformation in each wire within a strand. Wire contraction is measured with respect to strain and results are presented.

4. WIRE ROPE THEORY

In this chapter, a general wire rope theory is presented. First of all the kinematics of a thin wire is derived, subsequently general equilibrium equations are given and proved over a thin wire.

4.1 Deformations over a rod and relations with a helical spring

A coordinate system, with a standard basis $\{e_1, e_2, e_3\}$ is defined over an undeformed straight rod, which can be predicted as a cylinder in 3-D system. Position vector of a material particle at the reference configuration is $x = x_i e_i$, where $x_1 = x_2 = 0$ corresponds to the centroid of the cross section which is a circle, and x_3 is the height above the base of the cylinder. After deformation, the axis of the cylinder lies on a smooth curve and the point $x = x_3 e_3$ moves to a new position $x' = r(x_3)$. Deformed cross-section are shown by a new basis which is $\{v_1, v_2, v_3\}$ and, v_3 is chosen to be parallel to the axis of the deformed rod, v_1 is parallel to the line of material points at the cross section and perpendicular to v_3, and it should be impressed that the new basis vectors are all functions of x_3. Deformed cross-section and its representation by using $\{v_1, v_2, v_3\}$ basis are related with the Euler angles (θ, ϕ, ψ). Euler angles are a means of representing the spatial orientation of any frame of the space as a composition of rotations from a reference frame. In the following, the fixed system is denoted by $\{e_1, e_2, e_3\}$ and the rotated system is denoted by $\{v_1, v_2, v_3\}$. The definition is static. The intersection of $e_1 e_2$ and $v_1 v_2$ coordinate planes is called the *line of nodes* (Q) and given in Figure 4.1.

- ϕ is the angle between the e_1-axis and the line of nodes Q,

- θ is the angle between the e_3-axis and the v_3-axis,

- ψ is the angle between the line of nodes Q and the v_1-axis.
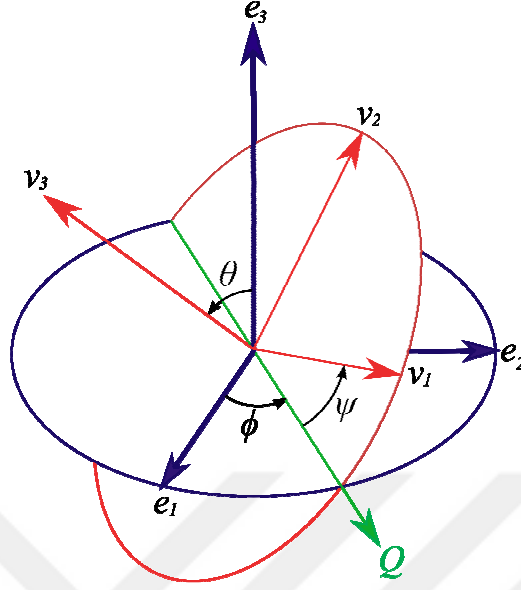
Figure 4.1: Euler angles and cylindrical coordinates over a cross-section.

Let s denote the arc length of the rod in deformed configuration and velocity vector is given by $V = \dfrac{dr}{dt}$. Rate of rotation of the rod is given by the angular velocity $\omega = \omega_i v_i$ of the basis $\{v_1, v_2, v_3\}$ and it is related by velocity vector V and the twist ψ by,

$$\omega = v_3 \times \frac{dV}{ds} + \psi v_3 .$$

Over the deformed curve; tangent vector, normal vector and curvature, and binormal vector are defined respectively as,

$$t = \frac{dr}{ds} = \frac{dr}{dx_3}\frac{dx_3}{ds} = v_3, \quad \kappa n = \frac{dt}{ds} = \frac{dv_3}{dx_3}\frac{dx_3}{ds}, \quad b = t \times n,$$

where n is a unit vector. These vectors correspond to a basis of $\{t, n, b\}$ and known as Frenet-Serret triad. The torsion of the curve is defined as $\tau = -n\dfrac{db}{ds}$. Relation of $\{e_1, e_2, e_3\}$ and $\{v_1, v_2, v_3\}$ basis with respect to Euler angles are given in equation (4.1),

$$v_1 = \left(\cos\psi\cos\theta\cos\phi - \sin\psi\sin\theta\right)e_1 + \left(\cos\psi\cos\theta\sin\phi + \sin\psi\cos\theta\right)e_2$$
$$- \cos\psi\sin\theta e_3,$$
$$v_2 = -\left(\cos\psi\sin\phi + \sin\psi\cos\theta\cos\phi\right)e_1 + \left(\cos\psi\cos\phi - \sin\psi\cos\theta\sin\phi\right)e_2 \quad \textbf{(4.1)}$$
$$+ \sin\psi\sin\theta e_3,$$
$$v_3 = \sin\theta\left(\cos\phi e_1 + \sin\phi e_2\right) + \cos\theta e_3.$$

The basis $\{v_1, v_2, v_3\}$ moves through the deformed rod. In this aspect the basis vector $\{v_1, v_2, v_3\}$ is rotated with an angular velocity which depends on curvature and twist along the deformed rod. The system of axes constructed is called as the "principal torsion-flexure axes" of the wire at any point on the deformed state. Curvature vector is characterized the rate of change with arc-length and defined with respect to the basis vectors $\{v_1, v_2, v_3\}$, as $\kappa = \kappa_i v_i$, and similar to an angular velocity vector. The curvature vector is related to the rate of change of v_i with s by $\dfrac{dv_i}{ds} = \kappa \times v_i$, and can be written for $i = 1, 2, 3$ as,

$$\frac{dv_1}{ds} = -\kappa_2 v_3 + \kappa_3 v_2, \quad \frac{dv_2}{ds} = \kappa_1 v_3 - \kappa_3 v_1, \quad \frac{dv_3}{ds} = -\kappa_1 v_2 + \kappa_2 v_1. \qquad \textbf{(4.2)}$$

The derivatives, $\dfrac{dv_i}{ds}$ with respect to s, can be computed in terms of the Euler angles. The following equation shows the derivative of v_3 with respect to s,

$$\frac{dv_3}{ds} = \cos\theta\frac{d\theta}{ds}\left(\cos\phi e_1 + \sin\phi e_2\right) + \sin\theta\left(-\sin\phi e_1 + \cos\phi e_2\right)\frac{d\phi}{ds} - \sin\theta\frac{d\theta}{ds}e_3. \quad \textbf{(4.3)}$$

In addition, it is straightforward to find the derivatives with respect to $i = 1, 2$. After the derivatives are computed as in equation (4.3), one can construct a system of equations relating these derivatives by using equations given in (4.2) with curvatures κ_1, κ_2 and the twist κ_3 by putting the equation (4.1) in (4.2) to relate the $\{v_1, v_2, v_3\}$ basis with the $\{e_1, e_2, e_3\}$ basis. One can solve these systems of equations to find unknown curvatures κ_1, κ_2 and the twist κ_3 related to the Euler angles as follows,

$$\kappa_1 = \sin\psi\,\frac{d\theta}{ds} - \cos\psi\,\sin\theta\,\frac{d\phi}{ds},$$

$$\kappa_2 = \cos\psi\,\frac{d\theta}{ds} + \sin\psi\,\sin\theta\,\frac{d\phi}{ds}, \qquad \textbf{(4.4)}$$

$$\kappa_3 = \frac{d\psi}{ds} + \cos\theta\,\frac{d\phi}{ds}.$$

Arc length s along the rod's centerline is related to the position vector of the rod's axis by,

$$\frac{ds}{dx_3} = \sqrt{\frac{dr}{dx_3}\frac{dr}{dx_3}}. \qquad \textbf{(4.5)}$$

4.2 Rod bent and twisted into a single helix

Consider an initially straight and unstressed rod with a circular cross-section. Then it is subjected to forces F and moments M on its ends to bend and twist it into a helical shape with helix radius r, helix angle α, pitch length of the helix is given as p and related to helix angle α as, $\tan\alpha = \dfrac{p}{2\pi r}$. The deformed rod geometry is easily explained by using the cylindrical coordinate system $\left(r,\hat{\theta},z\right)$ and basis $\{e_r,e_\theta,e_z\}$ as shown in Figure 4.2.
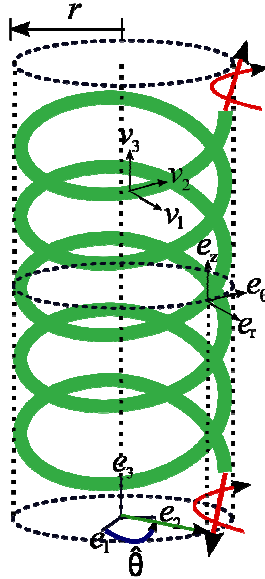
Figure 4.2: Cylindrical coordinate system $\left(r,\hat{\theta},z\right)$ and basis $\{e_r,e_\theta,e_z\}$.

Tangent and binormal vectors are written in terms of basis vectors as,

$$t = v_3 = \cos\alpha e_\theta + \sin\alpha e_z,$$
$$b = -\sin\alpha e_\theta + \cos\alpha e_z. \tag{4.6}$$

Taking $\hat{\theta} = z = 0$ at $s = 0$, cylindrical polar coordinates are related to arc-length by,

$$\hat{\theta} = \frac{s}{r}\cos\alpha, \ z = s\sin\alpha, \tag{4.7}$$

and the basis vectors are also satisfies,

$$\frac{de_r}{d\hat{\theta}} = e_\theta, \ \frac{de_\theta}{d\hat{\theta}} = -e_r, \ \frac{de_z}{d\hat{\theta}} = 0. \tag{4.8}$$

Using the relations given in equations (4.7) and (4.8) derivatives $\dfrac{de_r}{ds}$, $\dfrac{de_\theta}{ds}$ and $\dfrac{de_z}{ds}$ are given in the following form,

$$\frac{de_r}{ds} = \frac{\cos\alpha}{r}e_\theta, \ \frac{de_\theta}{ds} = -\frac{\cos\alpha}{r}e_r, \ \frac{de_z}{ds} = 0. \tag{4.9}$$

The position vector of a point on the axis of the rod is given as,

$$\mathrm{r} = re_r + ze_z, \tag{4.10}$$

and the tangent vector v_3 can be written with respect to this position vector as,

$$\frac{d\mathrm{r}}{ds} = r\frac{de_r}{ds} + \frac{dz}{ds}e_z, \tag{4.11}$$

which gives,

$$t = v_3 = \cos\alpha e_\theta + \sin\alpha e_z. \tag{4.12}$$

4.3 Curvatures and twist definition over a helical spring

Over a helical spring using the preceding theory, choosing v_1 and v_2 parallel to the normal vector n and binormal vector b of the undeformed spring respectively gives the relation,

$$v_1 = -e_r \tag{4.13}$$

$$v_2 = -\sin\alpha e_\theta + \cos\alpha e_z, \tag{4.14}$$

and v_3 as can be written from the equation (4.12) as,

$$v_3 = \cos\alpha e_\theta + \sin\alpha e_z. \tag{4.15}$$

Taking the derivatives of equation (4.13)-(4.15) with respect to s gives the following,

$$\frac{dv_1}{ds} = -\frac{de_r}{ds}, \quad \frac{dv_2}{ds} = -\sin\alpha\frac{de_\theta}{ds} + \cos\alpha\frac{de_z}{ds}, \quad \frac{dv_3}{ds} = \cos\alpha\frac{de_\theta}{ds} + \sin\alpha\frac{de_z}{ds}. \tag{4.16}$$

Using the relations given in equation (4.9),

$$\frac{dv_1}{ds} = -\frac{\cos\alpha}{r}e_\theta, \quad \frac{dv_2}{ds} = \frac{\sin\alpha\cos\alpha}{r}e_r, \quad \frac{dv_3}{ds} = \frac{-\cos^2\alpha}{r}e_r. \tag{4.17}$$

The equations given in (4.13)-(4.15) can be put in equations (4.2) to find the relations of this derivatives with Euler angles and simplifying the equations will give the relations as follow,

$$\frac{dv_1}{ds} = \left(-\kappa_2\cos\alpha - \kappa_3\sin\alpha\right)e_\theta + \left(-\kappa_2\sin\alpha + \kappa_3\cos\alpha\right)e_z,$$

$$\frac{dv_2}{ds} = \kappa_3 e_r + \kappa_1\cos\alpha e_\theta + \kappa_1\sin\alpha e_z, \tag{4.18}$$

$$\frac{dv_3}{ds} = -\kappa_2 e_r + \kappa_1\sin\alpha e_\theta - \kappa_1\cos\alpha e_z.$$

The equations given in (4.17) and (4.18) constructs a pair for each derivatives of v_i and could be solved for the curvatures κ_1, κ_2 and the twist κ_3 as,

$$\kappa_1 = 0, \quad \kappa_2 = \frac{\cos^2\alpha}{r}, \quad \kappa_3 = \frac{\sin\alpha\cos\alpha}{r}. \tag{4.19}$$

These curvatures and twist $\left(\kappa_1, \kappa_2, \kappa_3\right)$ are named as $\left(\kappa_0, \kappa_0', \tau_0\right)$ in the proceeding sections while the angular velocity is defined as,

$$\vec{\omega}_0 = \frac{2\pi}{2\pi r_0 / \cos\alpha_0} \vec{k} = \frac{\cos\alpha_0}{r_0} \vec{k}, \qquad (4.20)$$

where $\vec{k}$ is the unit vector in the direction of z as shown in Figure 4.3, α_0 is the helix angle with (x_1, y_1) plane, r_0 is the helix radius. The curvatures and twist is defined in the initial condition as,

$$\kappa_0 = 0; \quad \kappa_0' = \frac{\cos^2\alpha_0}{r_0} \quad \text{and} \quad \tau_0 = \frac{\sin\alpha_0 \cos\alpha_0}{r_0}. \qquad (4.21)$$
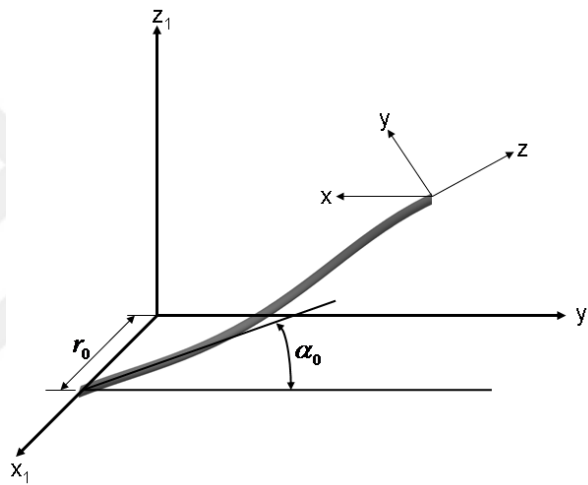
Figure 4.3: Undeformed helical spring and torsion-flexural axis.

4.4   Loads and moments acting on a thin wire

A loaded thin wire, with the force distribution over it, is shown in Figure 4.4.
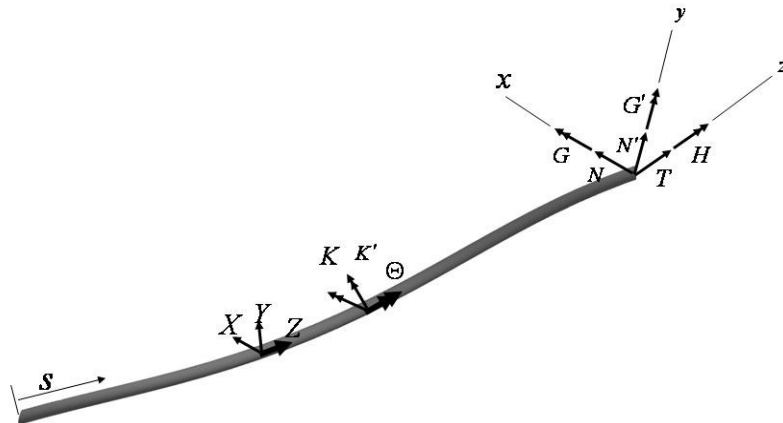
Figure 4.4: Loads and moments over a thin wire.

31

The arc length is described by the variable s over the thin wire. The direction cosines of the forces $N + dN$, $N' + dN'$ and $T + dT$ with the x, y and z axes are given in Table 4.1.

Table 4.1: Direction cosines for the forces.

Direction cosines	$N + dN$	$N' + dN'$	$T + dT$
l	1	$-\tau ds$	$\kappa' ds$
m	τ	1	$-\kappa ds$
n	$-\kappa' ds$	$\kappa' ds$	1

Summation of the forces in the x direction gives $\sum Fx = 0$, resulting,

$$N + dN - N + Xds + (T + dT)\kappa' ds + (N' + dN')(-\tau)ds = 0, \qquad \textbf{(4.22)}$$

where $dsdT = 0$ and $dsdN' = 0$ can be taken such that, due to the small value of ds, dT and dN', and their multiplication can be neglected for this reason here. If the necessary simplifications are made in equation (4.22), it becomes to,

$$Xds + dN + T\kappa' ds - N'\tau ds = 0. \qquad \textbf{(4.23)}$$

In a similar way, summation of the forces in y direction gives $\sum Fy = 0$, resulting,

$$N\tau ds + dN\tau ds + N' + dN' - T\kappa ds - \kappa dTds + Yds - N' = 0, \qquad \textbf{(4.24)}$$

where $dsdN$ and $dsdT$ are taken as zero because of the assumption of small values of each multiplier considered in the same way. If the necessary simplifications are made in equation (4.24), it becomes to the form,

$$Yds + dN' - T\kappa ds + N\tau ds = 0. \qquad \textbf{(4.25)}$$

At the end, the same procedure can be applied to the summation of the forces in z direction which gives, $\sum Fz = 0$, resulting,

$$-N'\kappa' ds - dN\kappa' ds + N'\kappa ds + dN'\kappa ds + T + dT - T + Zds = 0, \qquad \textbf{(4.26)}$$

where $dsdN$ and $dsdN'$ are taken as zero. If the necessary simplifications are made in equation (4.26), it becomes to the form,

$$Zds + dT - N\kappa'ds + N'\kappa ds = 0. \qquad (4.27)$$

If equations (4.23), (4.25) and (4.27) are divided by ds in x, y and z directions respectively, the following equations are obtained,

$$\frac{dN}{ds} - N'\tau + T\kappa' + X = 0, \qquad (4.28)$$

$$\frac{dN'}{ds} - T\kappa + N\tau + Y = 0, \qquad (4.29)$$

$$\frac{dT}{ds} - N\kappa' + N'\kappa + Z = 0. \qquad (4.30)$$

Similarly the same element length ds with the couples $G + dG$, $G' + dG'$ and $H + dH$ makes the same angles with x, y and z axes as in the previous loads. In the same way using Table 4.1 and taking into account the right hand rule, the following equations for the moments in x axes can be written as,

$$G + dG - G + Kds - \tau G'ds - \tau dG'ds + \kappa'Hds + \kappa'dHds - N'ds = 0. \qquad (4.31)$$

Simplifying the equation (4.31), the following is found,

$$dG - G'\tau ds + H\kappa'ds - N'ds + Kds = 0. \qquad (4.32)$$

In a similar way, the moments by summations over y and z axes in a simplified manner yields,

$$dG' - H\kappa ds + G\tau ds + Nds + K'ds = 0, \qquad (4.33)$$

$$dH - G\kappa'ds + G'\kappa ds + \Theta ds = 0. \qquad (4.34)$$

Again dividing by ds and rearranging equations (4.32)-(4.34) gives,

$$\frac{dG}{ds} - G'\tau + H\kappa' - N' + K = 0, \qquad (4.35)$$

33

$$\frac{dG'}{ds} - H\kappa + G\tau + N + K' = 0, \tag{4.36}$$

$$\frac{dH}{ds} - G\kappa' + G'\kappa + \Theta = 0. \tag{4.37}$$

These equations, (4.28)-(4.30) and (4.35)-(4.37), are the six differential equations which constitutes the equations of equilibrium for the thin wire loaded and shown in Figure 4.4.

4.5 Relations between loads and deformations

The changes in curvature and twist per unit length to the internal loads are given by the expression below [11],

$$G = EI_x(\kappa - \kappa_0); \quad G' = EI_y(\kappa' - \kappa_0'); \quad and \quad H = C(\tau - \tau_0), \tag{4.38}$$

where the thin wire is assumed elastic with cross-sectional moments of inertia I_x and I_y. The torsional rigidity and the modulus of elasticity of the wire material are denoted by C and E respectively. When the wire cross section is circular, with radius R, the equation (4.38) becomes to the following formulation,

$$G = \frac{\pi R^4}{4}E(\kappa - \kappa_0); \quad G' = \frac{\pi R^4}{4}E(\kappa' - \kappa_0'); \quad and \quad H = \frac{\pi R^4 E}{4(1+v)}(\tau - \tau_0), \tag{4.39}$$

where v is Poisson's ratio for the wire material. The tension T in the wire is given by the expression,

$$T = AE\xi, \tag{4.40}$$

where A is the cross-sectional area of the wire and ξ is the axial wire strain. For a circular cross section, $A = \pi R^2$, and the equation (4.40) becomes to,

$$T = \pi R^2 E\xi. \tag{4.41}$$

4.6 Geometric consideration of a straight strand

A loaded simple straight strand is shown in Figure 4.5. Configuration and cross section of this strand consists initially of a straight center wire of radius R_1, surrounded by $m = 6$ helical wires of radius R_2. Center wire radius is chosen sufficiently such that to prevent outer wires touching each other. This is the general aim to decrease frictional effects due to bending of the strand.
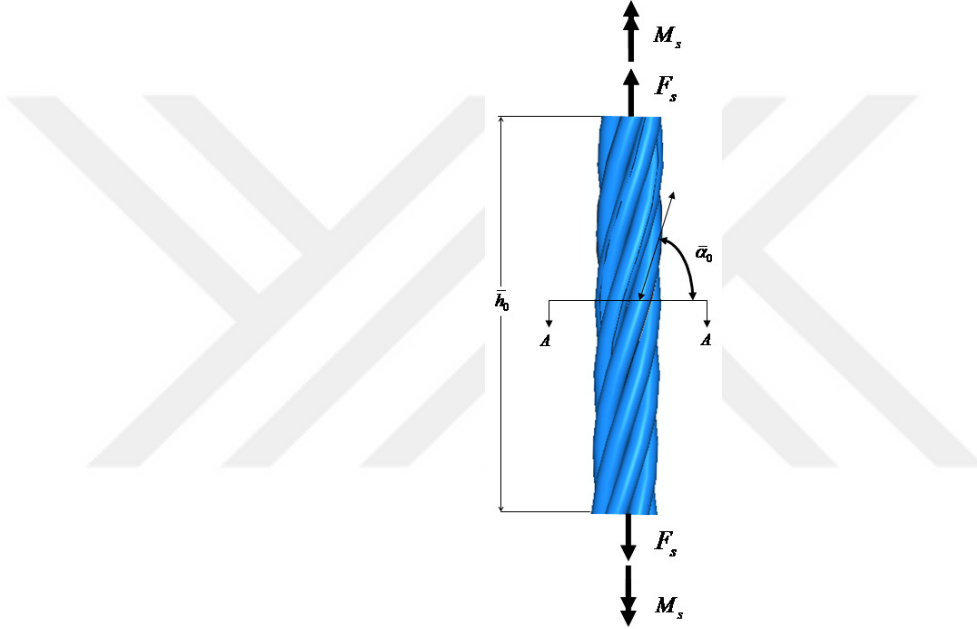
Figure 4.5: Axially loaded simple straight strand

The initial helix radius of an outside wire is given by,

$$r_2 = R_1 + R_2. \tag{4.42}$$

Minimum value for R_1 which will prevent the outer wires to touch each other should be found. To do this, first consider m helical wires in a strand just touching each other. Cross-section perpendicular to the strand is shown in Figure 4.6. Radius of the helix, the wire radius and the helix angle are denoted by r, R and α respectively. The cross-section is assumed elliptical and hence the equation for this cross-section can be given as,

$$\left(\frac{p}{R/\sin\alpha} \right)^2 + \left(\frac{q}{R} \right)^2 = 1, \tag{4.43}$$

35

where (p, q) shows a point on the ellipse. From equation (4.43) the following equation can be written for q,

$$q^2 = \left(1 - \frac{p^2 \sin^2 \alpha}{R^2}\right) R^2,$$

and it is found to be,

$$q = \pm\sqrt{R^2 - p^2 \sin^2 \alpha}. \qquad \textbf{(4.44)}$$

The slope of $\dfrac{dq}{dp}$ is represented by differentiating the equation given for q as,

$$\frac{dq}{dp} = \pm \frac{p \sin^2 \alpha}{R\sqrt{1 - \left(\dfrac{p \sin \alpha}{R}\right)^2}}. \qquad \textbf{(4.45)}$$
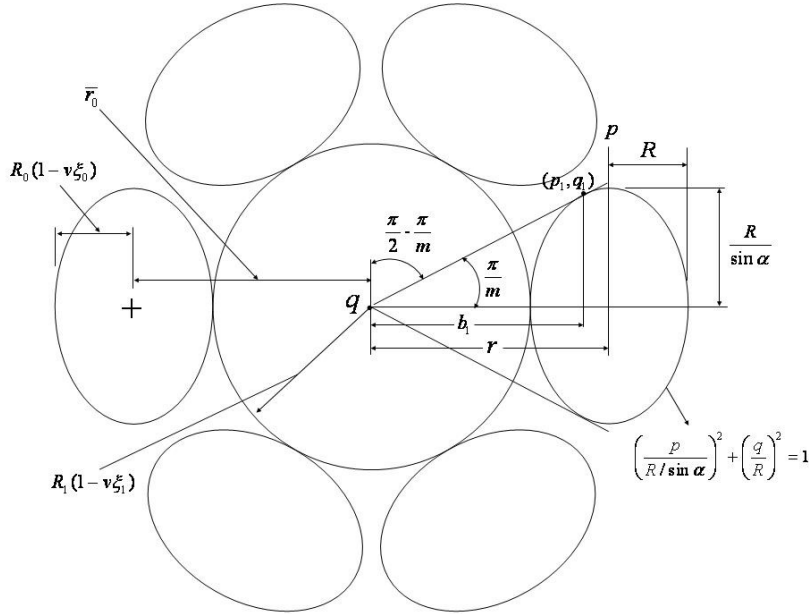
Figure 4.6: Cross section of a strand perpendicular to the strand axis.

From the Figure 4.6 the slope at the point (p_1, q_1) is equal to $-\tan\left(\dfrac{\pi}{2} - \dfrac{\pi}{m}\right)$ and from

equation (4.45) $\tan\left(\dfrac{\pi}{2} - \dfrac{\pi}{m}\right)$ can be denoted as,

36

$$\tan\left(\frac{\pi}{2}-\frac{\pi}{m}\right)=\frac{p_1\sin^2\alpha}{R\sqrt{1-\left(\dfrac{p_1\sin\alpha}{R}\right)^2}}. \tag{4.46}$$

$\dfrac{\pi}{2}-\dfrac{\pi}{m}$ can be denoted by θ, and solving equation (4.46) for p_1 and q_1 respectively

gives the following equations,

$$p_1\sin^2\alpha=R\sqrt{1-\left(\frac{p_1\sin\alpha}{R}\right)^2}\tan\theta,$$

$$p_1^2\sin^4\alpha=(R^2-p_1^2\sin^2\alpha)\tan^2\theta,$$

$$p_1^{\,2}=\frac{R^2\tan^2\theta}{\sin^2\alpha(\sin^2\alpha+\tan^2\theta)},$$

and hence p_1 is derived as follows,

$$p_1=\frac{R}{\sin\alpha}\tan\left(\frac{\pi}{2}-\frac{\pi}{m}\right)\frac{1}{\sqrt{\sin^2\alpha+\tan^2\left(\dfrac{\pi}{2}-\dfrac{\pi}{m}\right)}}. \tag{4.47}$$

From the equation (4.43), q_1 can be solved as,

$$q_1^{\,2}=\left(1-\frac{p_1^{\,2}}{R^2/\sin^2\alpha}\right)R^2$$

$$=R^2-\frac{R^2\tan^2\theta}{\sin^2\alpha(\sin^2\alpha+\tan^2\theta)}\sin^2\alpha$$

$$=\frac{R^2\sin^2\alpha}{(\sin^2\alpha+\tan^2\theta)},$$

so q_1 can be written in the form of,

$$q_1=\frac{R\sin\alpha}{\sqrt{\sin^2\alpha+\tan^2\left(\dfrac{\pi}{2}-\dfrac{\pi}{m}\right)}}. \tag{4.48}$$

From Figure 4.6, one can write b_1 as,

37

$$b_1 = p_1 \tan\left(\frac{\pi}{2} - \frac{\pi}{m}\right),$$ (4.49)

and r can be represented by

$$r = b_1 + q_1,$$ (4.50)

which can be derived using equations (4.48) and (4.49) as,

$$
\begin{aligned}
r &= p_1 \tan\theta + \frac{R\sin\alpha}{\sqrt{\sin^2\alpha + \tan^2\theta}} \\
&= \frac{R}{\sin\alpha}\tan\theta\frac{1}{\sqrt{\sin^2\alpha + \tan^2\theta}}\tan\theta + \frac{R\sin\alpha}{\sqrt{\sin^2\alpha + \tan^2\theta}} \\
&= \frac{R}{\sqrt{\sin^2\alpha + \tan^2\theta}}\left(\frac{\tan^2\theta + \sin^2\alpha}{\sin\alpha}\right) \\
&= \frac{R\sqrt{\sin^2\alpha + \tan^2\theta}}{\sin\alpha} \\
&= R\sqrt{1 + \frac{\tan^2\theta}{\sin^2\alpha}},
\end{aligned}
$$

and hence r can be written as,

$$r = R\sqrt{1 + \frac{\tan^2\left(\dfrac{\pi}{2} - \dfrac{\pi}{m}\right)}{\sin^2\alpha}}.$$ (4.51)

Equation (4.51) yields the radius of the wire helix in which the wires are just touching each other. Hence, in the simple straight strand, if the outside wires are not touching each other the equation given below holds,

$$R_2\sqrt{1 + \frac{\tan^2\left(\dfrac{\pi}{2} - \dfrac{\pi}{m}\right)}{\sin^2\alpha}} < R_1 + R_2.$$ (4.52)

4.7 Axially loaded simple straight strand

A simple straight strand with the given cross section as in Figure 4.6 is taken into account. The helix angle of an outside strand, α_2, is found by the relation,

38

$$\tan \alpha_2 = \frac{p_2}{2\pi r_2}, \tag{4.53}$$

where p_2 is the pitch of an outside wire. The initial curvature and the twist per unit length are given as,

$$\kappa_2 = 0; \quad \kappa_2' = \frac{\cos^2 \alpha_2}{r_2} \quad and \quad \tau_2 = \frac{\sin \alpha_2 \cos \alpha_2}{r_2}. \tag{4.54}$$

Let the wires in the strand are deformed under action of the total axial force F, and the total axial twisting moment M_t. Under the loads, it is assumed that the outside wires are deformed into a new helix, which has the following components of curvature and twist per unit length,

$$\bar{\kappa}_2 = 0; \quad \bar{\kappa}_2' = \frac{\cos^2 \bar{\alpha}_2}{\bar{r}_2} \quad and \quad \bar{\tau}_2 = \frac{\sin \bar{\alpha}_2 \cos \bar{\alpha}_2}{\bar{r}_2}, \tag{4.55}$$

where the bar symbols over the quantities shows the deformed states here and during the scope of this thesis.

To keep the general formulation of the equilibrium equations, it is assumed that an outside wire is not subjected to external bending moments per unit length in each direction, $K_2 = K_2' = \Theta_2 = 0$. Components of the external line load per unit length of the centerline in y and z directions are assumed to be zero, $Y_2 = Z_2 = 0$, and the axial wire tension T_2 is assumed to be constant along the length of the wire. Using the equations (4.39), (4.54) and (4.55) the equilibrium equations given before in equations (4.28)-(4.30) and (4.35)-(4.37) becomes to the following form,

$$-\frac{\sin \alpha_2 \cos \alpha_2}{r_2} N_2'(s) + \frac{\cos^2 \alpha_2}{r_2} T_2(s) + X_2(s) = 0, \tag{4.56}$$

$$\frac{dN_2'}{ds}(s) = 0, \tag{4.57}$$

$$\frac{dT_2}{ds}(s) = 0, \tag{4.58}$$

$$\frac{dG_2(s)}{ds} - \frac{\sin\alpha_2\cos\alpha_2}{r_2}G_2'(s) + \frac{\cos^2\alpha_2}{r_2}H_2(s) - N_2'(s) = 0, \qquad (4.59)$$

$$\frac{dG_2'(s)}{ds} + \frac{\sin\alpha_2\cos\alpha_2}{r_2}G_2(s) = 0, \qquad (4.60)$$

$$\frac{dH_2(s)}{ds} - \frac{\cos^2\alpha_2}{r_2}G_2(s) = 0, \qquad (4.61)$$

where subscript 2 refers to the outside wires. Figure 4.7 shows the loads acting on a helical wire. The system of equations (4.56) through (4.61) is solved using Maple®, and found that,

$$G_2'(s) = C_1 - \frac{\sin 2\alpha_2 e^{\left(\frac{\sqrt{-2-2\cos(2\alpha_2)}}{2r}s\right)}}{\sqrt{-2-2\cos(2\alpha_2)}}C_2 + \frac{\sin 2\alpha_2 e^{\left(-\frac{\sqrt{-2-2\cos(2\alpha_2)}}{2r}s\right)}}{\sqrt{-2-2\cos(2\alpha_2)}}C_3, \qquad (4.62)$$

$$G_2(s) = e^{\left(\frac{\sqrt{-2-2\cos(2\alpha_2)}}{2r}s\right)}C_2 + e^{\left(-\frac{\sqrt{-2-2\cos(2\alpha_2)}}{2r}s\right)}C_3, \qquad (4.63)$$

$$N_2'(s) = C_4, \qquad (4.64)$$

$$T_2(s) = C_5, \qquad (4.65)$$

$$H_2(s) = C_1\frac{\sin\alpha_2}{\cos\alpha_2} + \frac{2\cos^2\alpha_2 e^{\left(\frac{\sqrt{-2-2\cos(2\alpha_2)}}{2r}s\right)}}{\sqrt{-2-2\cos(2\alpha_2)}}C_2 - \frac{2\cos^2\alpha_2 e^{\left(-\frac{\sqrt{-2-2\cos(2\alpha_2)}}{2r}s\right)}}{\sqrt{-2-2\cos(2\alpha_2)}}C_3$$
$$+ \frac{r}{\cos^2\alpha_2}C_4, \qquad (4.66)$$

$$X_2(s) = \frac{\sin 2\alpha_2}{2r}C_4 - \frac{1+\cos 2\alpha_2}{2r}C_5. \qquad (4.67)$$

Equations (4.62) through (4.67) can be rewritten for G_2', G_2, H_2, X_2 as,

$$G_2'(s) = C_1 - \frac{\sin 2\alpha_2 e^{iks}}{2i\cos\alpha_2}C_2 + \frac{\sin 2\alpha_2 e^{-iks}}{2i\cos\alpha_2}C_3, \qquad (4.68)$$

$$G_2(s) = e^{iks}C_2 + e^{-iks}C_3, \qquad (4.69)$$

40

$$H_2(s) = C_1 \frac{\sin\alpha_2}{\cos\alpha_2} + \frac{2\cos^2\alpha_2 e^{iks}}{2i\cos\alpha_2} C_2 - \frac{2\cos^2\alpha_2 e^{-iks}}{2i\cos\alpha_2} C_3 + \frac{r}{\cos^2\alpha_2} N_2'(s), \quad \textbf{(4.70)}$$

$$X_2(s) = \frac{\sin 2\alpha_2}{2r} N_2'(s) - \frac{1+\cos 2\alpha_2}{2r} T_2(s). \quad \textbf{(4.71)}$$

Equations (4.69) can be written as,

$$G_2(s) = (C_2 + C_3)\cos ks + i(C_2 - C_3)\sin ks. \quad \textbf{(4.72)}$$
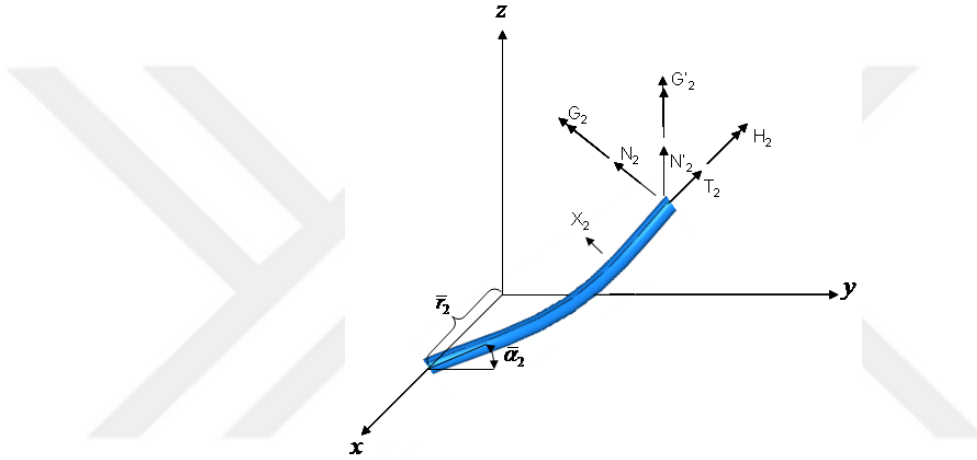
Figure 4.7: Loads and moments over a single helical wire.

Using equations (4.54) and (4.55) in equation (4.39) gives the result, $G(s) = 0$. Using the result $G(s) = 0$, and taking $s = 0$ simultaneously, equation (4.72) will yield,

$$C_2 + C_3 = 0. \quad \textbf{(4.73)}$$

As in the same way, using the equation (4.73), and $G(s) = 0$ in equation (4.72) give the following result,

$$C_2 - C_3 = 0. \quad \textbf{(4.74)}$$

Solving equations (4.73) and (4.74) simultaneously gives the results, $C_2 = C_3 = 0$. Using these values the equation (4.68) yields,

$$C_1 = G_2'(s). \quad \textbf{(4.75)}$$

Substituting these coefficients in equation (4.70), one can find,

$$H_2 = \frac{\sin \alpha_2}{\cos \alpha_2} G_2' + \frac{r}{\cos^2 \alpha_2} N_2'. \tag{4.76}$$

Equations (4.76) and (4.71) are reorganized to find N_2' and X_2 as follows,

$$N_2' = \frac{\cos^2 \alpha_2}{r} H_2 - \frac{\sin \alpha_2 \cos \alpha_2}{r} G_2', \tag{4.77}$$

$$X_2 = \frac{\sin \alpha_2 \cos \alpha_2}{r} N_2' - \frac{\cos^2 \alpha_2}{r} T_2. \tag{4.78}$$

The results found and given in equations (4.77) and (4.78) are harmonious with the equations found by Costello [11].

Equations (4.77) and (4.78) can be regarded as determining the values of N_2' and X_2 required to hold an outside helical wire in equilibrium for given values of $\bar{\alpha}_2$, $\bar{r}_2$ and T_2. It should be noted that normally the equations of equilibrium ((4.28)-(4.30) and (4.35)-(4.37)) and equation (4.39) constitute a set of nonlinear equations and are valid for large deflections. Large deflections could occur, for instance, in the case of a thin wire helical spring in which the value of α_2 is generally small. In the case of wire rope, however, the value of α_2 is generally large and the change in α_2, which is denoted by $\Delta \alpha_2$,

$$\Delta \alpha_2 = \bar{\alpha}_2 - \alpha_2, \tag{4.79}$$

is small [11]. This reality is taken into account while simplifying the solution throughout the rest of this part.

The axial strain ε of a straight strand is defined as,

$$\varepsilon = \frac{\bar{h} - h}{h}, \tag{4.80}$$

where h is the original length of the strand and $\bar{h}$ is the final length of the strand. Figure 4.8 shows a developed view of the centerline of an outer wire, indicates the length h and $\bar{h}$.
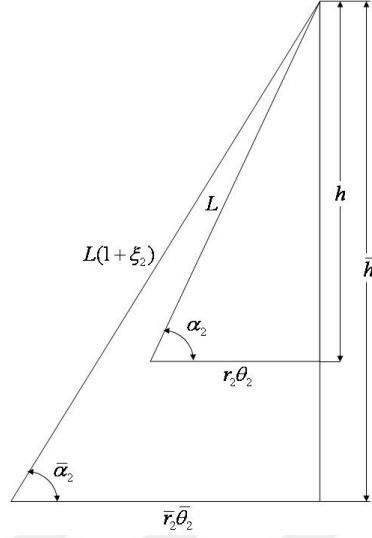
Figure 4.8: Undeformed and deformed view of an outer wire centerline.

The rotational strain β_2 of an outer wire is defined as,

$$\beta_2 = r_2 \frac{(\bar{\theta}_2 - \theta_2)}{h}, \tag{4.81}$$

where θ_2 and $\bar{\theta}_2$ are initial and final angle respectively, that an outer wire sweeps out in a plane perpendicular to the axis of the strand. The angle of twist per unit length τ_s, of the strand is defined by,

$$\tau_s = \frac{(\bar{\theta}_2 - \theta_2)}{h}. \tag{4.82}$$

Using the configuration shown in Figure 4.8 an analysis of this configuration yields that, $\bar{h} = L(1+\xi_2)\sin\bar{\alpha}_2$, and from the equation (4.80) the axial strain can be written in the form of,

$$\varepsilon = \frac{L(1+\xi_2)\sin\bar{\alpha}_2 - L\sin\alpha_2}{L\sin\alpha_2}.$$

Therefore, the axial strain can be written in the following form,

$$\varepsilon = \xi_1 = (1+\xi_2)\frac{\sin\bar{\alpha}_2}{\sin\alpha_2} - 1. \tag{4.83}$$

Starting from the equation (4.82) and using the trigonometric relations obtained from Figure 4.8 the following results can be obtained for θ_2, $\bar{\theta}_2$ and $\bar{\tau}_2$,

$$\theta_2 = \frac{L \cos \alpha_2}{r_2},$$

$$\bar{\theta}_2 = \frac{L(1+\xi_2) \cos \bar{\alpha}_2}{\bar{r}_2},$$

$$\tau_s = \frac{L(1+\xi_2) \cos \bar{\alpha}_2}{\bar{r}_2 L \sin \alpha_2} - \frac{L \cos \alpha_2}{r_2 L \sin \alpha_2}.$$

From the equations (4.81) and (4.82), one can find,

$$\beta_2 = r_2 \tau_s = \frac{r_2}{\bar{r}_2}(1+\xi_2) \frac{\cos \bar{\alpha}_2}{\sin \alpha_2} - \frac{\cos \alpha_2}{\sin \alpha_2}. \tag{4.84}$$

by using the equation (4.83) $(1+\xi_2)$ can be written such that,

$$(1+\xi_2) = \frac{\sin \alpha_2}{\sin \bar{\alpha}_2}(1+\xi_1). \tag{4.85}$$

The equation (4.84) using the equation (4.85) will give,

$$\beta_2 = (1+\xi_1) \frac{r_2}{\bar{r}_2} \frac{\sin \alpha_2}{\sin \bar{\alpha}_2} \frac{\cos \bar{\alpha}_2}{\sin \alpha_2} - \frac{\cos \alpha_2}{\sin \alpha_2},$$

and finally rearranging β_2 will yield,

$$\beta_2 = \frac{r_2}{\bar{r}_2} \frac{(1+\xi_1)}{\tan \bar{\alpha}_2} - \frac{1}{\tan \alpha_2}, \tag{4.86}$$

where ξ_1 is the axial strain in the center wire $(\varepsilon = \xi_1)$, and ξ_2 is the axial strain in an outer wire. Here $|\Delta \alpha_2|$ is defined as,

$$|\Delta \alpha_2| = |\bar{\alpha}_2 - \alpha_2| \ll 1, \tag{4.87}$$

44

which is valid for most metallic strands. The trigonometric representation of the $\sin \bar{\alpha}_2$ can be defined as,

$$\sin \bar{\alpha}_2 = \sin(\alpha_2 + \Delta \alpha_2) = \sin \alpha_2 \cos(\Delta \alpha_2) + \sin(\Delta \alpha_2) \cos \alpha_2.$$

Using the equation (4.87), $\cos(\Delta \alpha_2) = 1$, $\sin(\Delta \alpha_2) = \Delta \alpha_2$, and neglecting the higher-ordered terms, $\sin \bar{\alpha}_2$ can be written as,

$$\sin \bar{\alpha}_2 = \sin \alpha_2 + \Delta \alpha_2 \cos \alpha_2. \qquad \textbf{(4.88)}$$

Starting with equation (4.83) and using the equation (4.88), ξ_1 can be written as,

$$\xi_1 = (1 + \xi_2) \frac{\sin \alpha_2 + \Delta \alpha_2 \cos \alpha_2}{\sin \alpha_2} - 1$$
$$= 1 + \frac{\Delta \alpha_2}{\tan \alpha_2} + \xi_2 + \frac{\Delta \alpha_2 \xi_2}{\tan \alpha_2} - 1,$$

where higher ordered term $\Delta \alpha_2 \xi_2$ is vanished, ξ_1 and ξ_2 are assumed to be small. So the relation below is found,

$$\xi_1 = \xi_2 + \frac{\Delta \alpha_2}{\tan \alpha_2} = \varepsilon. \qquad \textbf{(4.89)}$$

Equation (4.86) is transformed to a new formulation in a similar way. Equation (4.83) can be rewritten as,

$$\xi_1 + 1 = (1 + \xi_2) \frac{\sin \bar{\alpha}_2}{\sin \alpha_2}, \qquad \textbf{(4.90)}$$

and both sides of equation (4.90) can be divided by $\tan \bar{\alpha}_2$ which gives,

$$\frac{\xi_1 + 1}{\tan \bar{\alpha}_2} = (1 + \xi_2) \frac{\cos \bar{\alpha}_2}{\sin \alpha_2}. \qquad \textbf{(4.91)}$$

Here $\cos \bar{\alpha}_2$ can be written as,

$$\cos \bar{\alpha}_2 = \cos(\alpha_2 + \Delta \alpha_2) = \cos \alpha_2 \cos(\Delta \alpha_2) - \sin \alpha_2 \sin(\Delta \alpha_2),$$

and again using equation (4.87), $\cos(\Delta\alpha_2) = 1$, $\sin(\Delta\alpha_2) = \Delta\alpha_2$, and neglecting the higher-ordered terms $\cos\bar{\alpha}_2$ can be written as,

$$\cos\bar{\alpha}_2 = \cos\alpha_2 - \Delta\alpha_2\sin\alpha_2.$$
(4.92)

Using equation (4.92) in equation (4.91) the following equation is derived,

$$\frac{\xi_1 + 1}{\tan\bar{\alpha}_2} = \frac{1 + \xi_2}{\tan\alpha_2} - \Delta\alpha_2 - \Delta\alpha_2\xi_2,$$
(4.93)

where $\Delta\alpha_2\xi_2 = 0$. The equation (4.93) becomes to,

$$\frac{\xi_1 + 1}{\tan\bar{\alpha}_2} = \frac{1 + \xi_2}{\tan\alpha_2} - \Delta\alpha_2.$$
(4.94)

Equation (4.94) and (4.86) combined and new form of β_2 can be written as,

$$\beta_2 = \frac{r_2}{\bar{r}_2}\left(\frac{1 + \xi_2}{\tan\alpha_2} - \Delta\alpha_2\right) - \frac{1}{\tan\alpha_2}.$$
(4.95)

As a result of Poisson's ratio effect v, the final radius $\bar{r}$ becomes to,

$$\bar{r} = R_1(1 - v\xi_1) + R_2(1 - v\xi_2),$$
(4.96)

where the contact deformations in the center and outer wires are neglected. The representation for $r_2/\bar{r}_2$ can be derived as,

$$\begin{aligned}
\frac{r_2}{\bar{r}_2} &= \frac{R_1 + R_2}{R_1 + R_2 - v(R_1\xi_1 + R_2\xi_2)} \\
&= \frac{1}{1 - v\dfrac{(R_1\xi_1 + R_2\xi_2)}{R_1 + R_2}} \\
&= 1 + v\frac{(R_1\xi_1 + R_2\xi_2)}{R_1 + R_2},
\end{aligned}$$

from the descriptions given above $r_2/\bar{r}_2$ can be written as,

$$\frac{r_2}{\bar{r}_2} = 1 + v\frac{(R_1\xi_1 + R_2\xi_2)}{r_2}.$$
(4.97)

46

The equation (4.97) can be put into the equation (4.95) and gives the following result,

$$\beta_2 = \left(1 + v\frac{(R_1\xi_1 + R_2\xi_2)}{R_1 + R_2}\right)\left(\frac{1+\xi_2}{\tan\alpha_2} - \Delta\alpha_2\right) - \frac{1}{\tan\alpha_2}$$

$$= \frac{1+\xi_2}{\tan\alpha_2} - \Delta\alpha_2 + v\frac{(R_1\xi_1 + R_2\xi_2)}{(R_1 + R_2)\tan\alpha_2}(1+\xi_2) - \Delta\alpha_2 v\frac{(R_1\xi_1 + R_2\xi_2)}{R_1 + R_2} - \frac{1}{\tan\alpha_2}.$$

By using the relation; $\xi_1\xi_2 \ll 1$, $\xi_2\xi_2 \ll 1$, $\Delta\alpha_2\xi_1 \ll 1$, $\Delta\alpha_2\xi_2 \ll 1$, the equation for β_2 is written as,

$$\beta_2 = r_2\tau_s = \frac{\xi_2}{\tan\alpha_2} - \Delta\alpha_2 + v\frac{(R_1\xi_1 + R_2\xi_2)}{r_2\tan\alpha_2}. \tag{4.98}$$

The change in curvature $\Delta\kappa'$ and the change in twist per unit length $\Delta\tau_2$ can also be linearized. Using the change in curvature $\Delta\kappa'$, $R_2\Delta\kappa_2'$ can be written as,

$$R_2\Delta\kappa_2' = R_2\left(\frac{\cos^2\bar{\alpha}_2}{\bar{r}_2} - \frac{\cos^2\alpha_2}{r_2}\right) = \frac{R_2}{r_2}\left(\frac{r_2}{\bar{r}_2}\cos^2\bar{\alpha}_2 - \cos^2\alpha_2\right). \tag{4.99}$$

$\cos^2\bar{\alpha}_2$ written as,

$$\cos^2\bar{\alpha}_2 = \cos^2\alpha_2 + (\Delta\alpha_2)^2\sin^2\alpha_2 - 2\Delta\alpha_2\sin\alpha_2\cos\alpha_2,$$

and taking $(\Delta\alpha_2)^2 \ll 1$, small enough, $\cos^2\bar{\alpha}_2$ can be given as follows,

$$\cos^2\bar{\alpha}_2 = \cos^2\alpha_2 - 2\Delta\alpha_2\sin\alpha_2\cos\alpha_2.$$

This new formulation of $\cos^2\bar{\alpha}_2$ can be put into equation (4.99) gives,

$$R_2\Delta\kappa_2' = \frac{R_2}{r_2}\left(\frac{r_2}{\bar{r}_2}\left(\cos^2\alpha_2 - 2\Delta\alpha_2\sin\alpha_2\cos\alpha_2\right) - \cos^2\alpha_2\right). \tag{4.100}$$

As well, $r_2/\bar{r}_2$ given in equation (4.97) can be put in (4.100) and gives,

$$R_2 \Delta \kappa_2' = \frac{R_2}{r_2} \left(\left(1 + \nu \frac{(R_1 \xi_1 + R_2 \xi_2)}{r_2} \right) \left(\cos^2 \alpha_2 - 2 \Delta \alpha_2 \sin \alpha_2 \cos \alpha_2 \right) - \cos^2 \alpha_2 \right).$$

Making the necessary simplifications, such as $\xi_1 \Delta \alpha_2 \ll 1$, $\xi_2 \Delta \alpha_2 \ll 1$, the following equation for $R_2 \Delta \kappa_2'$ is found,

$$R_2 \Delta \kappa_2' = R_2 \left(\frac{-2 \sin \alpha_2 \cos \alpha_2}{r_2} \Delta \alpha_2 + \nu \frac{(R_1 \xi_1 + R_2 \xi_2) \cos^2 \alpha_2}{r_2^2} \right). \qquad \textbf{(4.101)}$$

For $R_2 \Delta \tau_2$ a similar procedure can be followed. Using equations (4.54) and (4.55) $R_2 \Delta \tau_2$ can be written as,

$$\begin{aligned}
R_2 \Delta \tau_2 &= R_2 \left(\frac{\sin \bar{\alpha}_2 \cos \bar{\alpha}_2}{\bar{r}_2} - \frac{\sin \alpha_2 \cos \alpha_2}{r_2} \right) \\
&= \frac{R_2}{r_2} \left[\frac{(\sin \alpha_2 + \Delta \alpha_2 \cos \alpha_2)(\cos \alpha_2 - \Delta \alpha_2 \sin \alpha_2) r_2}{\bar{r}_2} - \sin \alpha_2 \cos \alpha_2 \right].
\end{aligned} \qquad \textbf{(4.102)}$$

Using the property $(\Delta \alpha_2)^2 \ll 1$, a portion of equation (4.102) can be presented as,

$(\sin \alpha_2 + \Delta \alpha_2 \cos \alpha_2)(\cos \alpha_2 - \Delta \alpha_2 \sin \alpha_2) = \sin \alpha_2 \cos \alpha_2 - \Delta \alpha_2 \sin^2 \alpha_2 + \Delta \alpha_2 \cos^2 \alpha_2$,

and using $r_2 / \bar{r}_2$ from the equation (4.97) simplifies the equation (4.102). $R_2 \Delta \tau_2$ can be written in the following form,

$$\begin{aligned}
R_2 \Delta \tau_2 &= \frac{R_2}{r_2} \left[\begin{array}{l} \left(\sin \alpha_2 \cos \alpha_2 - \Delta \alpha_2 \sin^2 \alpha_2 + \Delta \alpha_2 \cos^2 \alpha_2 \right) \left(1 + \nu \frac{(R_1 \xi_1 + R_2 \xi_2)}{r_2} \right) \\ - \sin \alpha_2 \cos \alpha_2 \end{array} \right] \\
&= \frac{R_2}{r_2} \left[\begin{array}{l} \sin \alpha_2 \cos \alpha_2 + \sin \alpha_2 \cos \alpha_2 \nu \frac{(R_1 \xi_1 + R_2 \xi_2)}{r_2} + \\ \Delta \alpha_2 (\cos^2 \alpha_2 - \sin^2 \alpha_2) \nu \frac{(R_1 \xi_1 + R_2 \xi_2)}{r_2} - \sin \alpha_2 \cos \alpha_2 \end{array} \right],
\end{aligned}$$

where $\xi_1 \Delta \alpha_2 \ll 1$ and $\xi_2 \Delta \alpha_2 \ll 1$. Making simplifications finally gives $R_2 \Delta \tau_2$ as,

$$R_2 \Delta \tau_2 = R_2 \frac{1 - 2 \sin^2 \alpha_2}{r_2} \Delta \alpha_2 + \nu R_2 \frac{(R_1 \xi_1 + R_2 \xi_2)}{r_2} \frac{\sin \alpha_2 \cos \alpha_2}{r_2}. \qquad \textbf{(4.103)}$$

The following equations can now be written for an outside wire using equations (4.39) and from the solution of the equilibrium equations found in equations (4.77) and (4.78) as,

$$G_2' = \frac{\pi}{4} ER_2{}^4 \Delta \kappa_2', \tag{4.104}$$

$$H_2 = \frac{\pi}{4(1+v)} ER_2{}^4 \Delta \tau_2, \tag{4.105}$$

$$N_2' = \frac{\cos^2 \alpha_2}{r} H_2 - \frac{\sin \alpha_2 \cos \alpha_2}{r} G_2', \tag{4.106}$$

$$T_2 = \pi \xi_2 ER_2{}^2, \tag{4.107}$$

$$X_2 = \frac{\sin \alpha_2 \cos \alpha_2}{r} N_2' - \frac{\cos^2 \alpha_2}{r} T_2, \tag{4.108}$$

where the displacements are assumed to be small.

A projection of the forces, acting on the outside wires, in the axial direction of the strand yields F_2, which is the total axial force in the strand acting on m_2 outer wires is given in the following form,

$$F_2 = m_2 \left[T_2 \sin \alpha_2 + N_2' \cos \alpha_2 \right]. \tag{4.109}$$

The total axial twisting moment M_2 acting on the outside wires is given as,

$$M_2 = m_2 \left[H_2 \sin \alpha_2 + G_2' \cos \alpha_2 + T_2 Er_2 \cos \alpha_2 - N_2' Er_2 \sin \alpha_2 \right]. \tag{4.110}$$

The preceding theory represents the behavior of a right lang lay rope shown in Figure 2.5-(c). The response of the left lay rope can be obtained from the response of the right lay rope. If a left lay rope is acted upon by a positive axial force F, and a positive axial twisting moment M as in Figure 4.5, the rotational strain β and the axial strain ε, can be determined by loading a right lay rope with the same axial force F, and an axial twisting moment $-M$. The axial strain then computed for the right lay rope will be the same as that for the left lay rope but the rotational strain computed for the right lay rope will be minus that of the left lay rope [4]. Thus if the rope is a right regular lay equations (4.81) and (4.110) becomes to,

$$\beta_2 = -r_2 \frac{(\bar{\theta}_2 - \theta_2)}{h}, \tag{4.111}$$

$$M_2 = m_2 \left[-H_2 \sin \alpha_2 + G_2' \cos \alpha_2 + T_2 Er_2 \cos \alpha_2 - N_2' Er_2 \sin \alpha_2 \right]. \tag{4.112}$$

The axial force and the axial twisting moment acting on the center wire are given with the symbols, F_1 and M_1 respectively, by the expressions,

$$F_1 = \pi \xi_1 ER_1^2, \tag{4.113}$$

and

$$M_1 = \frac{\pi}{4(1+v)} ER_1^4 \tau_s. \tag{4.114}$$

The total axial force F and the total axial twisting moment M_t acting on the strand can be written as [11],

$$F = F_1 + F_2, \tag{4.115}$$

$$M_t = M_1 + M_2. \tag{4.116}$$

Analytical examples and solutions related to the theory are presented in Appendix A for convenience.

4.8 Stresses over a simple straight strand

The stresses caused by the loads acting on a simple straight strand are investigated in this section. The axial wire stress on the center wire can be given by,

$$_F\sigma_1 = \frac{F_1}{\pi R_1^2}, \tag{4.117}$$

and the maximum shearing stress on the cross section is,

$$_M\sigma_1 = \frac{2M_1}{\pi R_1^3}. \tag{4.118}$$

The outside wires, in addition to the shearing load N_2', are subjected to axial, bending, and torsional loadings. The stresses caused by the shearing force N_2' are in general very small and neglected. The axial stress caused by the load T_2 is,

$$_T\sigma_2 = \frac{T_2}{\pi R_2^2}.$$

(4.119)

The maximum normal stress on an outside wire due to bending moment G_2' is,

$$_{G'}\sigma_2 = \frac{4G_2'}{\pi R_2^3},$$

(4.120)

and the maximum shearing stress on an outside wire due to the twisting moment H_2 is,

$$_H\sigma_2 = \frac{2H_2}{\pi R_2^3}.$$

(4.121)

4.9 General strain and rotation relation due to load and moments over a simple straight strand

The behavior of a strand is given in a general formulation by using the total axial force F, and the total axial twisting moment M as in the following equations,

$$\frac{F}{AE} = C_1\varepsilon + C_2\beta,$$

(4.122)

$$\frac{M_t}{ER^3} = C_3\varepsilon + C_4\beta,$$

(4.123)

where A represents the total area of the strand and given by,

$$A = \sum \pi R_i^2.$$

(4.124)

R_i is the radius of i'th wire of the strand, $C_1,...,C_4$ are the unknown constants (which can be determined analytically), ε is the axial strain, and β is the rotational strain of the strand defined by the equation,

$$\beta = R\tau_s , \tag{4.125}$$

where R is the radius of the strand and τ_s is the angle of twist per unit length of the strand. Equations (4.122) and (4.123) relates the total axial force F, and the total axial twisting moment M_t, with the axial and rotational strain of the strand.

The problem here is to find the constant values defined in equations (4.122) and (4.123). To do this first of all β is taken as zero and $\varepsilon = \xi_1$. Then equations (4.115) and (4.116) are used to find F and M_t. In this way F, M_t, ε and β are known, using equations (4.122) and (4.123) the constant values of C_1 and C_3 can be found with using $\beta = 0$ and $\varepsilon = \xi_1$ conditions. In a similar way, on the second part of the solution procedure, ε can be chosen as zero, β is defined, and then F and M_t are computed. Using equations (4.122) and (4.123), C_2 and C_4 constants can be found.

The analytical solution, basically explained above, can be extended to the multi-layered strands to find the total axial force F, and the total axial twisting moment M_t, acting on each strand as in equation (4.122).

4.10 Contact stresses

Contact of two semicircular disks will be assumed as a starting point for the contact analysis. As an initial condition, two disks are assumed in contact at a point. As material properties, two disks are assumed homogeneous, isotropic, and elastic. Two disks are pressed together with forces F. Before applying the force, boundaries of two disks are smooth curves. R_1 and R_1' shows the minimum and maximum radius of curvatures on the first disk, R_2 and R_2' shows the same radiuses for the second disk at the point of contact as shown in Figure 4.9-(a).

The load F applied along the centerline of two disks makes them pressed. Friction is not included which ensures that disks will not slide at the point of contact. The lines V_1 and V_2 makes the angle α and lie in the plane sections containing the minimum radiuses R_1 and R_2 respectively. As a result of the load F, two disks are in contact and deformed elastically near the contacting point with a contact area which is shaped as an elliptical region as shown in Figure 4.9-(b). Contact stresses over each

disk are the purpose to derive at any point over the contact region caused by the load applied along the z-axes in this theory.

(a) Initial contact   **(b)** Contact region after loading
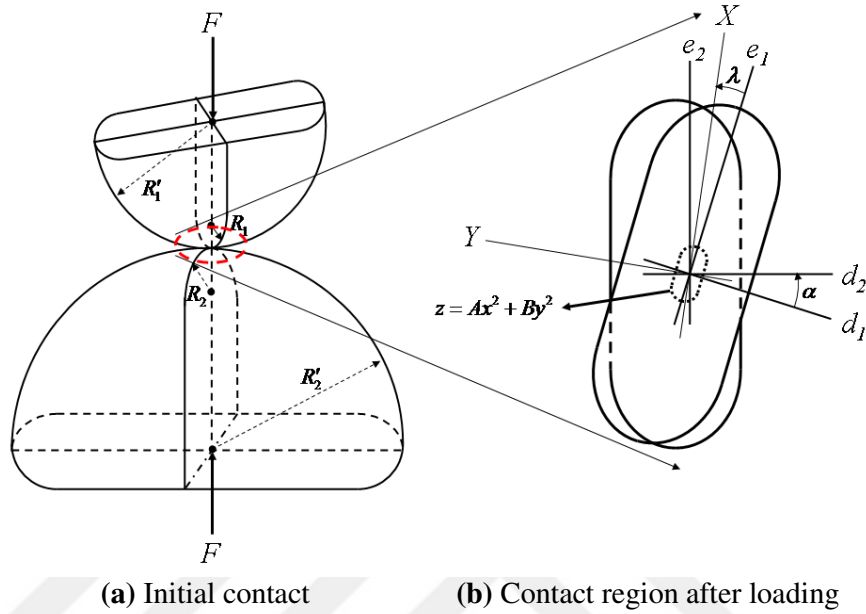
Figure 4.9: Two semicircular disks in contact before and after axial loading.

At the contact area before contact, distances z between corresponding points on any two surfaces can be defined by the following equation,

$$z = Ax^2 + By^2.$$

(**4.126**)

It can be easily seen from the equation (4.126) that for the constant values of z it corresponds to an ellipse.

When the loads F applied to the disks, there will be a contact area due to the deformation over the each disk. This small contact area will be constructed by the points, which are equidistant before loading. These equidistant points on the surfaces of the two disks lie on an ellipse as given in equation (4.126) and its equation is,

$$\frac{x^2}{a^2} + \frac{y^2}{b^2} = 1.$$

(**4.127**)

Derivation of the equation (4.126) is investigated in [97]. Constants A and B can be derived as,

$$B = \frac{1}{4}\left(\frac{1}{R_1} + \frac{1}{R_2} + \frac{1}{R_1'} + \frac{1}{R_2'}\right)$$
$$+ \frac{1}{4}\sqrt{\left[\left(\frac{1}{R_1} - \frac{1}{R_1'}\right) + \left(\frac{1}{R_2} - \frac{1}{R_2'}\right)\right]^2 - 4\left(\frac{1}{R_1} - \frac{1}{R_1'}\right)\left(\frac{1}{R_2} - \frac{1}{R_2'}\right)\sin^2\alpha}, \quad \textbf{(4.128)}$$

$$A = \frac{1}{4}\left(\frac{1}{R_1} + \frac{1}{R_2} + \frac{1}{R_1'} + \frac{1}{R_2'}\right)$$
$$- \frac{1}{4}\sqrt{\left[\left(\frac{1}{R_1} - \frac{1}{R_1'}\right) + \left(\frac{1}{R_2} - \frac{1}{R_2'}\right)\right]^2 - 4\left(\frac{1}{R_1} - \frac{1}{R_1'}\right)\left(\frac{1}{R_2} - \frac{1}{R_2'}\right)\sin^2\alpha}. \quad \textbf{(4.129)}$$

If the lines v_1 and v_2 are parallel then angle $\alpha = 0°$ and equations (4.128) and (4.129) are reduced to,

$$B = \frac{1}{2}\left(\frac{1}{R_1} + \frac{1}{R_2}\right),$$
$$A = \frac{1}{2}\left(\frac{1}{R_1'} + \frac{1}{R_2'}\right). \quad \textbf{(4.130)}$$

If the angle $\alpha = 90°$ then equations (4.128) and (4.129) are reduced to,

$$B = \frac{1}{2}\left(\frac{1}{R_1} + \frac{1}{R_2'}\right),$$
$$A = \frac{1}{2}\left(\frac{1}{R_1'} + \frac{1}{R_2}\right). \quad \textbf{(4.131)}$$

4.10.1 Line contact between two surfaces

Two circular cylindrical bodies can be put in contact along a straight-line element as shown in Figure 4.10. Stresses over these two bodies in contact, which is a line contact and loads, are applied in the normal direction to the contact area.

In the cylinders shown in Figure 4.10, the maximum radiuses of R_1' and R_2' are each indefinitely large so that, $1/R_1'$ and $1/R_2'$ are each equal to zero and also the angle $\alpha = 0°$. Therefore, from equation (4.130) B and A are found as follows,

$$B = \frac{1}{2}\left(\frac{1}{R_1} + \frac{1}{R_2}\right), \qquad A = 0. \quad \textbf{(4.132)}$$
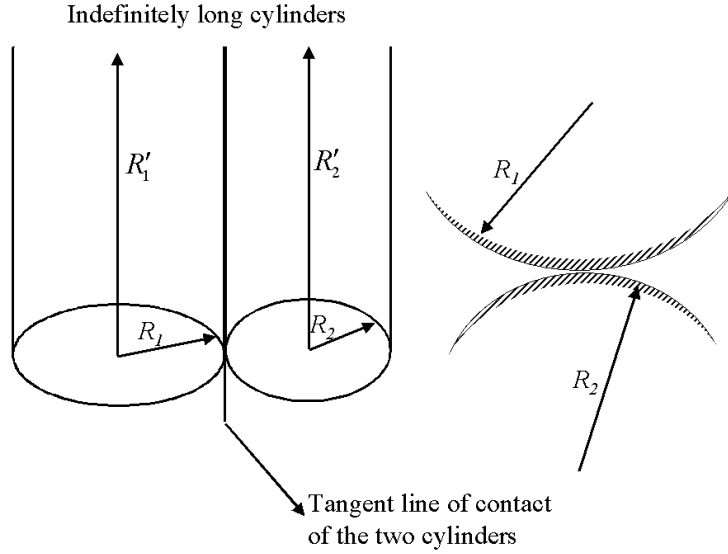
Figure 4.10: Line contact between two cylindrical surfaces.

Here a and b shows the semi-major axis and semi-minor axis of the area of contact respectively and semi-major axis of the area of contact a is indefinitely large in this line of contact. The area of contact when a load of q per unit length is applied along the contact line, the contact stresses are written as follows,

$$\sigma_x = -2\mu \left[\sqrt{1 + \left(\frac{z}{b}\right)^2} - \frac{z}{b} \right] \frac{b}{\Delta}, \tag{4.133}$$

$$\sigma_y = - \left[\frac{\left(\sqrt{1 + \left(\frac{z}{b}\right)^2} - \frac{z}{b} \right)^2}{\sqrt{1 + \left(\frac{z}{b}\right)^2}} \right] \frac{b}{\Delta}, \tag{4.134}$$

$$\sigma_z = -\frac{1}{\sqrt{1 + \left(\frac{z}{b}\right)^2}} \frac{b}{\Delta}. \tag{4.135}$$

Furthermore, b can be given as in the following,

$$b = \sqrt{\frac{2q\Delta}{\pi}}, \tag{4.136}$$

where q is the load per unit length of the contact area and Δ is given as,

$$\Delta = \frac{1}{\left(\dfrac{1}{2R_1} + \dfrac{1}{2R_2}\right)}\left(\frac{1-\mu_1^2}{E_1} + \frac{1-\mu_2^2}{E_2}\right),$$ (4.137)

while R_1 and R_2 are the radius of curvature of the cylindrical surfaces as shown in Figure 4.10. E_1, E_2, μ_1, μ_2 are the parameters found from the test results of the material.

The values of the stresses at a point on the line of contact are obtained from equations (4.133)-(4.135) by taking $z/b=0$ and maximum principal stresses becomes to,

$$\sigma_x = -2v\left(\frac{b}{\Delta}\right),$$ (4.138)

$$\sigma_y = -\frac{b}{\Delta},$$ (4.139)

$$\sigma_z = -\frac{b}{\Delta}.$$ (4.140)

4.10.2 Contact stresses of a simple straight strand

Simple straight strand geometry consists of a straight wire surrounded by six outer single helical wires. Thus, the line of contact between the center wire and the outer single helical wire is a helix with the radius of R_1 as shown in Figure 4.11. Contact stresses can be found only if the contact force is known. Because of the theory of Costello, contact force per unit length X_2 is calculated for the centerline of the outer single helical wire and it should therefore to be computed along the contact line. This results an approximate equation, which is as follows [11],

$$X_c\sqrt{p_2^2 + (2\pi R_1)^2} = -X_2\sqrt{p_2^2 + \left[2\pi\left(R_1 + R_2\right)\right]^2},$$ (4.141)

where X_c is the contact force per unit length along the line of contact.

A cross sectional view of the strand is given in Figure 4.11 where the outside wire cross-section is circular. Meanwhile the cross-section of the center wire is elliptical and the radius of curvature of the center wire at the contact point is defined as,

$$\rho_1 = \frac{R_1}{\sin^2 \alpha_2}.$$ (4.142)

56
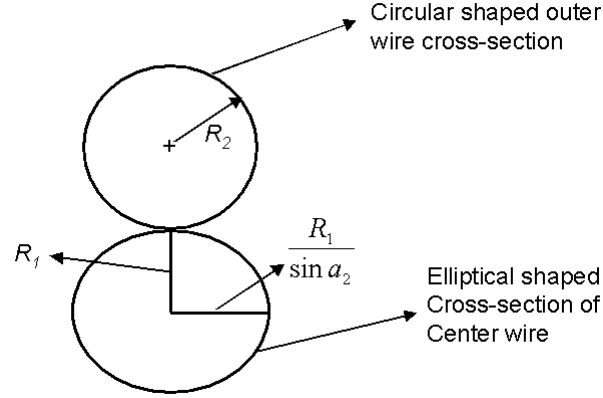
Figure 4.11: Contact between center straight and outer single helical wires.

Contact stress is assumed to be same as in the two cylindrical bodies in line contact determined in equation (4.140). Hence, the maximum contacts stress is given by,

$$\sigma_c = -\frac{b}{\Delta}.$$

(4.143)

Owing to the same material is used in each wire $E_1 = E_2 = E$ shows the elasticity modulus, and $\mu_1 = \mu_2 = v$ shows the Poisson's ratio for the wire material. Under this circumstance using equation (4.137) one can write Δ as,

$$\Delta = \frac{4(1-v^2)}{\left(\dfrac{1}{\rho_1} + \dfrac{1}{R_2}\right)E},$$

(4.144)

and b using the equation (4.136) as,

$$b = \sqrt{\frac{2X_c\Delta}{\pi}}.$$

(4.145)

4.10.3 Contact between helical wires in a strand

It is assumed that each wire in a strand has the same radius. In this aspect, outer wires of a simple straight strand are in contact with each other because of the helical shape of the outer wires. Figure 4.12 shows the elliptical view of the projection of an outer wire on a plane, which is perpendicular to the strand.

Cross sectional view of the outer single helical wires are elliptical in this case and wire to wire contact gives a helical line of contact with radius d which is given by [11],

$$d = \frac{R_2 \tan(\frac{\pi}{2} - \frac{\pi}{m_2})}{\sin \alpha_2 \cos(\frac{\pi}{2} - \frac{\pi}{m_2}) \sqrt{\sin^2 \alpha_2 + \tan^2(\frac{\pi}{2} - \frac{\pi}{m_2})}} . \qquad \textbf{(4.146)}$$
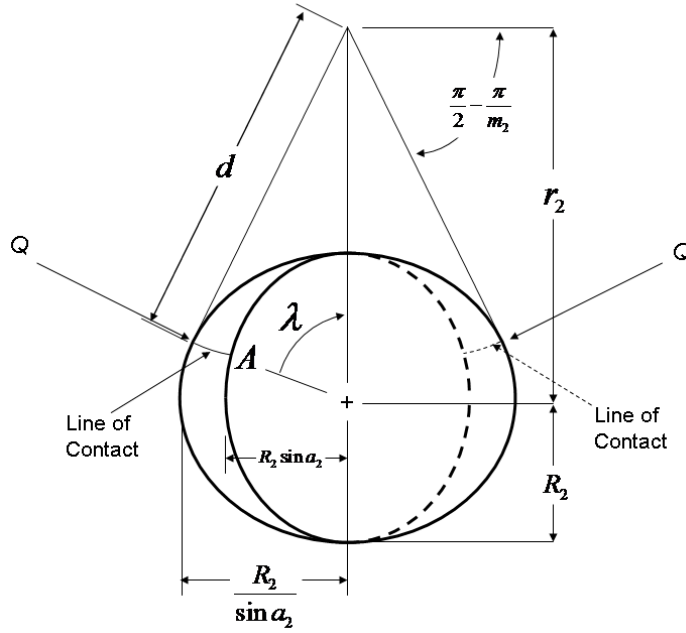
Figure 4.12: Line of contact between two outer wires.

The contact angle λ can be given by,

$$\cos \gamma = \frac{1}{\cos^2 \alpha_2} \left\{ \sqrt{1 + \frac{\tan^2(\frac{\pi}{2} - \frac{\pi}{m_2})}{\sin^2 \alpha_2}} \right. $$
$$\left. - \sqrt{\tan^2(\frac{\pi}{2} - \frac{\pi}{m_2}) \left\{ 1 + \frac{1}{\tan^2 \alpha_2 \cos^2(\frac{\pi}{2} - \frac{\pi}{m_2}) \left[\sin^2 \alpha_2 + \tan^2(\frac{\pi}{2} - \frac{\pi}{m_2}) \right]} \right\} + \sin^4 \alpha_2} \right\} .$$

Normal contact force over an outer wire per unit length is given by,

$$Q = -\frac{X}{2 \cos \gamma} . \qquad \textbf{(4.147)}$$

5. BENDING OF A SIMPLE STRAND AND IWRC OVER A SHEAVE

In this section, first a simple straight strand subjected to a bending moment m_s is investigated. Then the equilibrium equations for the bending moment are solved and the bending moment m_s derived. Bending of a loaded strand over a sheave is investigated, and the relation between wire rope diameter and sheave diameter are presented. A frictional effect of a strand is mentioned. Construction and static response of an IWRC is presented and generalized solution of IWRC and bending over a sheave problem is considered at the end of this section.

5.1 Equilibrium equations for the bending moment

Bending moment is applied perpendicular to the original axis of the spring and the helix angle of the spring is denoted by α. The initial curvatures and the twist per unit length are given by the following equations,

$$\kappa = 0, \quad \kappa' = \frac{\cos^2 \alpha}{r} \ and \ \tau = \frac{\sin \alpha \cos \alpha}{r}, \tag{5.1}$$

where r is the radius of the helix. The spring given in Figure 5.1 subjected to bending moment only. Considering this the following result occurs,

$$X = Y = Z = K = K' = \Theta = N = N' = T = 0. \tag{5.2}$$

The equations of the equilibrium given in (4.28)-(4.30) and (4.35)-(4.37), while only the bending applied to a simple straight strand, becomes to the following form,

$$\frac{dG(s)}{ds} - \tau_1 G'(s) + \kappa_1' H(s) = 0, \tag{5.3}$$

$$\frac{dG'(s)}{ds} - \kappa_1 H(s) + \tau_1 G(s) = 0, \tag{5.4}$$

$$\frac{dH(s)}{ds} - \kappa_1' G(s) + \kappa_1 G'(s) = 0, \tag{5.5}$$

where κ_1, κ_1' and τ_1 are the final curvatures and twist per unit length. κ_1, κ_1' and τ_1 are used in equation (4.39) as final values and equation (5.1) is used as the initial values. Under these circumstances, the equation (4.39) is transformed to the following form,

$$G(s) = \frac{\pi R^4}{4} E(\kappa_1 - \kappa_0) = \frac{\pi R^4}{4} E\kappa_1,$$

$$G'(s) = \frac{\pi R^4}{4} E(\kappa_1' - \kappa_0') = \frac{\pi R^4}{4} E(\kappa_1' - \frac{\cos^2 \alpha}{r}),$$

$$H(s) = \frac{\pi R^4 E}{4(1+v)}(\tau_1 - \tau_0) = \frac{\pi R^4 E}{4(1+v)}(\tau_1 - \frac{\sin \alpha \cos \alpha}{r}).$$
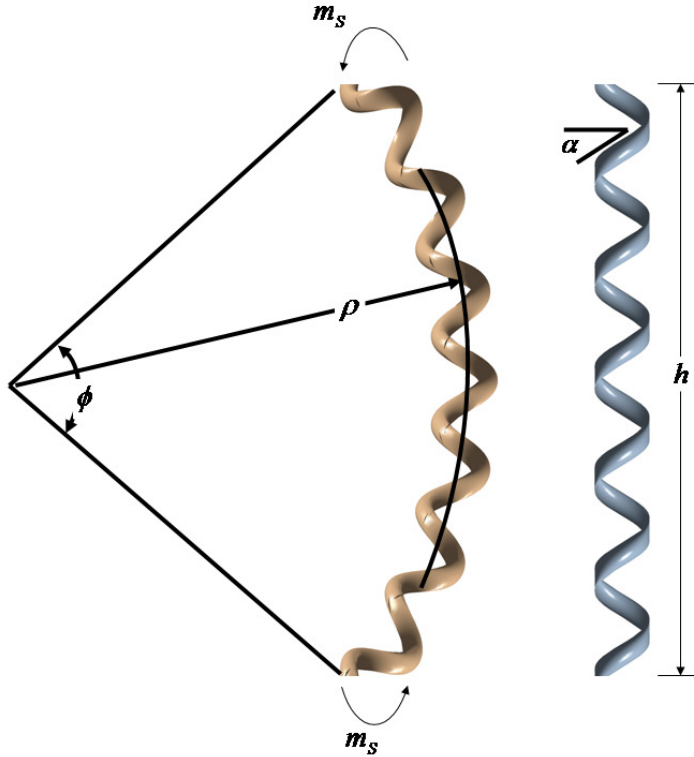
Figure 5.1: Bending applied to a helical spring.

Finally κ_1, κ_1' and τ_1 can be obtained as,

$$\kappa_1 = \frac{4}{\pi R^4 E} G(s), \tag{5.6}$$

$$\kappa_1' = \frac{4}{\pi R^4 E} G'(s) + \frac{\cos^2 \alpha}{r}, \tag{5.7}$$

$$\tau_1 = \frac{4(1+v)}{\pi R^4 E} H(s) + \frac{\sin \alpha \cos \alpha}{r}. \tag{5.8}$$

Putting these representations of the curvatures and twist per unit length in equations (5.3)-(5.5) results to three nonlinear equations,

$$\frac{dG(s)}{ds} - \frac{4v}{\pi R^4 E} G'(s)H(s) - \frac{\sin \alpha \cos \alpha}{r} G'(s) + \frac{\cos^2 \alpha}{r} H(s) = 0, \tag{5.9}$$

$$\frac{dG'(s)}{ds} + \frac{4v}{\pi R^4 E} G(s)H(s) + \frac{\sin \alpha \cos \alpha}{r} G(s) = 0, \tag{5.10}$$

$$\frac{dH(s)}{ds} - \frac{\cos^2 \alpha}{r} G(s) = 0. \tag{5.11}$$

Equations (5.9)-(5.11) constitutes first order nonlinear ordinary differential equations, and can be solved by a numerical method. However, to do this an initial condition is required. This system will be solved by using Poisson's ratio $v = 0$, as the initial condition at first. Then the solution found for $v = 0$ is used as the initial condition to solve this first order nonlinear ordinary differential equation by one of the well-known numerical method, Picard's method. For $v = 0$ the equations (5.9)-(5.11) becomes to,

$$\frac{dG(s)}{ds} - \frac{\sin \alpha \cos \alpha}{r} G'(s) + \frac{\cos^2 \alpha}{r} H(s) = 0, \tag{5.12}$$

$$\frac{dG'(s)}{ds} + \frac{\sin \alpha \cos \alpha}{r} G(s) = 0, \tag{5.13}$$

$$\frac{dH(s)}{ds} - \frac{\cos^2 \alpha}{r} G(s) = 0. \tag{5.14}$$

Equations (5.12) through (5.14) constitutes a system of linear ordinary differential equations and solved by using Maple®, and the following results are found,

$$G(s) = e^{\left(\frac{\sqrt{-2-2\cos(2\alpha)}}{2r}s\right)}C_2 + e^{\left(-\frac{\sqrt{-2-2\cos(2\alpha)}}{2r}s\right)}C_3, \tag{5.15}$$

$$G'(s) = C_1 + \int\left(-\frac{\sin 2\alpha}{2r}G(s)\right)ds, \tag{5.16}$$

$$H(s) = -\frac{r}{\cos^2\alpha}\frac{dG(s)}{ds} + \frac{\sin\alpha}{\cos\alpha}G'(s). \tag{5.17}$$

Equation (5.15) can be regarded as,

$$G(s) = A\cos(ks) + B\sin(ks). \tag{5.18}$$

Using the equation (5.18), representations for the equations given in (5.16) and (5.17) can be found with respect to $G'(s)$ and $H(s)$ as,

$$G'(s) = -\frac{\sin 2\alpha}{2kr}\big(A\sin(ks) - B\cos(ks)\big) + C_1, \tag{5.19}$$

$$H(s) = \frac{kr}{\cos^2\alpha}\big(A\sin(ks) - B\cos(ks)\big) - \frac{\sin^2\alpha}{kr}\big(A\sin(ks) - B\cos(ks)\big) + \frac{\sin\alpha}{\cos\alpha}C_1. \tag{5.20}$$

Applying a bending moment in x direction; $G = m_s$, zero bending moment in y direction; $G' = 0$, and twisting moment; $H = 0$, with $s = 0$, equations (5.18) through (5.20) results respectively,

$$A = m_s, \tag{5.21}$$

$$0 = \sin(2\alpha)B + 2krC_1, \tag{5.22}$$

and

$$0 = (\sin^2\alpha\cos^2\alpha - k^2r^2)B + kr\sin\alpha\cos\alpha C_1. \tag{5.23}$$

Multiplying equation (5.22) by $\sin\alpha\cos\alpha/2$ and adding to equation (5.23) yields,

$$B = 0, \ C_1 = 0. \tag{5.24}$$

Using equations (5.21) and (5.24), equations (5.18)-(5.20) results such that,

$$G(s) = m_s \cos(ks),$$

$$G'(s) = -\frac{\sin 2\alpha}{2kr} m_s \sin(ks) = -m_s \sin\alpha \sin(ks),$$

$$H(s) = \left(\frac{kr}{\cos^2\alpha} - \frac{\sin^2\alpha}{kr}\right) m_s \sin(ks) = m_s \cos\alpha \sin(ks),$$

where $k = r/\cos\alpha$. As a result, the solution of the first order linear differential equation can be written, which will be the initial conditions while solving the nonlinear part of the problem when the Poisson's ratio $v \neq 0$, as follows,

$$G(s) = m_s \cos(ks), \qquad (5.25)$$

$$G'(s) = -m_s \sin\alpha \sin(ks), \qquad (5.26)$$

$$H(s) = m_s \cos\alpha \sin(ks). \qquad (5.27)$$

Furthermore solutions of equation (5.12)-(5.14) given in equations (5.25)-(5.27) are harmonious with the solutions of Costello given in reference [11].

5.2 Bending moment derivation using the strain energy

The strain energy U in the spring can be written as [56],

$$U = \frac{1}{2}\int_0^l \left[A(\kappa_1 - \kappa)^2 + A(\kappa_1' - \kappa')^2 + C(\tau_1 - \tau)^2 \right] ds, \qquad (5.28)$$

where $A = \pi R^4 E / 4$ and $C = \pi R^4 E / 4(1+v)$, For the Poisson's ratio $v = 0$, results in $A = C$, and equation (5.28) is integrated such that,

$$U = \frac{1}{2}\int_0^l \frac{1}{A}\left[G^2 + G'^2 + H^2 \right] ds = \frac{1}{2A}\int_0^l m_s^2 ds = \frac{m_s^2 l}{2A}, \qquad (5.29)$$

where l is the length of the wire. When the work done by the bending moment m_s is equated to the strain energy, the result is,

$$\int_0^\phi m_s(\phi)d\phi = \frac{m_s^2 l}{2A}. \qquad (5.30)$$

Differentiating equation (5.30) yields,

$$m_s = \frac{m_s l}{A} \frac{dm_s}{d\phi}, \qquad (5.31)$$

and also, an integration of equation (5.31) yields, since $m_s(0)=0$,

$$m_s = \frac{A\phi}{l}. \qquad (5.32)$$

The length of the spring h is equated as, $h = l\sin(a)$, $l = \dfrac{\sin(a)}{h}$, and equation (5.32)

becomes to,

$$\frac{m_s}{A\sin(a)} = \frac{\phi}{h} = \frac{1}{\rho}. \qquad (5.33)$$

The exact solution of the nonlinear equations (5.12)-(5.14), found in equations (5.25)-(5.27), is used as the first approximation in Picard's method. Substituting $G(s)$, $G'(s)$ and $H(s)$, which are found in equations (5.25)-(5.27), into the nonlinear equations (5.9)-(5.11) and making the necessary trigonometric simplifications will yield,

$$\frac{dG(s)}{ds} = \left(\frac{1}{A} - \frac{1}{C}\right)\sin(\alpha)\cos(\alpha)m_s^2 \sin^2(ks) - \frac{\cos(\alpha)}{r}m_s\sin(ks), \qquad (5.34)$$

$$\frac{dG'(s)}{ds} = \left(\frac{1}{A} - \frac{1}{C}\right)m_s^2 \cos\alpha \sin(ks)\cos(ks) - \frac{\sin\alpha\cos\alpha}{r}m_s\cos(ks), \qquad (5.35)$$

$$\frac{dH(s)}{ds} = \frac{\cos^2(\alpha)}{r}m_s\cos(ks). \qquad (5.36)$$

Using the initial conditions; $G(0)=m_s$, $G'(0)=0$ and $H(0)=0$, for the first approximation of Picard's method in equations (5.34)-(5.36) results in,

$$G(s) = \left(\frac{1}{A} - \frac{1}{C}\right)\frac{\sin(\alpha)\cos(\alpha)}{2}m_s^{\,2}\left(s - \frac{\sin(2ks)}{2k}\right) + m_s\cos(ks),$$ **(5.37)**

$$G'(s) = \left(\frac{1}{A} - \frac{1}{C}\right)\frac{\cos(\alpha)}{2k}m_s^2\sin^2(ks) - m_s\sin(\alpha)\sin(ks),$$ **(5.38)**

$$H(s) = m_s\cos(\alpha)\sin(ks).$$ **(5.39)**

The strain energy U, can be written for the spring as,

$$U = \frac{1}{2}\int_0^l\left[\frac{G^2}{A} + \frac{G'^2}{A} + \frac{H^2}{C}\right]ds,$$

and computed as follows,

$$
U = \frac{(-C+A)^2\cos^2(a)}{32A^3C^2k^3}\left[\left(4\phi + \frac{4}{3}\phi^3\right) + \left(-\frac{5}{2}\phi - \frac{4}{3}\phi^3\right)\cos^2(a)\right]m_s^4
$$
$$
+ \frac{(-C+A)}{32A^3C^2k^3}\left(\frac{32}{3}ACk\sin(2a) - \frac{64}{3}kAC\sin(a)\cos(a)\right)m_s^3
$$
$$
+ \frac{1}{32A^3C^2k^3}\left[16\phi A^2C^2k^2 + 8(-C+A)Ck^2A^2\phi\cos^2(a)\right]m_s^2,
$$

where $\phi = kl$.

As a result of the trigonometric simplifications, coefficient of the m_s^3 vanishes and assuming the spring has n coils, $\phi = 2\pi n$, the equation above becomes to,

$$
U = \frac{v^2\cos^2(a)}{32A^3k^3}\left[8\pi n + \frac{32}{3}(\pi n)^3 + \left(-5\pi n - \frac{4}{3}(\pi n)^3\right)(1-\sin^2(a))\right]m_s^4
$$
$$
+ \frac{\pi n}{2ACk}\left[2C + (-C+A)\cos^2(a)\right]m_s^2.
$$

Replacing $C = \dfrac{A}{(1+v)}$ in the equation given above will yield the final form of U as,

$$
U = \frac{1}{8}\frac{v^2\cos^2(a)}{A^3k^3}2\pi n\left(\frac{3}{8} + \left(\frac{5}{8} + \frac{(2\pi n)^2}{3}\right)\sin^2(a)\right)m_s^4
$$
$$
+ \frac{1}{4Ak}2\pi n\left(2 + v\cos^2(a)\right)m_s^2.
$$
(5.40)

The equation given in (5.40) is identical with the given equation in reference [56] and can be written in the form of,

$$U = \lambda_1 m_s^4 + \lambda_2 m_s^2,$$ (5.41)

where

$$\lambda_1 = \frac{1}{8} \frac{v^2 \cos^2(a)}{A^3 k^3} 2\pi n \left[\frac{3}{8} + \left(\frac{(2\pi n)^2}{3} + \frac{5}{8} \right) \sin^2(a) \right],$$ (5.42)

and

$$\lambda_2 = \frac{1}{4Ak} 2\pi n \left[2 + v \cos^2(a) \right].$$ (5.43)

Equating the work done by strain energy to the bending moment m_s gives,

$$\lambda_1 m_s^4 + \lambda_2 m_s^2 = \int_0^\phi m_s(\phi) d\phi,$$ (5.44)

and differentiation of equation (5.44) with respect to ϕ after necessary simplifications yields,

$$(4\lambda_1 m_s^2 + 2\lambda_2) \frac{dm_s}{d\phi} = 1.$$ (5.45)

Again integrating back equation (5.45) will yield,

$$\frac{4}{3} \lambda_1 m_s^3 + 2\lambda_2 m_s = \phi.$$ (5.46)

Considering ϕ and k as; $\phi = l \sin(a) / \rho$ and $k = \cos(\alpha)/r$, and using λ_1 and λ_2 given in equations (5.42) and (5.43) into the equation (5.46) yields,

$$\frac{1}{\rho} = \frac{v^2 r^2}{6\sin(a)} \left[\frac{3}{8} + \left(\frac{(2\pi n)^2}{3} + \frac{5}{8} \right) \sin^2(a) \right] \frac{m_s^3}{EI} + \frac{2 + v \cos^2(a)}{2\sin(a)} \frac{m_s}{EI},$$ (5.47)

where $I = \pi R^4 / 4$.

66

In most practical cases, the term involving m_s^3 in equation (5.47) can be neglected in comparison with the term involving m_s due to its small effect to the curvature $1/\rho$. The result for curvature $1/\rho$ can be obtained in this aspect as,

$$\frac{1}{\rho} = \frac{2+v\cos^2(a)}{2\sin(a)}\frac{m_s}{EI},\qquad(5.48)$$

which is also harmonious with the angular deflection (curvature) given in [6]. The bending moment m_s can be written using equation (5.48) in the following form,

$$m_s = \frac{1}{\rho}\frac{\pi ER^4}{4}\frac{2\sin(a)}{2+v\cos^2(a)}.\qquad(5.49)$$

Equation (5.48) provides a result that is valid for large rotations provided with $v=0$. An application of Picard's method shows that, for the first approximation, in the case of large rotations and $v\neq0$, equation (5.48) yields valid results for most practical cases. An extension of Picard's method would yield a power series in m_s for the curvature $1/\rho$ in which the coefficient m_s remains the same. For most practical applications, the resulting series converges very rapidly and it is felt that equation (5.48) would also yield excellent results for the curvature for relatively large rotations and $v\neq0$ [56].

5.3 Bending stiffness of a simple straight strand

When a simple straight strand bent over a circle of radius ρ, as in Figure 5.1 by a bending moment of M_b, bending stiffness A^* of this strand is approximated by summing the bending stiffness of each wire in the strand [11]. During this process, friction is neglected and while bending outer wires are assumed to act independently. The bending moment M_b of a simple straight strand can be written by summing the bending stiffness of the center wire plus the multiplicity m_l of the number of outer wires where l represents the layer number and M_b is,

$$M_b = \frac{\pi E}{4}\left[\frac{2m_2\sin(a_2)}{2+v\cos^2(a_2)}R_2^4 + R_1^4\right]\frac{1}{\rho} = \frac{A^*}{\rho},\qquad(5.50)$$

67

where A^* is the bending stiffness of a simple straight strand which can be written as,

$$A^* = \frac{\pi E}{4} \left[\frac{2m_2 \sin(a_2)}{2 + v\cos^2(a_2)} R_2^4 + R_1^4 \right]. \tag{5.51}$$

5.4   Frictional effects of a strand

The general equilibrium equations are given in (4.28)-(4.30) and (4.35)-(4.37) with the curvatures given in equations (4.39). Assuming under sufficient axial loading condition over a simple straight strand, contact occurs between an outer wire and the center wire. If the wire strand is bent only while the contact condition is maintained, an external load can be applied to the outer wire only through the line of contact between any two cross sections. In Figure 5.2, a force applied to a boundary section of a wire with radius R. Transforming the force on the boundary to an equivalent force and couple acting along the centerline of the wire the following equations can be written,

$$Zds = Z_0 ds_0 \cos\beta - Y_0 ds_0 \sin\beta, \tag{5.52}$$

$$Yds = Z_0 ds_0 \sin\beta + Y_0 ds_0 \cos\beta, \tag{5.53}$$

$$K = 0, \tag{5.54}$$

$$K' = -ZR, \tag{5.55}$$

and,

$$\Theta = YR, \tag{5.56}$$

where Y_0 and Z_0 are the forces per unit length acting along the contact curve, β is the angle shown in Figure 5.2, ds_0 is a differential length along the contact curve corresponding to a differential length ds along the centerline of an outside wire, and K, K', and Θ are the components of the external moments per unit length along the centerline of an outside wire.

The bending moment and twisting moment in the wire can be expressed as in equation (4.39). The equilibrium equations (4.28)-(4.30), (4.35)-(4.37) and equations (5.54)-(5.56) considered together to find the following system of equations,

$$\frac{dN}{ds} - N'\tau + T\kappa' + X = 0, \tag{5.57}$$

$$\frac{dN'}{ds} - T\kappa + N\tau + Y = 0, \tag{5.58}$$

$$\frac{dT}{ds} - N\kappa' + N'\kappa + Z = 0, \tag{5.59}$$

$$\frac{dG}{ds} - G'\tau + H\kappa' - N' = 0, \tag{5.60}$$

$$\frac{dG'}{ds} - H\kappa + G\tau + N - RZ = 0, \tag{5.61}$$

$$\frac{dH}{ds} - G\kappa' + G'\kappa + RY = 0. \tag{5.62}$$
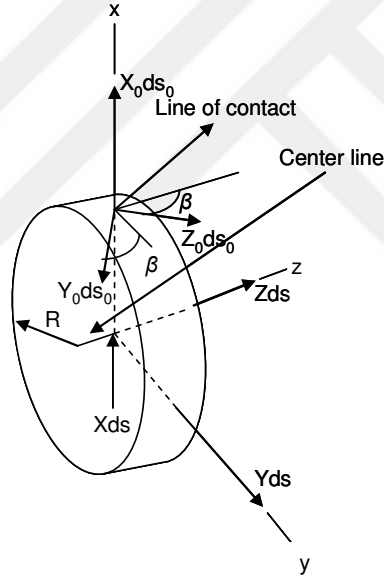
Figure 5.2: Loads over an outer wire with differential element length of *ds*.

The original curvature and twist for an outside wire are given in equation (4.54). It is assumed that the initially straight center wire is deformed into a circle of radius ρ and the relation between α and ρ is known as, $\tan\alpha = \rho\theta / r\phi$. Deformed states of the curvature and twist can be written as,

$$\kappa = \frac{\sin\alpha}{\rho}\cos\phi, \quad \kappa' = \frac{\cos^2\alpha}{r} - \frac{\sin^2\alpha}{\rho}\sin\phi,$$

$$\tau = \frac{\sin\alpha\cos\alpha}{r} + \frac{\sin\alpha\cos\alpha}{\rho}\sin\phi. \tag{5.63}$$

Solving equations (4.35)-(4.37) yields,

$$N' = \frac{(A-C)}{\rho}\sin\alpha\cos\alpha\left[\frac{\cos^2\alpha\sin\phi}{r} + \frac{\sin^2\alpha\sin^2\phi}{\rho}\right],\tag{5.64}$$

$$RZ = N + \frac{(A-C)}{\rho^2}\sin^2\alpha\cos\alpha\sin\phi\cos\phi,\tag{5.65}$$

$$RY = \frac{(A-C)}{\rho r}\sin\alpha\cos^2\alpha\cos\phi,\tag{5.66}$$

where $A = \frac{\pi E R^4}{4}$; $C = \frac{\pi E R^4}{4(1+v)}$ and $s = \frac{r}{\cos\alpha}\phi$. Equation (5.64) results in,

$$\frac{dN'}{ds} = \frac{dN'}{d\phi}\frac{d\phi}{ds} = \frac{(A-C)}{r\rho}\sin\alpha\cos^2\alpha\left[-\frac{\cos^2\alpha}{r} + 2\frac{\sin^2\alpha}{\rho}\sin\phi\right]\cos\phi.\tag{5.67}$$

A combination of the equations (4.29), (4.30), (5.64)-(5.67) yields,

$$\frac{dT}{d\phi} + \frac{r}{\rho}\frac{\left[\frac{r}{R} - \cos^2\alpha + \frac{r}{\rho}\sin^2\alpha\sin\phi\right]}{\cos^2\alpha\left[1 + \frac{r}{\rho}\sin\phi\right]}(\cos\phi)T$$

$$= -\frac{(A-C)}{r^2\rho}\frac{r}{\rho}\left[\frac{r}{R} - \cos^2\alpha + \frac{r}{\rho}\sin^2\alpha\sin\phi\right]\tag{5.68}$$

$$*\left\{\frac{r}{\rho}\sin^2\alpha\sin\phi - \frac{\left[\frac{r}{R} - \cos^2\alpha + \frac{r}{\rho}2\sin^2\alpha\sin\phi\right]}{\left[1 + \frac{r}{\rho}\sin\phi\right]}\right\}\cos\phi.$$

Letting $r/\rho \ll 1$ equation (5.68) becomes to,

$$\frac{dT}{d\phi} + \frac{r}{\rho\cos^2\alpha}\left[\frac{r}{R} - \cos^2\alpha\right](\cos\phi)T = \frac{(A-C)}{r^2}\frac{r}{\rho}\left[\frac{r}{R} - \cos^2\alpha\right]^2\cos\phi,\tag{5.69}$$

and the solution of equation (5.69) gives [98],

$$T = \frac{C_3}{e^{C_1\sin\phi}} + \frac{C_2}{C_1},\tag{5.70}$$

where,

$$C_1 = \frac{r}{\rho \cos^2 \alpha} \left[\frac{r}{R} - \cos^2 \alpha \right],$$

$$C_2 = \frac{(A-C)}{r^2} \left[\frac{r}{R} - \cos^2 \alpha \right]^2,$$

(5.71)

in addition, C_3 is an arbitrary constant, which is determined by the following equation,

$$\int_0^{2\pi} T d\phi = 0.$$

(5.72)

Equation (5.72) indicates that the change in length because of bending of an outer wire in one lay length is assumed zero when the strand is subjected to bending. Although this change in length may not be zero, it is certainly small, and the value of C_3 will not be significantly changed by assuming equation (5.72) is valid. Since $C_1 \ll 1$, equation (5.72) yields,

$$C_3 = -\frac{C_2}{C_1}.$$

(5.73)

The equation (5.70) can be written with these constants as,

$$T = \frac{\pi E R^4}{4r^2} \frac{r}{\rho} \frac{v}{(1+v)} \left[\frac{r}{R} - \cos^2 \alpha \right]^2 \sin \phi.$$

(5.74)

According to equations (5.64)-(5.66) and the previous definitions of forces and couples, the following results can be written down,

$$G = \frac{\pi E R^4}{4} \frac{\sin \alpha}{\rho} \cos \phi,$$

(5.75)

$$G' = -\frac{\pi E R^4}{4} \frac{\sin^2 \alpha}{\rho} \sin \phi,$$

(5.76)

$$H = \frac{\pi E R^4}{4(1+v)} \frac{\sin \alpha \cos \alpha}{\rho} \sin \phi,$$

(5.77)

$$Y = \frac{\pi E R^4}{4R\rho r} \frac{v}{(1+v)} \sin\alpha\cos^2\alpha\cos\phi, \tag{5.78}$$

$$N' = -\frac{\pi E R^4}{4\rho r} \frac{v}{(1+v)} \sin\alpha\cos^3\alpha\sin\phi, \tag{5.79}$$

$$N = -\frac{\pi E R^4}{4\rho} \frac{v}{(1+v)} \left[\frac{1}{R} - \frac{\cos^2\alpha}{r}\right] \cos\alpha\cos\phi, \tag{5.80}$$

$$Z = -\frac{\pi E R^4}{4R\rho} \frac{v}{(1+v)} \left[\frac{1}{R} - \frac{\cos^2\alpha}{r}\right] \cos\alpha\cos\phi, \tag{5.81}$$

$$X = -\frac{\pi E R^4}{4\rho r^2} \frac{v}{(1+v)} \cos^2\alpha\left[\left(\frac{r}{R}\right)^2 + \frac{r}{R}(1-2\cos^2\alpha)\right]\sin\phi. \tag{5.82}$$

The foregoing equations are for the bending only under the curvatures and twist given in equation (5.63).

5.5   Construction and static response of an IWRC

A simple straight seven wire (1+6) strand is surrounded by six seven wire (1+6) strand and its cross section is given in Figure 5.3. Strand 2 is deformed into the single helical shape over the strand 1, which composes a well-know core type named IWRC. No external loads are applied to these strands and they are in unloaded preformed shapes. Here again the bending stiffness of the strand 2 will be written as in equation (5.50). By summing the bending stiffness of the each wire of the strand 2,

$$A_2^* = \frac{\pi E}{4}\left[\frac{2m_4\sin(a_4)}{2+v\cos^2(a_4)}R_4^4 + R_3^4\right], \tag{5.83}$$

where a_4 is the helix angle of an outer wire in strand 2. Helix angle of the strand 2 is denoted by α_2^* and its loaded form can be denoted by $\bar{\alpha}_2^*$. The angle of twist for the strand 2 is represented by $\Delta\tau_2^*$ which is,

$$\Delta\tau_2^* = \frac{\sin\bar{\alpha}_2^*\cos\bar{\alpha}_2^*}{\bar{r}_2^*} - \frac{\sin\alpha_2^*\cos\alpha_2^*}{r_2^*}, \tag{5.84}$$

where $r_2^* = R_1 + 2R_2 + R_3 + 2R_4$.

72

6 strand is wound around Strand 1
in counterclockwise direction

R_2

R_4

R_1

R_3
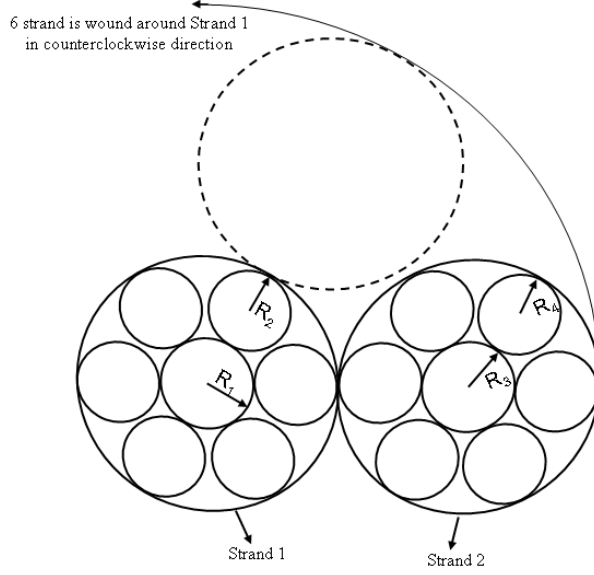
Strand 1

Strand 2

Figure 5.3: An IWRC cross sectional view.

Because of the Poisson's ratio effect,

$$\bar{r}_2^* = r_2^* - \nu(R_1\xi_1 + 2R_2\xi_2 + R_3\xi_3 + 2R_4\xi_4),$$ (5.85)

where ξ_i are the axial wire strains for $i = 1,..,4$. Following equations can be written for strand 2 as,

$$\xi_1 = \xi_3 + \frac{\Delta\alpha_2^*}{\tan\alpha_2^*},$$ (5.86)

$$\xi_3 = \xi_4 + \frac{\Delta\alpha_4}{\tan\alpha_4},$$ (5.87)

$$r_2^*\tau = \frac{r_2^*}{\bar{r}_2^*}\left(\frac{1+\xi_3}{\tan\alpha_2^*} - \Delta\alpha_2^*\right) - \frac{1}{\tan\alpha_2^*}$$
$$= \frac{\xi_3}{\tan\alpha_2^*} - \Delta\alpha_2^* + \frac{\nu}{r_2^*}\frac{(R_1\xi_1 + 2R_2\xi_2 + R_3\xi_3 + 2R_4\xi_4)}{\tan\alpha_2^*},$$ (5.88)

$$(R_3 + R_4)\Delta\tau_2^* = \frac{\xi_4}{\tan\alpha_4} - \Delta\alpha_4 + \nu\frac{(R_3\xi_3 + R_4\xi_4)}{(R_3 + R_4)\tan\alpha_4}$$
$$= \frac{(R_3 + R_4)}{r_2^*}\left[\begin{array}{l}(1 - 2\sin^2\alpha_2^*)\Delta\alpha_2^* \\ +\nu\frac{(R_1\xi_1 + 2R_2\xi_2 + R_3\xi_3 + 2R_4\xi_4)}{r_2^*}\sin\alpha_2^*\cos\alpha_2^*\end{array}\right],$$ (5.89)

where τ is the twist of the rope and $\Delta\tau_2^*$ is the angle of twist of the strand 2. Also,

$$\xi_1 = \xi_2 + \frac{\Delta\alpha_2}{\tan\alpha_2},$$

$$(R_1 + R_2)\tau = \frac{\xi_2}{\tan\alpha_2} - \Delta\alpha_2 + v\frac{(R_1\xi_1 + R_2\xi_2)}{(R_1 + R_2)\tan\alpha_2},$$

(5.90)

for strand 1. The rotational strain for the rope can be written as,

$$\beta = R\tau,$$

(5.91)

where $R = R_1 + 2R_2 + 2R_3 + 4R_4$.

The following procedure will give the axial response of a wire rope shown in Figure 5.3. Axial strain ξ, and rotational strain β are chosen. Taking into account that $\xi_1 = \xi$ and $\beta = R\tau$, ξ_2 and $\Delta\alpha_2$ can be found by solving equations (5.90). ξ_3, ξ_4, $\Delta\alpha_2^*$ and $\Delta\alpha_4$ can be found by solving equations (5.86)-(5.89).

Using equation (5.89), $\Delta\tau_2^*$ can be determined, T_2^* and H_2^* can be computed for strand 2 by equations (4.105) and (4.107) respectively. Bending moment $G_2'^*$ for strand 2 is given by,

$$G_2'^* = A_2^* \Delta\kappa_2^* = A_2^* \left(\frac{\cos^2\bar{\alpha}_2^*}{\bar{r}_2^*} - \frac{\cos^2\alpha_2^*}{r_2^*} \right),$$

(5.92)

which can be linearized and found that,

$$G_2'^* = A_2^* \Delta\kappa_2^* = A_2^* \left[\begin{array}{c} v\dfrac{\cos^2\alpha_2^*}{\left(r_2^*\right)^2}\left(R_1\xi_1 + 2R_2\xi_2 + R_3\xi_3 + 2R_4\xi_4\right) \\[2ex] -\dfrac{2\sin\alpha_2^* \cos\alpha_2^*}{r_2^*}\Delta\alpha_2^* \end{array} \right].$$

(5.93)

Using equation (4.106) $N_2'^*$ can be computed as in,

$$N_2'^* = \frac{\cos^2\alpha_2^*}{r_2^*}H_2^* - \frac{\sin\alpha_2^* \cos\alpha_2^*}{r_2^*}G_2'^*.$$

(5.94)

Axial force and axial twisting moment over strand 2 can be written as,

$$F_2^* = m_2 \left[T_2^* \sin \alpha_2^* + N_2'^* \cos \alpha_2^* \right], \tag{5.95}$$

$$M_{t2}^* = m_2 \left[H_2^* \sin \alpha_2^* + G_2'^* \cos \alpha_2^* + T_2^* Er_2^* \cos \alpha_2^* - N_2'^* Er_2^* \sin \alpha_2^* \right]. \tag{5.96}$$

The total axial force F and the axial twisting moment M_t is derived as follows [11],

$$F = F_1^* + F_2^* \tag{5.97}$$

$$M = M_{t1}^* + M_{t2}^*. \tag{5.98}$$

5.6   Generalized solution of IWRC and bending over a sheave

Axial behavior of a strand can be analyzed using the same equilibrium equations for the axial behavior of a helical wire given in equations (4.28)-(4.30) and (4.35)-(4.37). It is assumed that the generalized forces are independent of s, and wires are not subjected to bending moments thus $K = K' = 0$, also T is assumed to be constant along the wire. The equilibrium equations are independent of the position and will be in the following form [63],

$$X = N'\tau - T\kappa', \tag{5.99}$$

and,

$$N' = -G'\tau + H\kappa', \tag{5.100}$$

where κ, κ' and τ are defined in initial condition as in equation (4.21). Considering a helical wire in a strand under axial loading, it will be depend on an axial strain and twisting. The elements of wire rope are considered using the indices given in Table 5.1.

The initial forms of the normal and binormal curvatures and twist of each wire are,

$$\kappa_{si} = 0; \quad \kappa_{si}' = \frac{\cos^2 \alpha_{si}}{r_{si}} \text{ and } \tau_{si} = \frac{\sin \alpha_{si} \cos \alpha_{si}}{r_{si}}. \tag{5.101}$$

Table 5.1: Indices of a wire within a strand.

s	Strand number
m_s	Number of strands in the s'th layers of wire rope
l_s	Within a strand shows the number of layers of helically wrapped wires
i	Wire layer number
m_{si}	Number of identical wires in the i'th layer
R_{si}	Wire radiuses of the individual wire within a strand s in layer i
α_{si}	Helix angle of the individual wire within a strand s in layer i
r_{si}	Helix radius of the individual wire within a strand s in layer i

Pulling and twisting results strain ξ_{si} and change in the binormal curvature and twist $\Delta\kappa'_{si}$, $\Delta\tau_{si}$ respectively in each wire in a strand. There will be no change in the normal curvature κ_{si}, which results in $G_{si} = 0$. Wire loads depending on these changes can be written as,

$$T_{si} = \pi R_{si}^2 \xi_{si} , \tag{5.102}$$

$$G'_{si} = \frac{\pi E R_{si}^4}{4} \Delta\kappa'_{si} , \tag{5.103}$$

$$H_{si} = \frac{\pi E R_{si}^4}{4(1+v)} \Delta\tau_{si} . \tag{5.104}$$

Caused by the small changes in r_{si} and α_{si} there will be small changes in curvature and twist. It can be shown by partial differentiation of equations (5.101) that,

$$\frac{\Delta r_{si}}{r_{si}} = -2\tan\alpha_{si}(r_{si}\Delta\tau_{si}) + (\tan^2\alpha_{si} - 1)(r_{si}\Delta\kappa'_{si}) , \tag{5.105}$$

$$\Delta\alpha_{si} = (r_{si}\Delta\tau_{si}) - \tan\alpha_{si}(r_{si}\Delta\kappa'_{si}). \tag{5.106}$$

While pulling and twisting a straight strand, an axial strain ξ_s and a change in twist $\Delta\tau_s$ occurs. Wire layers should be act according to these strains and adjacent wire layers must remain in contact with each other. Three compatibility conditions take places. First two conditions are comes from the extension and change in twist of the

strand. A small change in strain ξ_{si} and in helix angle $\Delta\alpha_{si}$ makes change in the axial strain of the strand ξ_s,

$$\xi_s = \xi_{si} + \cot\alpha_{si}\Delta\alpha_{si}. \tag{5.107}$$

In addition, change in strand twist $\Delta\tau_s$ is given by,

$$\Delta\tau_s = \frac{1}{r_{si}}\left[\cot\alpha_{si}\left(-\frac{\Delta r_{si}}{r_{si}} + \xi_{si}\right) - \Delta\alpha_{si}\right]. \tag{5.108}$$

The last condition comes from the idea that the wires in the i'th layer of a strand is in contact in the $(i-1)$'th layer of the same strand. The helix radius r_{si} can be written in terms of wire radius R_{sj} as,

$$r_{si} = \sum_{j=1}^{i}\eta_{sij}R_{sj}, \tag{5.109}$$

where η_{sij} are known dimensionless weighting factors (0 or 1) or they are complicated depending on the helix angle α_{si} [73]. Change in helix radius Δr_{si} is depended on the Poisson contraction of all the wires in the strand and is written as,

$$\Delta r_{si} = \Delta r_{si}^p - v\eta_{sii}R_{si}\xi_{si}, \tag{5.110}$$

where Δr_{si}^p is,

$$\Delta r_{si}^p = -v\sum_{j=1}^{i-1}\eta_{sij}R_{sj}\xi_{sj}. \tag{5.111}$$

Three compatibility conditions to determine generalized wire strains ξ_{si}, $\Delta\kappa_{si}'$ and $\Delta\tau_{si}$ can be determined in terms of generalized strand strains ξ_s, $\Delta\tau_s$ and Δr_{si}^p using the equations (5.107), (5.108), (5.110) with equation (5.105), (5.106). These relations can be written in matrix form as,

$$\begin{bmatrix} 1 & \cot\alpha_{si} & -1 \\ \cot\alpha_{si} & 1 & \cot\alpha_{si} \\ v\eta_{sii}\left(R_{si}/r_{si}\right)\cot^2\alpha_{si} & -2\cot\alpha_{si} & \left(1-\cot^2\alpha_{si}\right) \end{bmatrix} \begin{pmatrix} \xi_{si} \\ r_{si}\Delta\tau_{si} \\ r_{si}\Delta\kappa'_{si} \end{pmatrix}$$
$$= \begin{pmatrix} \xi_s \\ r_{si}\Delta\tau_s \\ \left(\cot^2\alpha_{si}/r_{si}\right)\Delta r_{si}^p \end{pmatrix}, \tag{5.112}$$

and solved by using Cramer's rule for $\cot\alpha_{si} \neq 0$. Generalized forces on a strand T_s can be computed by,

$$T_s = \sum_{i=1}^{l_s} m_{si}\left[T_{si}\sin\alpha_{si} + N'_{si}\cos\alpha_{si}\right], \tag{5.113}$$

while the torque H_s is,

$$H_s = \sum_{i=1}^{l_s} m_{si}\left[\left(H_{si}\sin\alpha_{si} + G'_{si}\cos\alpha_{si}\right) + r_{si}\left(T_{si}\cos\alpha_{si} - N'_{si}\sin\alpha_{si}\right)\right], \tag{5.114}$$

where T_{si}, G'_{si}, H_{si} and N'_{si} are computed using the equations (5.102)-(5.104) and (5.100) respectively once equation (5.112) is solved for $i = 1,...,l_s$. A value for the strand binormal bending moment G'_s for a well-lubricated frictionless case can be written as [73],

$$G'_s = \left(\sum_{i=1}^{l_s} m_{si}\frac{\sin\alpha_{si}}{1+\dfrac{1}{2}v\cos^2\alpha_{si}}\frac{\pi E R^4}{4}\right)\Delta\kappa'_s. \tag{5.115}$$

For a wire rope with an IWRC let R_s is the radius of a strand in the s'th strand layer. If number of wire layers l_s and the outermost wire layer is numbered as l_s'th layer in this strand then for $i = l_s$,

$$R_s = r_{si} + R_{si}. \tag{5.116}$$

The helix radius will be of the form that,

$$r_s = \sum_{t=1}^{s} \eta_{0st} R_t \qquad (5.117)$$

where η_{0st} are integers. Rope radius of R is given by for $s = l$,

$$R = r_s + R_s, \qquad (5.118)$$

where l is the number of strand layers in the rope. Each strand in the rope has its own twist τ_s and curvature κ_s' given by,

$$\tau_s = \frac{\sin \alpha_s \cos \alpha_s}{r_s} \quad \text{and} \quad \kappa_s' = \frac{\cos^2 \alpha_s}{r_s}, \qquad (5.119)$$

where α_s is the helix angle of the strand within the rope. There are three compatibility conditions for wire ropes as in strands. Two of them is similar to the strands given in equation (5.107) and (5.108). The last condition is about the change in strand radius. Strands in the s'th strand layer remain in contact with those in the $(s-1)$'th strand layer. Using equations (5.109) and (5.116) with the Poisson contraction of the wires within a strand ΔR_s can be defined as,

$$\Delta R_s = -v \sum_{j=1}^{l_s} \eta_{s0j} \xi_{sj} R_{sj}, \qquad (5.120)$$

and the η_{s0j} are known weighting factors and ξ_{sj} are the strains in the individual wires of a strand. ξ_{sj} are linear functions of both ξ_s and $\Delta \tau_s$ that,

$$\xi_{sj} = \frac{\partial \xi_{sj}}{\partial \xi_s} \xi_s + \frac{\partial \xi_{sj}}{\partial \Delta \tau_s} \Delta \tau_s, \qquad (5.121)$$

where the partial derivatives can be computed numerically by the previously developed solutions for wires within a loaded strand. Change in Δr_s can be shown by using the equations (5.117), (5.120) and (5.121) by,

$$\Delta r_s = \Delta r_s^p + \eta_{0ss} \frac{\partial R_s}{\partial \xi_s} \xi_s + \eta_{0ss} \frac{\partial R_s}{\partial \Delta \tau_s} \Delta \tau_s, \qquad (5.122)$$

where Δr_s^p can be represented by,

$$\Delta r_s^p \equiv \sum_{t=1}^{s-1} \eta_{0st} \left(\frac{\partial R_t}{\partial \xi_t} \xi_t + \frac{\partial R_t}{\partial \Delta \tau_t} \Delta \tau_t \right). \qquad \textbf{(5.123)}$$

Using the fundamental relation given in (5.105) which gives the change in helix radius Δr_s as a function of the change in twist $\Delta \tau_s$ and the change in curvature $\Delta \kappa_s'$. Applying this relation and multiplying with $\cot^2 \alpha_s / r_s$ and making the definitions,

$$C_s^\xi \equiv \eta_{0ss} \frac{\partial R_s}{\partial \xi_s}, \quad C_s^{\Delta\tau} \equiv \eta_{0ss} \frac{\partial R_s}{\partial \Delta \tau_s}, \qquad \textbf{(5.124)}$$

equation (5.122) becomes to,

$$-\frac{\cot^2 \alpha_s}{r_s} C_s^\xi \xi_s + \left(-2\cot \alpha_s - \frac{\cot^2 \alpha_s}{r_s} C_s^{\Delta\tau} \right)(r_s \Delta \tau_s)$$

$$+(1 - \cot^2 \alpha_s)(r_s \Delta \kappa_s') = \frac{\cot^2 \alpha_s}{r_s} \Delta r_s^p. \qquad \textbf{(5.125)}$$

Three compatibility conditions are ready with equation (5.125) and writing them into a matrix form gives,

$$\begin{bmatrix} 1 & \cot \alpha_s & -1 \\ \cot \alpha_s & 1 & \cot \alpha_s \\ -\left(\cot^2 \alpha_s / r_s\right) C_s^\xi & -2\cot \alpha_s - \left(\cot^2 \alpha_s / r_s\right) C_s^{\Delta\tau} & \left(1 - \cot^2 \alpha_s\right) \end{bmatrix}$$

$$\cdot \begin{pmatrix} \xi_s \\ r_s \Delta \tau_s \\ r_s \Delta \kappa_s' \end{pmatrix} = \begin{pmatrix} \xi \\ r_s \Delta \tau \\ \left(\cot^2 \alpha_s / r_s\right) \Delta r_s^p \end{pmatrix}. \qquad \textbf{(5.126)}$$

It can be seen easily that this matrix form is similar to the equations (5.112). Solving equation (5.126) for each strand in the rope one can find the tensile force T_s, the twisting moment H_s and the bending moment G_s' acting for each strand. Total force T and twisting moment H for the rope can be written in a similar way as in strands in equations (5.113) and (5.114) respectively and can be given as,

80

$$T = \sum_{s=1}^{l} m_s \left[T_s \sin \alpha_s + N_s' \cos \alpha_s \right], \qquad (5.127)$$

$$H = \sum_{s=1}^{l} m_s \left[\left(H_s \sin \alpha_s + G_s' \cos \alpha_s \right) + r_s \left(T_s \cos \alpha_s - N_s' \sin \alpha_s \right) \right]. \qquad (5.128)$$

5.7 Bending a loaded rope over a sheave

When axially loaded straight wire rope bent over a sheave, it is subjected to additional bending loads. It has been shown that the maximum change in normal curvature $\Delta \kappa_{si}$ in a helical wire in a straight strand is smaller then in strand curvature $\Delta \kappa_s$ by the following equation [73],

$$\Delta \kappa_{si} = \frac{\sin \alpha_{si}}{1 + \frac{1}{2} v \cos^2 \alpha_{si}} \Delta \kappa_s. \qquad (5.129)$$

The maximum change in strand curvature $\Delta \kappa_s$ is found by the axis of a straight strand bent over a sheave with radius D/2 as,

$$\Delta \kappa_s = \frac{\sin \alpha_s}{1 + \frac{1}{2} v \cos^2 \alpha_s} \frac{1}{D/2}. \qquad (5.130)$$

The maximum bending stresses σ_{si}^B for the wires within a strand is predicted by using equations (5.118), (5.129) and (5.130) together, because of sheave curvature depending on D/d parameter as,

$$\sigma_{si}^B = E R_{si} \Delta \kappa_{si} = E \frac{R_{si}}{R} \frac{\sin \alpha_s}{1 + \frac{1}{2} v \cos^2 \alpha_s} \cdot \frac{\sin \alpha_{si}}{1 + \frac{1}{2} v \cos^2 \alpha_{si}} \left(\frac{D}{d} \right)^{-1}, \qquad (5.131)$$

where $d = 2R$. The factors R_{si}/R in equation (5.131) suggests that, for a given D/d ratio, stresses owing to bending over a sheave can be minimized by using a rope having a large number of very fine wires [73]. Due to the change in twist is zero $\Delta \tau = 0$, the shearing stresses by reason of the twisting moments H_{si} and the

81

transverse shear forces N'_{si} are also negligible. The maximum tensile stress on the cross section of a given wire, the axial extension of a straight rope is given by,

$$\sigma_{si}^T = \frac{1}{\pi R_{si}^2} T_{si} + \frac{R_{si}}{\pi R_{si}^4 / 4} \left| G'_{si} \right| + \frac{E R_{si} \sin \alpha_{si}}{1 + \frac{1}{2} v \cos^2 \alpha_{si}} \left| \Delta \kappa'_s \right|,$$ (5.132)

where the last term comes from bending stresses induced in strand wires when the strand subjected to change in curvature using equation (5.115). The resulting data can be scaled for ropes with identical constructions for different rope diameter d. Force results will vary as d^2 whereas moment results will vary as d^3. Nominal stress σ_{nom} is defined as,

$$\sigma_{nom} \equiv \frac{T}{A},$$ (5.133)

where A is the metallic area of the rope and given by,

$$A = \sum_{s=1}^{l} m_s \sum_{i=1}^{l_s} m_{si} \pi R_{si}^2 .$$ (5.134)

The non-dimensional ratio or straight rope factor z_{si}^T is given by,

$$z_{si}^T \equiv \frac{\sigma_{si}^T}{\sigma_{nom}}.$$ (5.135)

This ratio is always greater than or equal to unity. Actually it is sufficient to compare the term $E\xi_{si}$ with the term $E_{eff}\varepsilon$, where E_{eff} is the effective modulus of the rope. Effective modulus is given by,

$$E_{eff} \equiv \frac{\sigma_{nom}}{\varepsilon} = \frac{T}{A\varepsilon}.$$ (5.136)

The values of ξ_{si} are consistently greater than $(E_{eff}/E)\varepsilon$ and thus the axial wire stresses consistently exceed the nominal rope stress.

When a loaded straight rope under a nominal stress σ_{nom} is bent over a sheave of diameter D, additional bending stresses given by equation (5.131) are imposed. By

82

superposition, the maximum stress σ_{si} in an arbitrary wire may be represented in a non-dimensional form as,

$$\frac{\sigma_{si}}{\sigma_{nom}} = \frac{\sigma_{si}^T}{\sigma_{nom}} + \frac{\sigma_{si}^B}{\sigma_{nom}}, \tag{5.137}$$

and it can be written with respect to z_{si}^T and z_{si}^B as follows,

$$\frac{\sigma_{si}}{\sigma_{nom}} = z_{si}^T + z_{si}^B \left(\frac{D}{d} \cdot \frac{\sigma_{nom}}{E} \right)^{-1}, \tag{5.138}$$

where the bending factor z_{si}^B is given by,

$$z_{si}^B = \frac{R_{si}}{R} \cdot \frac{\sin\alpha_s}{1 + \frac{1}{2}v\cos^2\alpha_s} \cdot \frac{\sin\alpha_{si}}{1 + \frac{1}{2}v\cos^2\alpha_{si}}. \tag{5.139}$$

Both z_{si}^T and z_{si}^B are independent of E and σ_{nom}. When σ_{si} is normalized with respect to σ_{nom}, σ_{nom} appears in the parameter multiplying z_{si}^B because the bending stresses owing to sheave curvature are actually independent of σ_{nom} [73]. Recommended values of D/d for sheaves lie between about 60 and about 100, depending on the rope diameter, the rope construction, and the type of application.

As an example of the preceding discussion, geometric parameters of such a lang lay IWRC given in Figure 5.3, are presented in Table 5.2.

Computed values of straight rope factor z_{si}^T and bending factor z_{si}^B are given in Table 5.3. Variation of the normalized maximum stresses for the lang lay IWRC with the bending parameter $D/d \cdot \sigma_{nom}/E$ according to equation (5.138) are plotted in Figure 5.4 using the geometric consideration given in Table 5.2 and corresponding results in Table 5.3.

Consider a 6x7 wire lang lay IWRC with a metallic area of $1\,inch^2$ and an axial load of 10 $tons$. The nominal stress of the IWRC is,

$$\sigma_{nom} = \frac{10*2000}{1} = 20000\,psi.$$

Table 5.2: Geometric parameters of an IWRC.

Type of rope	Strand data					Wire data			
	Layer	No	Angle	Factors		Layer	No	Angle	Radius
	s	m_s	α_s	$t =$	η_{0st}	l	m_{si}	α_{si}	R_{si}
IWRC	1	1	90.0°	1	0	1	1	90.0°	0.343
						2	6	83.5°	0.305
	2	6	82.8°	1	1	1	1	90.0°	0.292
				2	1	2	6	84.4°	0.267

Ratio of sheave and rope diameter is $D/d = 30$ and value of $D/d \cdot \sigma_{nom}/E$ is,

$$\frac{D}{d} \cdot \frac{\sigma_{nom}}{E} = 30 \cdot \frac{20000}{30*10^6} = 0.02 \,.$$

From the Figure 5.4, $\sigma_{max}/\sigma_{nom}$ ratio can be read corresponding to 0.02 as 1.41, and the maximum stress in the center wire of the IWRC can be computed as,

$$\sigma = 1.41*20000 = 28200\,psi = 194.43 N/mm^2 \,.$$
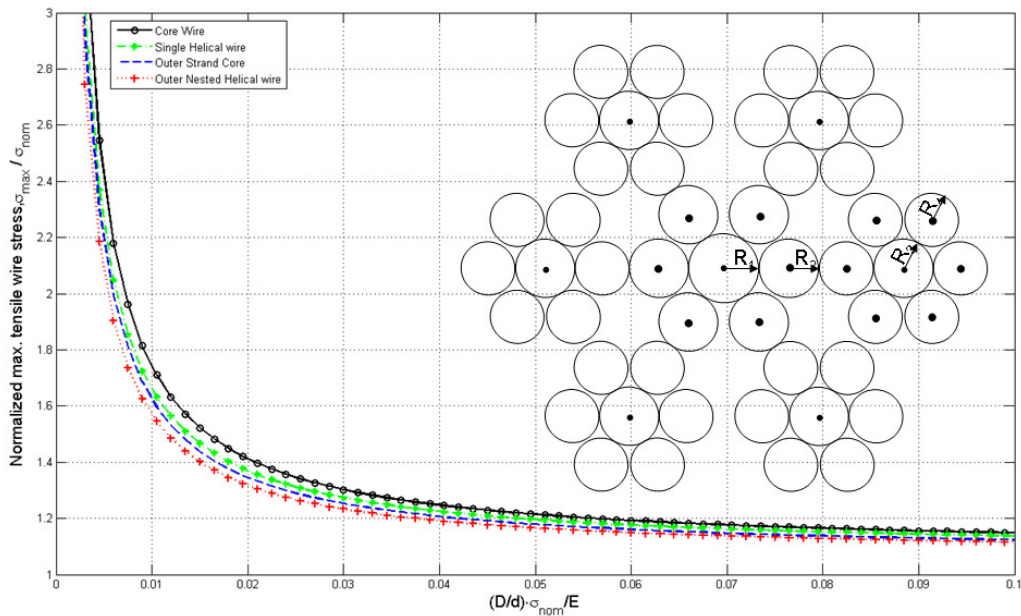
Figure 5.4: Variation of normalized maximum stresses for a lang lay IWRC with the bending parameter $D/d \cdot \sigma_{nom}/E$.

Table 5.3: Straight rope and bending rope factors.

Strand s	Component i	$\varepsilon \cdot 10^{-6}$	$\Delta\tau_1(m^{-1})$	$\Delta\kappa_1'(m^{-1})$	$T(kN)$	$G'(Nmm)$	$H(Nmm)$	$N'(N)$	$X(N/mm)$	Z_{si}^T	Z_{si}^B
1	**Strand**	1000	0	0	0.4312	0	25.0246	0	0	-	-
	Wire 1	1000	0	0	0.0765	0	0	0	0	1.0827	0.1317
	Wire 2	983.50	-0.1678	-0.0446	0.0595	-0.0627	-0.1831	0.0073	-1.1754	1.0795	0.1161
2	**Strand**	979.78	-0.0671	-0.0198	0.3212	-0.1212	13.6428	0.1289	-2.8274	-	-
	Wire 1	979.78	-0.0671	0	0.0543	0	-0.0615	0	0	1.0678	0.1110
	Wire 2	964.12	-0.2312	-0.0507	0.0447	-0.0419	-0.1481	0.0048	-0.7606	1.0647	0.1008

6. MODELING WIRE ROPE

Helix is one of the interesting curves among the space curves in 3-D spaces. Screws, Slinky, DNA molecules, wires, and ropes have helical substructures. The general form of a helix can be called as a single helix. Most of the CAD software are capable of constructing a single helical geometry and solid part easily. Coiling a helix around another helix creates a new geometry, which can be called double helix or nested helical structure. The word double helix is not defined explicitly now. Double helix is used mostly for the DNA molecules and structures in the literature [99-105]. A double helix typically consists of two similar helices with the same axis, differing by starting angle along the axis. Intertwined helices with different radii, i.e. successive layers will vary in their radii, to guarantee the maximum possible geometric distance in DNA molecules. Single helices are disconnected and inside one another and with an offset of half a winding to maximize the distance [99]. For this reason, this new type of complicated helix, which is nested over a single helix, will be called as nested helix (NH) throughout to distinguish these two helical geometry. Also the structure produced using NH will be called as nested helical structures (NHS). NHSs are difficult geometries to construct by using CAD software's and there is no available tool at present to produce such geometries.

6.1   General definition of helices and a special form

A helix can be defined that, tangent line at any point makes a constant angle with a fixed line. It can be viewed as a kind of 3-D spiral. A single helix can be represented in the parametric form as,

$$
\begin{aligned}
x_s &= r_s \cos(\theta_s), \\
y_s &= r_s \sin(\theta_s), \\
z_s &= h\theta_s,
\end{aligned}
\tag{6.1}
$$

where h represents the length of the helix, θ_s is the helix angle. The Slinky toy, which is invented by Richard James, is an interesting geometry because it can move

with preserving the startup energy. Its modified parametric representation can be written in the following form [106],

$$
\begin{aligned}
x &= [b + a\cos(\omega t)]\cos t, \\
y &= [b + a\cos(\omega t)]\sin t, \\
z &= ht + a\sin(\omega t),
\end{aligned}
\tag{6.2}
$$

where real constants a, b, ω and the part $[b + a\cos(\omega t)]$ is the parametric form for a circle, as a defines the radius while b shows the height and ω shows the number of wings, and the rest of the equation moves this circle around the helix. This parametric form also generates a logarithmic spiral moving around a helix, which is presented in Figure 6.1.

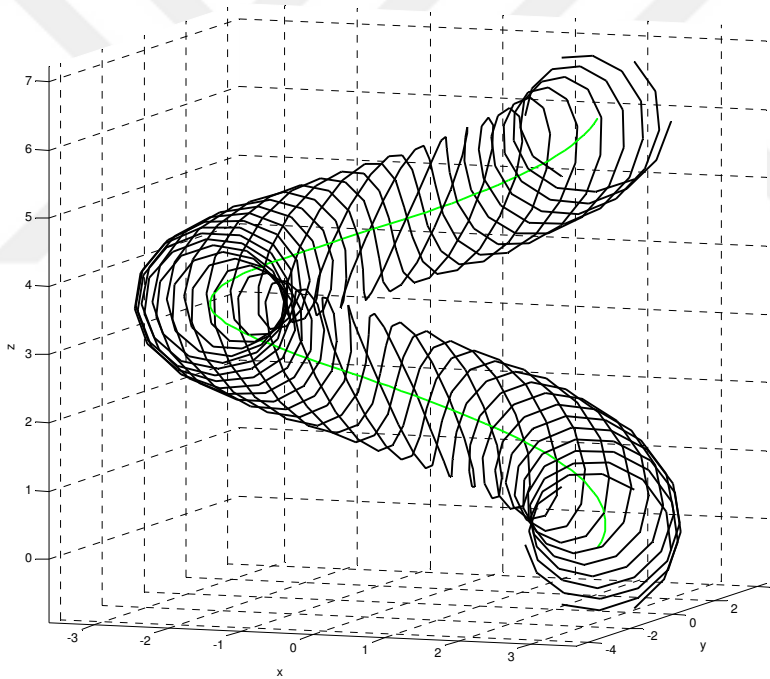**Figure 6.1:** Slinky: a spiral nested over a helix.

The importance of Slinky is that, it is one of the special forms of nested helical geometry defined over a single helix. However, it cannot be used while modeling a double or nested helical geometry. For this reason, a nested helical structure, which can be nested over another helix, is necessary for solid modeling of a wire rope structure.

88

A single helix nested by another helix creates a NH, which is defined as a double helix in [92] and shown in Figure 6.2 with a moving trihedron.
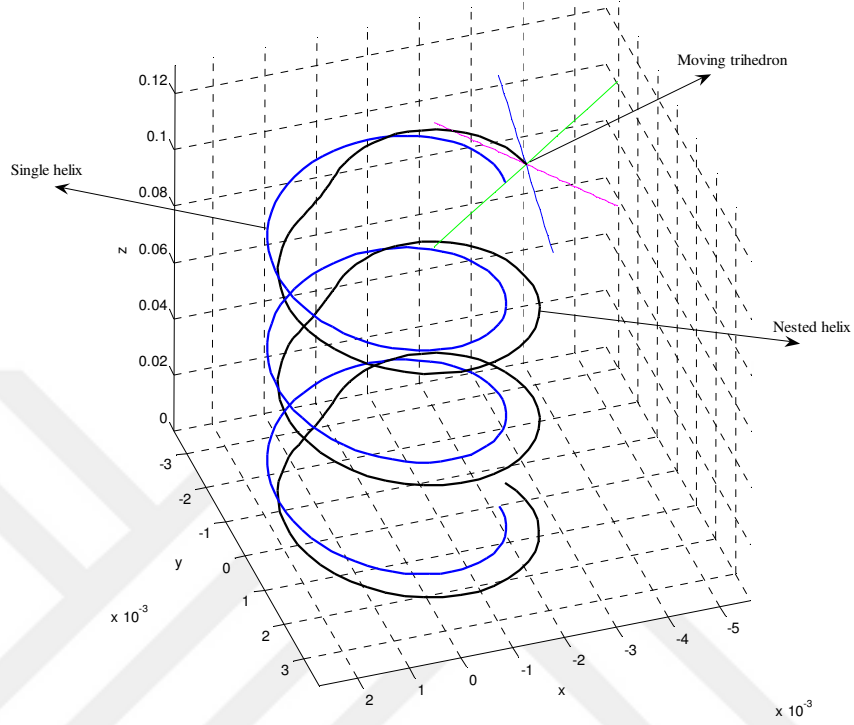
Figure 6.2: Nested helix (double helix) with Frenet-Serret frame.

6.2 Nested helical system

To define the location of a single helix centerline, Cartesian coordinate system (x, y, z) with the Cartesian frame $\{e_x, e_y, e_z\}$ is used and the location along the centerline of a single helix is,

$$
\begin{aligned}
x_s &= r_s \cos(\theta_s), \\
y_s &= r_s \sin(\theta_s), \\
z_s &= r_s \tan(\alpha_s)\theta_s,
\end{aligned}
\tag{6.3}
$$

where e_z shows the axis where the helix lies, r_s is the radius of the single helix, α_s is the single helix laying angle and $\theta_s = \theta_0 + \theta$. Free angle θ defines the location of the wire around the rope axis e_z relative to e_x. The single helix phase angle is defined as $\theta_0 = \theta_{(z=0)}$. The outer nested helix is wound around a single helix with

89

using the location along the centerline of a single helix given in equation (6.3). Location of the nested helix centerline can be written in the following form [92],

$$x_d = x_s(\theta_s) + r_d \cos(\theta_d)\cos(\theta_s) - r_d \sin(\theta_d)\sin(\theta_s)\sin(\alpha_s),$$
$$y_d = y_s(\theta_s) + r_d \cos(\theta_d)\sin(\theta_s) + r_d \sin(\theta_d)\cos(\theta_s)\sin(\alpha_s), \qquad \textbf{(6.4)}$$
$$z_d = z_s - r_d \sin(\theta_d)\cos(\alpha_s),$$

where $\theta_d = \eta\theta_s + \theta_{d0}$ and r_d shows the distance along the NH centerline and single helix centerline respectively as shown in Figure 6.3, η is the construction parameter which shows the frequency of the wire along the helix length and θ_{d0} is the wire phase angle.
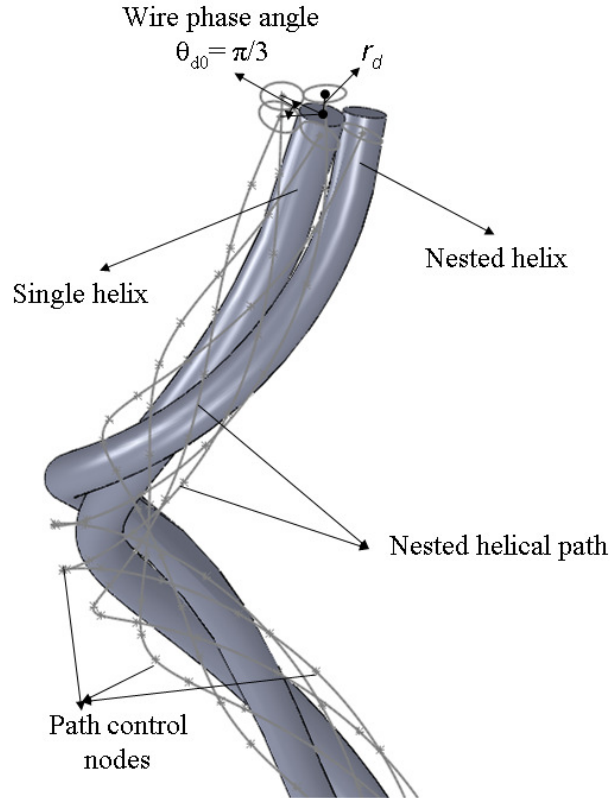
Figure 6.3: Nested helical wire path definitions.

The construction parameter η is a ratio of the angle of a nested helical wire rotation to the angle of the outer helical strand rotation. This ratio is dependent on the angles of both helices when both helical radii are fixed, so it is a constant value. It is considered important in characterizing the rope structure, specifically the relationship between the wire and strand helices, and is called the "relative rotation". The relative

90

rotation will be positive for lang lay ropes and negative for regular lay ropes. Centroidal axes of both strand and wire can be considered lying on right circular cylinders, which can be developed into a plane as shown in Figure 6.4.

(a) Strand helix   **(b)** Nested wire helix
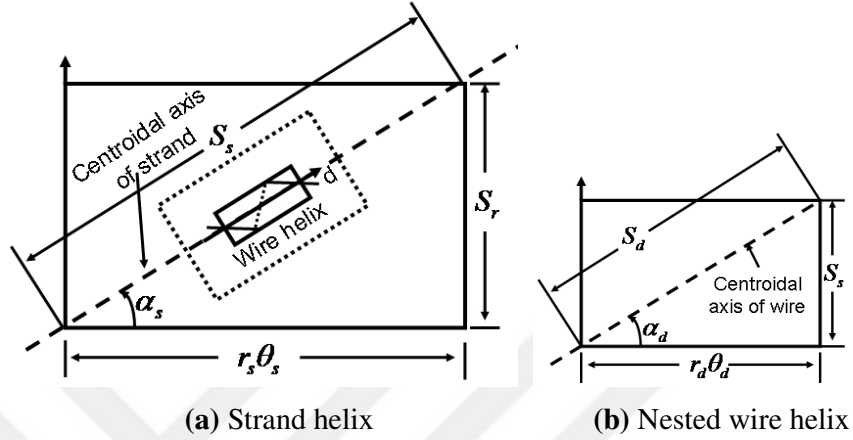
Figure 6.4: Developed view of strand helix and nested helical wire.

Using the developed view of the strand helix given in Figure 6.4-(a) the relationships between the length of rope S_r, length of strand S_s and the angle of strand rotation can be obtained as,

$$S_r = r_s \theta_s \tan \alpha_s, \qquad (6.5)$$

$$S_s = \frac{r_s \theta_s}{\cos \alpha_s}, \qquad (6.6)$$

where r_s, θ_s and α_s shows radius of the strand, angle of the strand rotation and strand helix angle respectively. Similarly, the relationships between the length of strand S_s, length of wire S_d and the angle of wire rotation also can be obtained by using the developed view of the wire helix given in Figure 6.4-(b) as,

$$S_s = r_d \theta_d \tan \alpha_d \qquad (6.7)$$

$$S_d = \frac{r_d \theta_d}{\cos \alpha_d} \qquad (6.8)$$

where r_d, θ_d and α_d shows radius of the wire helix, angle of the wire rotation and wire helix angle respectively. Because the length of strand obtained from the wire

91

helix must equal that obtained from the strand helix for a given length of rope, a new term η is defined to be the ratio of the angle of nested helical wire rotation θ_d to the angle of strand rotation θ_s, which can be obtained from equations (6.6) and (6.7) as [107-108],

$$\eta = \frac{\theta_d}{\theta_s} = \frac{r_s}{r_d \tan\alpha_d \cos\alpha_s} , \tag{6.9}$$

where η shows the ratio of the angle of nested helical wire rotation to the angle of strand rotation. The ratio of η is important wile modeling the nested helical wires. This parameter computed and used as a constant parameter while modeling all the nested helical wires along an outer strand.

According to equation (6.4) a right lay NH can be constructed. To construct a left lay NH, it is enough to negate one of the coordinate values of x_d, y_d or z_d given in equation (6.4).

6.3 A moving trihedron and plane construction

Frenet-Serret expressions describe the kinematic properties of a particle, which moves along a continuous, differentiable curve in 3-D Euclidean space R^3 [109-110]. Frenet-Serret frame is used to construct a normal plane perpendicular to the single helical or NHS to construct a 3-D solid part.

Let $I \subset R$ be an interval, and $\psi : I \to R^3$ be a parameterized space curve, assumed regular and free of points of inflection. The trajectory of a particle moving through 3-D space is defined by $\psi(\theta)$. The moving trihedron, as known the Frenet-Serret frame, corresponds to an orthonormal basis of 3-vectors; $T(\theta)$, $N(\theta)$ and $B(\theta)$. The unit tangent vector $T(\theta)$, the unit binormal vector $B(\theta)$ and the unit normal vector $N(\theta)$ can be defined respectively as in the following,

$$T(\theta) = \frac{\psi'(\theta)}{\|\psi'(\theta)\|}, \quad B(\theta) = \frac{\psi'(\theta) \times \psi''(\theta)}{\|\psi'(\theta) \times \psi''(\theta)\|}, \quad N(\theta) = \frac{B(\theta) \times \psi'(\theta)}{\|B(\theta) \times \psi'(\theta)\|}. \tag{6.10}$$

92

The line $\psi(\theta)+tT(\theta)$ is the tangent line at $\psi(\theta)$. Here $t \in R$ represents a parameter corresponding to create the tangent line in a given range. The binormal vector $B(\theta)$ is perpendicular to both $\psi'(\theta)$ and $\psi''(\theta)$, and hence perpendicular to the osculating plane. The line $\psi(\theta)+tB(\theta)$ is the binormal line at $\psi(\theta)$. Finally, the normal vector is the vector perpendicular to both tangent and binormal vectors with its direction determined by the right-handed system. The line $\psi(\theta)+tN(\theta)$ is the normal line at $\psi(\theta)$. Therefore, tangent vector $T(\theta)$, normal vector $N(\theta)$ and binormal vector $B(\theta)$ form a coordinate system with origin $\psi(\theta)$. The tangent line, normal line and binormal line are the three coordinate axes with positive directions given by the *TNB* vectors respectively. These three vectors are usually referred to as the moving trihedron or triad at point $\psi(\theta)$.

6.4   Frenet-Serret frames for single helical and NH wires

Using the single helix expression as described in equation (6.1), the single helix curve $\psi(\theta_s)$ is given by,

$$\psi(\theta_s) = (r_s \cos(\theta_s), r_s \sin(\theta_s), h\theta_s). \tag{6.11}$$

The tangent, binormal and normal vectors for a single helical wire can be found using Frenet-Serret formulas as follows;

$$T(\theta_s) = \frac{\psi'(\theta_s)}{\|\psi'(\theta_s)\|} = \left(\frac{-r\sin(\theta_s)}{\sqrt{r^2+h^2}}, \frac{r\cos(\theta_s)}{\sqrt{r^2+h^2}}, \frac{h}{\sqrt{r^2+h^2}} \right), \tag{6.12}$$

$$B(\theta_s) = \frac{\psi'(\theta_s)\times\psi''(\theta_s)}{\|\psi'(\theta_s)\times\psi''(\theta_s)\|} = \left(\frac{hr\sin(\theta_s)}{\sqrt{r^2+h^2}}, \frac{-hr\cos(\theta_s)}{\sqrt{r^2+h^2}}, \frac{r^2}{\sqrt{r^2+h^2}} \right), \tag{6.13}$$

$$N(\theta_s) = \frac{B(\theta_s)\times\psi'(\theta_s)}{\|B(\theta_s)\times\psi'(\theta_s)\|} = \left(\frac{-\cos(\theta_s)}{\sqrt{r^2+h^2}}, \frac{-\sin(\theta_s)}{\sqrt{r^2+h^2}}, 0 \right). \tag{6.14}$$

The location of the single helix is defined in equation (6.3) and the location of the NH is defined as in equation (6.4). The helix curve $\psi(\theta_w)$ can be written in the following vector form,

$$\psi(\theta_d) = (x_s(\theta_s) + r_d \cos(\theta_d)\cos(\theta_s) - r_d \sin(\theta_d)\sin(\theta_s)\sin(\alpha_s),$$
$$y_s(\theta_s) + r_d \cos(\theta_d)\sin(\theta_s) + r_d \sin(\theta_d)\cos(\theta_s)\sin(\alpha_s), \qquad \textbf{(6.15)}$$
$$z_s - r_d \sin(\theta_d)\cos(\alpha_s)).$$

The tangent, binormal and normal vectors of a NH for the Frenet-Serret frame can be written as,

$$T(\theta_d) = \frac{\psi'(\theta_d)}{\|\psi'(\theta_d)\|}$$
$$= (r_d \sin(\theta_d) \cos(\theta_s) + r_d \cos(\theta_d) \sin(\theta_s) \sin(\alpha_s), \qquad \textbf{(6.16)}$$
$$- r_d \sin(\theta_d) \sin(\theta_s) + r_d \cos(\theta_d) \cos(\theta_s) \sin(\alpha_s),$$
$$- r_d \cos(\theta_d) \cos(\alpha_s)),$$

$$B(\theta_d) = \frac{\psi'(\theta_d) \times \psi''(\theta_d)}{\|\psi'(\theta_d) \times \psi''(\theta_d)\|}$$
$$= ((-\sin(\theta_d) \sin(\theta_s) + \cos(\theta_d) \cos(\theta_s) \sin(\alpha_s)) \sin(\theta_d) \cos(\alpha_s)$$
$$+ \cos(\theta_d) \cos(\alpha_s) (-\cos(\theta_d) \sin(\theta_s) - \sin(\theta_d) \cos(\theta_s) \sin(\alpha_s)),$$
$$- \cos(\theta_d) \cos(\alpha_s) (\cos(\theta_d) \cos(\theta_s) - \sin(\theta_d) \sin(\theta_s) \sin(\alpha_s)) \qquad \textbf{(6.17)}$$
$$- (\sin(\theta_d) \cos(\theta_s) + \cos(\theta_d) \sin(\theta_s) \sin(\alpha_s)) \sin(\theta_d) \cos(\alpha_s),$$
$$(\sin(\theta_d) \cos(\theta_s) + \cos(\theta_d) \sin(\theta_s) \sin(\alpha_s)) (-\cos(\theta_d) \sin(\theta_s)$$
$$- \sin(\theta_d) \cos(\theta_s) \sin(\alpha_s)) - \sin(\theta_d) \sin(\theta_s) \sin(\alpha_s))$$
$$- (-\sin(\theta_d) \sin(\theta_s) + \cos(\theta_d) \cos(\theta_s) \sin(\alpha_s)) (\cos(\theta_d) \cos(\theta_s))),$$

$$N(\theta_d) = \frac{B(\theta_d) \times \psi'(\theta_d)}{\|B(\theta_d) \times \psi'(\theta_d)\|}$$
$$= (\cos(\theta_d) \cos(\theta_s) - \sin(\theta_d) \sin(\theta_s) \sin(\alpha_s), \qquad \textbf{(6.18)}$$
$$- \cos(\theta_d) \sin(\theta_s) - \sin(\theta_d) \cos(\theta_s) \sin(\alpha_s),$$
$$\sin(\theta_d) \cos(\alpha_s))).$$

The Frenet-Serret frames can be calculated by equations (6.12)-(6.14) for the single helix and by equations (6.16)-(6.18) for NH. The tangent line $(\psi(\theta) + tT(\theta))$, the normal line $(\psi(\theta) + tN(\theta))$ and the binormal line $(\psi(\theta) + tB(\theta))$ can be written with respect to θ_s and θ_d respectively by using their given tangent, normal and binormal vectors for single helix and NH respectively. Therefore, using these lines one can obtain three points to construct a circle in a plane, which will be perpendicular to the single helix or NH body.

In the subsequent section, a solid part construction using single helix or NH, and analysis over this solid part will be discussed.

6.5 A single helical or NH solid part construction

The idea of using the single helix or NH geometry to construct a solid part is based on the difficulties experienced at the modeling and analysis stages of wire ropes. Single helical geometry design can be accomplished by using the well-known CAD software's easily, while NH is not available as a tool at present. NHS is mostly encountered in rope constructions at first glance. To have a NHS, it is enough to wrap a strand over another one in a helical route. To perform the numerical analysis over this kind of construction, one should prepare the fully defined model of the problem first and convert it to an acceptable form for numerical analysis. There exists some problematic areas while conducting, modeling and analysis stages such as,

- It is not possible to model NH and NHS using CAD tools directly for the moment,

- Exporting NH geometry to an importable format by FEA software destroys the solid structures, even the single helical solid structures includes problems at their surfaces after imported for analysis purposes,

- Meshing is not successful due to the irregularities faced on the surfaces of NH geometries.

To illustrate the above-mentioned problems, a single helix and NH geometry are modeled in a 300*mm* and 1000*mm* lengths by using SolidWorks®, and transferred to finite element software Abaqus/CAE® using IGES and Parasolid file formats. It should be emphasized that, the procedures mentioned here are evaluated by using different modeling and analysis tools such as CATIA® and ANSYS®, and also the similar results are found for the helical geometries.

Single helical parts are modeled using helix tools available at the SolidWorks and solid parts are meshed in Abaqus/CAE. NHs are modeled using parametric equations of nested helices given in equation (6.4). Script language interface of SolidWorks is used to write the proposed code of the NH geometry. helical parts which are constructed using the proposed method are presented in Figure 6.5 and Figure 6.6.

Column (a) represents helices created in SolidWork, column (b) and (c) represents imported forms of IGES format and Parasolid format in Abaqus/CAE respectively, and column (d) represents the helical geometry created with the parametric equations using HyperMesh®.

The proposed script is written to create the meshed models with the help of HyperMesh. In these scripts, single helical/NH wire locations are defined with the control nodes. A spline is generated using these control nodes then a normal plane perpendicular to the spline curve centerline is created by using the Frenet-Serret frame defined in equations (6.12)-(6.14) and equations (6.16)-(6.18) respectively. A circle is created over this plane and swept along the single helical/NH spline. This method creates the meshed solid part in HyperMesh which is presented in column (d) of Figure 6.5 and Figure 6.6. When the numbers of control nodes and the wire length are increased, it has been concluded that the created solid geometry is spoiled out more. This situation is demonstrated by comparing the cross sections of the solid parts presented in columns (b) and (c) with item numbers (1) and (3) in Figure 6.5 and Figure 6.6 respectively. It can be seen that the solid structures are worse when the part lengths increased from a 300*mm* to 1000*mm*. A comparison of the solid parts and meshed parts quality scale is given at the last columns of Figure 6.5 and Figure 6.6. It can be seen that the NH mesh quality is the best among the others. In fact, there is no distortion at the NH geometry, which can be seen clearly while using the NH meshed solid parts with FEA software.

While meshing the solid parts, FEA software gives error due to the complex geometry of the mesh region for sweep meshing. It has been observed that the meshed parts are in unusable quality. In fact, this situation shows the main problem area while meshing NHS. This problem do not occurs while using the proposed script for modeling solid wires in HyperMesh. To see the problematic meshed surfaces closely, enlarged front view of item 4-column (b) of Figure 6.6 is represented in Figure 6.7. The meshed surface is split out, and it is unusable for FEA anymore. Using the proposed script, single helical and NH meshed solid parts are generated in HyperMesh and shown in Figure 6.8. It can be clearly seen that the meshed surfaces have no problems at the surfaces and precisely defined. It can be concluded that the NH meshed parts for each length is the best choice to use in FEA purposes.
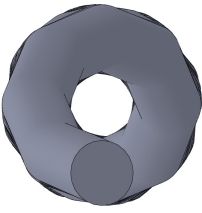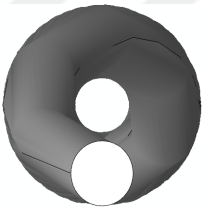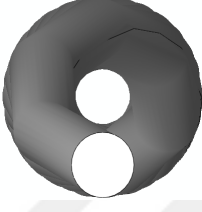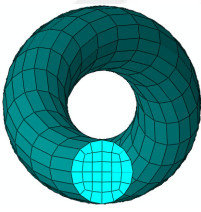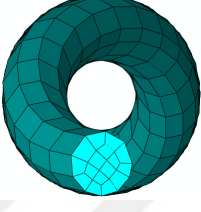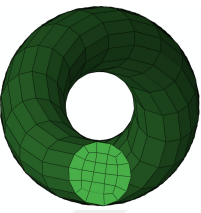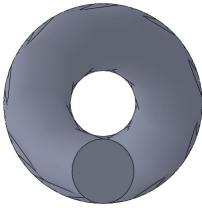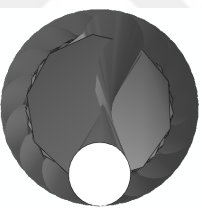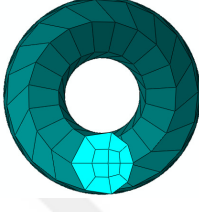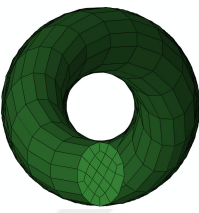
Helix type and length	Item No	Solid/Meshed model	SolidWorks projection (a)	Abaqus/CAE imported and meshed forms		HyperMesh model exported and imported in Abaqus/CAE (d)	Solid and Mesh Projection quality		
				IGES format solid and mesh (b)	Parasolid format solid and mesh (c)		Low	Normal	High
Single 300mm	(1)	Solid				—		(a,b,c)	
	(2)	Mesh	—					(c)	(b,d)
	(3)	Solid				—	(b,c)	(a)	
Single 1000mm	(4)	Mesh	—					(c)	(b,d)

Figure 6.5: Single helical wire solid and meshed models.

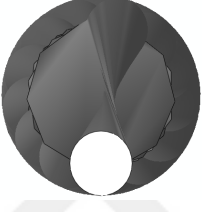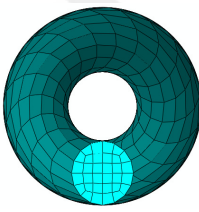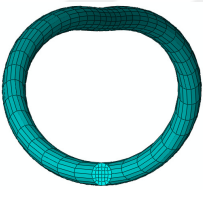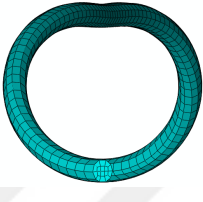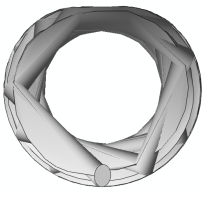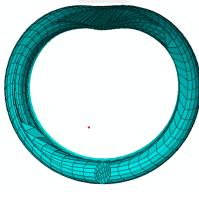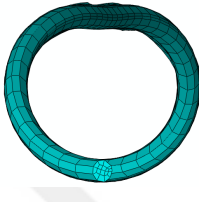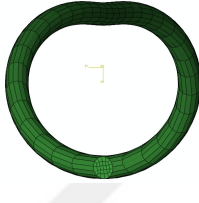| Helix type and length	Item No	Solid/Meshed model	SolidWorks projection (a)	Abaqus/CAE imported and meshed forms		HyperMesh model exported and imported in Abaqus/CAE (d)	Solid and Mesh Projection quality		
				IGES format solid and mesh (b)	Parasolid format solid and mesh (c)		Low	Normal	High
Nested Helix 300mm	(1)	Solid				—		(a,b,c)	
	(2)	Mesh	—				(b,c)		(d)
Nested Helix 1000mm	(3)	Solid				—	(b,c)	(a)	
	(4)	Mesh	—				(b,c)		(d)

Figure 6.6: Nested helical wire solid and meshed models.
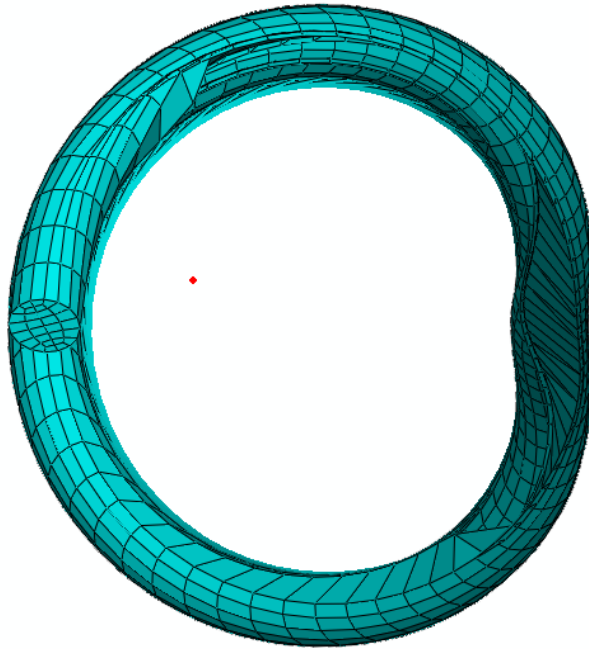
Figure 6.7: Zoomed front view of a NH wire.
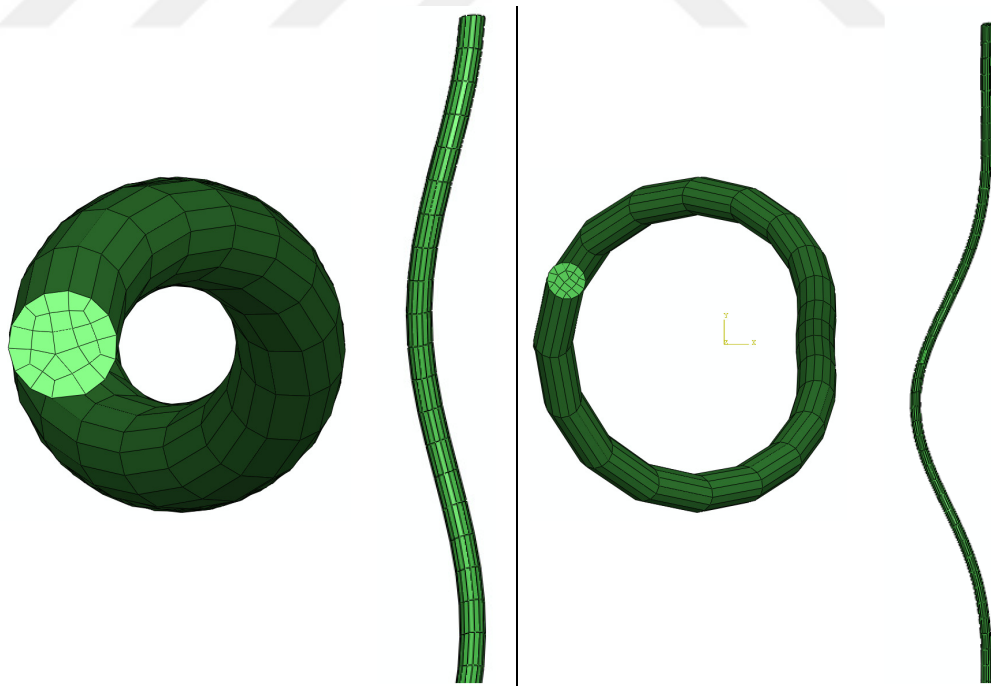
(a) Single helical solid wire mesh | **(b)** NH solid wire mesh

Figure 6.8: Single helical and NH meshed parts in Abaqus/CAE.

6.6 Construction of a complex single helical and NH wire mesh

During the modeling issue, it has been concluded that FEA software needs smooth and precisely defined solid meshed surfaces. Meanwhile commercial CAD softwares are not suitable to construct NH geometry because of the early mentioned irregularities at the meshing stage. FEA code first of all needs a precise meshed solid structure of the model. The idea of designing meshed model of a single helical or NH wire is proposed for this reason. An algorithm to develop a meshed model of a single or NH wire is given in Figure 6.9. The algorithm includes mainly four stages;

- Geometry generation,

- Solid part and mesh generation,

- Model generation,

- Analysis result post processing.
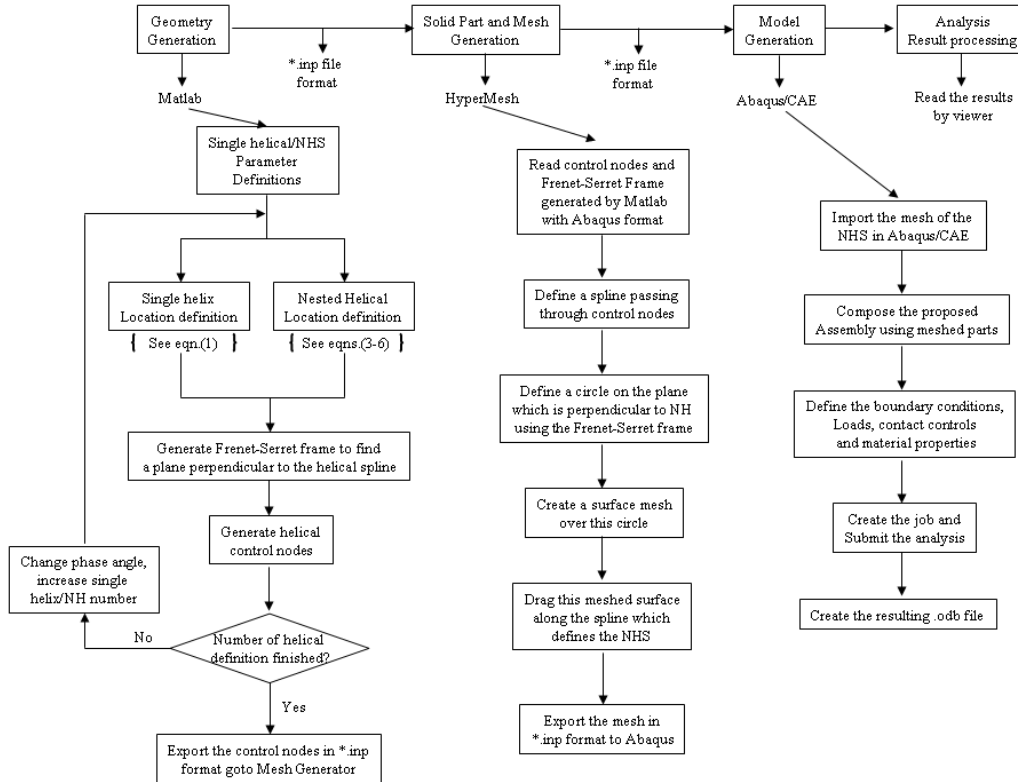
Figure 6.9: Generation of the NH wire solid model and analysis algorithm.

In the geometry generation stage a new code is generated to find the single helical control nodes using equation (6.1) and NH control nodes using equation (6.1) and

equations (6.3)-(6.4). To construct the solid geometry, a normal plane which should be perpendicular to the single helical or NH spline is needed. Frenet-Serret frame is constructed over the single helix and NH using the equations (6.12)-(6.14) and equations (6.16)-(6.18) respectively. Using the Frenet-Serret equations tangent, normal and binormal lines as depicted in Figure 6.2 are defined and three points are generated to construct a plane perpendicular to the helical spline. At the end of the geometry generation stage, the control nodes to construct single or NH wire and the nodes to build a plane which is perpendicular to the single helical or NHS are written to an output file in Abaqus/CAE format as illustrated in Figure 6.10.

In the solid part and mesh generation stage, the meshed helical wire models are produced that are the main elements used to construct the wire strand or rope assembly. The control nodes generated in the first stage, which is in Abaqus/CAE model file format, is imported in HyperMesh as temporary nodes. A spline is constructed using these control nodes which corresponds to a single or NH wire. Using the three control nodes, which is created to define the normal plane by the help of Frenet-Serret formulas, a circle is generated over this plane which is perpendicular to the helical wire centerline. The surface of this 2-D circle geometry is divided by quadratic brick elements and these elements are dragged along the helical wire path to construct a meshed single helical or NH wire geometry. The generated shape is constituted with meshes and known as orphan mesh in Abaqus/CAE. At the end of this operation, meshed helical wire geometry is exported to finite element model file format, which can be imported by Abaqus/CAE.

```
*NODE
  1,  -0.0024960000,  -0.0005455786,  0.0001871124  ⎫
  2,  -0.0025937458,  -0.0002398581,  0.0008352452  ⎪
  3,  -0.0026489732,   0.0000844312,  0.0014814629  ⎪
  ...                                                ⎬   Single or NH control nodes
 60,  -0.0023603958,  -0.0008267729,  0.0391639295  ⎪
 61,  -0.0024960000,  -0.0005455786,  0.0398141124  ⎪
 62,  -0.0025937458,  -0.0002398581,  0.0404622452  ⎭
 63,  -0.0003068671,  -0.0021929485,  0.0410464275  ⎫
 64,   0.0040518237,   0.0067564359,  0.0378376927  ⎬   Points to define a plane using
 65,  -0.0025937458,  -0.0002398581,  0.0404622452  ⎭      Frenet-Serret formulae
*****
```

Figure 6.10: Geometry definition in Abaqus/CAE file format.

In the model generation stage, the orphan mesh geometry is imported in Abaqus/CAE, which is constructed by HyperMesh as explained previously. It can be concluded that the wires developed by using the written scripts gives perfect results even for the wires with longer lengths than 300*mm* and there were no problems

encountered with FEA software. This gives the opportunity to model the NH geometry without any length limitations and surface irregularities. In this way, FEA software will not be responsible to mesh the NH model. While defining the contacts between wires using the mesh created by IGES format and Parasolid format, there were errors because of the conflicts between the wires due to irregular meshed surfaces. The new meshed NH solid model get rids of such problems, defining precise surfaces, which never conflicts with the other wires in a strand or a rope. Analysis stage can be conducted with safe definitions made over the solid meshed geometry.
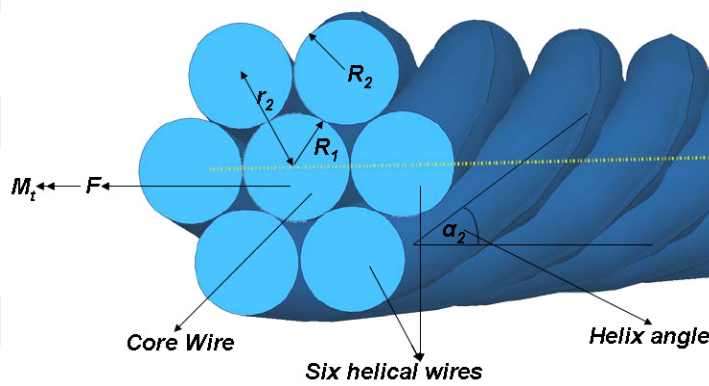
Figure 6.11: (1+6) wire straight strand model.

Generated meshed solid parts are assembled together and as a result a wire strand or a wire rope is constructed. A straight wire is wrapped around with identical six single helical wires to compose a simple straight strand model and shown in Figure 6.11. To compose an IWRC in addition to the wires used to compose a simple straight strand, a single outer helical six outer NH wires are imported which are modeled using HyperMesh before. Using these two outer wires an outer strand is assembled and it is wrapped around the core simple straight strand to obtain final form of the IWRC model as shown in Figure 6.12. It can be clearly seen that the wire rope structure includes 36 NH wire and this makes the analysis enormously complicated. Boundary conditions, load definitions, material properties and contact controls for the problem are defined in Abaqus/CAE to compose a job which is submitted for the analysis of the proposed problem. Finally, the analysis result file is ready to read by the Abaqus/CAE viewer to obtain the numerical results.

This process removes the surface irregularities encountered over the complex helical structures and generates precise geometries. Data loses are obstructed while

transferring solid parts between CAD and FEA software by the proposed modeling strategy and algorithm. At the same time, the length limitation problem is left behind by the given method.
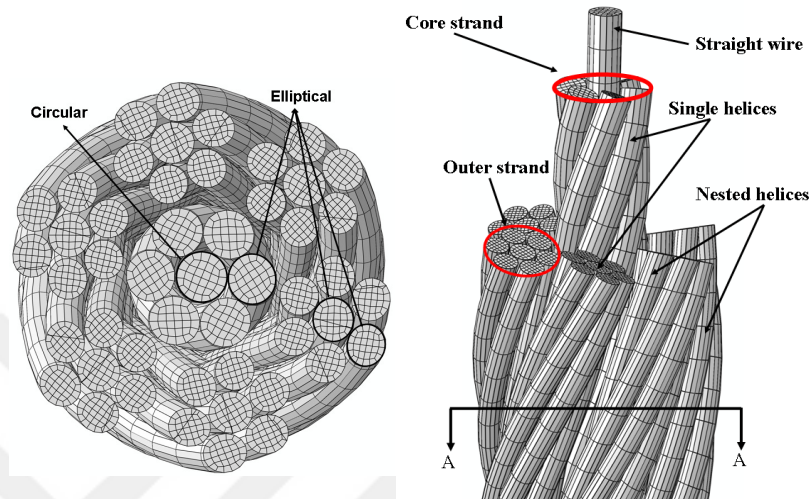
Figure 6.12: A left lang lay meshed wire rope structure.

6.7   IWRC modeling depending on different lay types

The term lay refers to the direction of the twist of the wires in a strand and to the direction that the strands are laid in the rope. In some instances, both the wires in the strand and the strands in the rope are laid in the same direction, and in other instances, the wires are laid in one direction and the strands are laid in the opposite direction depending on the intended use of the rope. Four different lay types are modeled and presented for an IWRC is presented in Figure 6.13.

- Right Lang Lay: The wires in the strands and the strands in the rope are laid in the same direction; in this instance, the lay is to the right.

- Left Lang Lay: The wires in the strands and the strands in the rope are also laid in the same direction; in this instance, the lay is to the left.

- Right Regular Lay: The wires in the strands are laid to the left, while the strands are laid to the right to form the wire rope.

- Left Regular Lay: The wires in the strands are laid to the right, while the strands are laid to the left to form the wire rope. In this lay, each step of fabrication is exactly opposite from the right regular lay.

The lay of a rope affects its operational characteristics. Regular lay is more stable and more resistant to crushing than lang lay. While lang lay is more fatigue resistant and abrasion resistant, use is normally limited to single layer spooling and when the rope and load are restrained from rotation.

(a) Right Lang Lay (RLL-zZ)   **(b)** Left Lang Lay (LLL-sS)

(c) Right Regular Lay (RRL-sZ)   **(d)** Left Regular Lay (LRL-zS)

Figure 6.13: IWRC modeled in four different lay types.

Strands wrapped around center strand are shown in Figure 6.14 and a nested helical wire without and with indentations are shown in Figure 6.15. The tightening nature of the regular lay wire ropes are depends on these indentations and can be clearly seen from the Figure 6.14. Some other cross-sectional views are presented in Appendix B for different lay types of IWRCs for convenience.
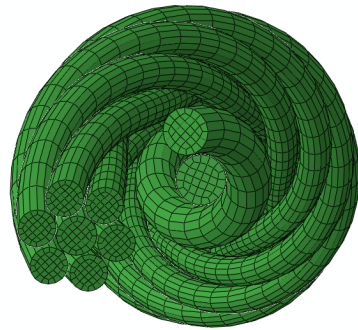
(a) Right Lang Lay (RLL)　　　　　　　**(b)** Left Lang Lay (LLL)
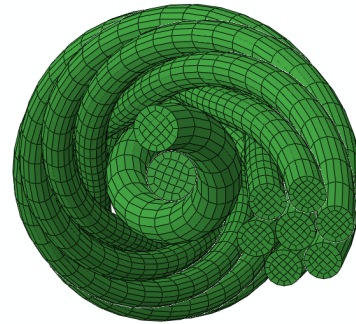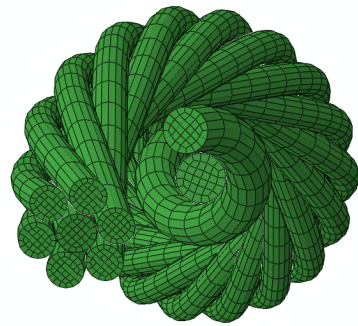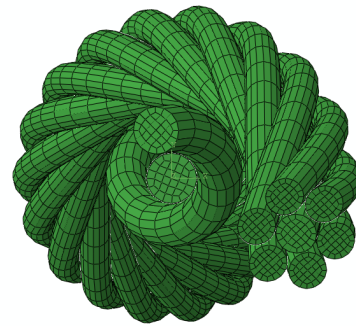
(c) Right Regular Lay (RRL)　　　　　　**(d)** Left Regular Lay (LRL)

Figure 6.14: Strand wrapping for RLL, LLL, RRL and LRL IWRCs.
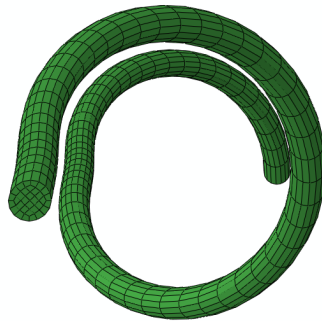
(a) Right Lang Lay (RLL)　　　　　　　**(b)** Left Lang Lay (LLL)
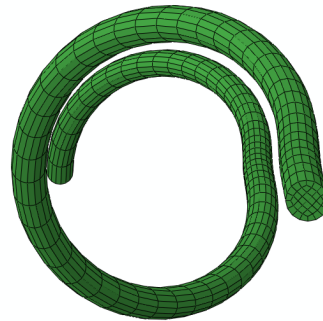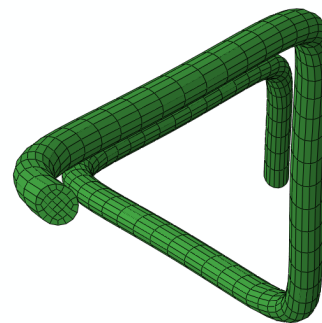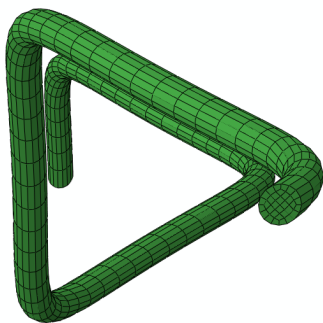
(c) Right Regular Lay (RRL)　　　　　　**(d)** Left Regular Lay (LRL)

Figure 6.15: Nested helical wires without indentations for RLL and LLL IWRC, and with indentations for RRL and LRL IWRC.

6.8   Fundamentals of FEA with virtual work

8-node linear hexahedral brick element is presented in Figure 6.16, Cartesian coordinates of x,y,z showing global space while ξ, η, ζ shows parametric space over the element. The mapping function for the 8-node volume element can be written as [111],

$$x = a_1 + a_2\xi + a_3\eta + a_4\zeta + a_5\xi\eta + a_6\eta\zeta + a_7\xi\zeta + a_8\xi\eta\zeta .$$ **(6.19)**

Mapping the global element to the parent can be established as,

$$x(1,-1,-1) = x_a,$$
$$x(1,\ \ 1,-1) = x_b,$$
$$...$$
$$x(-1,-1,1) = x_h.$$
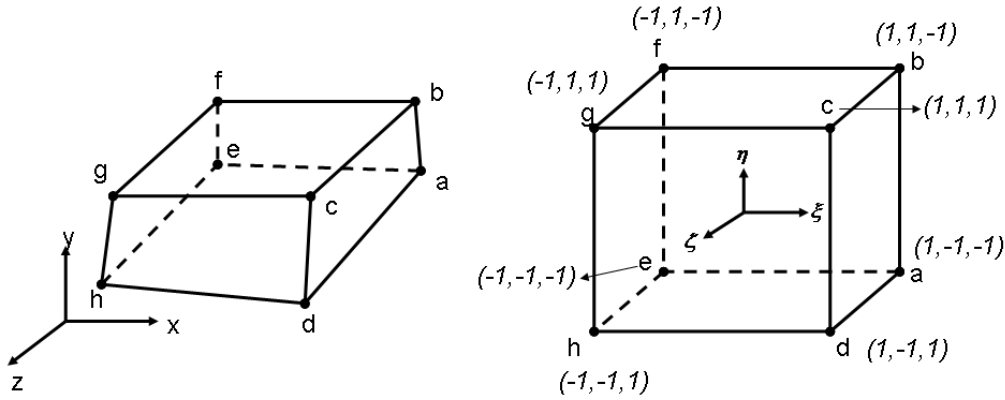
Figure 6.16: Eight-node linear hexahedral (brick) element definition.

It can be expressed in matrix form as,

$$\begin{bmatrix} 1 & 1 & -1 & -1 & ... & 1 \\ 1 & 1 & 1 & -1 & ... & -1 \\ & & & \vdots & & \\ 1 & -1 & -1 & 1 & ... & 1 \end{bmatrix} \begin{Bmatrix} a_1 \\ a_2 \\ \vdots \\ a_8 \end{Bmatrix} = \begin{Bmatrix} x_a \\ x_b \\ \vdots \\ x_h \end{Bmatrix}.$$ **(6.20)**

Following the similar procedure the unknown $a_i's$ in (6.20) are determined and substituted in (6.19) and the resulting equation gives the interpolation function for $x(\xi,\eta,\zeta)$ with the eight shape functions as given below,

106

$$N_1 = \frac{1}{8}(1-\xi)(1-\eta)(1-\zeta), \; N_2 = \frac{1}{8}(1+\xi)(1-\eta)(1-\zeta),$$

$$N_3 = \frac{1}{8}(1+\xi)(1+\eta)(1-\zeta), \; N_4 = \frac{1}{8}(1-\xi)(1+\eta)(1-\zeta),$$

$$N_5 = \frac{1}{8}(1-\xi)(1-\eta)(1+\zeta), \; N_6 = \frac{1}{8}(1+\xi)(1-\eta)(1+\zeta),$$

$$N_7 = \frac{1}{8}(1+\xi)(1+\eta)(1+\zeta), \; N_8 = \frac{1}{8}(1-\xi)(1+\eta)(1+\zeta).$$

(6.21)

Mapping functions for the y and z coordinate values can also found with the same procedure as,

$$x(\xi,\eta,\zeta) = N_1 x_a + N_2 x_b + N_3 x_c + N_4 x_d + N_5 x_e + N_6 x_f + N_7 x_g + N_8 x_h,$$
$$y(\xi,\eta,\zeta) = N_1 y_a + N_2 y_b + N_3 y_c + N_4 y_d + N_5 y_e + N_6 y_f + N_7 y_g + N_8 y_h,$$
$$z(\xi,\eta,\zeta) = N_1 z_a + N_2 z_b + N_3 z_c + N_4 z_d + N_5 z_e + N_6 z_f + N_7 z_g + N_8 z_h.$$

The same interpolation functions can be used for displacements as,

$$u(\xi,\eta,\zeta) = N_1 u_a + N_2 u_b + N_3 u_c + N_4 u_d + N_5 u_e + N_6 u_f + N_7 u_g + N_8 u_h,$$
$$v(\xi,\eta,\zeta) = N_1 v_a + N_2 v_b + N_3 v_c + N_4 v_d + N_5 v_e + N_6 v_f + N_7 v_g + N_8 v_h,$$
$$w(\xi,\eta,\zeta) = N_1 w_a + N_2 w_b + N_3 w_c + N_4 w_d + N_5 w_e + N_6 w_f + N_7 w_g + N_8 w_h.$$

(6.22)

For the isoparametric volume element with 8-node brick elements, the element stiffness matrix *B* must be specified. Six strain components are relevant in full three-dimensional analysis. The strain matrix following the standard notation of Timoshenko's elasticity text can be given as,

$$\{\varepsilon\} = \begin{Bmatrix} \varepsilon_{xx} \\ \varepsilon_{yy} \\ \varepsilon_{zz} \\ \gamma_{xy} \\ \gamma_{yz} \\ \gamma_{zx} \end{Bmatrix} = \begin{Bmatrix} \dfrac{\partial u}{\partial x} \\ \dfrac{\partial v}{\partial y} \\ \dfrac{\partial w}{\partial z} \\ \dfrac{\partial u}{\partial y}+\dfrac{\partial v}{\partial x} \\ \dfrac{\partial v}{\partial z}+\dfrac{\partial w}{\partial y} \\ \dfrac{\partial w}{\partial x}+\dfrac{\partial u}{\partial z} \end{Bmatrix}$$

(6.23)

The first strain term of $\varepsilon_{xx} = \dfrac{\partial u}{\partial x}$ in x coordinate can be computed by submitting

$u(\xi, \eta, \zeta)$ from equation (6.22) as,

$$\varepsilon_{xx} = \frac{\partial u}{\partial x} = \frac{\partial}{\partial x}\left(N_1 u_a + N_2 u_b + N_3 u_c + N_4 u_d + N_5 u_e + N_6 u_f + N_7 u_g + N_8 u_h\right) \quad \textbf{(6.24)}$$

To find the derivative of u with respect to x, chain rule is used as,

$$\frac{\partial u}{\partial \xi} = \frac{\partial x}{\partial \xi}\frac{\partial u}{\partial x} + \frac{\partial y}{\partial \xi}\frac{\partial u}{\partial y} + \frac{\partial z}{\partial \xi}\frac{\partial u}{\partial z}. \qquad\qquad \textbf{(6.25)}$$

In the same manner derivative of y and z can be obtained as,

$$\frac{\partial u}{\partial \eta} = \frac{\partial x}{\partial \eta}\frac{\partial u}{\partial x} + \frac{\partial y}{\partial \eta}\frac{\partial u}{\partial y} + \frac{\partial z}{\partial \eta}\frac{\partial u}{\partial z}, \qquad\qquad \textbf{(6.26)}$$

$$\frac{\partial u}{\partial \zeta} = \frac{\partial x}{\partial \zeta}\frac{\partial u}{\partial x} + \frac{\partial y}{\partial \zeta}\frac{\partial u}{\partial y} + \frac{\partial z}{\partial \zeta}\frac{\partial u}{\partial z}. \qquad\qquad \textbf{(6.27)}$$

Equations (6.25)-(6.27) can be established in matrix form as,

$$\begin{Bmatrix} \dfrac{\partial u}{\partial \xi} \\[2mm] \dfrac{\partial u}{\partial \eta} \\[2mm] \dfrac{\partial u}{\partial \zeta} \end{Bmatrix} = [J]\begin{Bmatrix} \dfrac{\partial u}{\partial x} \\[2mm] \dfrac{\partial u}{\partial y} \\[2mm] \dfrac{\partial u}{\partial z} \end{Bmatrix} = \begin{bmatrix} \dfrac{\partial x}{\partial \xi} & \dfrac{\partial y}{\partial \xi} & \dfrac{\partial z}{\partial \xi} \\[2mm] \dfrac{\partial x}{\partial \eta} & \dfrac{\partial y}{\partial \eta} & \dfrac{\partial z}{\partial \eta} \\[2mm] \dfrac{\partial x}{\partial \zeta} & \dfrac{\partial y}{\partial \zeta} & \dfrac{\partial z}{\partial \zeta} \end{bmatrix}\begin{Bmatrix} \dfrac{\partial u}{\partial x} \\[2mm] \dfrac{\partial u}{\partial y} \\[2mm] \dfrac{\partial u}{\partial z} \end{Bmatrix}. \qquad \textbf{(6.28)}$$

$\varepsilon_{xx} = \dfrac{\partial u}{\partial x}$ can be obtained by multiplying the both side of equation (6.28) with the

inverse matrix of the $[J]$ giving,

$$\begin{Bmatrix} \dfrac{\partial u}{\partial x} \\[2mm] \dfrac{\partial u}{\partial y} \\[2mm] \dfrac{\partial u}{\partial z} \end{Bmatrix} = \left[J^{-1}\right]\begin{Bmatrix} \dfrac{\partial u}{\partial \xi} \\[2mm] \dfrac{\partial u}{\partial \eta} \\[2mm] \dfrac{\partial u}{\partial \zeta} \end{Bmatrix} \qquad\qquad \textbf{(6.29)}$$

In the same manner derivatives of *v* and *w* with respect to *x,y,z* can be found as,

$$\left\{\begin{array}{c}\dfrac{\partial v}{\partial x}\\[2mm]\dfrac{\partial v}{\partial y}\\[2mm]\dfrac{\partial v}{\partial z}\end{array}\right\}=\left[J^{-1}\right]\left\{\begin{array}{c}\dfrac{\partial v}{\partial \xi}\\[2mm]\dfrac{\partial v}{\partial \eta}\\[2mm]\dfrac{\partial v}{\partial \zeta}\end{array}\right\} \tag{6.30}$$

$$\left\{\begin{array}{c}\dfrac{\partial w}{\partial x}\\[2mm]\dfrac{\partial w}{\partial y}\\[2mm]\dfrac{\partial w}{\partial z}\end{array}\right\}=\left[J^{-1}\right]\left\{\begin{array}{c}\dfrac{\partial w}{\partial \xi}\\[2mm]\dfrac{\partial w}{\partial \eta}\\[2mm]\dfrac{\partial w}{\partial \zeta}\end{array}\right\} \tag{6.31}$$

The strain vector in terms of a strain-displacement matrix can be represented in,

$$\{\varepsilon\}=[B]\{d^e\} \tag{6.32}$$

Remembering the equation (6.23), right hand side of the strain vector can be presented using the equations of (6.28)-(6.31) in terms of the strain-displacement matrix as,

$$\left\{\begin{array}{c}\dfrac{\partial u}{\partial x}\\[2mm]\dfrac{\partial v}{\partial y}\\[2mm]\dfrac{\partial w}{\partial z}\\[2mm]\dfrac{\partial u}{\partial y}+\dfrac{\partial v}{\partial x}\\[2mm]\dfrac{\partial v}{\partial z}+\dfrac{\partial w}{\partial y}\\[2mm]\dfrac{\partial w}{\partial x}+\dfrac{\partial u}{\partial z}\end{array}\right\}=[B]\{d^e\}, \tag{6.33}$$

The general form of the strain-displacement matrix given in equation (6.33) can be expressed as in follows,

109

$$\{\varepsilon\} = [B]\{d^e\} = [B_1 \quad B_2 \quad B_3 \quad B_4 \quad B_5 \quad B_6 \quad B_7 \quad B_8]\{d^e\} \qquad (6.34)$$

in which [112],

$$B_i = \begin{bmatrix} \dfrac{\partial N_i}{\partial x} & 0 & 0 \\ 0 & \dfrac{\partial N_i}{\partial y} & 0 \\ 0 & 0 & \dfrac{\partial N_i}{\partial z} \\ \dfrac{\partial N_i}{\partial y} & \dfrac{\partial N_i}{\partial x} & 0 \\ 0 & \dfrac{\partial N_i}{\partial z} & \dfrac{\partial N_i}{\partial y} \\ \dfrac{\partial N_i}{\partial z} & 0 & \dfrac{\partial N_i}{\partial x} \end{bmatrix}, \text{ for } i=1,\ldots,8. \qquad (6.35)$$

The strain-displacement matrix can be obtained as a 6x24 for total of 24 nodal displacement variables (8 nodes times 3 variables per node). A general representation can be shown for the $[B]$ matrix as follows,

$$[B] = \begin{bmatrix} B_{1/1} & 0 & 0 & B_{1/4} & \cdots & 0 \\ 0 & B_{2/2} & 0 & 0 & \cdots & 0 \\ 0 & 0 & B_{3/3} & 0 & \cdots & B_{3/24} \\ B_{4/1} & B_{4/2} & 0 & B_{4/4} & \cdots & 0 \\ 0 & B_{5/2} & B_{5/3} & 0 & \cdots & B_{5/24} \\ B_{6/1} & 0 & B_{6/3} & B_{6/4} & \cdots & B_{6/24} \end{bmatrix}, \text{ and } \{d^e\} = \begin{Bmatrix} u_a \\ v_a \\ w_a \\ u_b \\ v_b \\ w_b \\ \vdots \\ u_h \\ v_h \\ w_h \end{Bmatrix}. \qquad (6.36)$$

The stress-strain relations for an isotropic homogeneous material are given as follows [113],

$$
\begin{Bmatrix} \sigma_x \\ \sigma_y \\ \sigma_z \\ \tau_{xy} \\ \tau_{xz} \\ \tau_{yz} \end{Bmatrix} = \frac{E}{(1+v)(1-2v)} \begin{bmatrix} 1-v & v & v & 0 & 0 & 0 \\ v & 1-v & v & 0 & 0 & 0 \\ v & v & 1-v & 0 & 0 & 0 \\ 0 & 0 & 0 & \dfrac{1-2v}{2} & 0 & 0 \\ 0 & 0 & 0 & 0 & \dfrac{1-2v}{2} & 0 \\ 0 & 0 & 0 & 0 & 0 & \dfrac{1-2v}{2} \end{bmatrix} \begin{Bmatrix} \varepsilon_{xx} \\ \varepsilon_{yy} \\ \varepsilon_{zz} \\ \gamma_{xy} \\ \gamma_{xz} \\ \gamma_{yz} \end{Bmatrix} \qquad \textbf{(6.37)}
$$

where E and v are Young's modulus and Poisson's ratio of the wire material. Stress-strain law given in equation (6.37) can be written in a simpler form as,

$$
\{\sigma\} = [D]\{\varepsilon\}. \qquad \textbf{(6.38)}
$$

Applying the virtual work principle on the element level one can write,

$$
\delta U_e = \delta W_e, \qquad \textbf{(6.39)}
$$

where, δU_e is the virtual energy of internal stresses, and δW_e is the virtual work of external forces acting through the virtual displacements. Displacement within the element and node point displacements is related by the following equation,

$$
\{u\} = [N]\{d^e\}, \qquad \textbf{(6.40)}
$$

where $\{u\}$ are the field displacement components, $\{u\} = \{u \quad v \quad w\}^T$, $[N]$ are the element interpolation functions, and $\{d^e\}$ are the node displacement component values for the element. Strain displacement can be given for any point as,

$$
\{\varepsilon\} = [B]\{d^e\}, \qquad \textbf{(6.41)}
$$

where $[B]$ is the strain-displacement matrix and $\{d^e\}$ is the nodal displacement vector of the element defined as in equation (6.36) for 8-node brick elements.

The stress in the member follows from the stress-strain relation is given as,

$$
\{\sigma\} = [D]\{\varepsilon\} = [D][B]\{d^e\}. \qquad \textbf{(6.42)}
$$

For any given set of small virtual displacements $\{\delta d^e\}$ the internal virtual strain energy and δU_e is defined by [113],

$$\delta U_e = \int_V (\delta \varepsilon) \sigma dV, \tag{6.43}$$

where $\delta \varepsilon$ is the virtual strain produced by the small virtual displacements, σ is the stress level at equilibrium, and dV indicates the differential volume element of the member.

The external virtual work of nodal forces is,

$$\delta W_e = \{\delta d^e\}^T \{f\}, \tag{6.44}$$

where $\{f\}$ are the nodal forces. Using the principle of virtual work,

$$\int_V (\delta \varepsilon) \sigma dV = \{\delta d^e\}^T \{f\}, \tag{6.45}$$

and hence,

$$\int_V [B]\{\delta d^e\}[D][B]\{d^e\}dV = \{\delta d^e\}^T \{f\}, \tag{6.46}$$

$$\{\delta d^e\}^T \int_V [B]^T [D][B]\{d^e\}dV = \{\delta d^e\}^T \{f\}. \tag{6.47}$$

From both sides of equation (6.47), $\{\delta d^e\}^T$ is canceled and element equation is found as,

$$[k]\{d^e\} = \{f\}, \tag{6.48}$$

where the element stiffness matrix is given by,

$$[k] = \int_V [B]^T [D][B]dV. \tag{6.49}$$

For the volume of the integral,

$$dV = dxdydz = \left(\det[J]\right)d\xi d\eta d\zeta, \tag{6.50}$$

and [k] can be written as,

$$[k] = \int\limits_{-1}^{+1}\int\limits_{-1}^{+1}\int\limits_{-1}^{+1} [B]^{T} [D][B](\det[J])\,d\xi d\eta d\zeta .$$ **(6.51)**

The stiffness matrix of the element can be obtained by numerical integration using Gauss quadrature formula.

Because of the complicated geometry of the wire ropes and the interactions between wires in a wire rope, manual solution of the stiffness matrices for analyzing wire ropes is not straightforward, cost effective, and fast. In addition, problems including fine mesh size with higher number of DOF require more computational time and have to be solved using parallelization processes. For this reasons, FEA code is preferred to use during this study while solving the stiffness matrices to find stress, strain, reaction force, reaction moment and shape alteration values by using capabilities of High Performance Computing Laboratory (HPC Lab.) located in Informatics Institute.

6.9   Element selection and property definitions during FEA

The element type and the mesh size are very important at the analysis stage. If the mesh is coarse, then problem could not converge and there will be no solution for this reason. To find accurate results at the analysis stage, C3D20R: A-20 node quadratic brick and C3D8R: A-8 node linear brick reduced integration hourglass control type elements are used. Triangular and tetrahedral elements are geometrically versatile and are used in many automatic meshing algorithms. It is very convenient to mesh a complex shape with triangles or tetrahedra, and the second-order and modified triangular and tetrahedral elements in Abaqus/CAE are suitable for general usage. However, a good mesh of hexahedral (brick) elements usually provides a solution of equivalent accuracy at less cost. Quadrilaterals and hexahedra have a better convergence rate than triangles and tetrahedra. For this reason, brick elements are preferred to use. The material density, elasticity, plasticity, friction and Poisson's ratio are defined according to the material and problem model used during the analysis. General contact controls and surface-to-surface contact behavior are defined because each wire in a strand is in interaction with the center and corresponding neighbor wires in the strand. Abaqus/Standard is used while

113

frictionless analysis of the models with C3D20R. Nevertheless, while frictional and plastic effects are brought into the models explicit analysis is needed and C3D20R type elements are not supported during explicit analysis. For this reason, C3D8R elements are used during explicit analysis with Abaqus/Explicit.

6.10 Axial loading and bending problem models

The constructional difficulties of the wire strand and wire rope model enters to a new position when the analysis stage starts. For the axial loading problems, the analysis model is designed with defining one edge of the strand to be stand stood by defining encastre boundary condition while the other edge is loaded with force or applied displacement boundary condition. Analysis procedure can be accomplished using only one-step for axial loading problems with Abaqus/Explicit. Load and mesh definition of a seven (7) wire strand is represented in Figure 6.17.
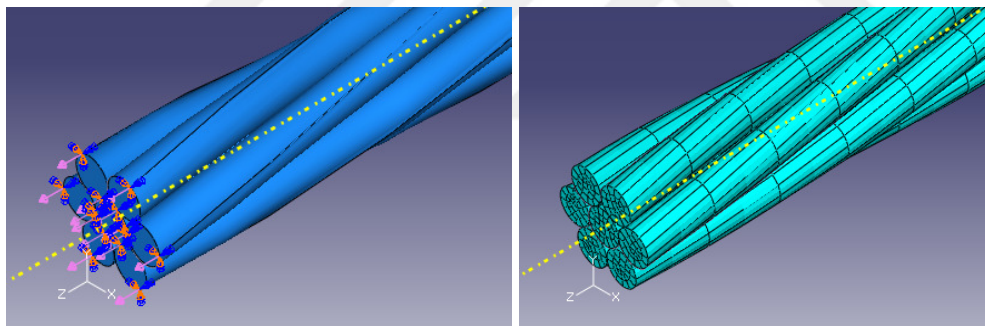
(a) Loads on a seven wire rope strand   **(b)** Mesh of the seven wire rope strand
Figure 6.17: Loads and mesh of a seven wire rope strand.

Bending problem structure differs from axial loading. Generally, bending problems arise when strand or rope runs over a sheave. To construct the bending problem a straight wire strand/rope and a rigid body sheave is assembled as shown in Figure 6.18.

To wrap the edges of the strand over the sheave, first a displacement boundary condition is defined at the first step of the analysis. With the help of this analysis stage, first a wire strand/rope is bent over a sheave, which is the starting point of the analysis in fact. Wire strand bent over a sheave problem is represented in Figure 6.19. At the second step of the analysis procedure, load/displacement boundary

114

condition is applied to the wire strand/rope to see the stress and displacement distributions over the wire strand/rope.
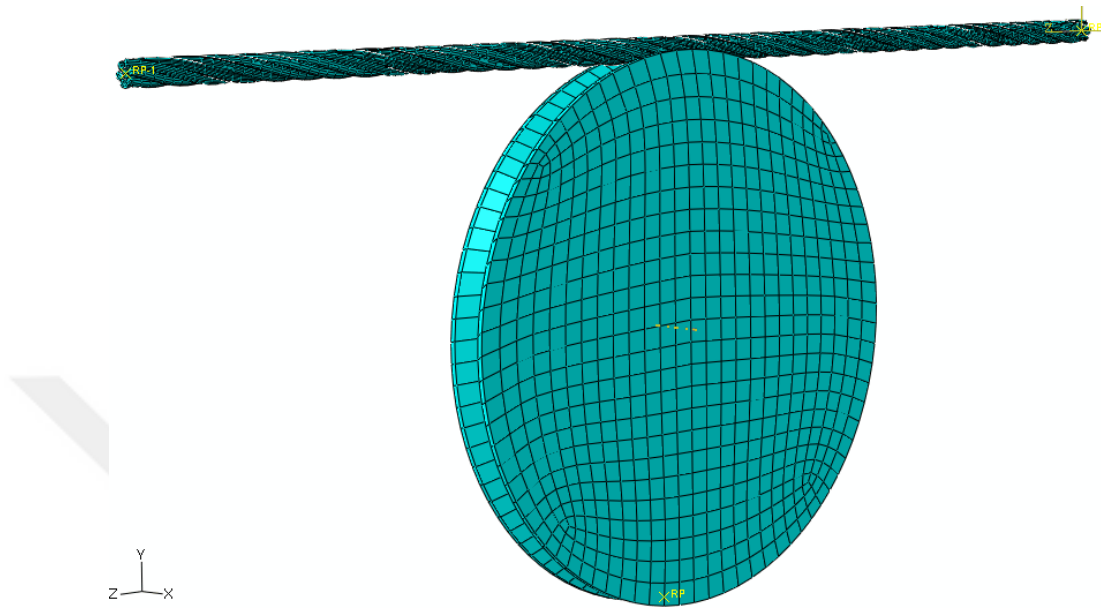
Figure 6.18: Meshed model of a wire strand prepared to bend over a sheave.
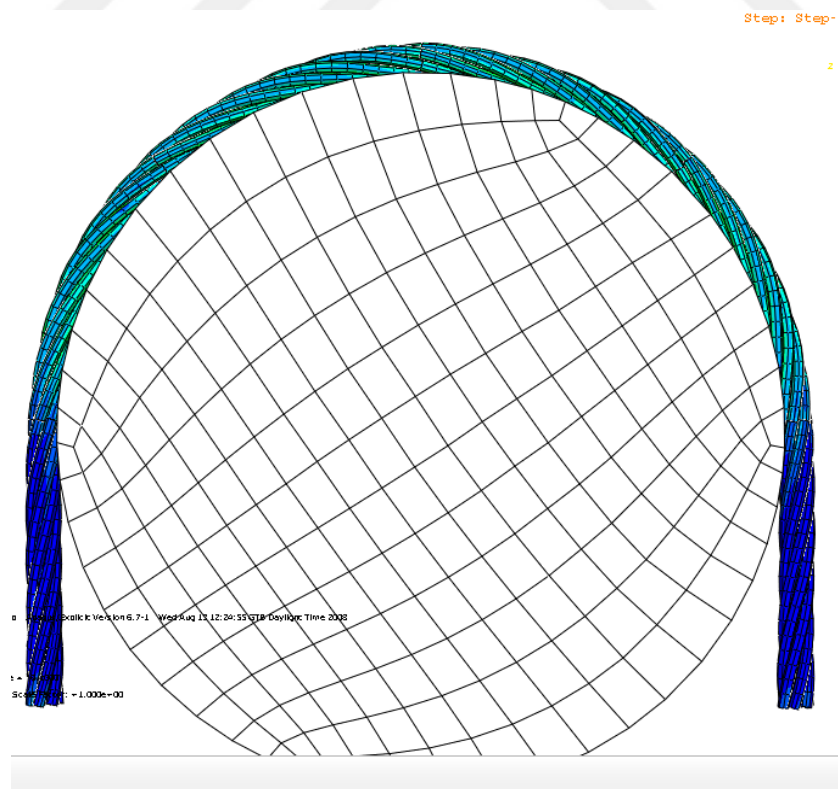
Figure 6.19: Wire strand bent over a 180*mm* diameter sheave.

6.11 Material properties

Density for steel is normally $\rho = 0.00785 g / mm^3$. However, because of the great carbon content of wires used for wire ropes, it is to use $\rho = 0.00780 g / mm^3$.

Total extension of steel wires for ropes amounts to about $\varepsilon_t = 1.5 - 4\%$ and the yield strength $R_{p0.2}$ is about 75-95% of the measured tensile strength R_m. For wires taken out of ropes and straightened, the total extension is about $\varepsilon_t = 1.4 - 2.9\%$ and the yield strength $R_{p0.2}$ is about 85-99% of the tensile strength R_m, Schneider (1973).

For straightened wires from wire ropes, Wolf (1987) evaluated a mean elasticity module $E = 199.000 N / mm^2$. For new wires, Häberle (1995) found the mean elasticity module $E = 195.000 N / mm^2$. Together with other measurements –after loading the wires close to the breaking point– a mean elasticity module has been evaluated for the stress field of practical usage. The mean elasticity module of rope wires made of carbon steel is $E = 196.000 N / mm^2$ [110].

7. NUMERICAL RESULTS

In this section, first of all an illustrative analytical example is given to show the force and moment acting along a simple straight wire strand. There are many analytical results are obtained using the theories presented in the literature. Some of the analytical results are also presented at the Appendix A for convenience.

Numerical examples are introduced to show deformation and stress distribution both over a simple straight strand, right regular lay and right lang lay IWRCs. Analytical results are obtained by solving the theory given in the literature via Matlab^{TM}. Analytical, finite element analysis results, and available test data are compared at the end.

In finite element analysis, wire-by-wire geometry construction is taken into account as in the analytical models developed by Elata et. al. in [92-93] and used by Usabiaga & Pagalday in [115] for an IWRC. Wire by wire insight of the wire strand and IWRC is obtained with FEA results. In addition, wire contraction effect over the IWRC is analyzed for Poisson's ratios, $v=0$ and $v=0.3$ respectively.

Bending of a wire rope strand over a sheave problem is taken into account lately. The structure of the problem and the solution are given. Figures show the stress and deformation distribution over the wire strand bent over a sheave. With the complicated nature of the bending problem, parallel solution of the problem is investigated and the parallelization results are presented.

A graphical user interface (GUI) code is generated based on the parametric mathematical equations of single and nested helical wires. It is named as Wire Rope Skeleton (WRS) and used to find control nodes of each wire within a wire rope and writes the nodes in a file which is processed by using HyperMesh as described early in Chapter 6. Later on the GUI code is developed to produce full-assembled wire rope solid model without using HyperMesh. Last version of the code is named as Wire Rope Model and Mesh Generator (WRMMG). It produces wire rope meshed model ready for analysis using Abaqus/CAE.

Contact analysis is conducted over a wire strand. Surface to surface interactions defined between wires within a wire strand. Deformations between wires force the wire radius to contract. In addition, mesh size of the wire strand is increased and their effects over the results are presented. Using the proposed modeling technique 1 through 5 meter length wire strands are modeled and analyzed under axial loading conditions. Analysis results are compared with using different helix angles and material types. The effect of mesh size also investigated.

7.1   Example showing the analytical solution of a simple straight strand

Consider a simple straight strand cross-section given in Figure 6.11 with the parameters   [11]; $R_1 = 2.6162\ mm$, $R_2 = 2.5654\ mm$, $p_2 = 247.65\ mm$, $E = 196497.52\ N/mm^2$, $v = 0.25$ and $m_2 = 6$. Outside wires are assumed not to touch each other and $r_2 = R_1 + R_2 = 5.1816\ mm$, $\alpha_2 = 82.510641°$. The angle of twist per unit length of the strand is $\tau_s = 0$, which means that the strand is not allowed to rotate and $\xi_1 = \varepsilon = 0.003$. $R_2 \Delta \kappa_2'$ and $R_2 \Delta \tau_2$ can be computed as,

$$R_2 \Delta \kappa_2' = -0.00005564,$$

$$R_2 \Delta \tau_2 = -0.0001838.$$

Finally forces F and moments M_t acting over the center wire and helical wire within a simple straight strand is computed and presented as follows,

$$F = F_1 + F_2 = 12675.65 + 70970.48 = 83646.12\ N,$$

$$M_t = M_1 + M_2 = 45877.83\ Nmm.$$

7.2   FEA of a simple straight strand and an IWRC subjected to axial loading

FEA are conducted for both a simple straight strand and an IWRC. By the proposed modeling strategy, wire-by-wire analysis give informations about the axial forces carried over each wire in a strand or rope. In the literature one of the most important test results are presented by Utting and Jones in [12]. Jiang *et.al.* created a finite element model for a simple straight strand and solved the axial loading problem over a cross-sectional part in [33]. In this thesis FEA of both a simple straight strand and

an IWRC are carried over a more realistic 3-D solid model taking into account friction and contact between wires thus wire-by-wire insight is obtained.

7.2.1 General considerations for the analysis models

Numerical examples of axially loaded, a 14mm length, (1+6) wires simple straight strand, and an 18mm length (6x7) IWRC are considered. The agreements of the proposed numerical model with other available models are shown by comparison. Geometrical design parameters are given in Table 7.1 and Table 7.2 respectively for both a simple straight strand and an IWRC models.

Table 7.1: Design parameters of the simple straight strand.

Parameter	Value
Strand diameter	11.4mm
Center wire diameter, R_1	3.94mm
Outer wire diameter, R_2	3.73mm
Strand length used in the model, h	14mm
Pitch length, p	115mm
Helix angle of the strand, α	78.2^o

Table 7.2: Design parameters of the IWRC.

Parameter	Value
IWRC diameter	29.80mm
Core strand center wire diameter, R_1	3.94mm
Core strand outer wire diameter, R_2	3.73mm
Outer strand center wire diameter, R_3	3.20mm
Outer strand nested helical wire diameter, R_4	3.00mm
IWRC length used in the model, h	18mm
Pitch length for core strand inner helical wire, p_2	70mm
Pitch length for outer strand center wire, p^*_2	193mm
Pitch length for nested helical wire, p_4	70mm
Helix angle for core strand inner helical wire, α_2	71.01^o
Helix angle for outer strand center wire, a^*_2	71.46^o
Helix angle for nested helical wire, α_4	74.45^o

The same material properties are used for both model as defined in Table 7.3. Quadratic hexahedral finite elements are preferred to analyze nonlinear effects of the complex geometry of a wire strand and an IWRC during the frictionless FEA. A

simple straight strand and an IWRC are meshed using 3584 and 18387 quadratic hexahedral elements of type C3D20, with 18039 and 94405 nodes respectively.

The boundary conditions applied to the model under axial loading are harmonious with the boundary conditions of Costello's model. In Costello's analytical model, force and moment are applied to the both ends of the simple straight strand and the analysis is carried over a cross-section A-A as illustrated in Figure 4.5. In this numerical model, half-length of the model is considered. Section A-A is considered as one end for the analysis model under the encastre boundary condition while the other end is restrained not to rotate in x and y directions. The axial strain of $\varepsilon = 0,...,0.015$ is applied to the free end of the model for analysis.

Table 7.3: Material properties of the wire.

Young's modulus, E	188000 N/mm^2
Plastic modulus	24600 N/mm^2
Yield stress	1540 N/mm^2
Limit stress	1800 N/mm^2
Poisson's ratio	0.3
Friction coefficient	0.115

To simulate and compare with Costello's theoretical model, 3D FEA models are constructed using the critical length of the geometry. Critical length is defined as 3 to 9 percent of the pitch length. The contact load increases from zero to the uniform value in the middle of the strand [89]. This leads to construct the validation model to be within 3 to 9 percent of the pitch length.

To build the wire geometry a code is developed in Matlab™. This code generates the control points of helical geometries using parametric mathematical equations of both single and nested helices (NH) given in equations (6.3) and (6.4). Matlab code to demonstrate how to create a NH wire is presented in Appendix C. The generated helical paths are used to create the desired 3-D mesh of single and NH wires of the proposed model using HyperMesh™. Helical paths used to create the outer wires of the outer strand are illustrated in Figure 6.3.

Using this developed code both a right regular lay and a right lang lay IWRCs are generated. Instead of geometry modeling and meshing of the wire rope, it is preferred to create meshed complete wire rope model due to encountered overlapping and

discontinuity problems during meshing and analysis stages. This procedure enables to construct models accurately for FEA purposes without length limitations. The main body of the wire rope model has been assembled in finite element solver Abaqus™. Both frictionless and frictional behavior of a simple straight strand and an IWRC analysis are accomplished using wire-by-wire bases with success, and the results are compared with theory and test results reported earlier. During the analysis von-Mises criteria and stress-strain relation is used which is defined in Figure 7.1 as material behavior curve according to the material properties given in Table 7.3.
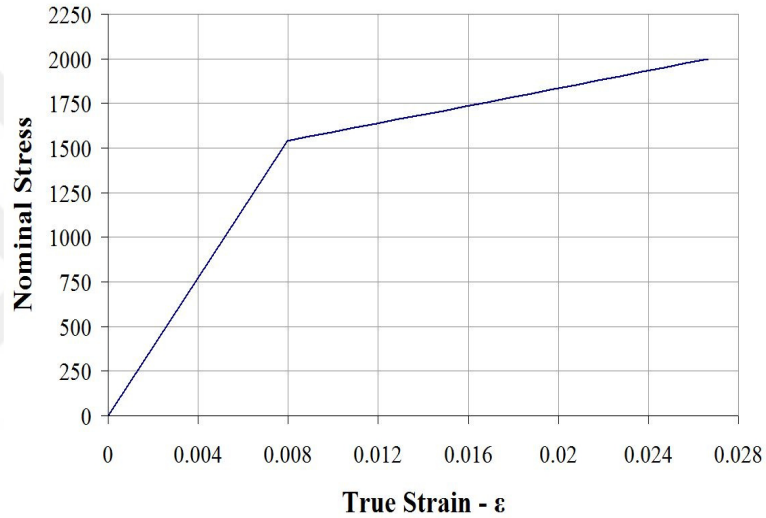
Figure 7.1: Material behavior curve.

7.2.2 Elastic analysis of simple straight strand for different helix angles

The angle between the tangent to the centroidal axis of the undeformed spring and x_1-y_1 plane is shown as α_0 and the radius of the wire helix is r_0 in Figure 4.3. During the construction of the FEA model, helix angles are selected between 65° and 84°. Wire strand behaves like parallel rods for the helix angle higher than 84°. In Figure 7.2, it can be seen that pitch length change of the strand near to helix angle 65° minimizes while pitch lengths are dramatically increased after 78°. Thus, helix angles are applied between 65°-84° for both modeling and numerical analysis of wire strand.

121

Figure 7.2: Variation of pitch length with helix angle for a wire strand.

The aim of this section is to gather analytical and numerical results considering the model without friction. For this purpose variation of reaction force with axial strain and variation of twisting moment with axial strain are compared in the following figures using the theoretical model of Costello with FEA results. Design parameters and material properties of a simple straight strand are given in Table 7.1 and Table 7.3 respectively. Boundary conditions are defined for each end of the strand. One end of the strand is fixed while the other end is constraint with no rotation. Axial strain of $\varepsilon = 0.015$ is applied to the free end of the strand.

Figure 7.3: Variation of reaction force with axial strain.

122

The variation of reaction force with axial strain for various helix angles are plotted in Figure 7.3. It can be clearly seen that numerical results of reaction force with axial strain are in good agreement with theoretical ones for all cases.

The variation of twisting moment with axial strain for various helix angles are plotted in Figure 7.4. It can be clearly seen that numerical results of twisting moment with axial strain have the same trend with theoretical ones for all cases.
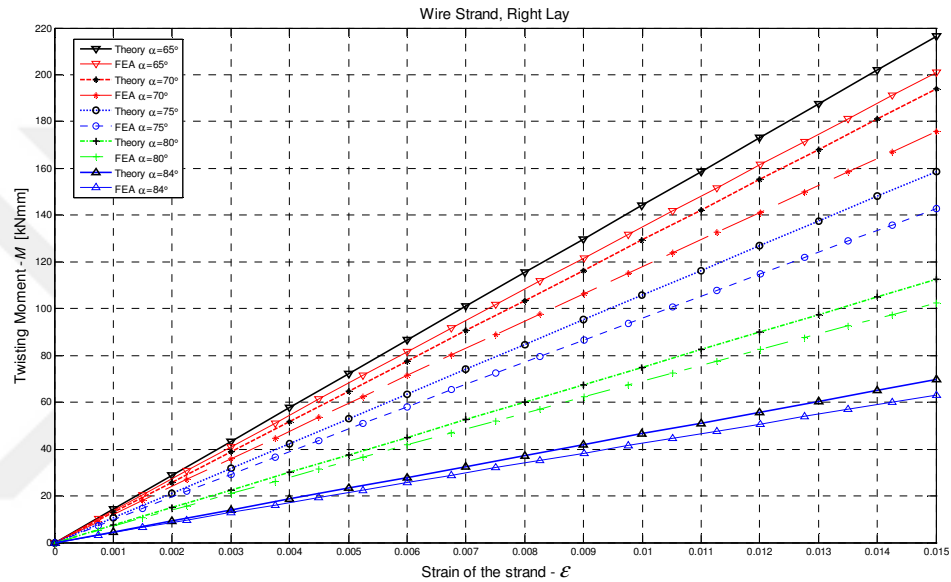
Figure 7.4: Variation of twisting moment with axial strain.

7.2.3 Plastic analysis of simple straight strand for different helix angles

For the finite element plastic analysis model, helix angles are selected between 65° and 84°. Wire strand behaves like parallel rods for the helix angle higher than 84°. In Figure 7.2, it can be seen that pitch length change of the strand near to helix angle 65° minimizes while pitch lengths are dramatically increased after 78°. Thus, helix angles are applied between 65°-84° for both modeling and numerical plastic analysis of wire strand.
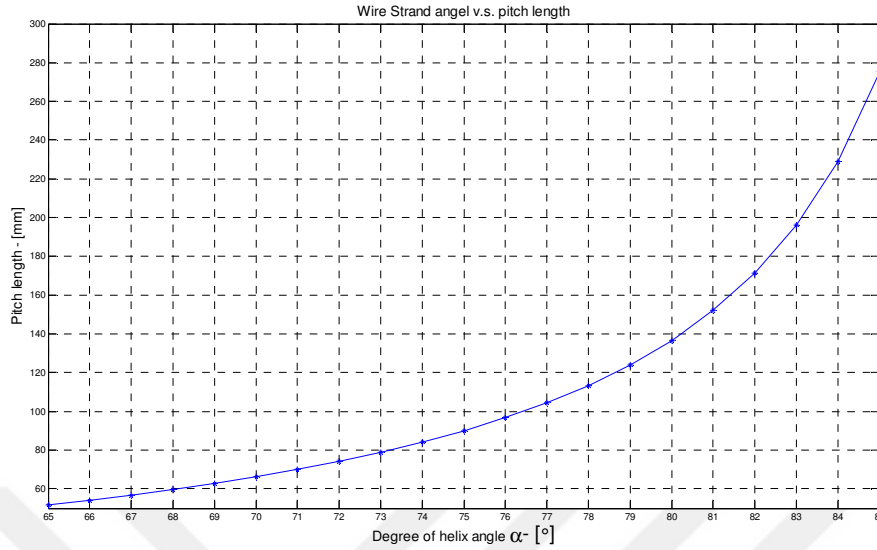
The aim of this section is to gather numerical results considering the model with frictional effect. For this purpose variation of reaction force with axial strain, variation of twisting moment with axial strain and variation of reaction force with twisting moment are compared in the following figures according to the FEA results obtained from frictional model. Design parameters and material properties of a simple straight strand are used from Table 7.1 and Table 7.3 respectively. Boundary

conditions are defined for each end of the strand. One end of the strand is fixed while the other end is constraint with no rotation. Axial strain of $\varepsilon = 0.015$ is applied to the free end of the strand.
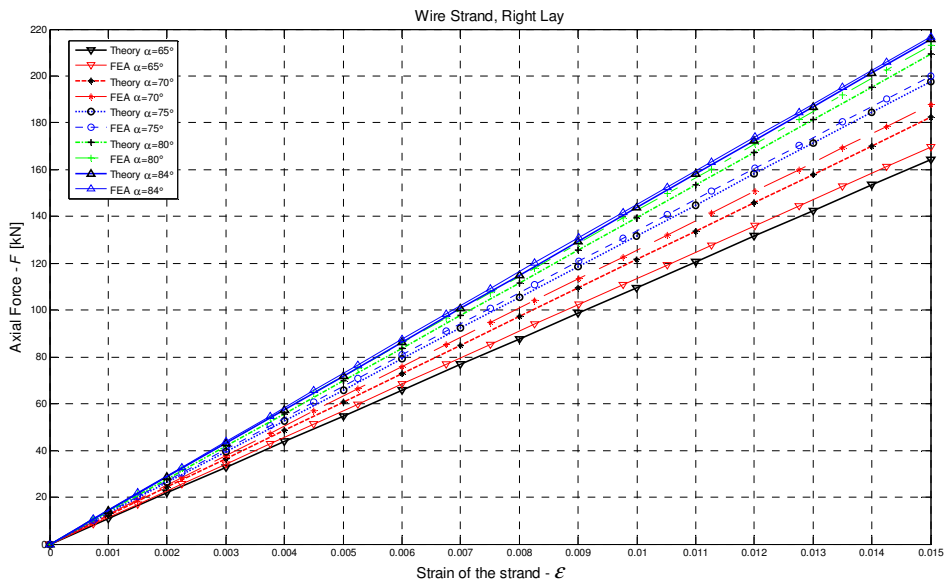
The variation of reaction force with the axial strain for various helix angles are plotted in Figure 7.5. Reaching the value of applied strain $\varepsilon = 0.008$, the simple straight strand starts to show plastic behavior for all cases.

The variation of twisting moment with axial strain for various helix angles are plotted in Figure 7.6. Reaching the value of applied strain $\varepsilon = 0.008$, the simple straight strand starts to show plastic behavior for all cases.
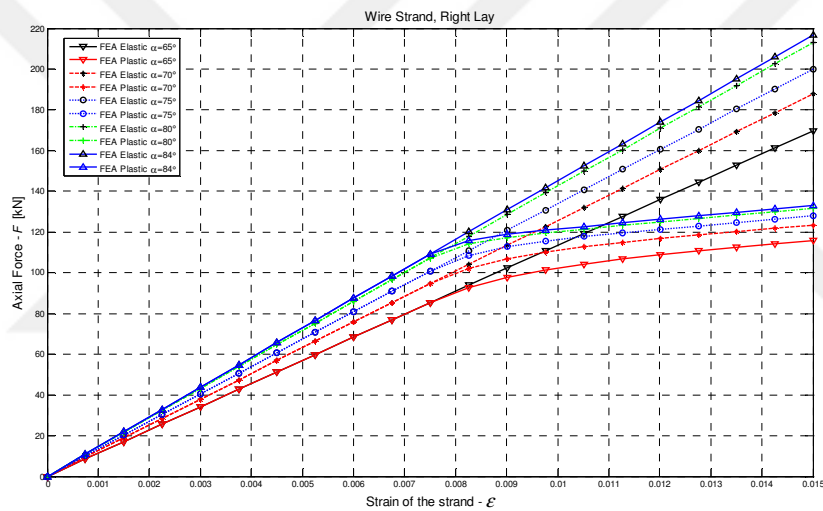
Figure 7.5: Variation of reaction force with axial strain in elastic-plastic analysis.
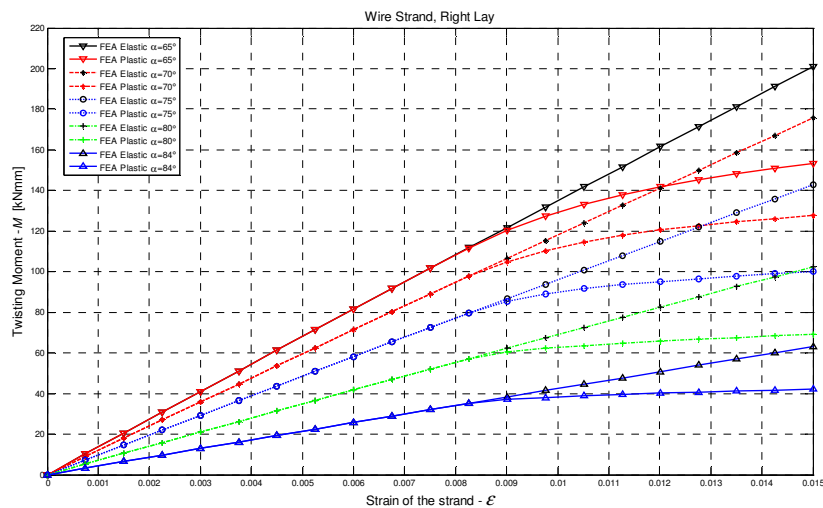
Figure 7.6: Twisting moment change with axial strain in elastic-plastic analysis.

von-Mises stress distribution over a simple straight strand with helix angles between 65° to 84° is presented by contour plots given in Figure 7.7. From the figure close fitting of the outer single helical wires over the straight center wire can be easily seen for α=65°. While the degree of helix angle increases the close fitting nature of the outer wires are changed and when the helix angle increases to α=84°, outer single helical wires are nearly parallel to the center wire strand. After the angle of α=84° FEA gives unreliable results.
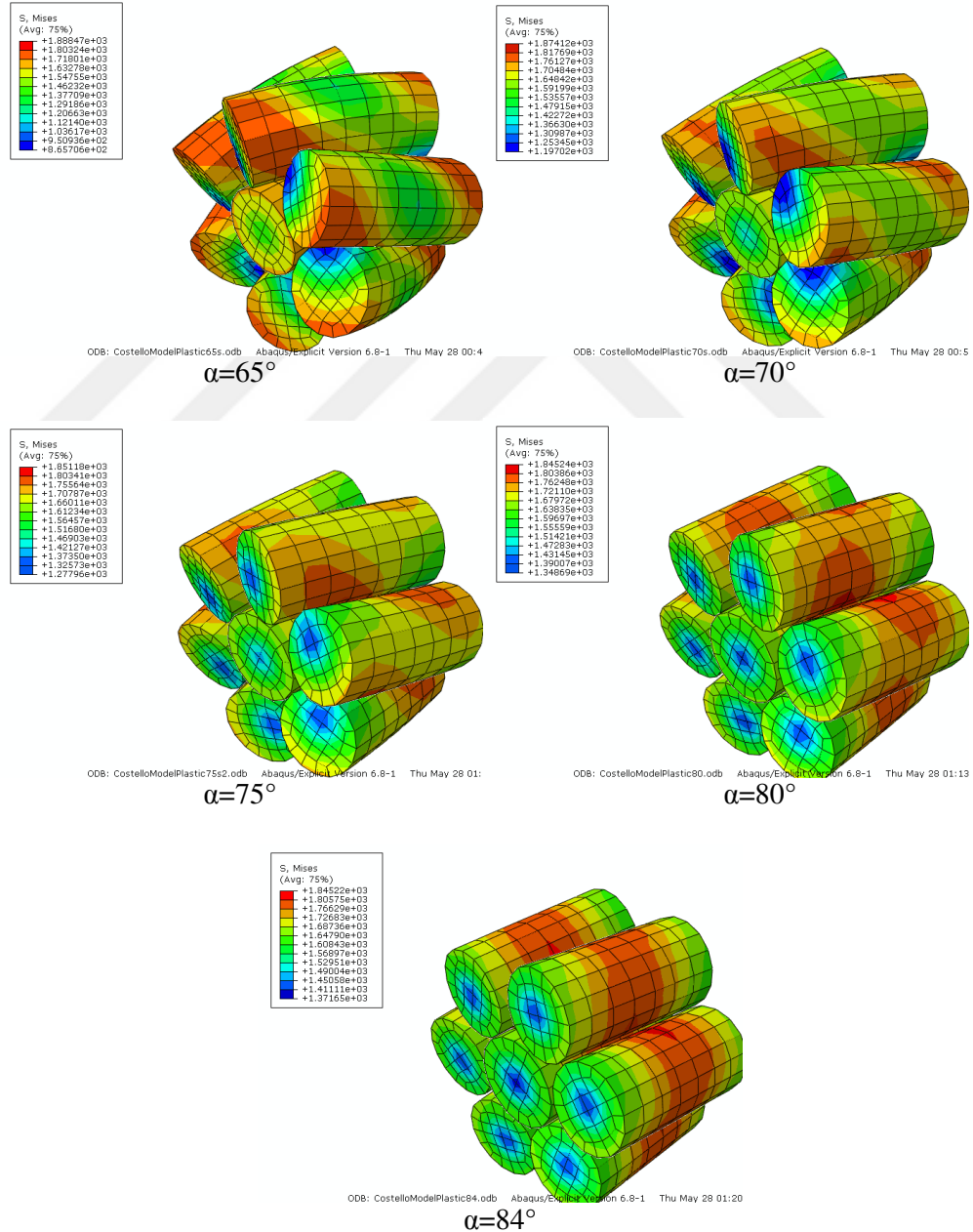
Figure 7.7: von-Mises stress distribution over the simple straight strand.

7.2.4 Simple straight strand FEA results

14mm length (1+6) wires simple straight strand is considered which is defined geometrically in Table 7.1 [33] and numerically obtained results are compared with both Costello's [11] model and test results reported by Utting & Jones [12,13]. Elastic frictionless and elastic-plastic frictional numerical models are developed. Wire material properties are obtained from [89] and given in Table 7.3 for elastic and plastic behaviors. Axial loading behavior of a simple straight strand is investigated. An axial strain ε of 0.015, was applied in increments of 0.001 in the analysis using the displacement equivalent to the axial strain computed by the equation $\varepsilon = (\bar{h} - h)/h$, where h is the original length of the strand and $\bar{h}$ is the final length of the strand. Rotation restrained, $\Theta = 0$, constant axial deformation results are illustrated in Figure 7.8 for the straight strand. It can be seen from the figure that the frictionless behavior of both theory of Costello and FEA results are in good agreement. The frictional plastic behavior of the strand is compared with the test results of Utting&Jones [12,13] given in the literature. Plastic behavior of the model is found to be in very good agreement with the available test results. In addition, FEA result of Jiang is compared. It can be seen from the Figure 7.8 that the present numerical FEA result is better than the FEA result of Jiang.
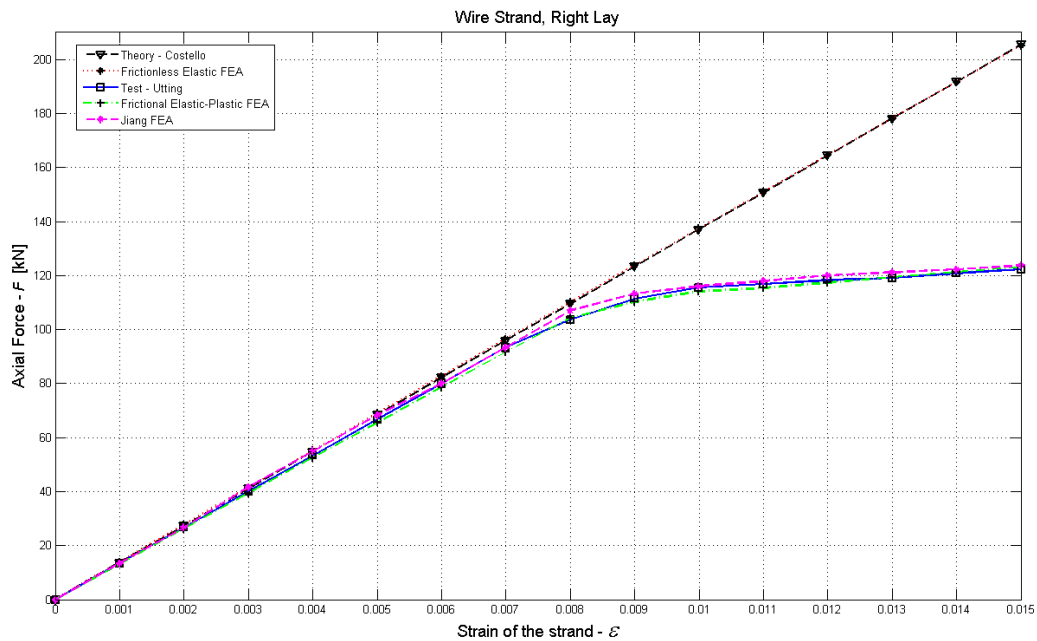
Figure 7.8: Force-Strain results for the straight strand; theory of Costello, test of Utting&Jones, frictionless elastic & frictional elastic-plastic FEA.

Figure 7.9 shows the variation of axial force with twisting moment. From this figure theory, test and finite element analysis results shows good agreement.
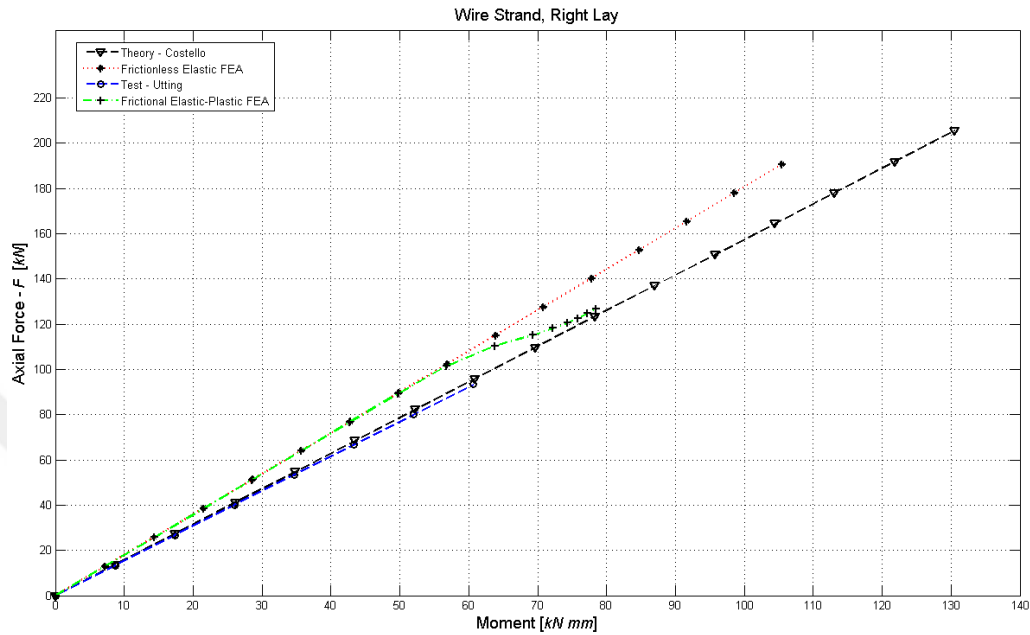
Figure 7.9: Force-Moment results for the straight strand; theory of Costello, test of Utting&Jones, frictionless elastic & frictional elastic-plastic FEA.

Figure 7.10 shows the wire-by-wire analysis comparison of theory with FEA. Wires are titled as CW corresponds to center wire and OH1-OH6 corresponds to outer single helical wires 1 through 6.
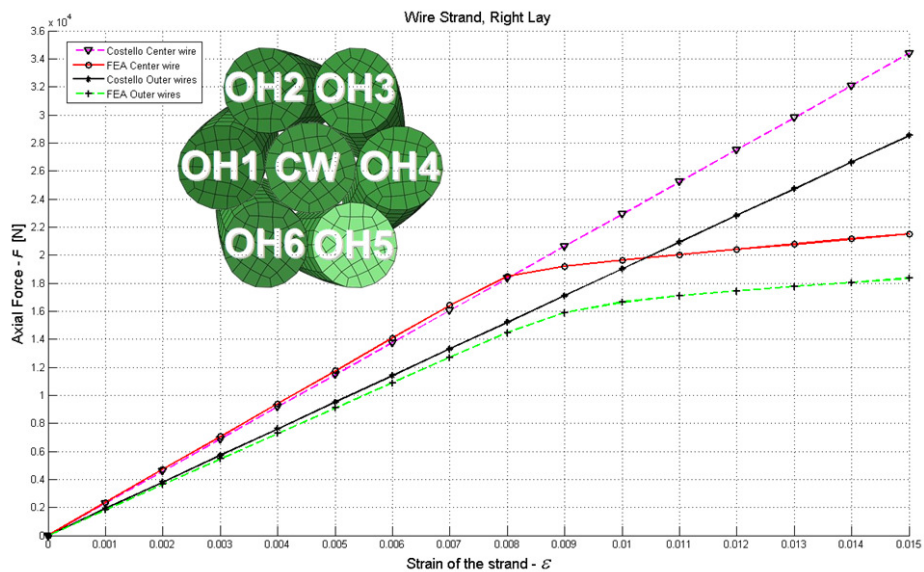

Figure 7.10: Wire by wire analysis for the simple straight strand, theory, and FEA comparison.

It can be seen that, from the computed numerical results, center wire of the strand is loaded with 17.1% of the total axial load while an outer wire is loaded with an average 13.82% of the total axial load. These results show that center wire carries the big portion of the axial load over the simple straight strand. The proposed model fully accounts the frictional and plastic behavior of the wire strand. Rotationally restrained numerical model for frictionless analysis shows reasonable agreement with Costello's [11] model and the frictional elastic-plastic model has in good agreement with both analytical results of Costello and the test results of Utting & Jones [12-13] for the application of tensile force.

7.2.5   Elastic analysis of an IWRC for different helix angles

The aim of this section is to gather analytical and numerical results considering the IWRC model without friction. For this purpose variation of reaction force with axial strain and variation of twisting moment with axial strain are compared in the following figures according to the theoretical model of Costello with the FEA results. All theoretical results and FEA results presented in these figures are obtained from frictionless models. Design parameters and material properties of an IWRC are used from Table 7.2 and Table 7.3 respectively. Boundary conditions are defined for each end of the IWRC. One end of the IWRC is fixed while the other end is constraint with no rotation. Axial strain of $\varepsilon = 0.015$ is applied to the free end of the IWRC.

An IWRC model includes three type of helical wires; inner single helical wire wrapped around the straight core wire, outer single helical wire which is also the center wire of the outer strand and finally the nested helical wire which is the outer wire of the outer strand. This construction is clearly shown in Figure 7.11. Three type of helical wire pitch lengths are denoted as p_2, p_2^* and p_4 respectively for inner single helical wire, outer center single helical wire and outer nested helical wire respectively. The helix angle for inner single helical wire and the outer strand center single helical wire are arranged to be similar as 71.01° and 71.46°. Taking care of this situation, the angles corresponding to pitch lengths p_2, p_2^* and p_4 are optimized and the results are presented for different lay lengths in Table 7.4 and change of pitch length with helix angle given in Figure 7.12. Constant parameter η, called relative rotation, is given in Table 7.4. This parameter decreases while the pitch length increases. For pitch length of 230, the constant η starts to increase back. In addition,

the results for pitch length of 230 gives unreliable results and not included in the analysis presented here.
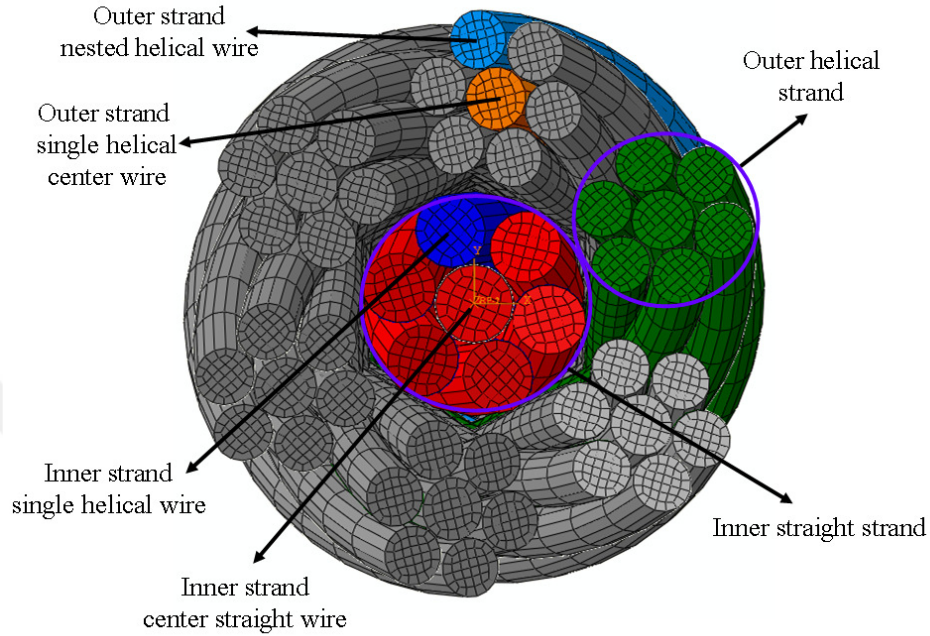
Figure 7.11: An IWRC model with inner and outer strand compositions.

Table 7.4: Helix angle changes for an IWRC.

Inner strand single helical wire		Outer strand single center helical wire		Outer strand nested helical wire		Constant parameter η
Angle α_2 (*degree*)	Pitch length $[p_2]$ (*mm*)	Angle α_2^* (*degree*)	Pitch length $[p_2^*]$ (*mm*)	Angle α_4 (*degree*)	Pitch length $[p_4]$ (*mm*)	
64.27	50	64.71	137	68.72	50	3.03
71.01	70	71.46	193	74.45	70	2.91
75.01	90	75.49	250	77.79	90	2.87
80.23	140	80.67	394	82.08	140	2.85
84.02	230	84.47	669	85.16	230	2.92
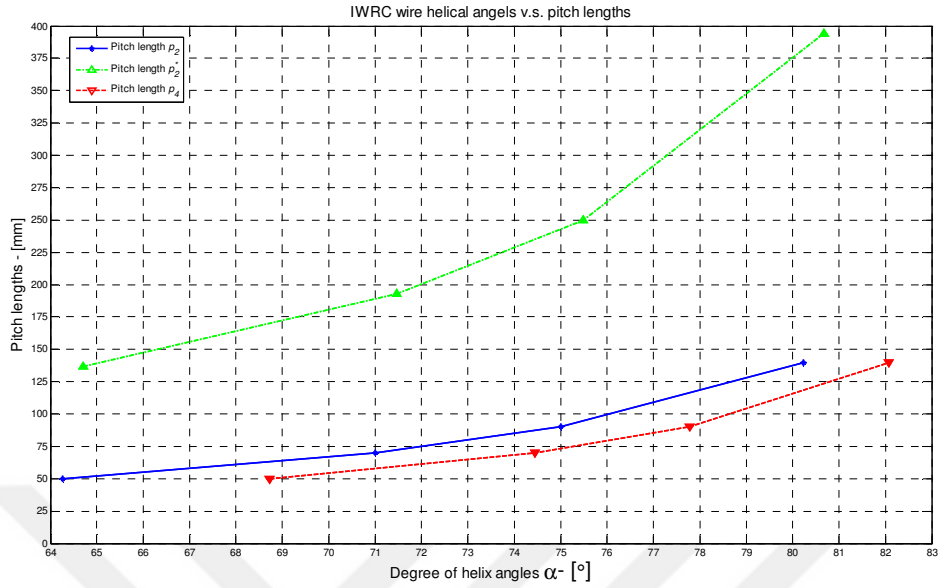
Figure 7.12: Variation of pitch length with helix angle for an IWRC.

The variation of reaction force with axial strain for various helix angles are plotted in Figure 7.13. It can be clearly seen that numerical results of reaction force with axial strain are in good agreement with theoretical ones for all cases. However, especially for the case of pitch length p_2=70, very good agreement is obtained.

Figure 7.13: Variation of reaction force with axial strain.

The variation of twisting moment with axial strain for various helix angles are plotted in Figure 7.14. It can be seen that numerical results of twisting moment with axial strain have separated for the theory and numerical solutions for all cases.
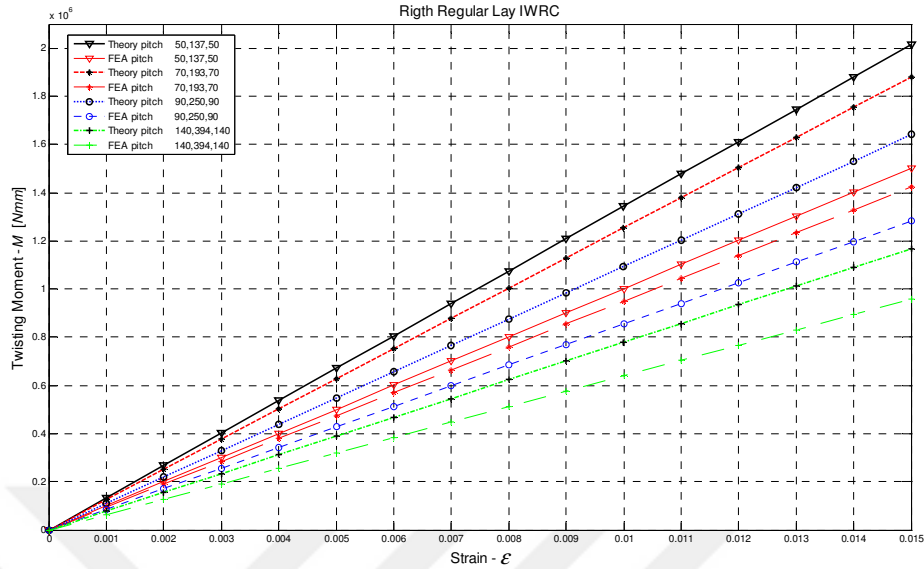
Figure 7.14: Variation of twisting moment with axial strain.

7.2.6 Plastic analysis of an IWRC for different helix angles

For the finite element plastic analysis model, helix angles are selected between 64.27° and 80.23°. In Figure 7.12, it can be seen that pitch length change of the IWRC near to helix angle 64.27° minimizes while pitch lengths are dramatically increased after 80.23°. Thus, helix angles were applied between 64.27°-80.23° for both modeling and numerical plastic analysis of an IWRC.

The aim of this section is to gather numerical results considering the model with frictional effect. For this purpose variation of reaction force with axial strain and variation of twisting moment with axial strain are compared in the following figures according to the FEA results obtained from frictional model. Design parameters and material properties of an IWRC are used from Table 7.2 and Table 7.3 respectively. Boundary conditions are defined for each end of the IWRC. One end of the strand is fixed while the other end is constraint no rotation. Axial strain of $\varepsilon = 0.015$ is applied to the free end of the IWRC.
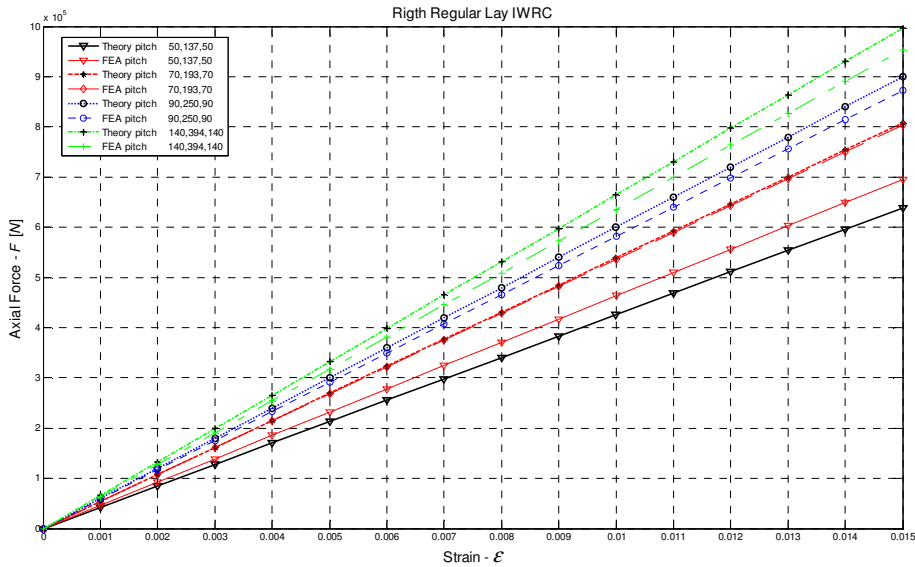
The variation of reaction force with axial strain for various helix angles are plotted in Figure 7.13. Reaching the value of applied strain $\varepsilon = 0.008$, IWRC shows plastic behavior for all cases.

131
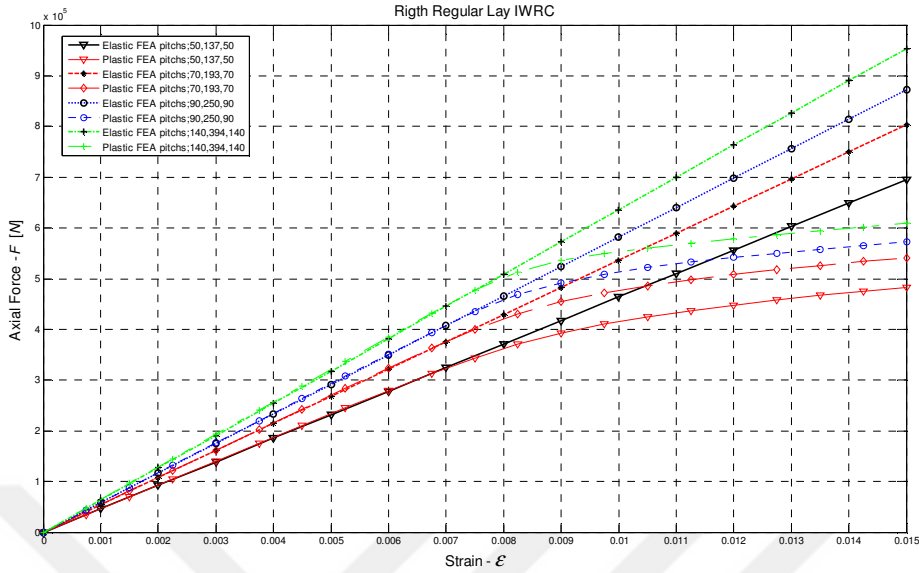
Figure 7.15: Variation of reaction force with axial strain in elastic-plastic FEA.

The variation of twisting moment with axial strain for various helix angles are plotted in Figure 7.16. Reaching the value of applied strain $\varepsilon = 0.008$, the IWRC shows plastic behavior for all cases.
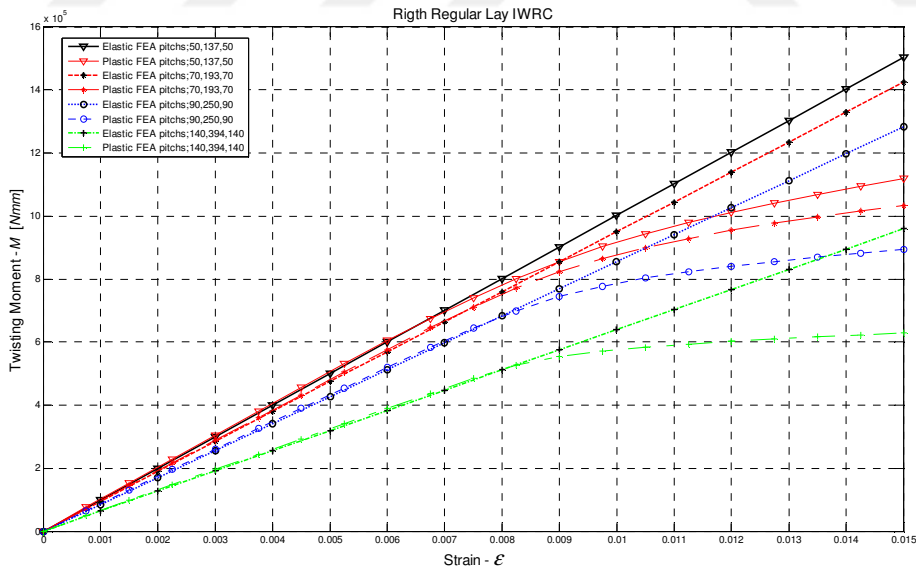
Figure 7.16: Twisting moment change with axial strain in elastic-plastic FEA.

Figure 7.17 shows the 3-D structure of the IWRC with the contour plots of the stress distribution over different helix pitch lengths. The helix pitch lengths are defined in Table 7.4. From the figure close fitting of the outer nested helical wires over the outer single center wires can be easily seen for p_2=50*mm*. While the helix length

increases the close fitting nature of the outer wires are changed and when the helix length increases to $p_2=140mm$, center strand single helical wires are nearly parallel to the center straight wire. This situation effects the behavior of the IWRC and center wire strand behaves like parallel rods, which reflects to the whole solution of the IWRC.

Pitch length; p_2, p_2^*, p_4; 50, 137, 50

Pitch length; p_2, p_2^*, p_4; 70, 193, 70

Pitch length; p_2, p_2^*, p_4; 90, 250, 90

Pitch length; p_2, p_2^*, p_4; 140, 394, 140
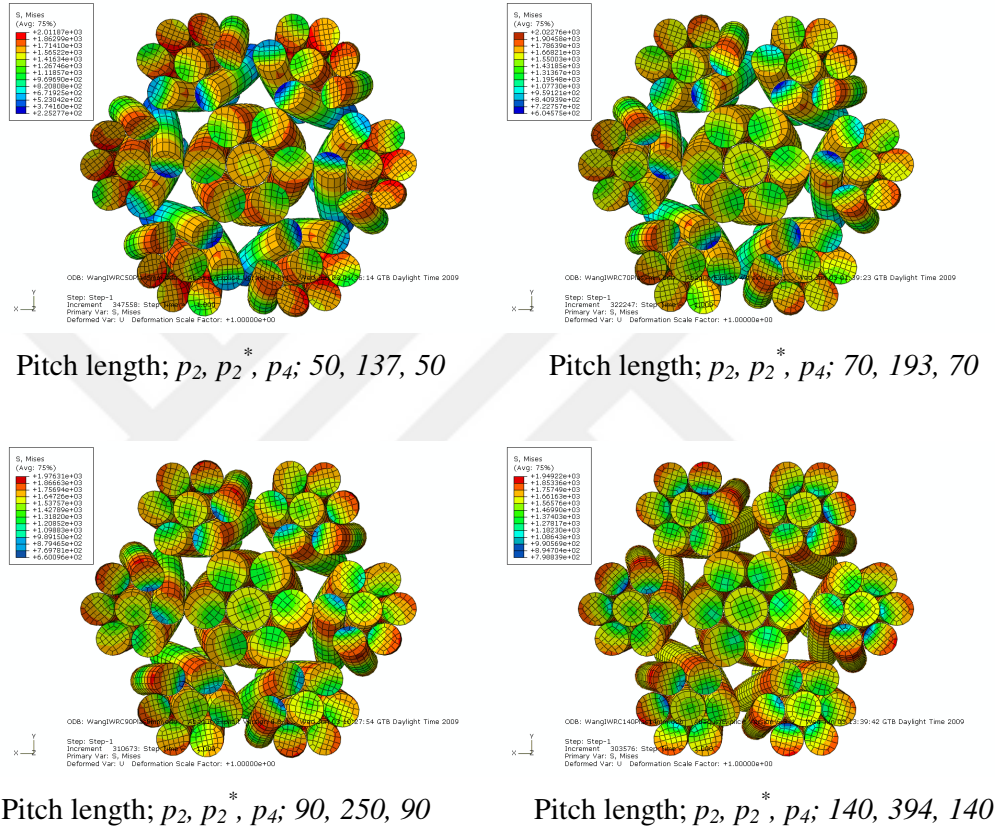
Figure 7.17: von-Mises stress distribution over a right regular lay IWRC.

7.2.7 IWRC wire contraction results using FEA

An 18mm length (6x7) wire of a three dimensional numerical IWRC model is considered. The geometrical parameters are given in Table 7.2, material properties are described in Table 7.3 and the comparison of the results are given in Figure 7.18 for both regular lay, and lang lay IWRCs. Frictionless contact controls are developed and tensile loading and twisting moments of an IWRC are proposed. A mean axial strain, ε of 0.006, was applied in increments of 0.001 in the analysis using the displacement equivalent to the axial strain ε, while rotation is restrained by $\Theta = 0$. Theoretical results are obtained by solving the well-known analytical model of Velinsky-Costello [60-11] model for a regular and lang lay IWRCs. The results are

obtained both numerically by FEA and using the theory of Costello [11] for the elasticity modulus of 188000 *N/mm²* and Poisson's ratio of *v*=0 and *v*=0.3, where wire radial contraction has been neglected and considered respectively. From the obtained results, it can be concluded that the wire contraction plays a very little role over the whole model analysis as discussed in [115]. Tensile forces obtained from proposed model have a good agreement with Costello's [11] results for both regular lay and lang lay rope constructions. However, twisting moments gives better agreement for regular lay construction than for the lang lay one when compared with Costello's [11] results.
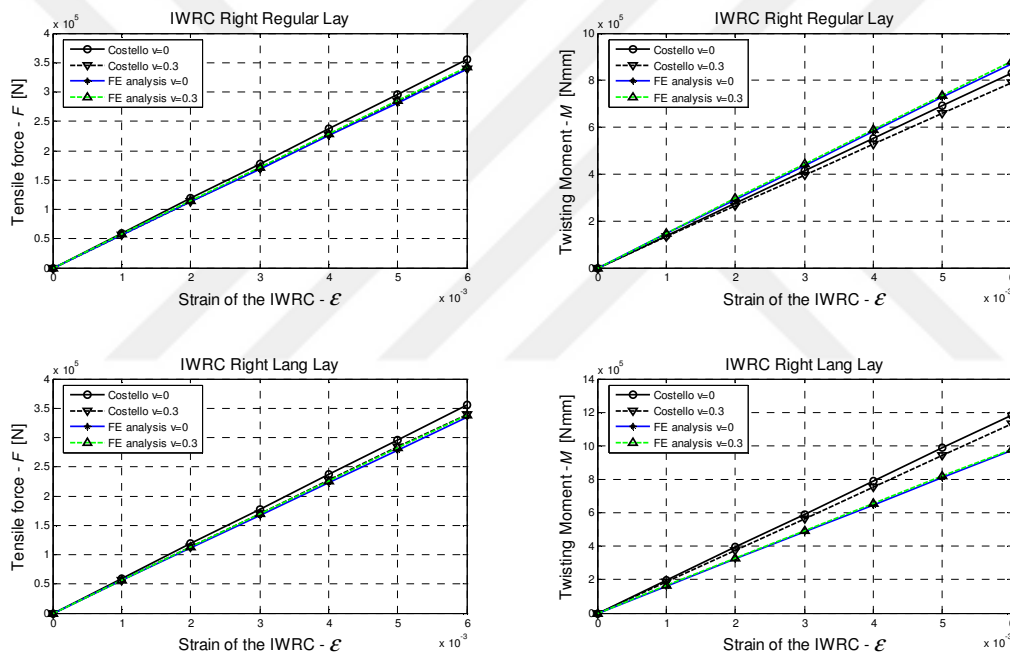
Figure 7.18: Radial contraction results of an IWRC, frictionless elastic, rotation restrained tensile test for $\varepsilon = 0,...,0.006$, $\Theta = 0$.

7.2.8 Wire by wire elastic-plastic FEA of IWRCs under axial loading

A frictional elastic-plastic finite element analysis is done over the geometrical model prescribed as an 18*mm* length (6x7) wire, for both regular lay and lang lay IWRCs defined in Table 7.2 and analysis results are given in Figure 7.19. For the frictional elastic-plastic analysis, wire material properties such as yield stress and friction values are given in Table 7.3. Surface to surface contact controls are developed and tensile loading and twisting moments of an IWRC are proposed. Axial strain ε of 0.015, was applied in increments of 0.001 in the analysis using the displacement

equivalent to the axial strain ε, while rotation is restrained by defining the boundary condition $\Theta = 0$. Theoretical results of Velinsky-Costello [60-11] models for a regular and lang lay IWRCs are compared with the finite element analysis results for the Poisson's ratio of v=0.3, where wire radial contraction has been considered. It can be easily concluded from Figure 7.19 that theoretical and frictionless behaviors are in good agreement both for regular and lang lay IWRCs.
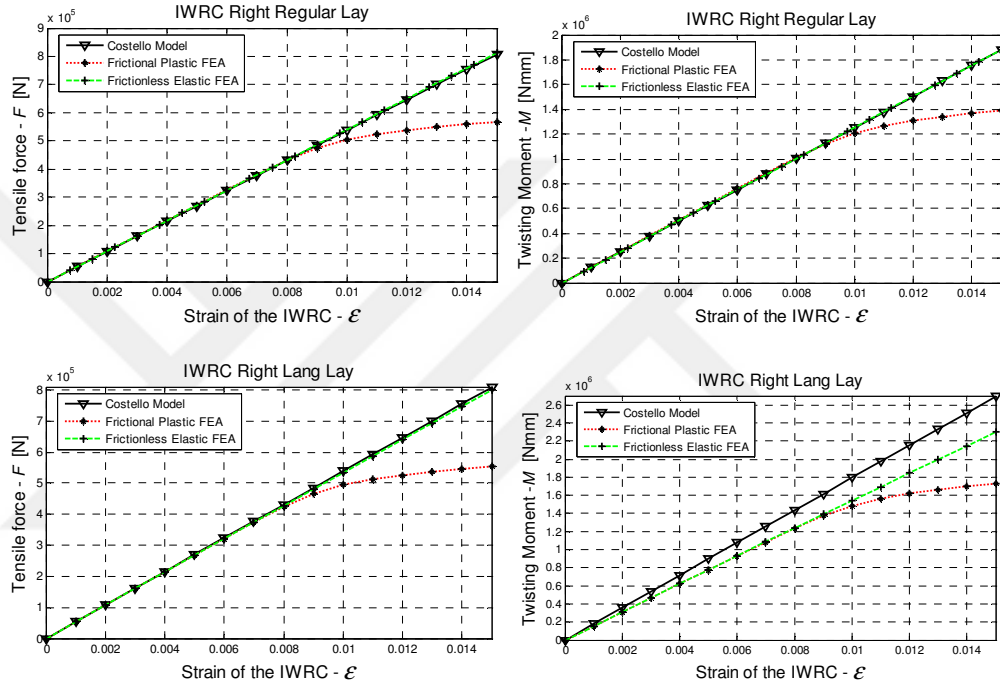
Figure 7.19: Regular lay and lang lay IWRCs, frictional elastic-plastic, rotation restrained tensile test for $\varepsilon = 0, ..., 0.015$, $\Theta = 0$.

It can be clearly seen by comparing Table 7.1 and Table 7.2 that the simple straight strand given in Table 7.1 is used as the core strand of the IWRCs, and the validity of the plastic behavior of the simple straight strand is presented in Figure 7.8 before. For this reason, when the plastic behavior of both simple straight strand given in Figure 7.8 and IWRCs given in Figure 7.19 are considered together, the plasticity results for both analysis shows the similar behavior. Figure 7.20 and Figure 7.21 shows the variation of axial force with moment of both right regular lay and right lang lay IWRCs. The results of a right regular lay IWRC is in good aggrement with theory of Costello for frictionless FEA while a right lang lay IWRC results shows similar trend with the theory of Costello.
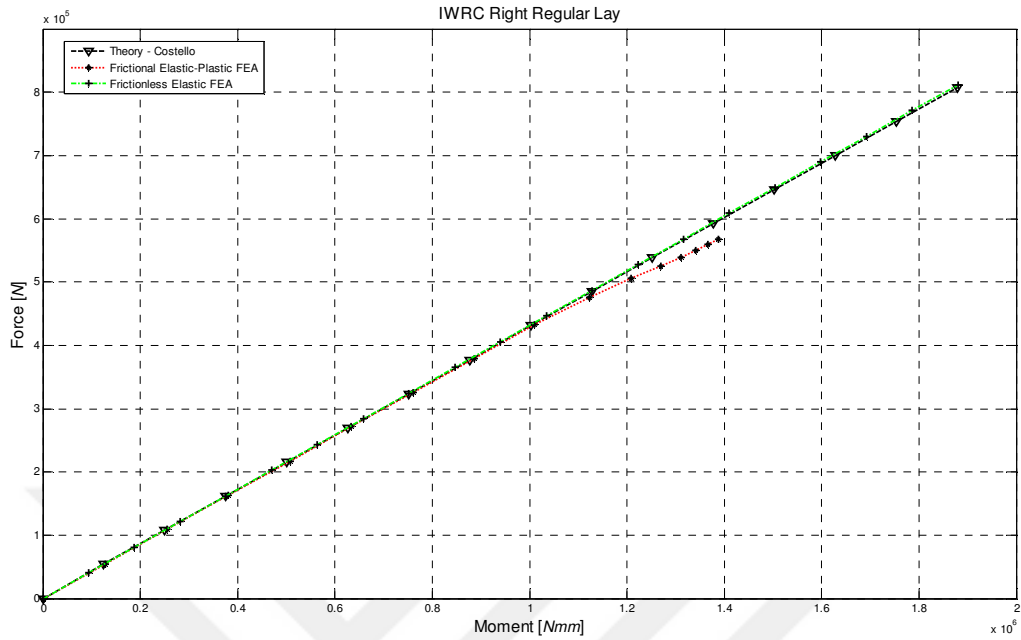
Figure 7.20: Force-moment results comparison of a right regular lay IWRC.
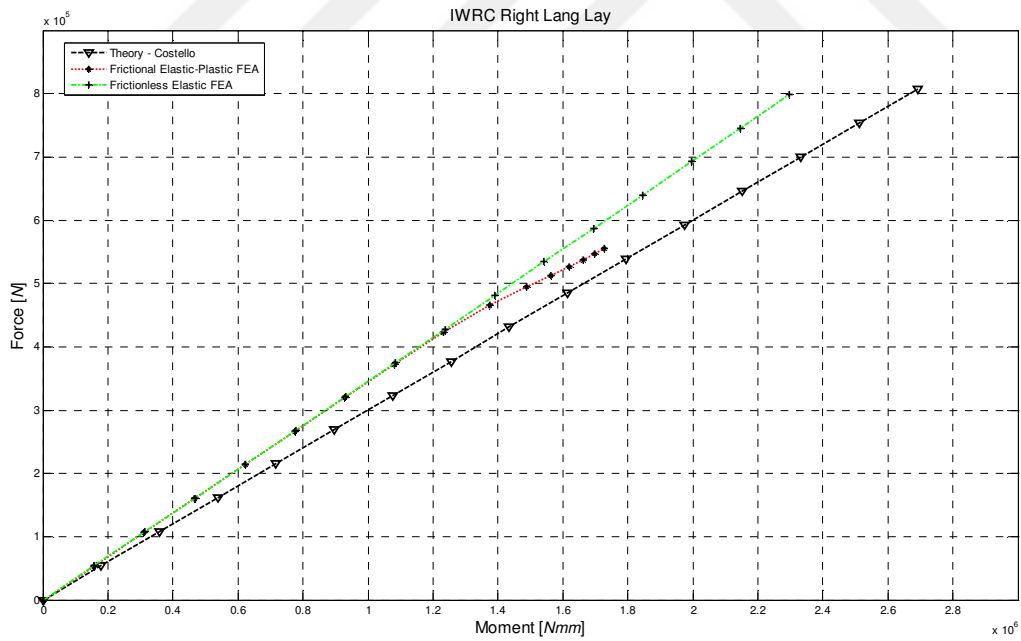
Figure 7.21: Force-moment results comparison of a right lang lay IWRC.

Figure 7.22 shows the von-Mises stress distribution of wire-by-wire analysis of a right lang lay IWRC. From the figure, it can be seen that the stresses over the center wires are the most among the other wires.

136
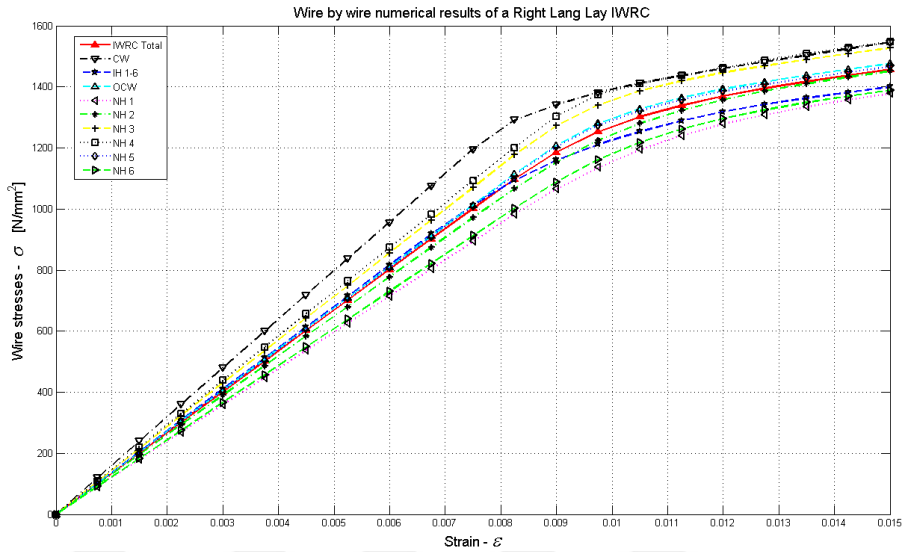
Figure 7.22: Wire-by-wire FEA of von-Mises stress for a right lang lay IWRC.

The insight of the wire-by-wire axial loading of the right lang lay IWRC is shown in Figure 7.23. Core and outer strand wire titles shown in Figure 7.23 are described in Table 7.5. Axial forces of a right lang lay IWRC is shown in wire by wire bases. The theoretical result of Costello and FEA results shows good agreement among the elastic area. After elastic behavior is finished, plastic behavior of the material affects the analysis as shown in Figure 7.23.
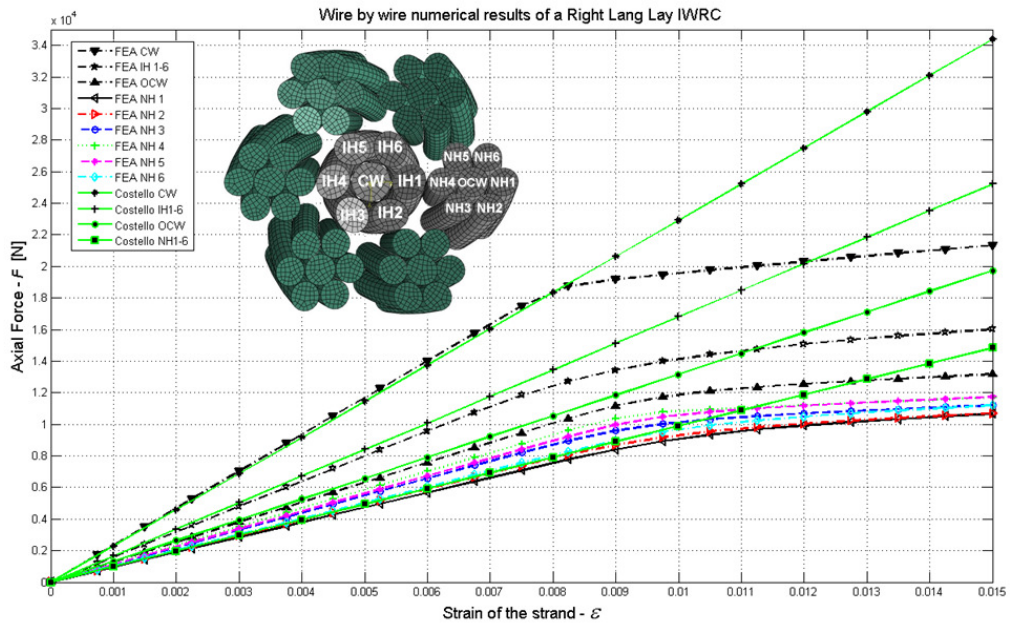
Figure 7.23: Wire-by-wire analysis, theory and FEA comparison of RLL IWRC.

137

A wire-by-wire loading is investigated by the analysis of a right lang lay IWRC and load percentage values for each wire are given in Table 7.5. When the loads are sorted according to their percentage magnitudes, center wire of the core strand carries the maximum axial load. In turn, inner helical wires IH1-IH6 and center wire of the outer strand (OCW) load value percentages follows the CW of the core strand in IWRC. Nested helical wires, which are located near to the center strand (NH3, NH4, and NH5) carries higher amount of the loads and among them NH4 has the maximum axial load. If the axial loads compared between the core strand and the outer strand of the IWRC, core strand has an average 20.18% of the total axial load, while the outer strand has an average 13.30% of the total axial load.

Table 7.5: Wire-by-wire axial loading percentages of the IWRC.

| Wire code	Strand	Title of the wires in an IWRC	Load (%)
CW	Core	Center straight wire	3.86
IH1-6	Core	Inner single helical wire 1-6	2.72
OCW	Outer	Center wire (single helix)	2.21
NH1	Outer	Nested helical wire 1	1.69
NH2	Outer	Nested helical wire 2	1.74
NH3	Outer	Nested helical wire 3	1.90
NH4	Outer	Nested helical wire 4	2.02
NH5	Outer	Nested helical wire 5	1.96
NH6	Outer	Nested helical wire 6	1.79

7.3 Wire rope analysis under forced torque

Wire rope behavior under forced torque condition is investigated in this section. Both a simple straight strand and an IWRC are modeled and analyzed using finite elements. Constant strain is applied while varying rotation during the analysis. Frictionless and frictional elastic and plastic behavior of the models are compared with the theoretical results.

7.3.1 Forced rotation of a simple straight strand

A simple straight strand of seven wires, 14*mm* length is considered under forced rotation. The geometrical and material properties of the simple straight strand are

given in Table 7.1 and Table 7.3 respectively. Proposed model is solved and compared with the theoretical results of Costello's [11] model. Surface to surface, nodal contacts are defined under the frictional analysis with a friction coefficient of 0.115. During FEA, a constant axial strain ε of 0.001 is applied, while a varying torque of Θ between -0.0002 to 0.001 with a constant increment 0.0002, and the force-strain and moment-strain results are given in Figure 7.24.

(a) F vs. Θ **(b)** M vs. Θ
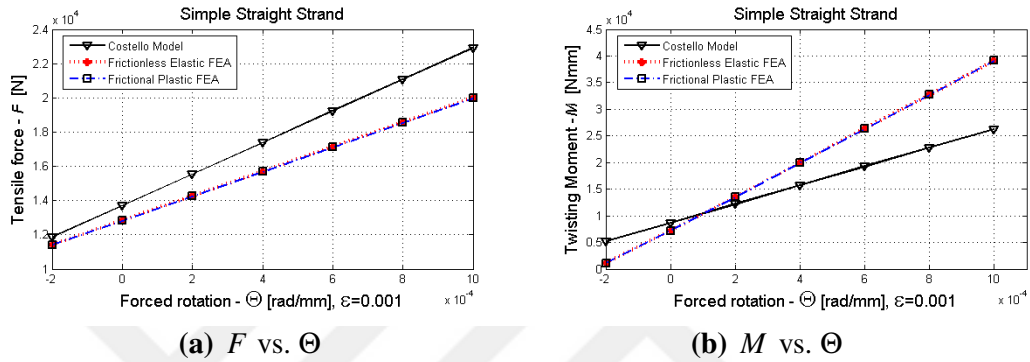
Figure 7.24: Forced torsion under constant deformation, $\varepsilon = 0.001$;
$\Theta = -2.10^{-4},...,0.001$.

As a result of the small axial strain ε of 0.001, frictionless elastic and frictional plastic FEA results shows linear behavior under forced rotation because of not reaching to the plasticity modulus of the material properties. Therefore, plasticity is considered applying a constant strain ε of 0.015, while the rotation of the strand is changed between -0.005 to 0.025 with 0.005 *rad/mm* increases in each step. Figure 7.25 shows the plastic behavior of the forced rotation and when the presented result is compared with the force-strain analysis presented in Figure 7.8, the plastic behavior of the strand can be seen clearly.

(a) F vs. Θ **(b)** M vs. Θ
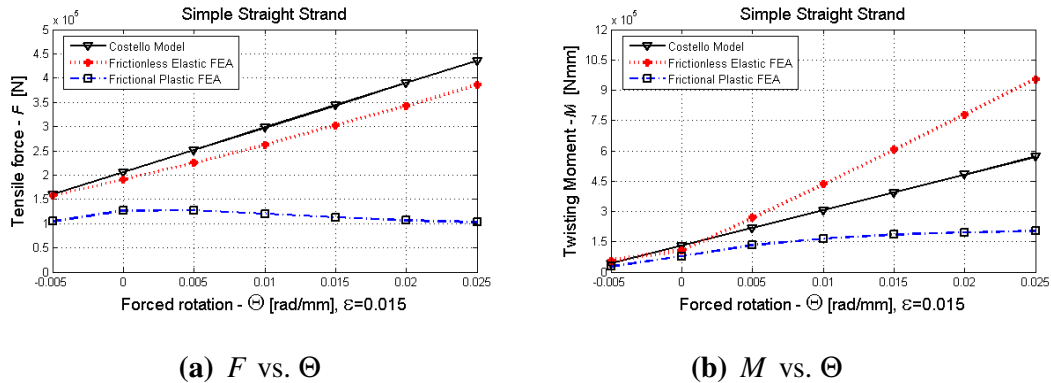
Figure 7.25: Forced torsion under constant deformation, $\varepsilon = 0.015$;
$\Theta = -5.10^{-3},...,0.025$.

7.3.2 IWRC under constant strain and varying rotation constraint

An 18mm length (6x7) wires lang lay IWRC under constant axial strain is forced to rotate. One side of the model is constrained to be fixed, while the other side is rotated in the z direction. The geometrical and material properties are given in Table 7.2 and Table 7.3 respectively. Proposed FEA solution is compared with the theoretical results of Velinsky-Costello [60-11] model. Surface to surface, nodal contacts are defined under the frictional analysis with a friction coefficient of 0.115. During the FEA, a constant axial strain ε of 0.001 is applied while a varying torque of Θ between -0.0002 to 0.001 with a constant increment 0.0002, and the force-strain and moment-strain results are given in Figure 7.26.


(a) F vs. Θ **(b)** M vs. Θ
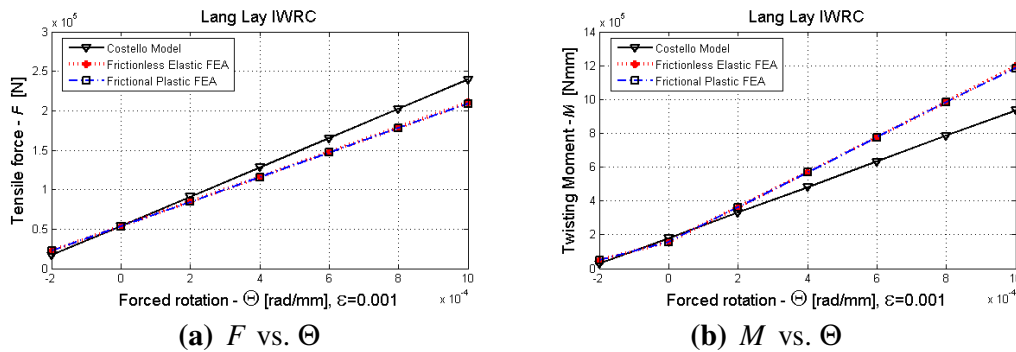
Figure 7.26: Forced torsion under constant deformation for a lang lay IWRC, $\varepsilon = 0.001$; $\Theta = -2.10^{-4}, ..., 0.001$.

Due to the small axial strain ε of 0.001, both frictionless elastic and frictional plastic FEA results shows linear behavior under forced rotation, because of not reaching to the plasticity modulus of the material properties. For this reason, the plastic behavior is investigated under a constant strain ε of 0.015, while the rotation varies between -0.005 to 0.025 with 0.005rad/mm increase in each step. Figure 7.27 shows the plastic behavior of the forced rotation. When the presented result is compared with the force-strain analysis of a lang lay IWRC presented in Figure 7.19, it can be seen clearly that the plasticity behavior is harmonious in each analysis.

(a) F vs. Θ **(b)** M vs. Θ
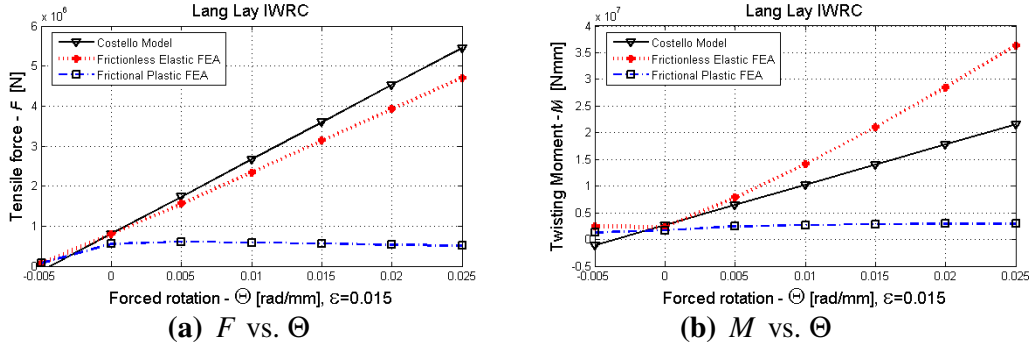
Figure 7.27: Forced torsion under constant deformation for a lang lay IWRC, $\varepsilon = 0.015$; $\Theta = -5.10^{-3},...,0.025$.

7.4 Strain and von-Mises stress distribution over a simple straight strand in a 3-D numerical model

Encastre boundary condition is given to one side of the wire rope strand which prohibits the strand to rotate $\beta = 0$. On the other side, each of the outer wires is loaded with force $11828.6N$ and the center wire is loaded with $12677.4N$ according to Costello's work. Wire material is selected as steel with the Young's modulus of $E = 196497.52N/mm^2$ and the Poisson's ratio has been taken as $v = 0.25$. In addition, the wires are constrained at the loaded side with another boundary condition, which allows the strain and displacements can occur only in the $u_3(z)$ directions. The other directions are prohibited to strain/displacement affects in $u_1(z)$ and $u_2(z)$ directions.

The proposed model is solved and resulting contour plots of the deformation and von-Mises stress distribution is presented in Figure 7.28 (a-b) respectively. It can be concluded that strain distribution along the strand is harmonious with the general behavior of a wire rope strand and in a good agreement with the analytical solution of 0.003 strain given in Costello's work. Strains are going to be stable near to the encastre side of the strand and shows a good von-Mises stress distribution along the wire rope strand.

141
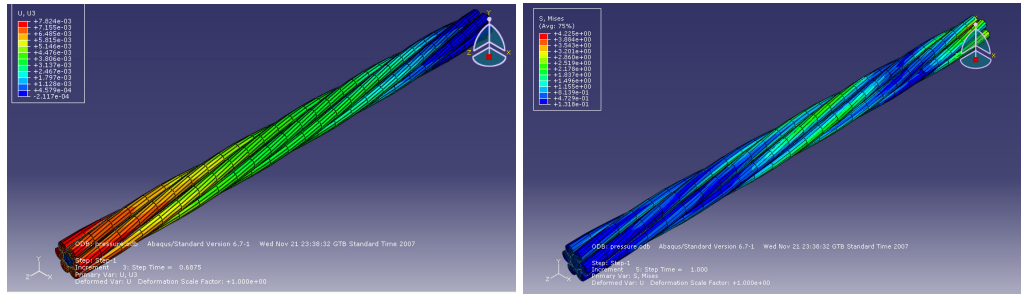
(a) Deformation over a straight wire rope strand,   **(b)** von-Mises stress distribution

Figure 7.28: Strain and von-Mises stress distribution on a wire rope strand.

7.5   Laying type effects of a 300*mm* IWRC FEA

Various lay types of IWRCs are modeled and shown in Figure 6.13. In this section a 300*mm* length (6x7) wire IWRCs are analyzed for different lay types; right lang lay (RLL), left lang lay (LLL), right regular lay (RRL) and left regular lay (LRL). Number of nodes and elements used in the analysis are shown in Table 7.6. During the FEA analysis, explicit method is used with linear hexahedral elements of type C3D8R. The geometrical and material properties are given in Table 7.2 and Table 7.3 respectively. Surface to surface contact is defined with the friction coefficient $\mu = 0.115$.

Table 7.6: Number of nodes and elements used in various IWRC models.

Lay types	Number of nodes	Number of elements
RLL	164492	126816
LLL	164492	126816
RLR	164000	126432
LRL	164000	126432

For different laying options of the IWRCs, one side of the rope is constraint to be fixed while the other end is constraint not to rotate. An axial strain of 0.015 is applied to the nonrotating end. Axial force variation with strain comparisons of the IWRCs for different lays are given in Figure 7.29 for fixed end.
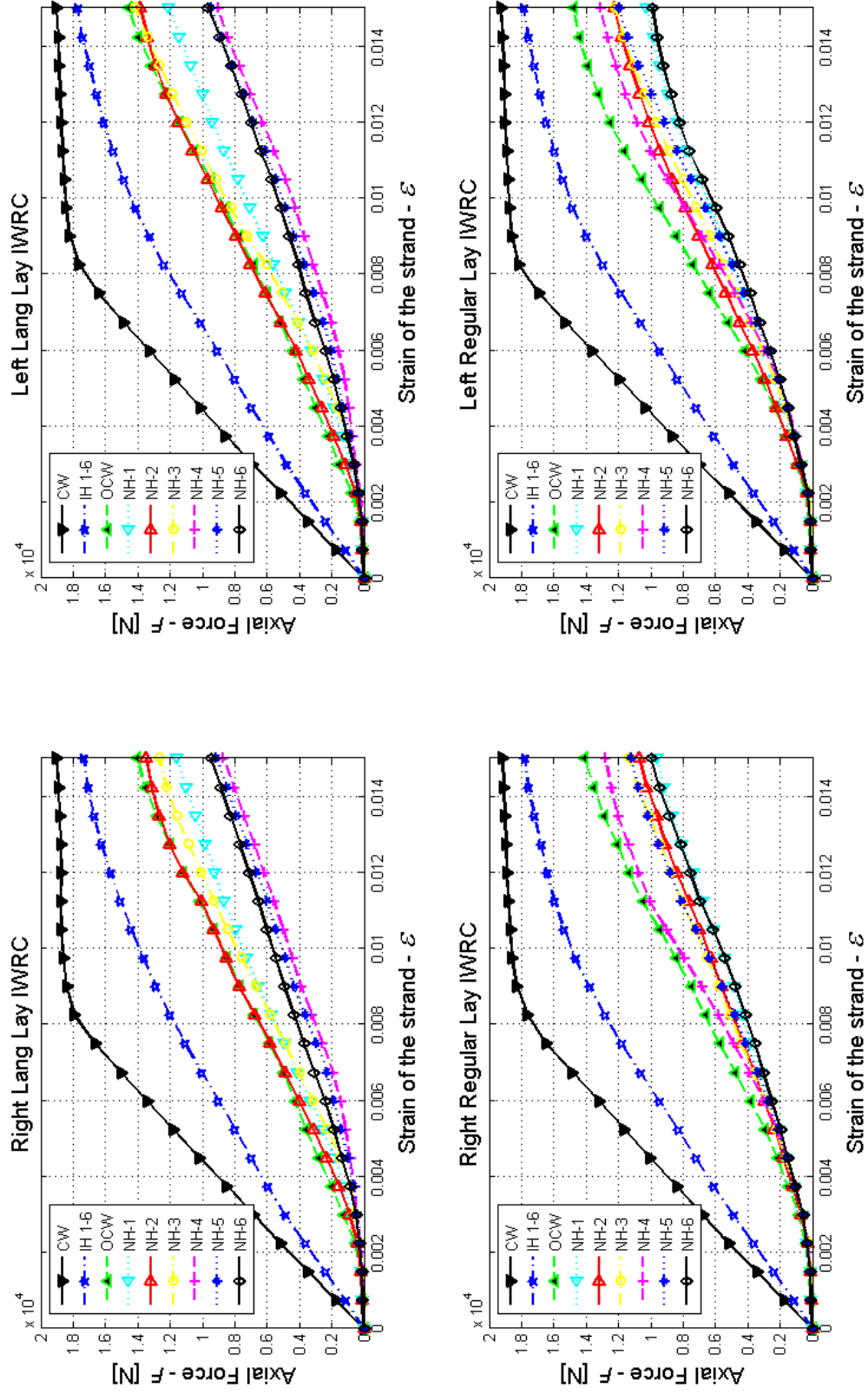
Figure 7.29: A 300*mm* fixed end reaction forces for RLL, LLL, RRL and LRL type IWRCs.
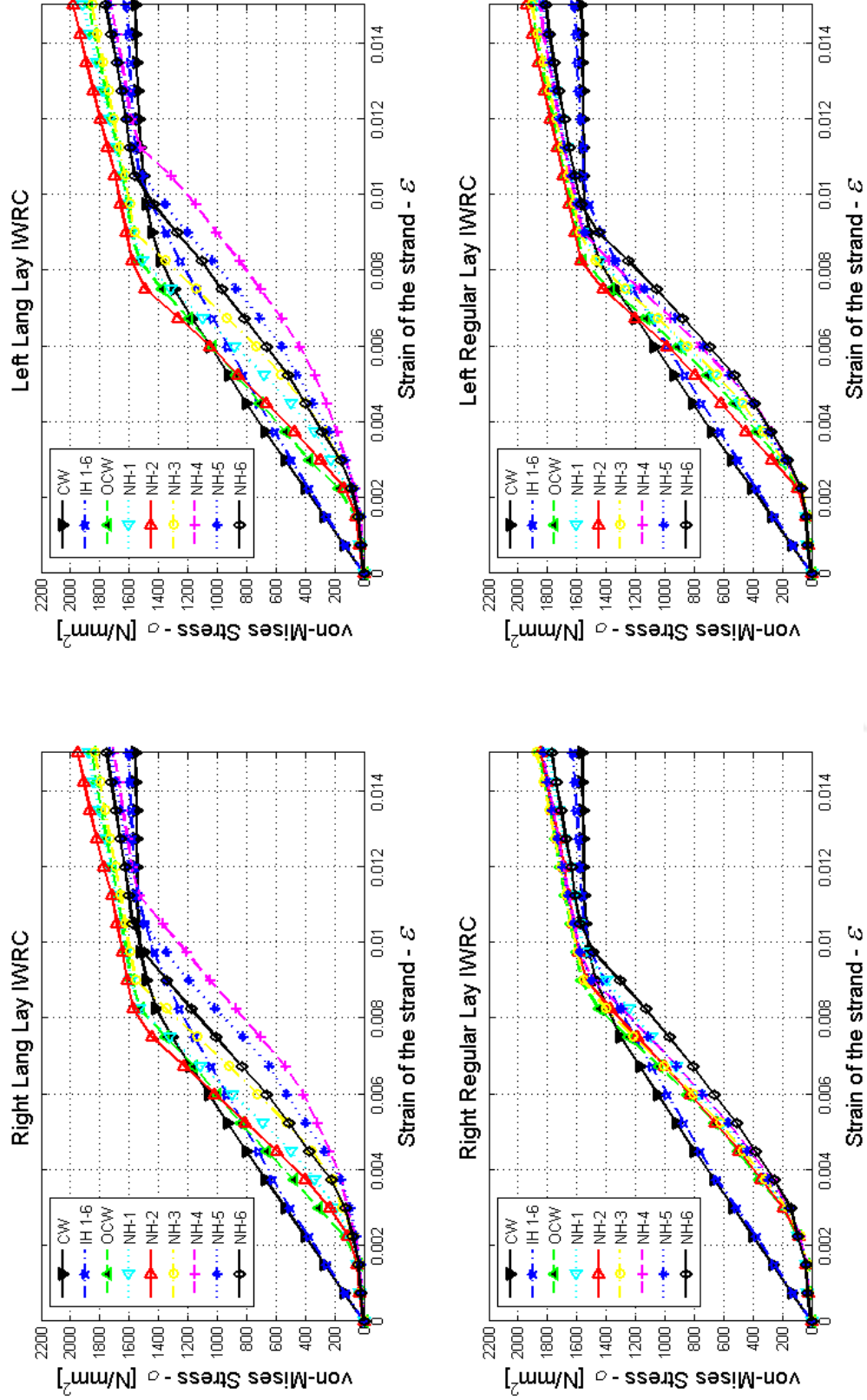
Figure 7.30: *A 300mm fixed end von-Mises stresses for RLL, LLL, RRL and LRL type IWRCs.*

From these figures, it can be seen that the behavior of the CW and IH 1-6 wires are in similar manner. Nested helical wires in a regular lay type IWRC loaded more than a lang lay type IWRCs. In addition, the force distributions are close to each other over the nested helical wires for regular lay types than the lang lay type IWRCs. Similar analysis are conducted for the non-rotating end conditions and results are presented in Appendix-D for convenience. von-Mises stress distribution over the fixed end IWRCs for different lay types are shown in Figure 7.30. From these figures, it can be concluded that the regular lay type IWRC stresses are close to each other while the stresses over the lang lay type IWRC are distributed in a larger band. In addition, nested helical wire stresses are got closer to the center wire stresses at the plastic area of the analysis.

Total reaction force comparisons given in Figure 7.31 for fixed end condition shows that the maximum reaction force is obtained at the LRL IWRC while the minimum reaction force is obtained at the RLL IWRC. When the LRL and RLL types IWRC are considered given in Figure 6.14 and Figure 6.15, it can be seen that the differences of the lay directions are important while force distributions within a rope. In LRL IWRC wires in the strands are laid to the right while the strands are laid to the left. Considereing the geometry of the LRL IWRC the axial force distribution given in Figure 7.31 is clearly understood.
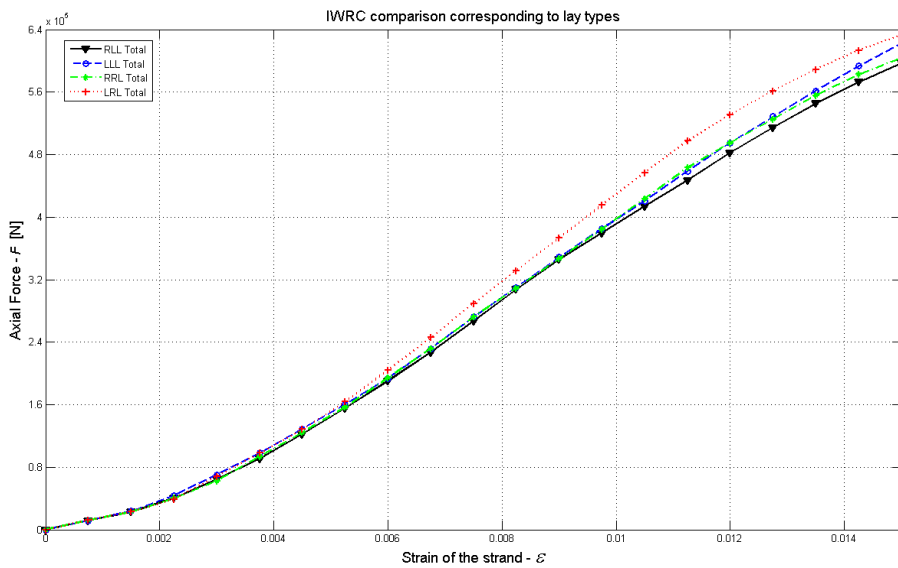
Figure 7.31: A 300*mm* fixed end total reaction force comparison for RLL, LLL, RRL and LRL type IWRCs.

Strands within an IWRC are compared next. Center strand comparisons for fixed end boundary conditions are shown in Figure 7.32. It can be concluded that the center strand force distributions are similar with small differences for each lay types. Outer strand comparisons for fixed end conditions are given in Figure 7.33. LRL takes maximum reaction force while RRL takes minimum reaction force values as depicted in Figure 7.31 due to the geometrical composition of the wires within an outer strands of the IWRCs. Figures for non-rotating end conditions for different lay types of IWRCs are presented in Appendix D for convenience.
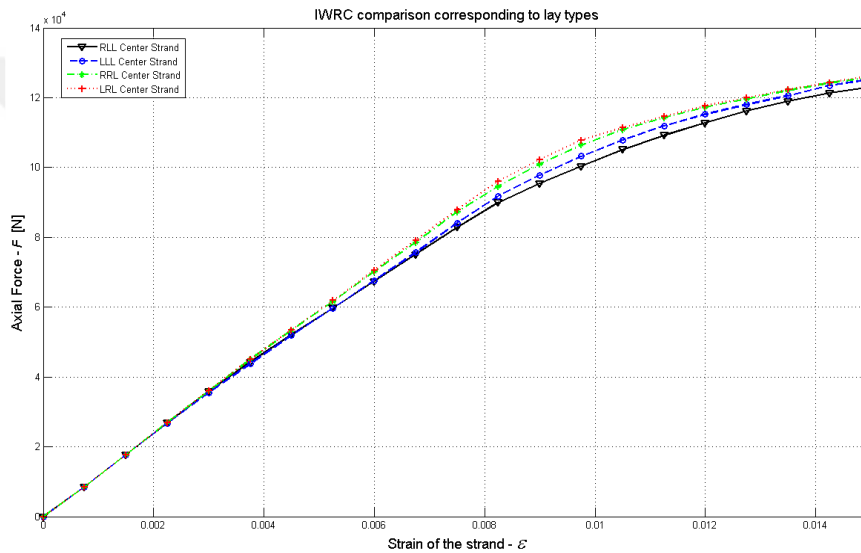
Figure 7.32: A 300*mm* fixed end center strand reaction force comparison for RLL, LLL, RRL and LRL type IWRCs.
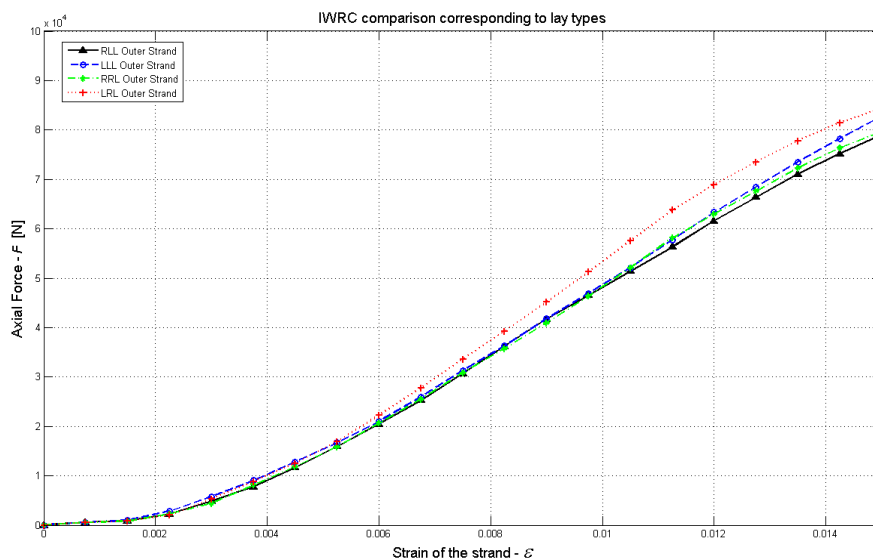
Figure 7.33: A 300*mm* fixed end outer strand reaction force comparison for RLL, LLL, RRL and LRL type IWRCs.

146

Reaction force percentages for each wire in the IWRCs for fixed end boundary conditions are presented in Figure 7.34. It can be seen that nested helical wires have closer percentages in regular lay type IWRCs.
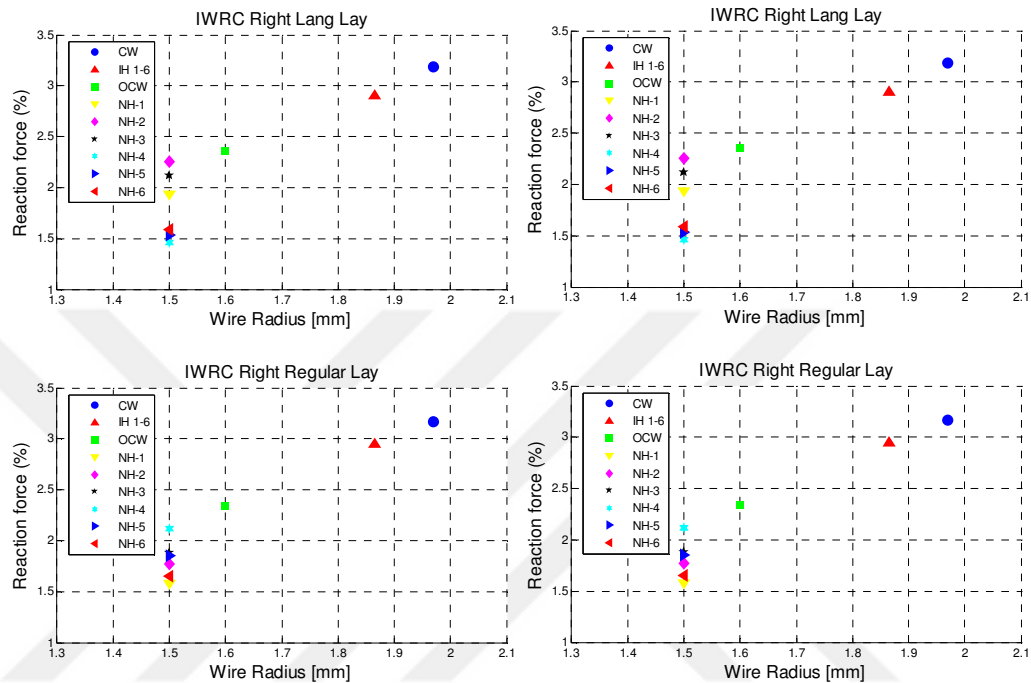
Figure 7.34: Reaction force (%) values for each wire in IWRCs.

It is interesting to compare the behavior of an 18*mm* length and a 300*mm* length right lang lay IWRCs with the same properties and under the same loading conditions. The resulting reaction force variations with strain at the fixed end of each model are presented in Figure 7.35.

Both models are constrained to be fixed at one end, and axial strain of ε=0.015 is applied to both IWRCs. From Figure 7.35, it can be concluded that the reaction forces over the nested helical wires are relaxed while the distance of the rope is increased. This situation shows that the center strands are faced to more load than the outer strands.
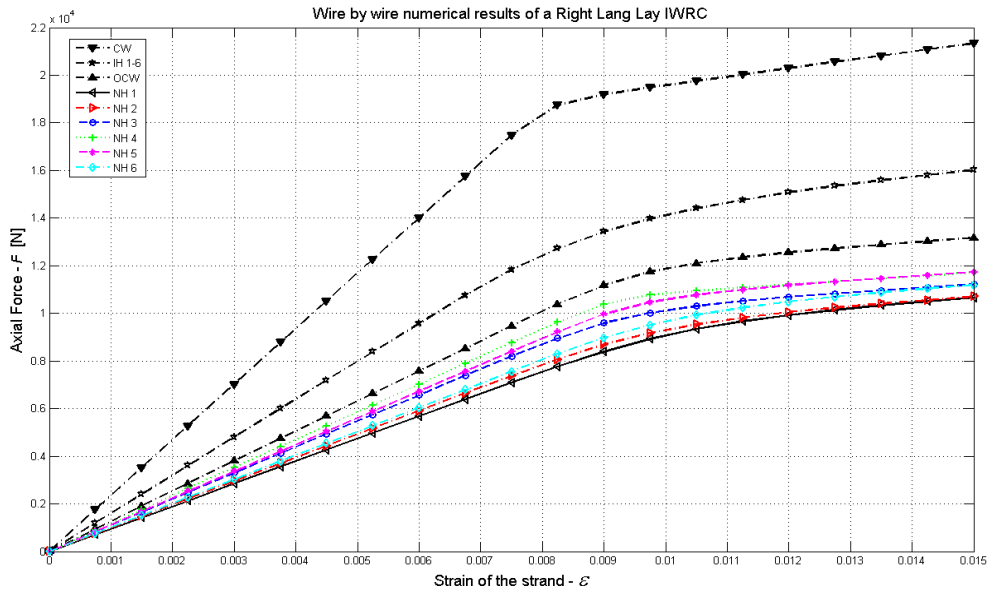
(a) 18*mm* length
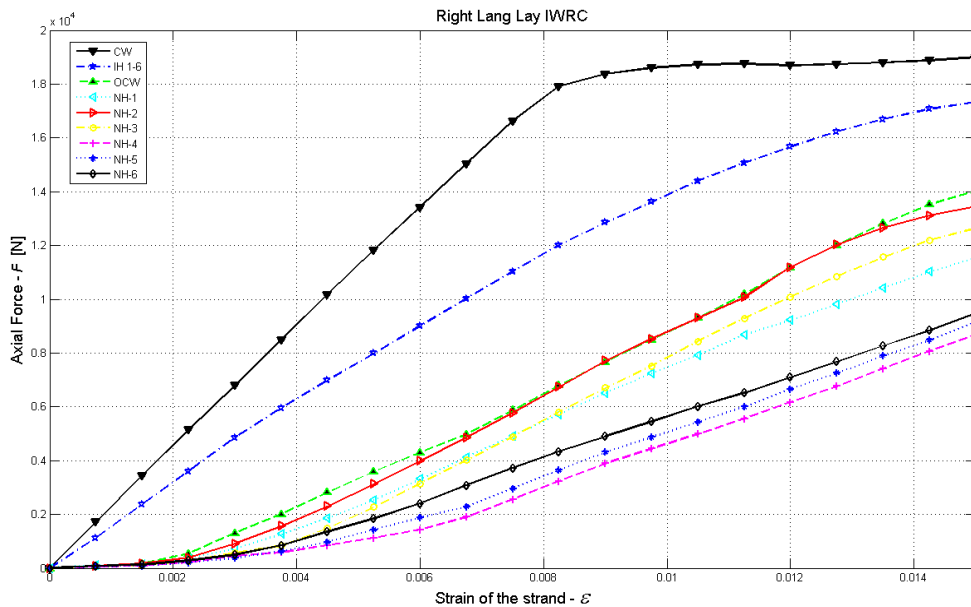
(b) 300*mm* length

Figure 7.35: Wire by wire reaction force over the fixed end RLL IWRC.

7.6   A simple straight strand bending over a sheave illustrative example

One of the most important application areas of wire ropes is known as bending over a sheave problem. A straight wire strand is considered for this problem. Geometrical and numerical analysis model parameters are defined in Table 7.7 and Table 7.8. A simple straight wire strand with the given parameters and a 12*mm* diameter sheave is modeled. The sheave is placed to be tangent to the straight wire strand at the mid

point in the first step of the analysis. Then a 20mm displacement boundary condition is applied to the each side of the strand to bend the wire strand around the sheave in the first step.

Table 7.7: Design parameters of a strand for bending problem.

Parameter	Value
Strand diameter	2.35mm
Center wire diameter R_1	0.83mm
Outer wire diameter R_2	0.76mm
Pitch length p	18.8mm
Helix angle of the strand α	75.12°
Strand length used in the model h	45mm
Sheave diameter	12mm

Table 7.8: Material properties of steel wire within a strand for bending problem.

Properties	Value
Elasticity modulus	190000 N/mm^2
Poisson's ratio	0.29
Friction coefficient	0.2
Minimum break load	6011 N
Applied force	1000 N

At the second step of the analysis one of the edges of the strand is fixed by defining encastre boundary conditions while 1000N concentrated force is applied to the other side of the strand. Thus pulling one of the edges of the strand is analyzed in this example. Figure 7.36 shows the contour plot of the von-Mises distribution over the bent wire strand and Figure 7.37 shows the contour plot of the displacement distribution over the wire strand.

From Figure 7.36, it can be easily seen that maximum stress value is reached at the upper midpoint position of the sheave. Maximum displacement value is reached at the fixed side of the strand as depicted in Figure 7.37. Wires are numbered as represented in Figure 7.37 and analysis results for the maximum stresses are 8605, 8358, 8760, 8668, 8847, 8686, 8039 N/mm^2 for wires W_1 through W_6 and 8039 N/mm^2 for the center wire. According to the analysis, W_5 has the maximum von-Mises stress value.
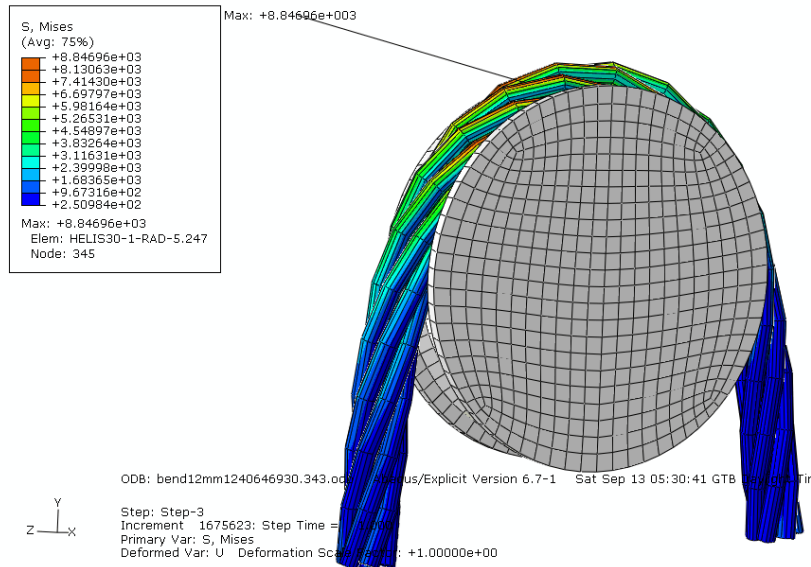
Figure 7.36: von-Mises stress distribution on a wire strand bent over sheave.
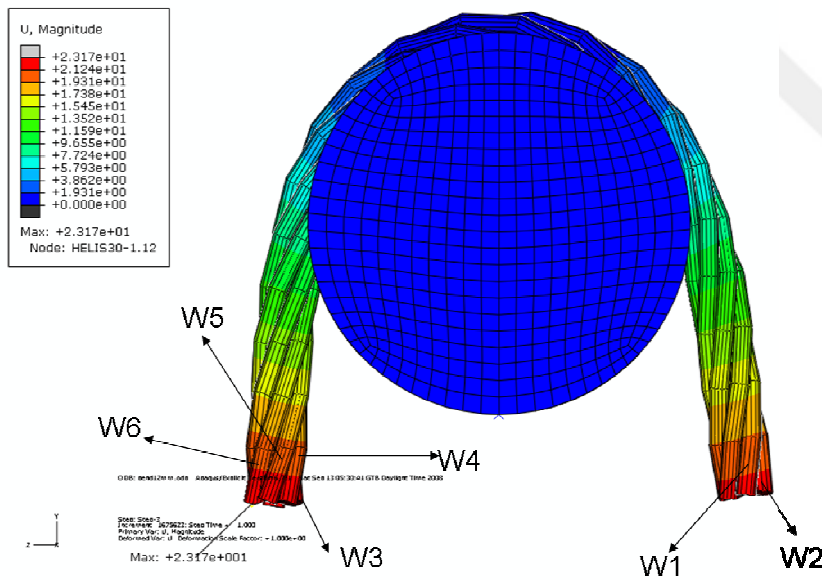
Figure 7.37: Deformation distribution on a wire strand bent over sheave.

As a second example, a 30*mm* wire strand is bent over a 6*mm* sheave. In this example, wire strand is bent over the sheave at first step of the FEA. At the second step, 1000*N* load is applied to one end while the other is constraint to be fixed end boundary conditions. Contour plots presented in Figure 7.38 shows the stress distribution over each wire of the strand. Variation of the von-Mises stress distribution with true distance for each wire is presented in Figure 7.39.
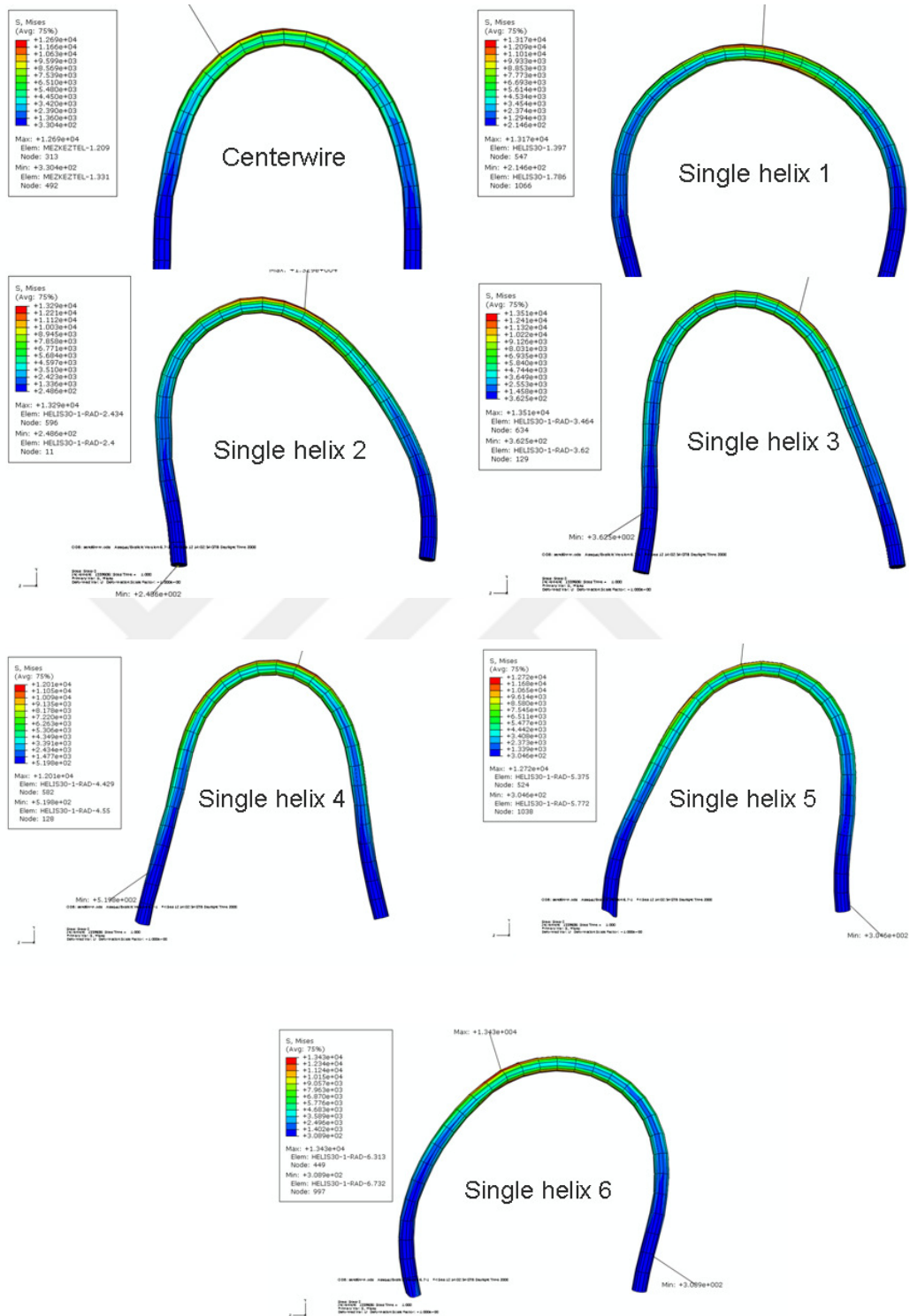
Figure 7.38: Stress distribution of each wire in a 30*mm* strand bent over a 6*mm* sheave.
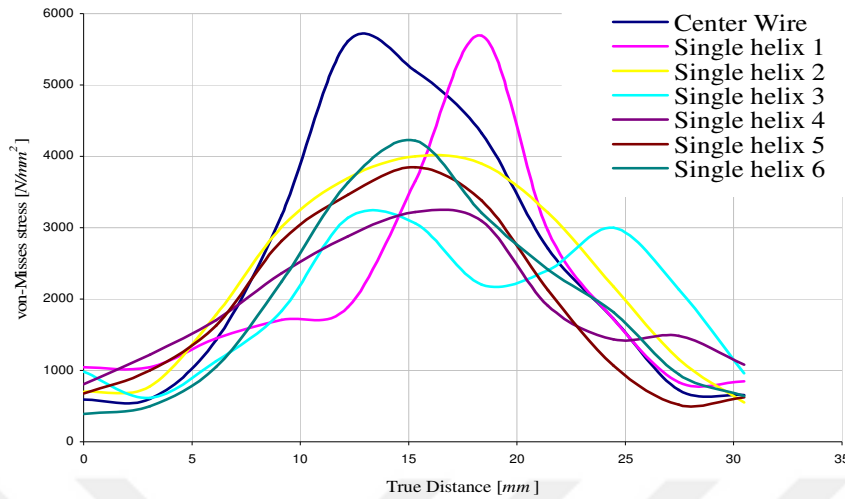
Figure 7.39: Variation of von-Mises stress over each wire with true distance.

7.7 Bending an IWRC over a sheave

Bending over a sheave problem for an IWRC is modeled and the FEA results are presented in wire-by-wire manner in this section. For the definition of the problem, the design parameters and material properties previously defined in Table 7.2 and Table 7.3 are considered. Two different lengths of IWRCs are analyzed for bending problem, a 9*mm* and a 300*mm* lengths respectively. The IWRC diameter and cross sectional area are 29.8*mm* and 380.48*mm²*. According to the standards, sheave diameter should be minimum 30 times to the rope diameter. Sheave diameter is computed as an 894*mm* with respect to the geometrical design parameters of the IWRC. It is constructed as a rigid body with encastre boundary conditions. The sheave is placed tangent to the IWRC at the mid point while constructing the bending problem geometry.

Boundary conditions of the IWRC is defined as fixed end over the sheave where the IWRC is tangent at the mid upper point of the sheave and free end boundary condition over the other side is defined. The analysis over a 9*mm* IWRC is processed for 0.2 second with two consecutive steps. An axial strain of $\varepsilon = 0.008$ is applied for the first step of the analysis which will not extend beyond the elastic region of the material properties defined in Table 7.3. At the second step, the displacement boundary condition is defined and run for 0.1 second. Due to the length of the IWRC is very small in the first numerical analysis, only 1*mm* displacement is considered.

152

Due to the geometry of bending over a sheave problem and wire position within the IWRC geometry, variation of axial force with respect to time shows differences between wires within the IWRC. Numerical results are obtained in wire-by-wire bases for reaction force and presented in Figure 7.40 for a 9*mm* IWRC that is bent over a sheave. The variation of the total reaction force with respect to time is presented in Figure 7.41. In the figures, only the results obtained at the second step of the analysis are considered and presented. From the figures, it can be seen that, while IWRC is displaced to bend over the sheave the value of reaction force increases with a slope and takes steady state after 0.18 seconds.
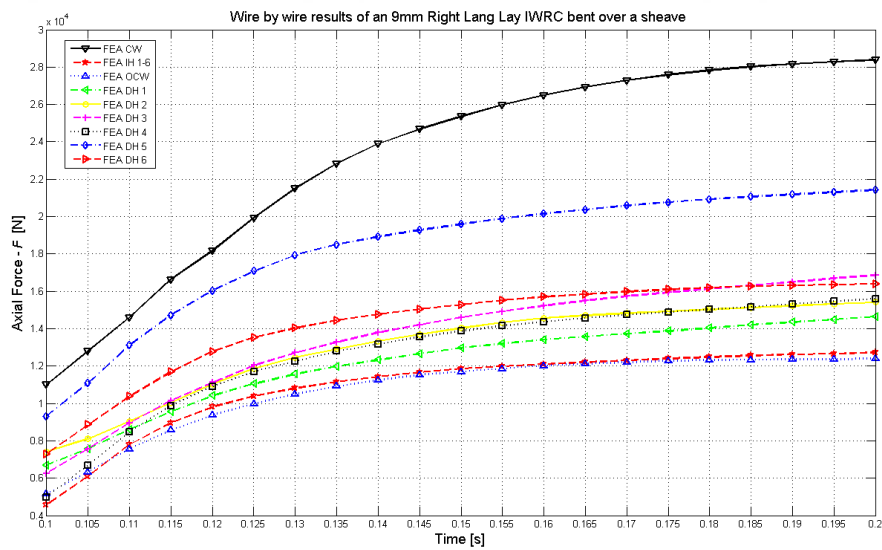
Figure 7.40: A 9*mm* IWRC bent over an 894*mm* diameter sheave.
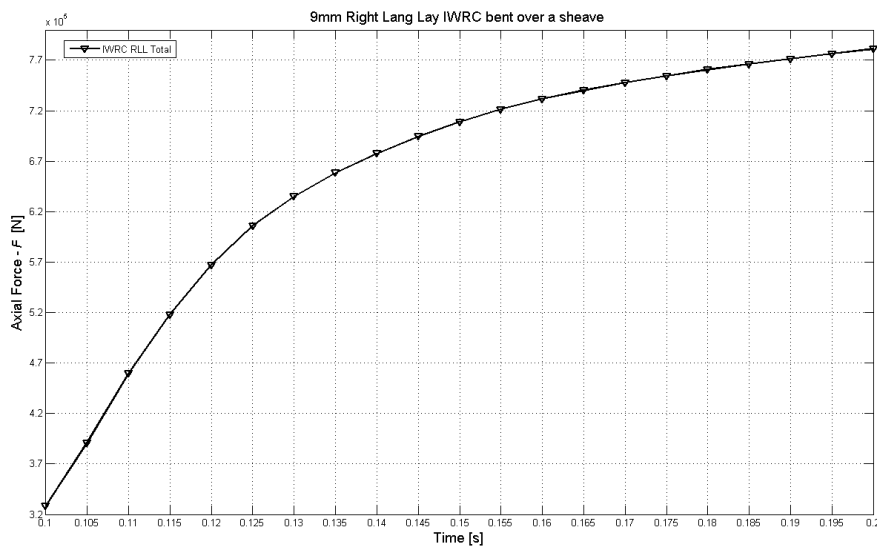
Figure 7.41: Variation of axial force with time for 9*mm* IWRC bent over sheave.

On the second bending problem, a 300*mm* IWRC and an 894*mm* diameter sheave are modeled and analyzed. An axial strain of $\varepsilon = 2.4e\text{-}4$ is applied to the free end of the IWRC as shown in Figure 7.42. Secondly, 90*mm* displacement boundary condition is applied to the free end of the IWRC, which bends the rope over the sheave as depicted in Figure 7.42. Outer strands are labeled as *S1,...,S6* and core strand is labeled as *C* and shown in Figure 7.43.
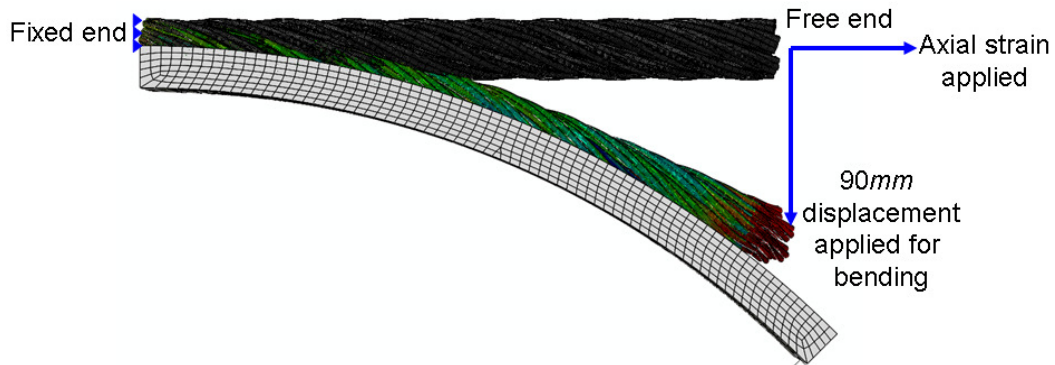
Figure 7.42: Fixed and free ends of a 300*mm* RLL IWRC bending over a sheave.

(a) Fixed end of the IWRC   **(b)** Free end of the IWRC
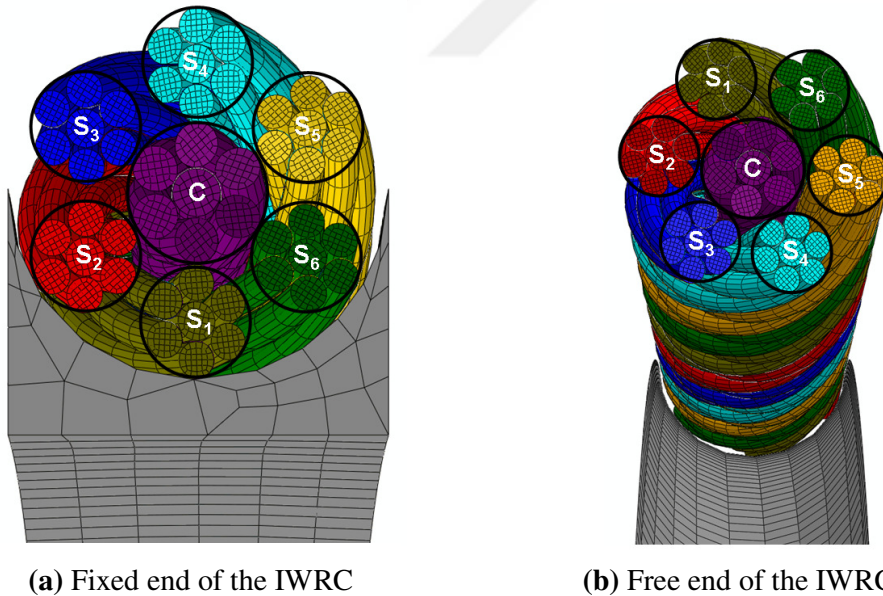
Figure 7.43: Strand numbers over the ends of an IWRC.

The analysis process is conducted using explicit scheme. Wire-by-wire results for each strand are presented in Figure 7.44 and Figure 7.45.

154
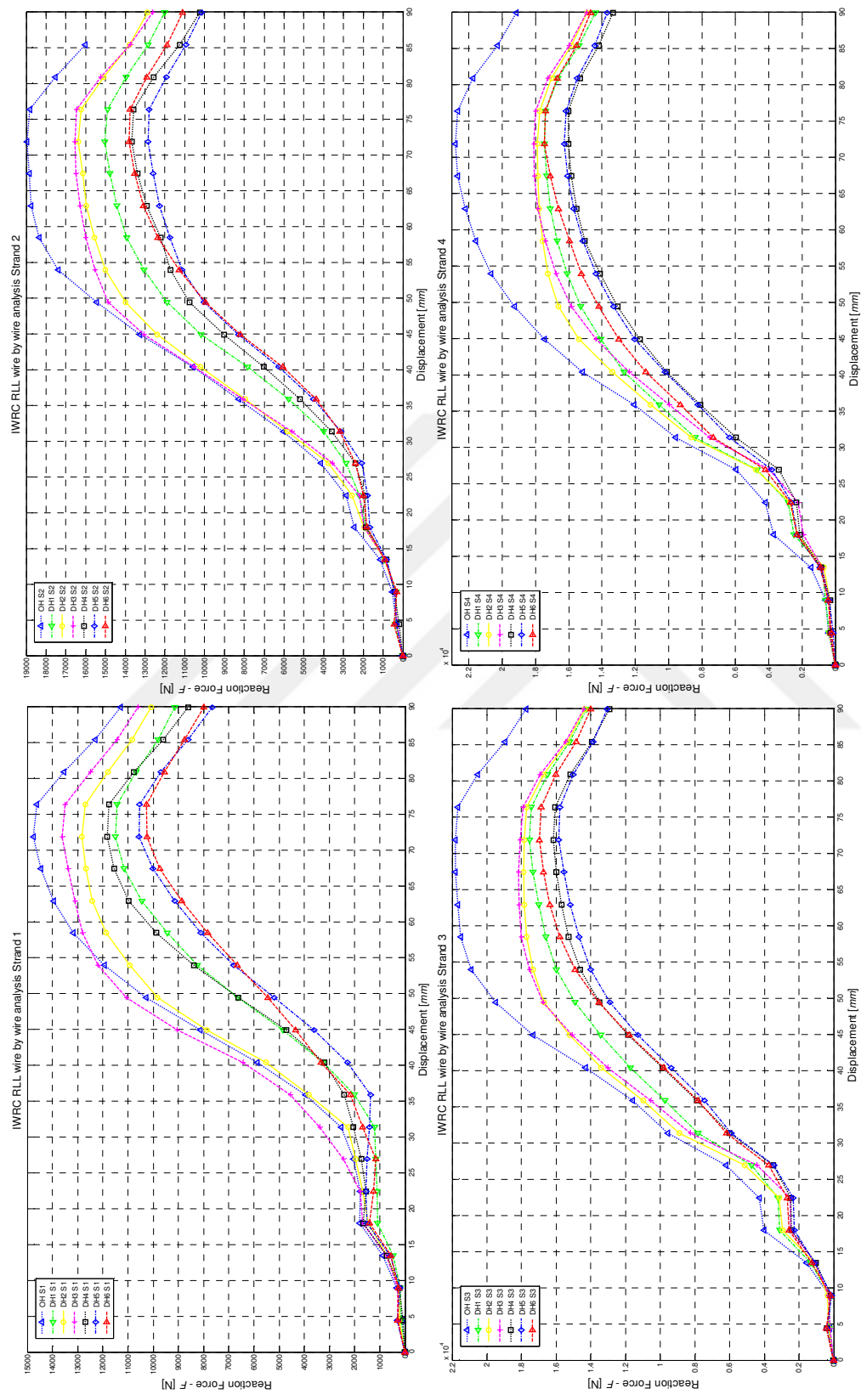
Figure 7.44: Strand by strand reaction force variation with displacement for bending problem of an IWRC: strands $S_1, ..., S_4$.

155
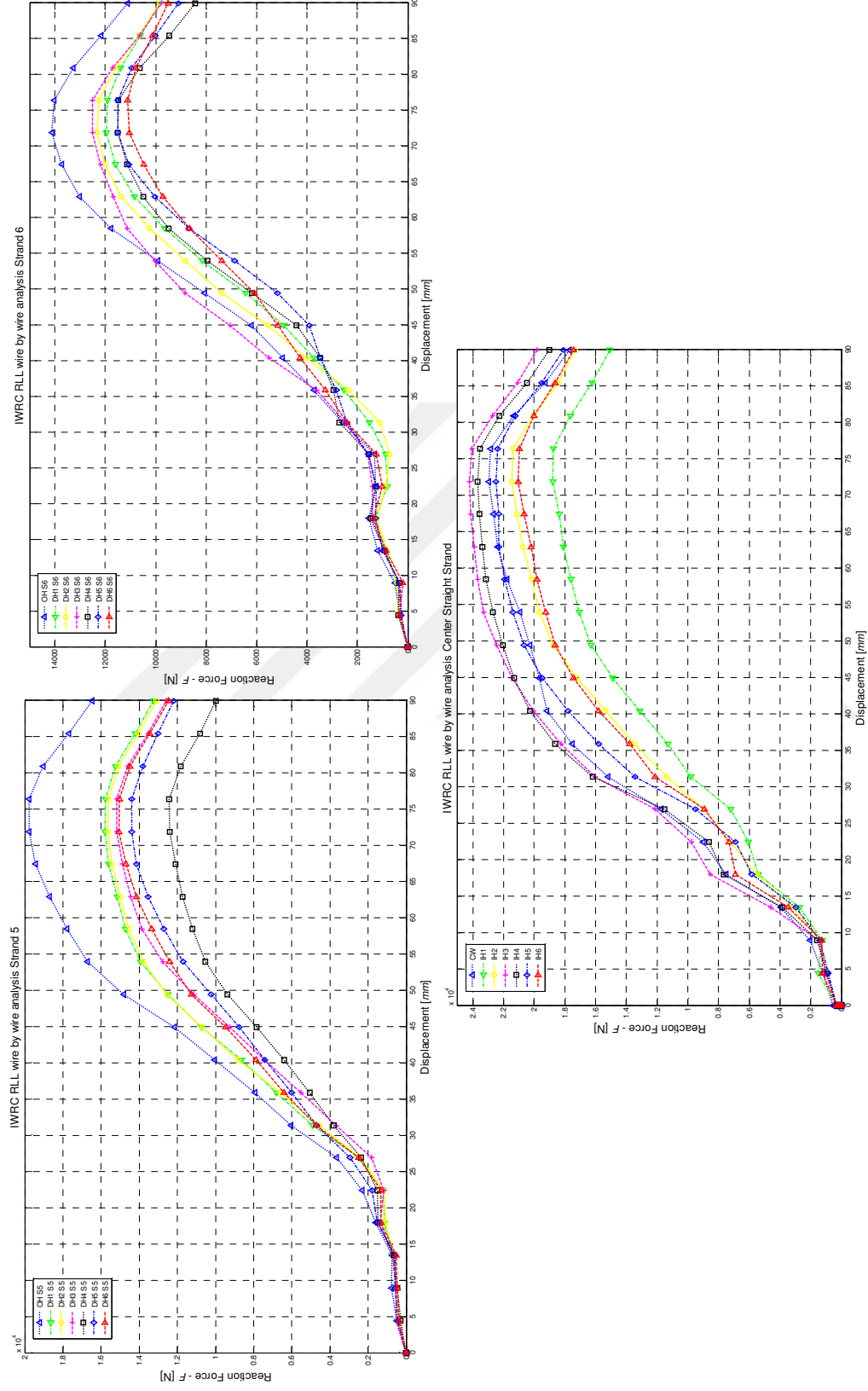
Figure 7.45: Strand by strand reaction force variation with displacement for bending problem of an IWRC: strands S_5, S_6 and C.

156

From these figures, it can be seen that the single helical core wires of each outer strand are loaded higher than the nested helical wires wrapped around the core wires. However, the load distribution over the core strand is regular with respect to the outer strands within an IWRC.

Reaction force variations with respect to displacement for strands are compared in Figure 7.46. It can be seen from the figure that the center strand has the maximum reaction force. Strands S_3&S_4, S_2&S_5 and S_1&S_6 behaves together and their positions within the IWRC affects their load distribution. Figure 7.43-(a) and Figure 7.43-(b) should be considered together with Figure 7.46. As an example, strands S_3 and S_4 are placed over the outer part of the IWRC with respect to sheave surface as it can be seen from Figure 7.43-(a). According to the bending analysis results, it can be seen from the Figure 7.46 that strand S_3 and S_4 are loaded more than the other strands and their reaction force distributions are in similar fashion. Analogous conclusions can be done for the other strands also. This shows that the compositions of the strands are effecting the load distributions of the strands. The closer strands to the bending area over the sheaves surface are loaded higher than the other strands during the bending over the sheave process.

In Figure 7.47 the total reaction force variation with displacement of the IWRC is presented. When the Figure 7.46 and Figure 7.47 are investigated together, reaction forces over each strand are increased during the bending process until application of the approximately 72*mm* displacement as depicted in Figure 7.42. Then the reaction forces begin to decrease slightly after this point is passed. In the literature there is no numerical result for bending over a sheave problem exists for the moment. For this reason it is not possible to compare these results with the previously obtained neither theoretical nor test results. However, the current numerical analysis encourages that bending analysis could be carried over 3-D wire rope models with success. The validity of the axial loading problems is analyzed previously, and the behavior of the IWRC during the bending process shows valuable results for further researches on this area.

von-Mises stress distribution over the IWRC is illustrated in Figure 7.48. From these contour plots, it can be seen that stress distribution over the center wire strand is much higher than the outer strands. This behavior can be explained as the

superposition rule used at the theoretical analysis. The wire rope behavior can be thought as a simple straight strand while bending process. The inner and outer strands in an IWRC can be expressed as center straight wire and outer single helical wires of a simple straight strand respectively. When the IWRC is bent over the sheave by superposition rule, core stand is loaded more than the outer strands and this situation can validate the stress distribution presented in Figure 7.48.
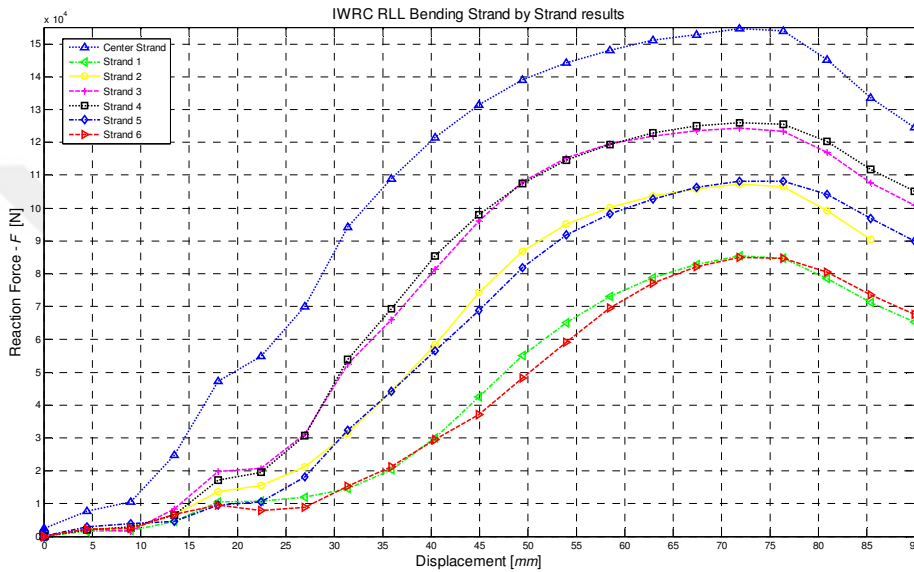
Figure 7.46: Reaction force variation with displacement comparison for strands on the bending problem of a 300*mm* IWRC.
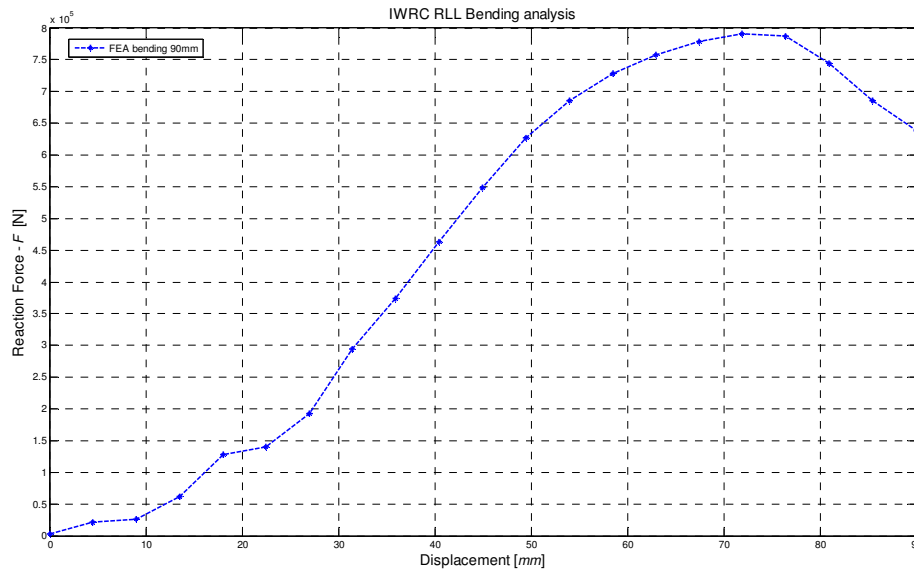
Figure 7.47: Variation of reaction force with displacement for a 300*mm* IWRC.
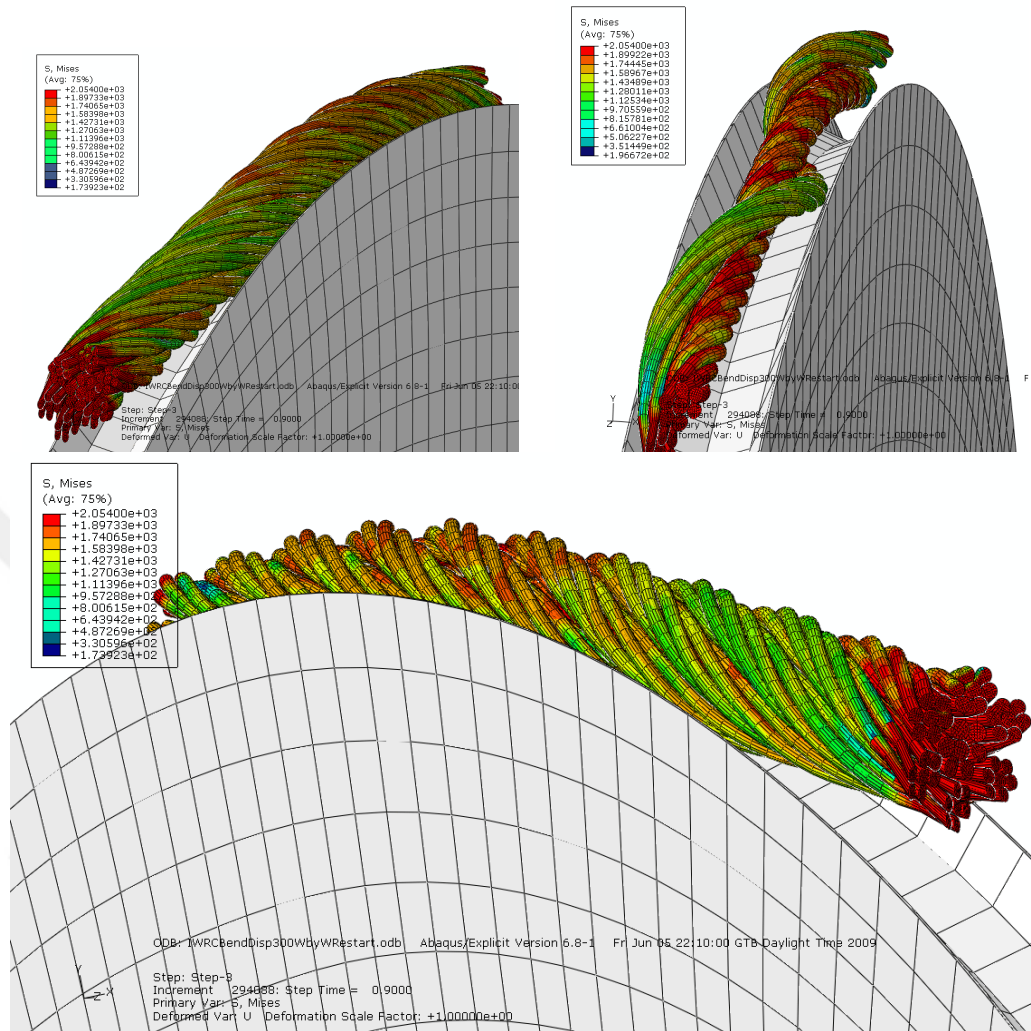
Figure 7.48: von-Mises stress distribution of a 300*mm* IWRC bent over an 894*mm* diameter sheave.

7.7.1 Parallel solution of the IWRC bending over a sheave problem

Bending an IWRC over a sheave problem is solved using FEA. During the analysis, a 300*mm* length of IWRC with C3D8R; 8-node linear brick, reduced integration with hourglass control elements are used to mesh the solid model. Total number of 17005 nodes, 135324 elements, and 531078 DOF of variables are exists in the model. FEA are conducted using the HPC Laboratory in Informatics Institute. CN02 system is used for the parallel FEA of the problems. System specifications are listed in Table 7.9. Problem solution with the given degrees of freedom (DOF) takes 2889 minutes using one CPU. Because of this difficulty, parallelization of the proposed model is taken into account. Parallelization of the bending over sheave problem using 1, 2, 4, 8, 16, and 32 CPU is done. Each trial is reported in Figure 7.49. It can be seen that

parallelization of the wire rope model works up to 16 CPU. From the figure, it can be concluded that increasing the number of CPU used beyond 16 CPU has no additional improvements while solving the considered wire rope problem.

Table 7.9: System specifications used for parallel FEA.

Orion host architecture
HP DL360 (thin) host group:
34 number of 2x3.4 GHz Intel Xeon
‐ 14 number of 2x2 GB RAM
‐ 20 number of 2x4 GB RAM
2 x 160 GB (IDE) HDD
HP DL380 (thin) host group:
10 number of 2x3.0 GHz Intel Xeon
2x4 GB RAM
HP DL580 (fat) host group:
41 number of 4x3.16 GHz Intel Xeon
‐ 36 number of 8x1 GB RAM
‐ 4 number of 8x2 GB RAM
‐ 1 number of 8x4 GB RAM
2 x 147 GB (SCSI) HDD
Total shared disk capacity: 27 TB
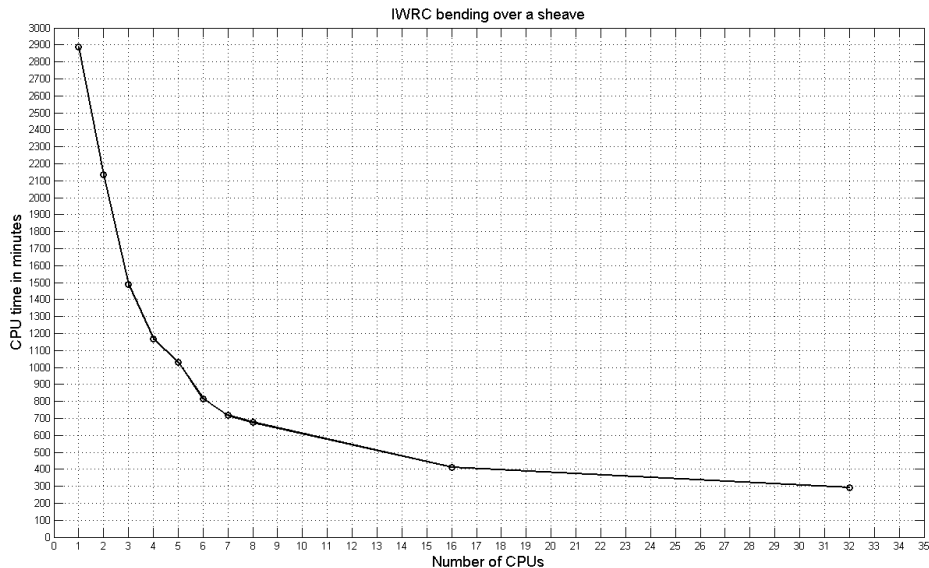
Figure 7.49: CPU time variation with number of CPUs for parallelization of the bending problem.

7.8 A 6x19 Seale IWRC solid model and FEA results

A Seale IWRC is one of the complicated types of wire rope. Modeling and numerical analysis of a 6x19 Seale IWRC is investigated. A cross section of the 6x19 Seale IWRC is given in Figure 7.50. Wires are numbered as W_{ij}, i indices indicates strand number while j indices indicates wire number starting from the center wire of a strand to the outer wire of the same strand as presented in Figure 7.51. The geometrical properties and wire lengths are presented in Table 7.10 and Table 7.11 respectively.
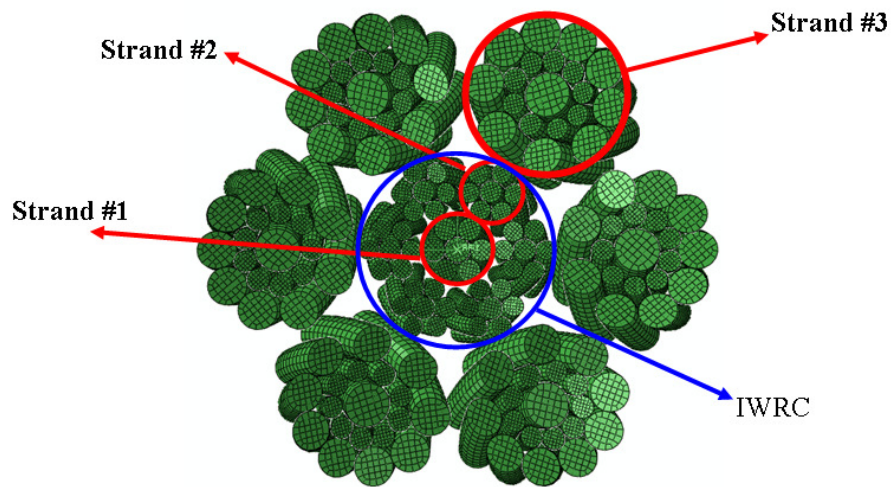
Figure 7.50: A 6x19 Seale IWRC cross section.
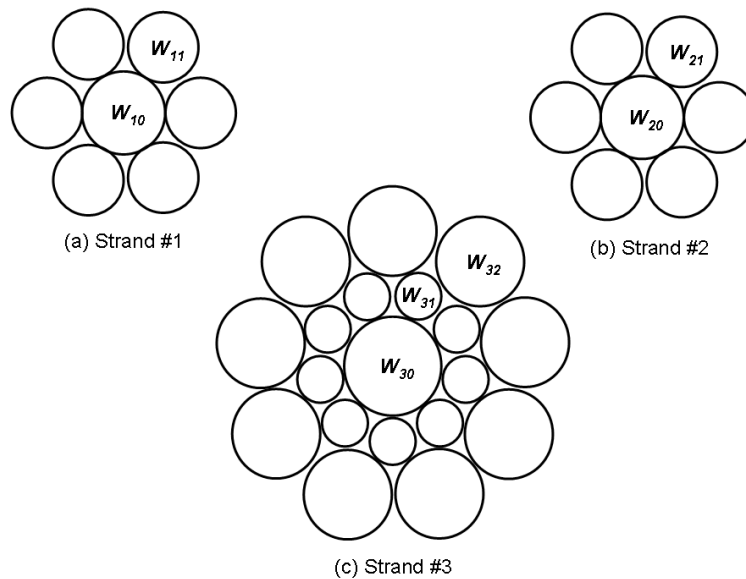
Figure 7.51: Wire numbers over a cross section of the 6x19 Seale IWRC strands.

Titles given in Table 7.10 and Table 7.11 are corresponds to the radius of strand helix r_s, radius of wire helix r_w, angle of strand helix α_s, angle of wire helix α_w, lay length of strand L_s, lay length of wire L_w, rotation of nested helix over a single helix η, Length of strand S_s, length of wire S_w respectively.

Table 7.10: Geometrical parameters of the 6x19 Seale IWRC.

S.No	No of Wires	Radius	r_s	α_s	L_s	r_w	α_w	L_w	η
1	1xW10	0.8014	0	0	0	0	0	0	0
	6xW11	0.7347	1.5361	1.2864	33.0228	0	0	0	0
2	1xW20	0.7042	4.2864	1.2362	77.4703	0	0	0	0
	6xW21	0.6557	4.2864	1.2362	77.4703	1.3599	1.4149	54.3555	1.5089
3	1xW30	1.4557	11.4443	1.2259	200.1544	0	0	0	0
	9xW31	0.7125	11.4443	1.2259	200.1544	2.1682	1.7849	62.6550	-3.3944
	9xW32	1.2682	11.4443	1.2259	200.1544	3.8741	1.9414	62.6551	-3.3944

Table 7.11: Strand and wire lengths of the 6x19 Seale IWRC.

Strand No	Wires	L_s	S_w	Wire to rope length ratio
1	W10	0	0	1
	W11	33.0228	34.4043	1.0418
2	W20	77.4703	82.0183	1.0587
	W21	77.4703	83.0255	1.0717
3	W30	200.1544	212.6789	1.0626
	W31	200.1544	217.6483	1.0874
	W32	200.1544	228.1653	1.1399

Wire paths for both single and nested helical wires in cross sectional and side views are presented in Figure 7.52, Figure 7.53 and Figure 7.54 for the corresponding strands of the 6x19 Seale IWRC.
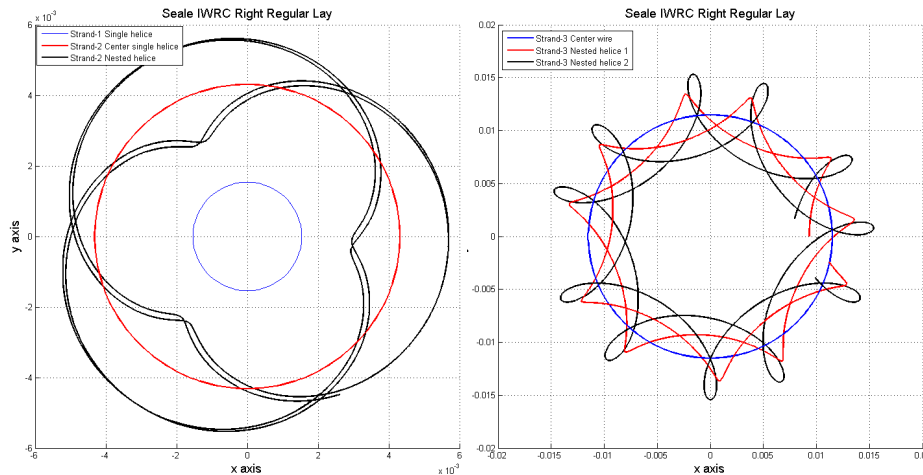
(a) Helices in Strand #1 and #2,   **(b)** Helices in Strand #3

Figure 7.52: 6x19 Seale IWRC wire centerline plots.
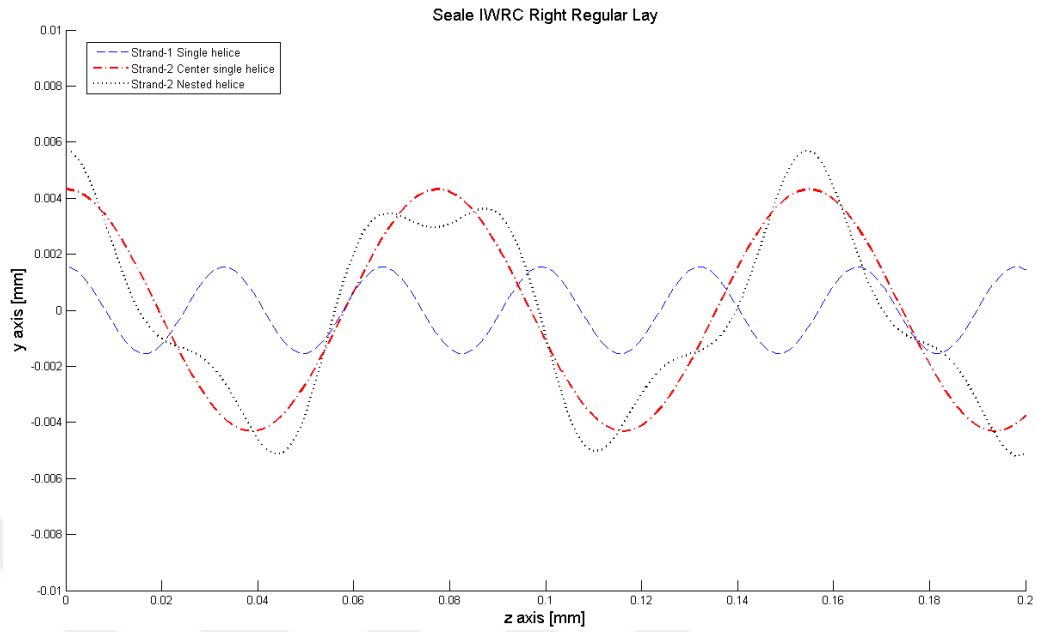
Figure 7.53: 6x19 Seale IWRC helical wire centerlines for Strand #1 and #2.
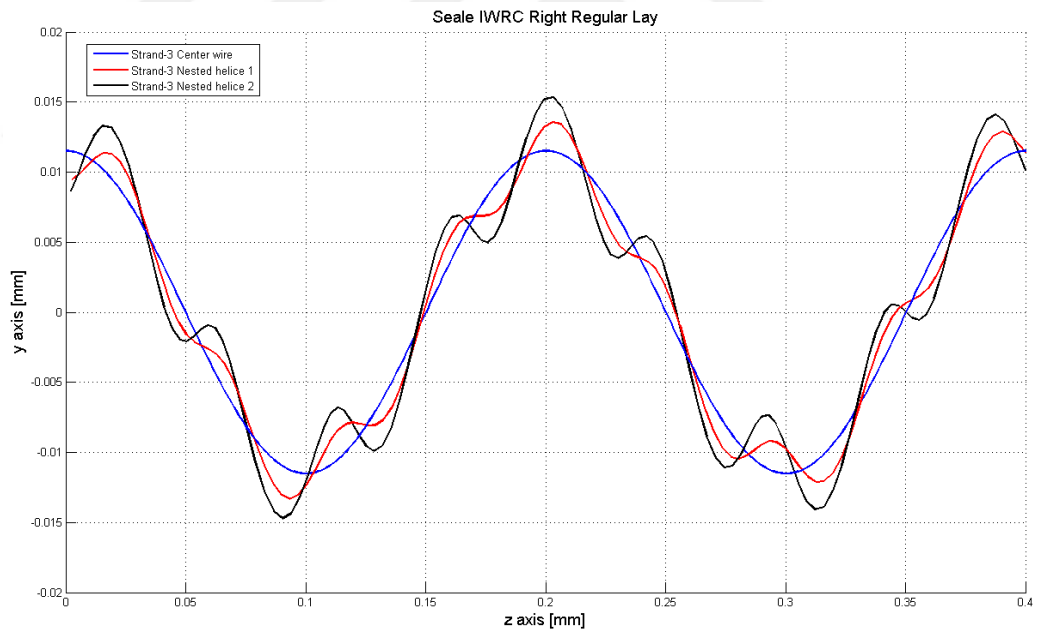
Figure 7.54: Paths of helical wire centerlines on 6x19 Seale IWRC for Strand #3.

Cross-sectional views of a 6x19 Seale IWRC for RRL and LRL types are presented in Figure 7.55.

163

(a) RRL   **(b)** LRL
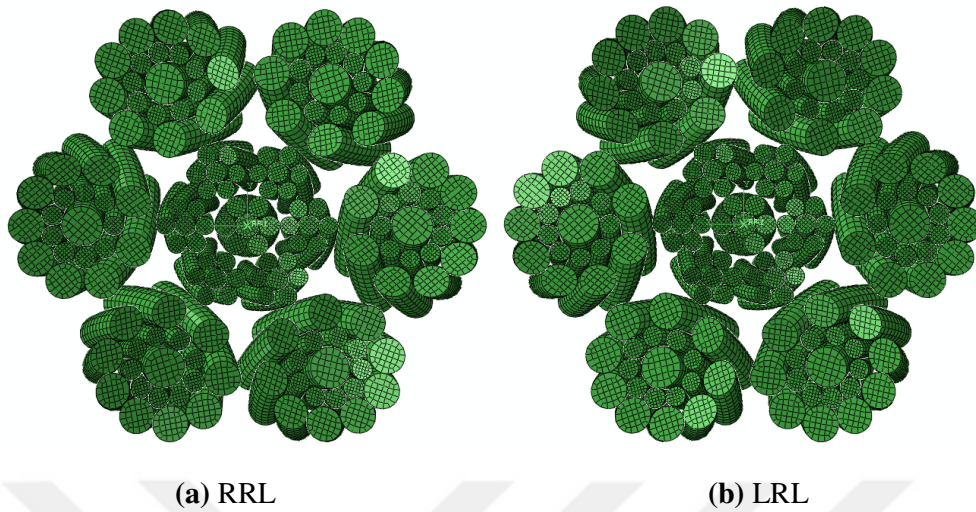
Figure 7.55: A 6x19 Seale IWRC cross sectional views.

For the FEA, one side of the 6x19 Seale IWRC is constraint with the encastre boundary condition as a fixed end, a displacement boundary condition is applied to the other side of the 6x19 Seale IWRC corresponding to a strain value of 0.015. Variation of reaction force with strain results for strands #1, #2 and #3 in wire-by-wire basis are presented in Figure 7.56, Figure 7.57 and Figure 7.58 respectively.
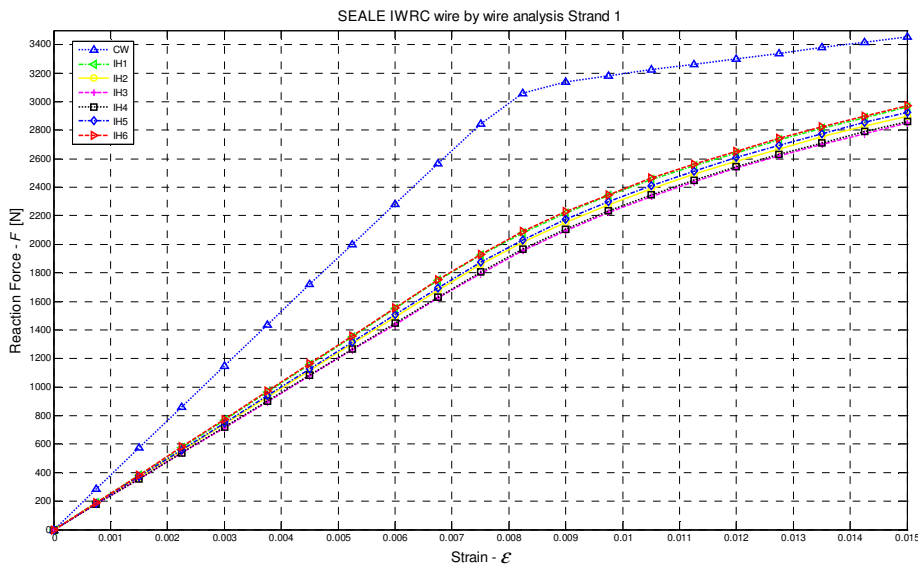
Figure 7.56: Variation of reaction force with strain, 6x19 Seale IWRC, Strand #1.
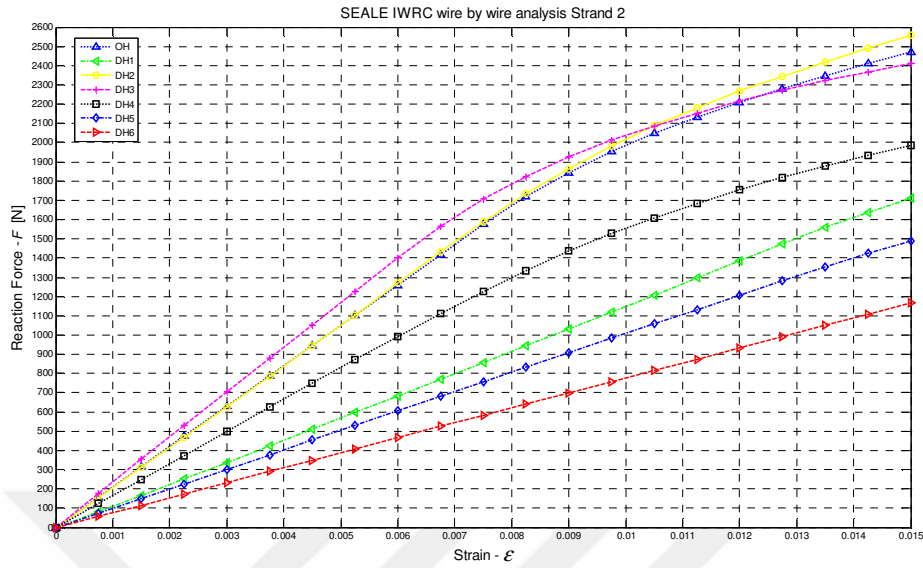
Figure 7.57: Variation of reaction force with strain, 6x19 Seale IWRC, Strand #2.
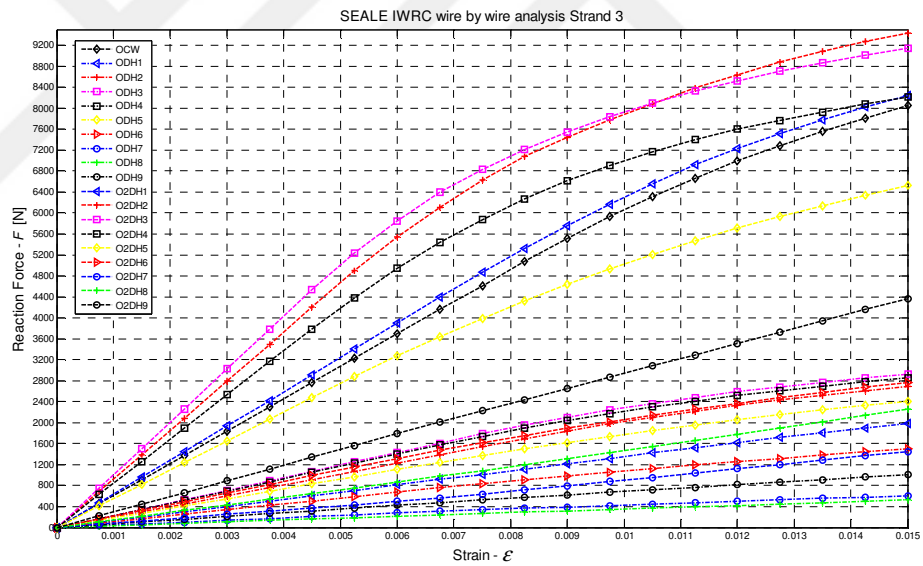
Figure 7.58: Variation of reaction force with strain, 6x19 Seale IWRC, Strand #3.

It can be seen from the Figure 7.56 that core wire W_0 of strand #1 is loaded with the maximum axial force, while outer wires in the same strand are loaded in similar manner. For the strand #2, core wire is also loaded highly, but differs than the typical behavior of the outer strands of the IWRC as presented in Figure 7.57. Wires in the second layer of the Seale part which corresponds to the strand #3, are loaded with higher reaction force corresponding to the wires placed in the third layer. Possible reason for this difference is based on the wire radiuses and positions of second and third layer wires with respect to the core wire of the Seale part as shown in strand #3.

As a complicated wire rope model, a Seale IWRC is also shows similar behaviors during axial loading problem. Various analyses can be conducted over the Seale IWRC to see different behavior under dissimilar circumstances.

7.9   GUI implementations for wire rope model generation

Wire ropes needs special treatment to implement solid models because of the complex constructional difficulties included to create each individual wire. For the construction of a wire strand, only a simple straight wire and single helical wires are needed. However, more complex rope models such as a Seale IWRC needs several different type of wires within the model. For a Seale IWRC; straight wire, single helical wire, double or nested helical wire are necessarily needed while rotation of a wire with respect to the others should be considered within a strand. In addition, for each wire within a wire rope, proposed solid modeling algorithm defined in Figure 6.9 needs to be followed in a systematic way. The first step of this algorithm consists of geometry generation and ir becomes a little bit cumbersome issue for complex wire ropes such as Seale IWRC. Model generation part of the analysis is considered to be time consuming and two graphical user interfaces are developed. First one is named as Wire Rope Skeleton (WRS) and the second one which is rely on the WRS is called as Wire Rope Model & Mesh Generator (WRMMG). Brief introductions of these two GUI implementations are given in the following parts.

7.9.1   Wire Rope Skeleton (WRS) GUI code

Seperately written code files corresponding to produce temporary nodes necessary to build individual wire centerline are gothered on WRS GUI code. To generate one of the wire centerline using this code one has to enter necessary wire radiuses and helix pitch lengths of the wire rope geometry at the beginning of the process. User also defines wire rope length. After these parameters are entered, user is responsible to choose the correct wire and wire rope type using the popup menus. At present WRS is designed to build wire rope geometry of a WS, an IWRC and a 6x19 Seale IWRC. The user also can select lay types during this process. To complete the generation of the wire centerline nodes user should select one of the wire rope types available. As a result, a file is produced including the locations of the centerline of the wire geometry in 3-D space. This file is imported using HyperMesh and the same

166

procedure explained widely in the algorithm defined in Figure 6.9 is applied starting from the solid part and mesh generation module. To this point, WRS GUI implementation makes it easy to generate temporary nodes required to construct a solid wire. It reduces time need for the geometry generation process and user interferance requirement is removed.

The interfacing GUI code main screen is presented in Figure 7.59. It is coded to be user friendly and produced wire centerline and Frenet-Serret triad is shown in its main screen as depicted in Figure 7.60.
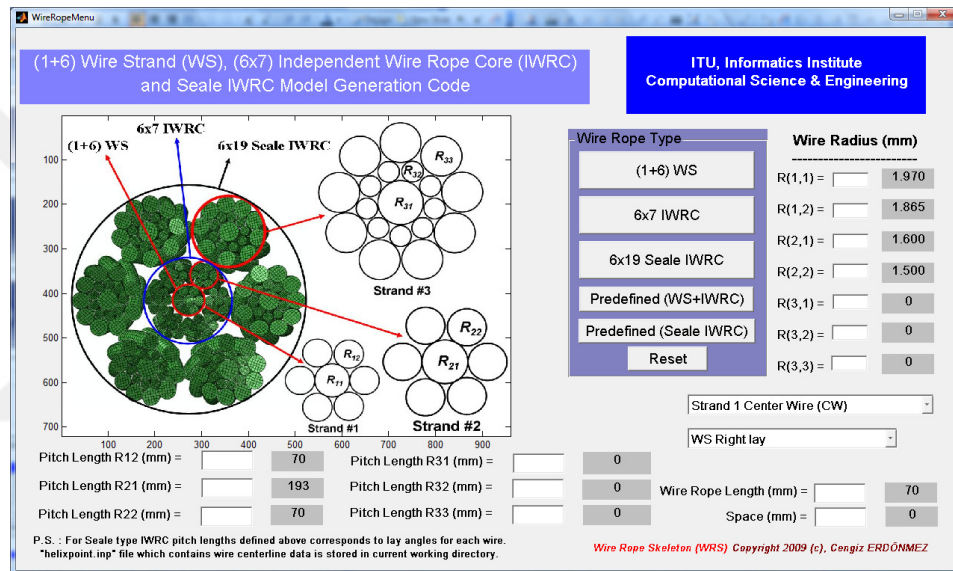
Figure 7.59: Wire Rope Skeleton GUI code user interface screen.
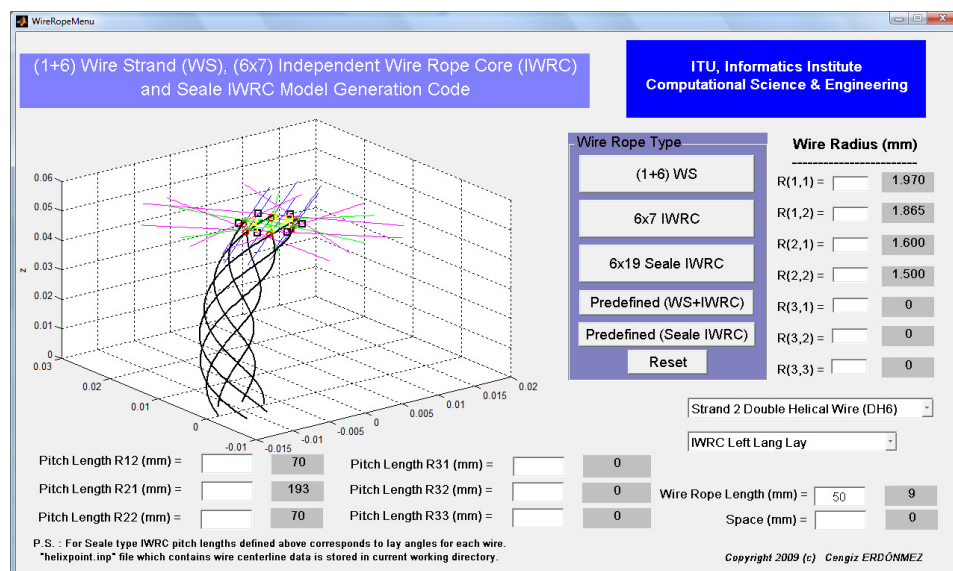
Figure 7.60: Wire Rope Skeleton GUI screen after geometry generation.

167

7.9.2   Wire Rope Model and Mesh Generator (WRMMG) GUI code

WRMMG GUI code is based on the precedessor WRS GUI code. The geometry and mesh generation process is done by the code automatically and a model file is generated ready to use for analysis. User has the responsibility to define the parameters of the wire rope to be modeled. A geometry generation process is simulation screen shot is presented in Figure 7.61. A wire strand model generated by using WRMMG is imported using Abaqus/CAE and presented in Figure 7.62.

With this new GUI code, any user interference during model and mesh generation stages are prevented by the code. Different from the WRS, this GUI code does the meshing of the wires and assembles them to generate the model automatically without usage of mesh generator such as HyperMesh. From this point of view, WRMMG GUI code solves the model generation problem with a practical approach. Mesh refinement is also possible using this GUI code. In addition, WRMMG code has improved with a tool, which gives user a very usefull data necessarily used at production level. This tool computes the wire lengths required to produce a wire rope according to the wire rope type. Depending of the wire type lengths of the wires are computed. As an illustrative example, 1*m* length 6x19 Seale IWRC wire lengths are computed with the prescribed radiuses and wire lengths are presented in Table 7.12. The capability of defining wire lengths reduces the production time costs of the producers. From this point of view, one can compute necessary lengths for each wire at the production time and arrange the production process according to these datas.
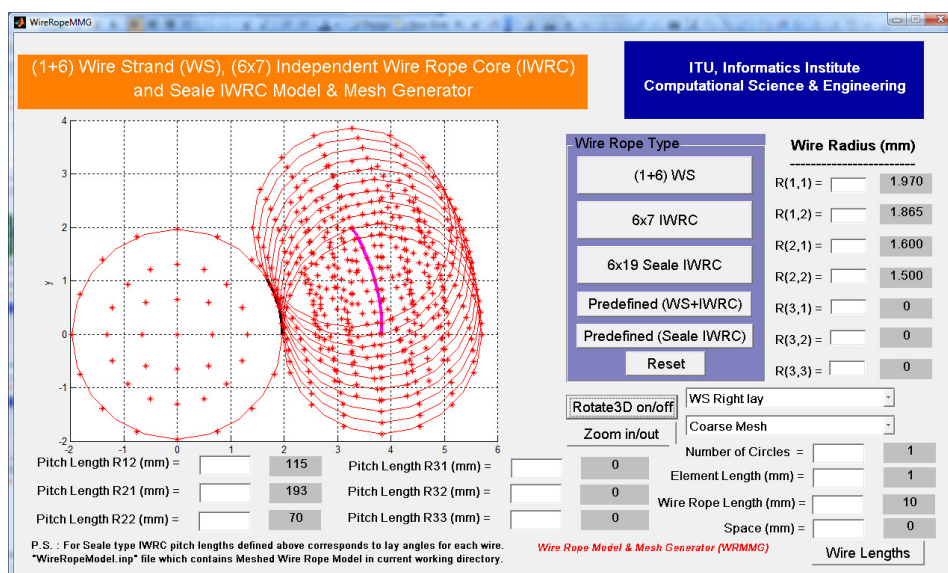
Figure 7.61: WRMMG GUI code screen shot.

168
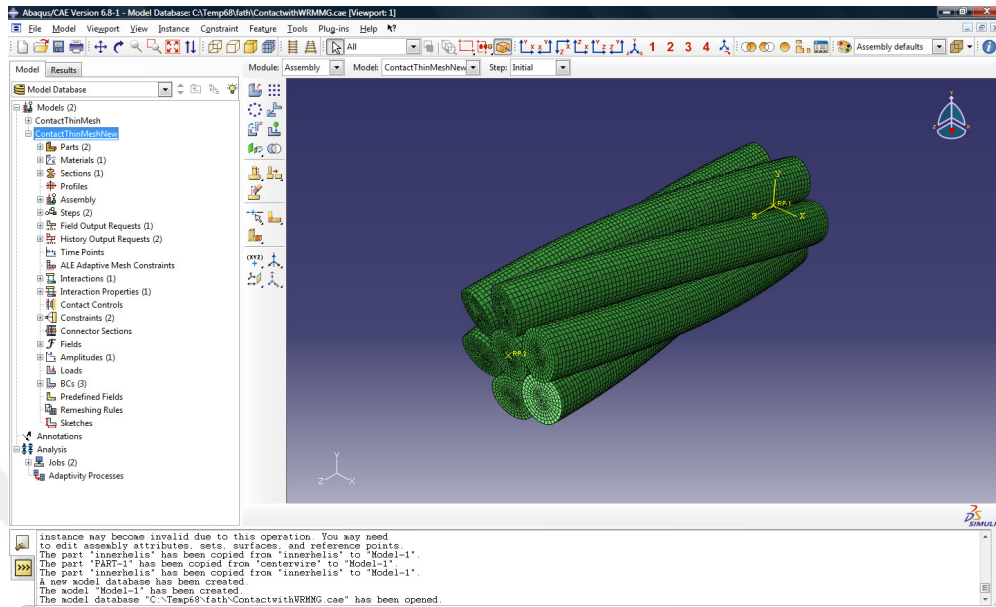
Figure 7.62: A wire strand model created using WRMMG GUI code.

Table 7.12: Wire length computation for a 1000*m* Seale IWRC.

Wire title	Wire radius (*mm*)	Pitch Length (*degree*)	Length of Wire (*m*)	Total Wire length needed (*m*)
CW	0.8014	0.00	1000.00	1000.00
IH	0.7347	73.71	1041.84	6251.02
OCW	0.7042	70.83	1064.66	6387.99
ODH	0.6557	81.07	1083.95	39022.29
SOCW	1.4557	70.24	1062.57	6375.45
SDH1	0.7125	102.27	1092.69	59005.11
SDH2	1.2682	111.23	1156.26	62437.81

7.10 Contact analysis of a simple straight strand

Center wire radius of a wire strand is chosen sufficiently such that to prevent outer wires touching each other. This is the general aim to decrease frictional effects due to bending of the strand. Outer wires of a simple straight strand are in contact with only the center wire at the initial position as shown in Figure 7.63. This phenomenon produces a line of contact between the center and outer wires of a strand which is a single helical contact line as presented in Figure 7.64. Using the design parameters defined in Table 7.1, a wire strand solid model is created. Strand length is selected, enough to guarantee contacts between center and outer wires of the strand, to be quarter of the pitch length of the strand as 28.75*mm*. Boundary conditions are defined

as in Figure 7.64; one side is constrained to be encastre (fixed end) while the other side is constrained for rotation along the *z*-axes (free end).
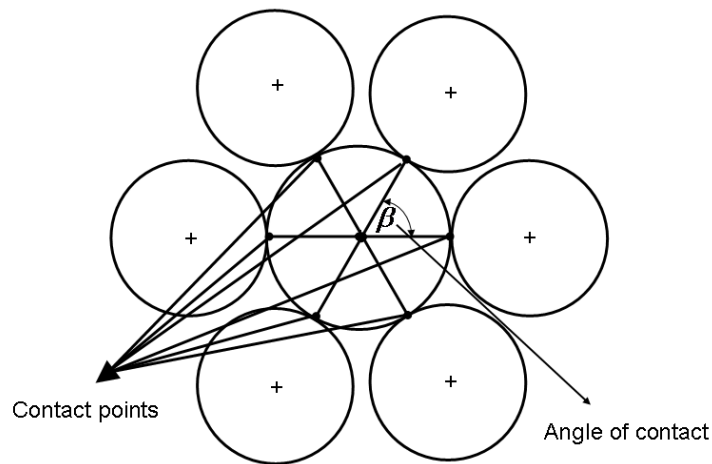
Figure 7.63: Contact points over the cross sectional view of a straight strand.

Surface to surface contact interactions between center and six outer single helical wires and between six helical wires are defined individually. During the numerical FEA, tangential and normal contact properties are defined. Contact property of tangential behavior with penalty frictional formulation is used with friction coefficient of $\mu = 0.115$, defined as in Table 7.1.
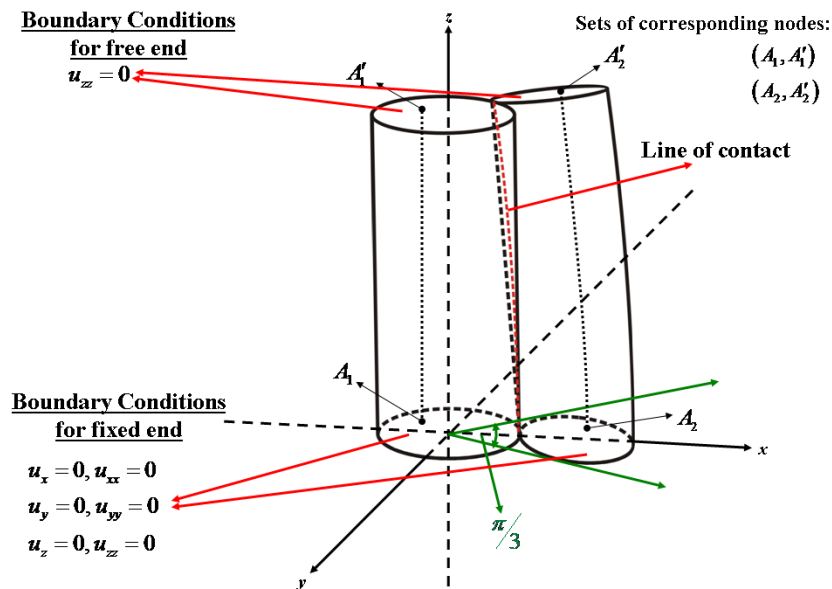
Figure 7.64: Helical line of contact and applied boundary conditions.

Contact property of normal behavior with "hard contact" pressure-over closure is defined as the second interaction property. During the numerical analysis, a strain of $\varepsilon = 0.015$ is applied to the free end of the strand. FEA results for different contact modes; without contact, with tangential contact and with tangential/normal contact interactions are analyzed and results are presented in Figure 7.65. As it can be seen from the Figure 7.65 that FEA result without the contact definitions gives slightly lower axial force variation with strain. Tangential and normal contact interaction definitions gives harmonious result with the test result of Utting&Jones by keeping the elastic-plastic properties of the wire material. This behavior of the contact interactions shows the validity of the proposed FEA model with contact definitions.
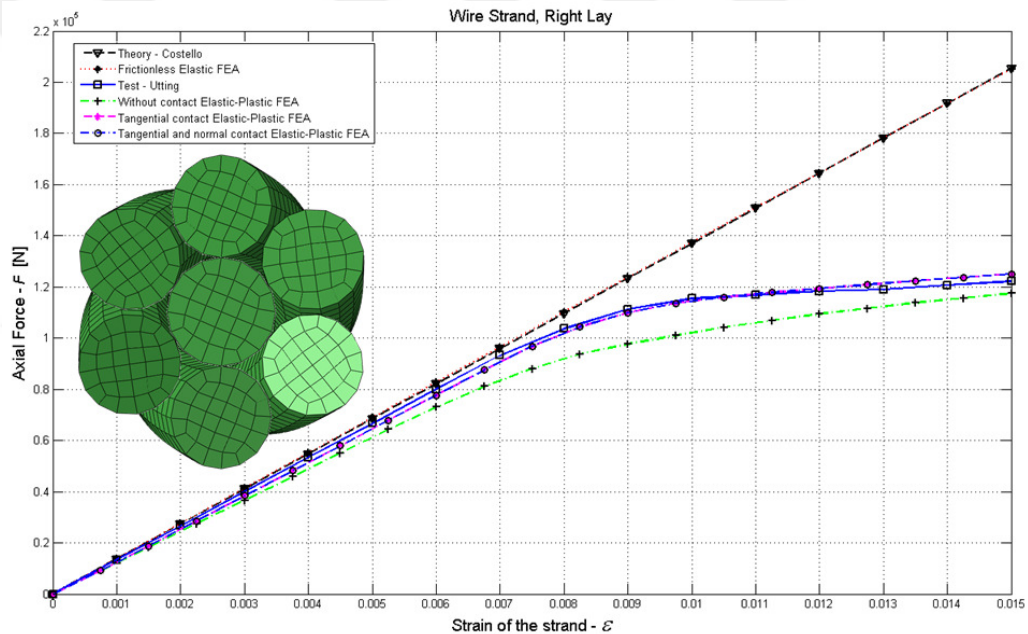
Figure 7.65: Axial force variation with strain comparison of a wire strand FEA results; with and without contact interactions.

Line of contact between center and outer single helical wires can be easily seen from the contour plot of the wires given in Figure 7.66. Fine mesh is used for the contact analysis presented here to see the interactions between wires and line of contact between core and outer wires shown in Figure 7.66. Total number of nodes used is 213690, while the total number of linear hexahedral elements of type C3D8R used is 196524, to model the contact behavior of the simple straight strand.
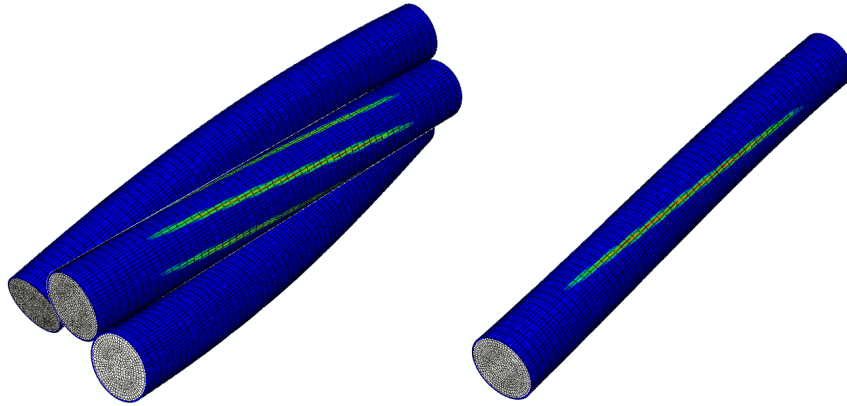
Figure 7.66: Line of contact over center and outer helical wires.

Contact and deformation between wires over a strand cross section is shown in Figure 7.67, which validates the preceding contact points shown in Figure 7.63.
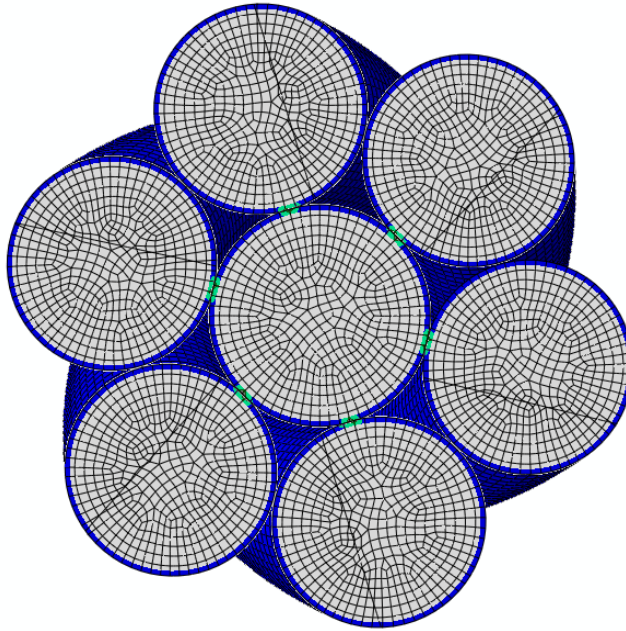
Figure 7.67: Cross sectional view of a contacting area.

An exaggerated representation of Figure 7.67 is presented in Figure 7.68. From this figure, deformations between wires within a wire strand can be clearly seen. There are 477 numbers of elements present in each wire cross section and 196524 elements exist in the whole model. Element length is defined to be 0.5*mm* for each wire along the wire strand. Increasing the mesh size makes it possible to clearly understand the deformations at the contact points.
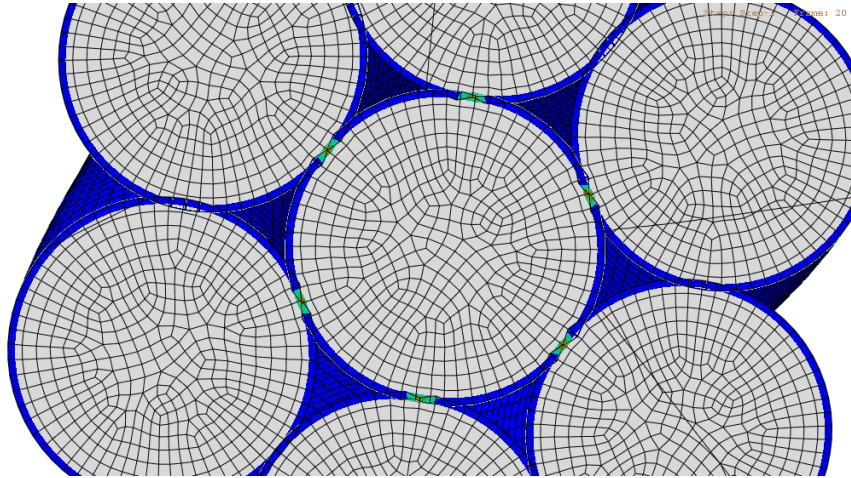
Figure 7.68: Cross sectional view of a contacting area.

Contact forces between wires are presented in Figure 7.69, contact pressure between wires are given in Figure 7.70 and wire stresses for each wire are given in Figure 7.71. These figures give insight about wire-by-wire behavior of individual wire along the wire strand.
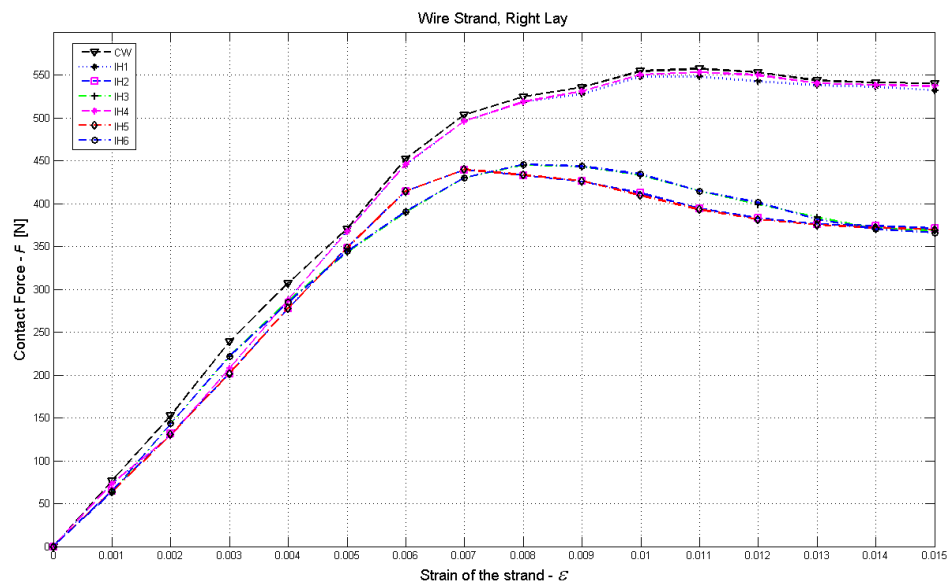
Figure 7.69: Contact force variation with strain of a simple straight strand.
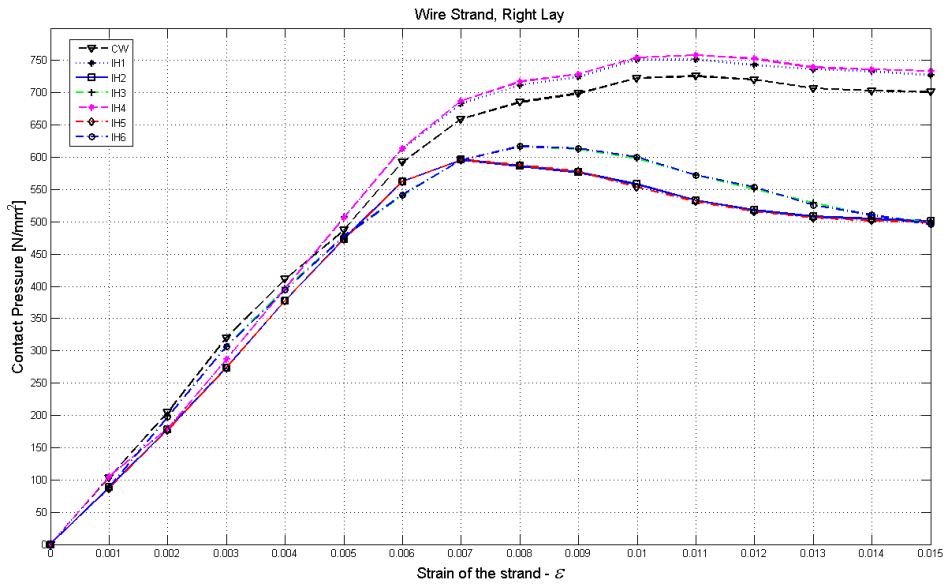
Figure 7.70: Contact pressure variation with strain of a simple straight strand.
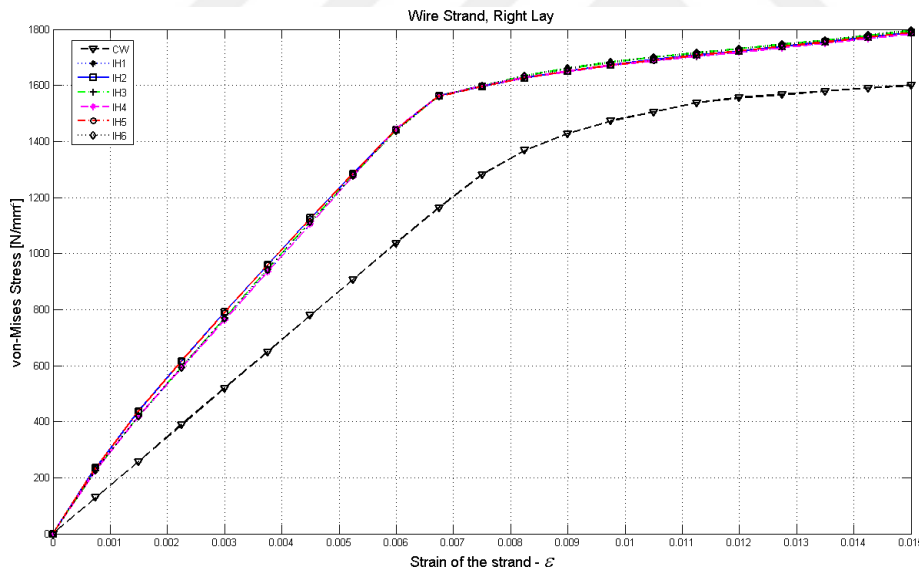
Figure 7.71: Stress variation with strain over wires of a simple straight strand considering contact interactions.

Variation of center wire diameter and helical wire diameter with strain are given in Figure 7.72. Diameters of the center and outer helical wires are reduced 1.16% and 0.92% respectively. This shows that while the wires are elongated, reduction occurs in wire diameters due to axial loading. As the center wire is loaded with the higher amount of total load, also the center wire diameter reduces more than the outer wires

in a strand. Wire diameter reduction for center wire and helical wire is computed as 2.1% and 1.81% respectively and shown in Figure 7.73.
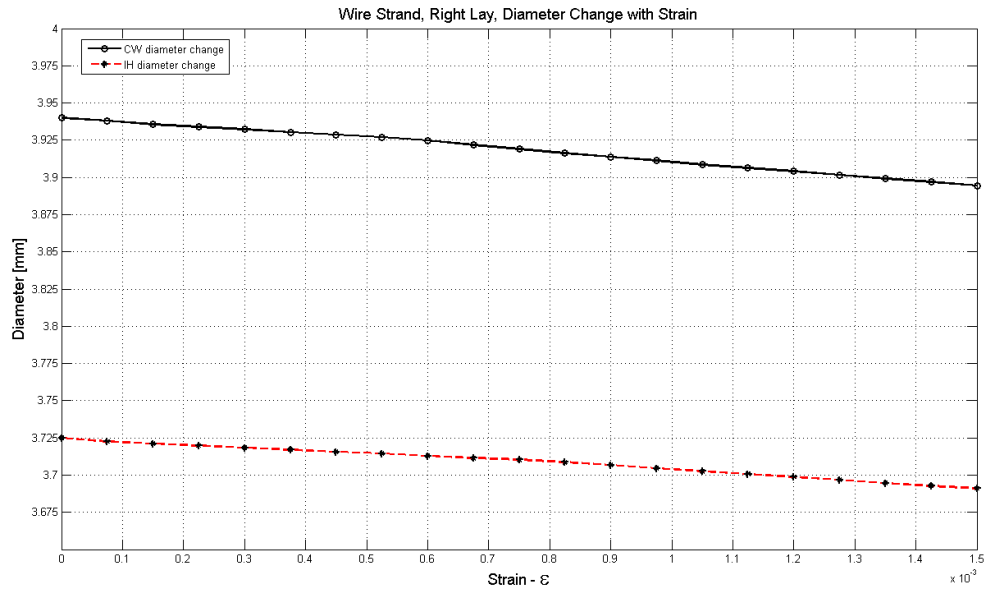
Figure 7.72: Wire diameter change with strain for a wire strand.
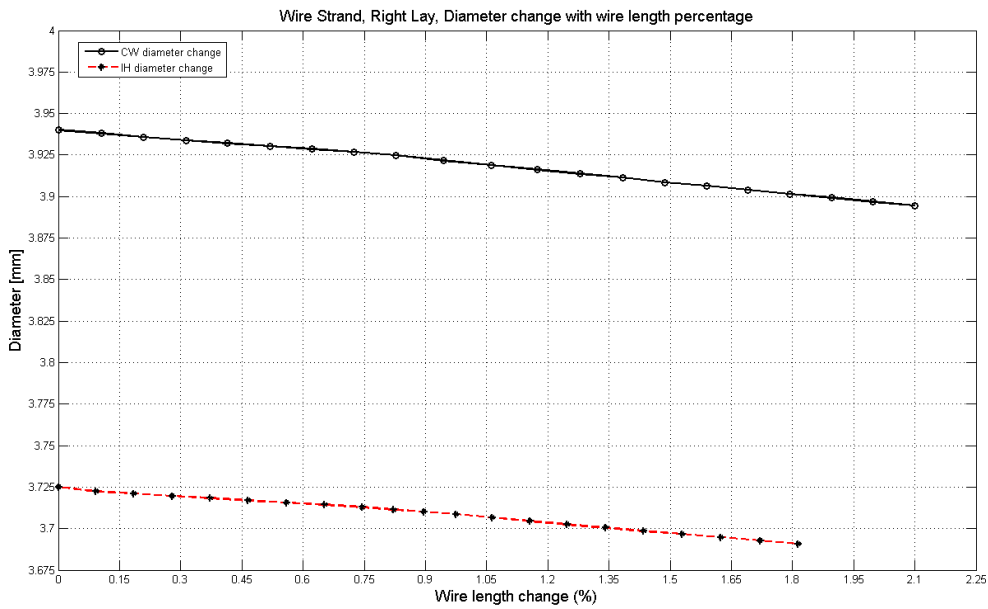
Figure 7.73: Wire diameter change with wire length change for a wire strand.

In this part of the analysis mesh sizes of the wire strand is increased and results for finer meshes are compared with coarser meshes. A 28.75*mm* simple straight wire strand model is used to investigate the importance of mesh size. Number of surface elements used on the cross section of a wire within a wire strand is presented on the first column of Table 7.13. Element lengths along a 28.75*mm* wire strand is defined

in decreasing order; 1*mm*, 0.5*mm* and 0.25*mm* respectively to generate finer meshes. von-Mises stress variation for strain value of 0.015 is compared for different mesh sizes and approximated error values are computed and listed in Table 7.13. von-Mises stress value for a wire strand with 0.25*mm* element length is accurately computed and the approximated error value of 0.004% is obtained as a result which shows the accuracy of the proposed model mesh size for FEA.

Table 7.13: Mesh sizes for a 28.75*mm* wire strand for various element lengths.

Number of elements on wire cross section	Element lengths along the wire strand					
	1*mm*		0.5*mm*		0.25*mm*	
	Number of Total Elements	Approx. Error (%)	Number of Total Elements	Approx. Error (%)	Number of Total Elements	Approx. Error (%)
32	6496	-	13184	-	26144	-
48	9744	2.1972	19776	1.0466	39216	0.0334
73	14819	0.8649	30076	0.4488	59641	0.0242
81	16443	0.7625	33372	0.3688	66177	0.0101
104	21112	0.4926	42848	0.1082	84968	0.0043

Variation of von-Mises stress and axial force with strain for element sizes of 1*mm*, 0.5*mm* and 0.25*mm* presented in Figure 7.74 and Figure 7.75 respectively. Both von-Mises stress distribution and axial force distribution converges while the quality of the wire strand mesh increased from total of 6496 elements to 84968 elements and approximated error value decreases to 2.19% to 0.0043% as presented in Table 7.13. As a result, it is enough to increase mesh size up to 104 elements on the cross section of a wire within a wire strand while the element length along the wire strand can be selected as 0.25*mm*. Increasing the mesh quality more than these values will increase the computational time and its benefit will be argued at that point. In addition, while the length of wire strand increased the mesh size should be carefully considered to control the computational difficulty of the problem for FEA.

(a) Element size = 1*mm*

(b) Element size = 0.5*mm*

(c) Element size = 0.25*mm*
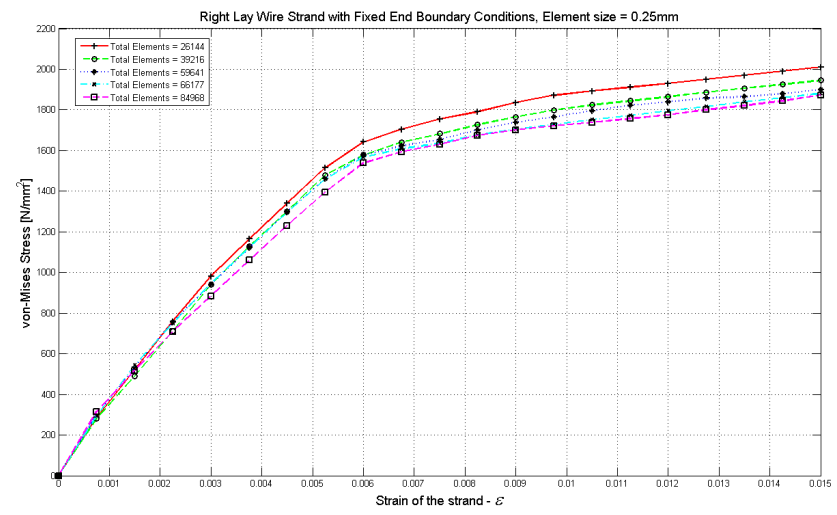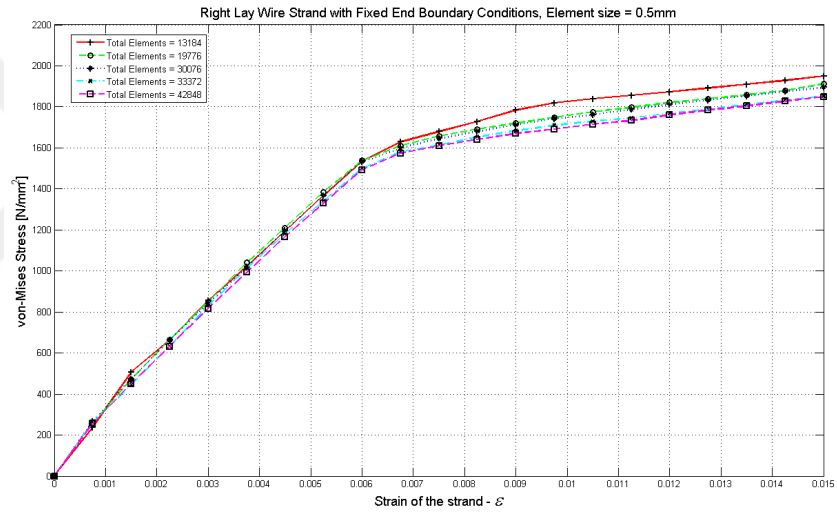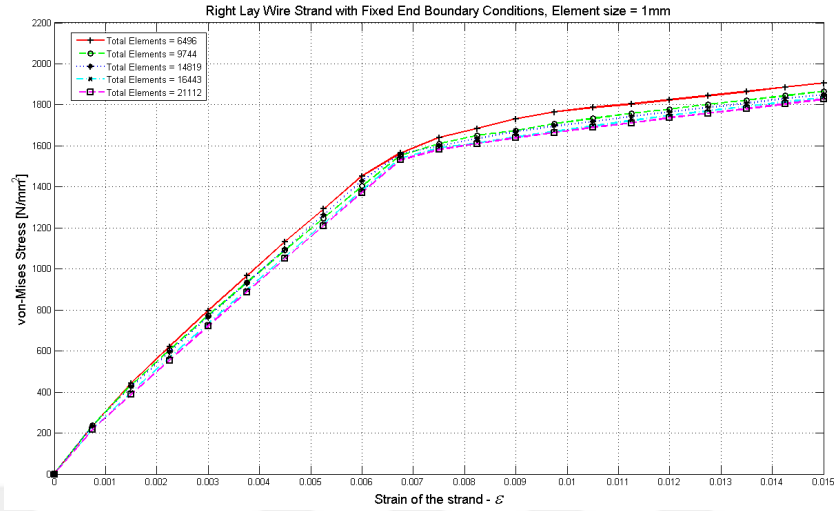
Figure 7.74: von-Mises stress variation with strain for a 28.75*mm* WS with element length=1*mm*, 0.5*mm* and 0.25*mm*.
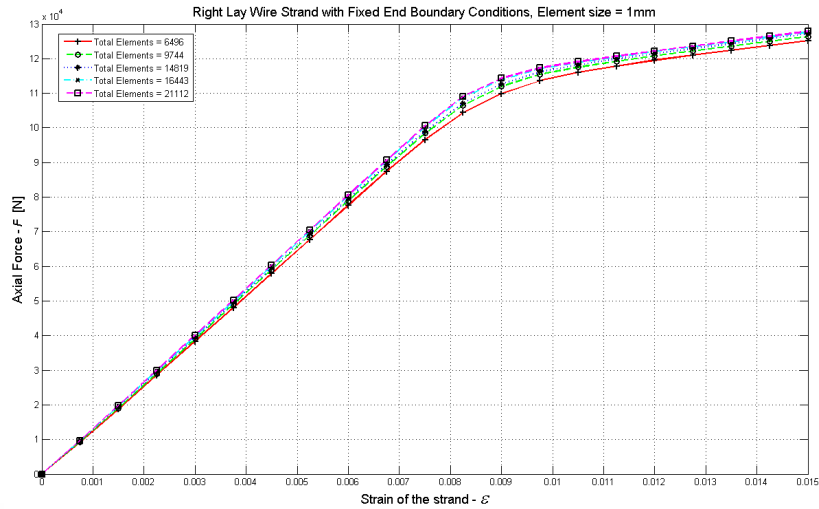
(a) Element size = 1*mm*
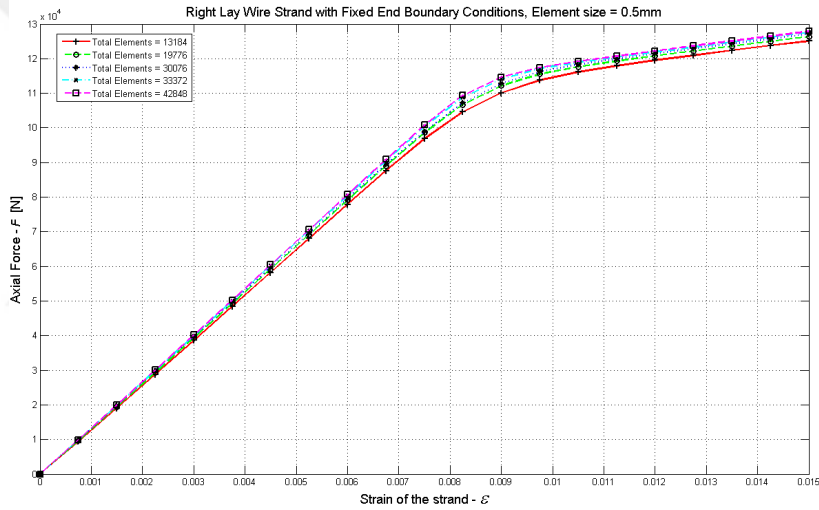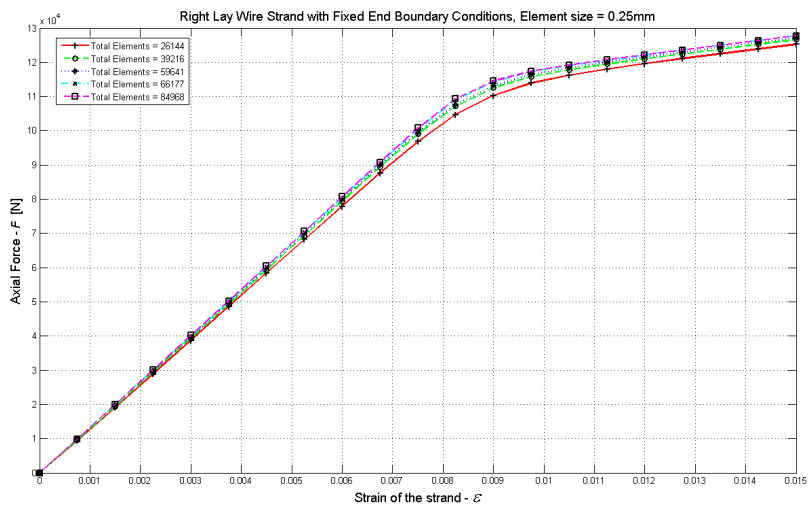
(b) Element size = 0.5*mm*

(c) Element size = 0.25*mm*

Figure 7.75: Axial force variation with strain for a 28.75*mm* WS with element length=1*mm*, 0.5*mm* and 0.25*mm.*

Comparison of von-Mises stress and axial force variation with strain for element sizes of 1*mm*, 0.5*mm* and 0.25*mm* with defining number of 104 elements in each wire cross section is presented in Figure 7.76 and Figure 7.77 respectively. As a result, it can be easily seen that total 84968 elements with element size of 0.25*mm* gives accurate results during the finite element analysis.
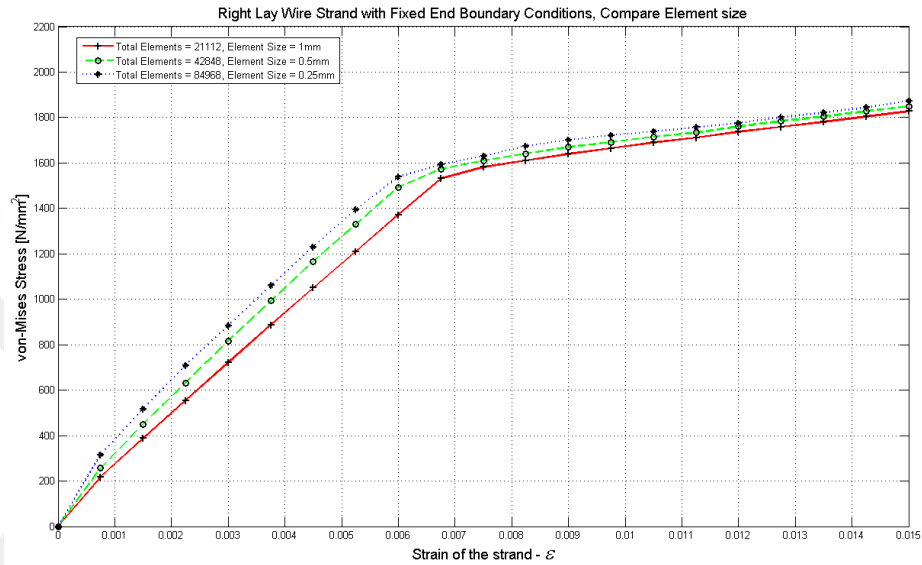
Figure 7.76: Comparison of von-Mises stress variation with strain for a 28.75*mm* WS with element lengths 1*mm*, 0.5*mm* and 0.25*mm*.
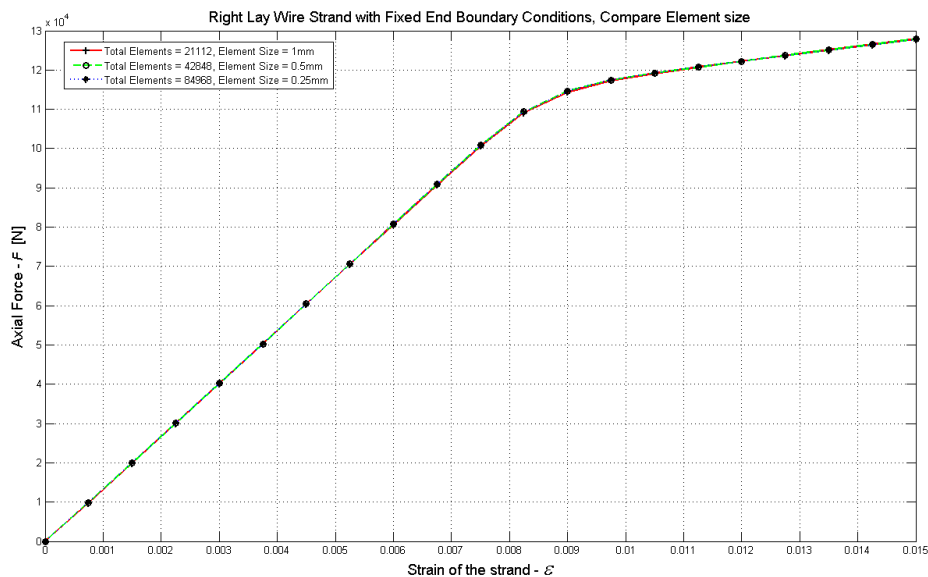
Figure 7.77: Comparison of axial force variation with strain for a 28.75*mm* WS with element lengths 1*mm*, 0.5*mm* and 0.25*mm*.

During the dynamic explicit FEA in Abaqus/CAE, process time is selected to be 1 second for the analysis. Solution time is increased to 3 and than 5 seconds

179

respectively to see the effect of solution time to the results. It can be seen from Figure 7.78 and Figure 7.79 both stress and force distributions are in good agreement while the solution time is increased. As a result, it is enough to use 1 second as the solution time for the dynamic explicit analysis.
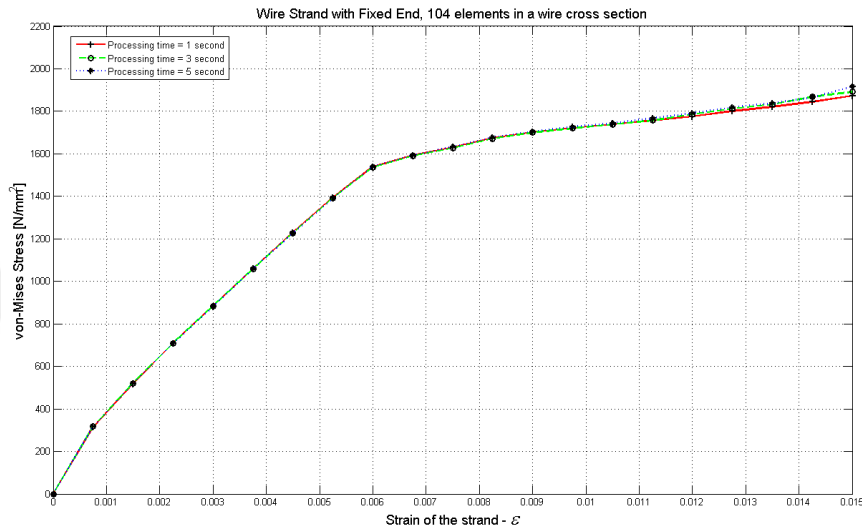
Figure 7.78: von-Mises stress variation with strain for dynamic explicit analysis with solution time 1, 3 and 5 seconds.
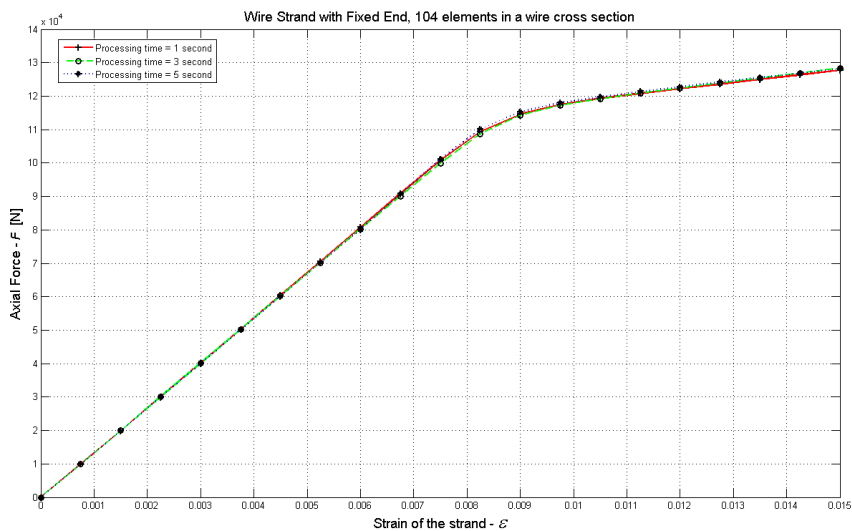
Figure 7.79: Axial force variation with strain for dynamic explicit analysis with solution time 1, 3 and 5 seconds.

7.11 Discussion on wire rope length effect

Because of the preceding proposed wire rope solid modeling method, it has been mentioned that it is possible to conduct FE analysis over long wire ropes. In this part $1m$ to $5m$ length wire strands are modeled and analyzed. Contact interactions are

defined over each individual wire as described before. Surface to surface contact with tangential and normal properties are proposed. Material properties are selected as in Table 7.1.

Surface-to-surface contact interactions between center and outer single helical wires, between six individual helical wires are defined. During the numerical FEA, tangential and normal contact properties are used. Contact property of tangential behavior with penalty frictional formulation is used with friction coefficient of $\mu = 0.115$, defined as in Table 7.1. Contact property of normal behavior with "hard contact" pressure-overclosure is defined as the second interaction property. Boundary conditions for wire strands are defined to be encastre condition to one end while the other side is constraint to rotate through *z*-axes. The cross sectional area of the wire strand is computed as $77.77mm^2$ and an axial load of 140000*N* is applied to the free end of the strand for the FEA. There are 32 elements in each wire cross sections and element lengths are selected to be 5*mm* along the wire strand. Number of nodes and elements defined over the wire strands are presented in Table 7.14. The analysis is conducted over 1*m*-5*m* wire strands using the prescribed boundary conditions and loads to see the behavior of long wires under these conditions. Stress distributions with distances for 1*m* to 5*m* strands are shown in Figure 7.80-Figure 7.84 respectively. It can be seen that stress is distributed along the wire strands and high oscillations along the stress distribution can be seen from the figures.

von-Mises stress distribution is homogeneous along 1*m* length wire strand for straight core wire and oscillates for outer helical wires along its length. von-Mises stress distributions are in sinusoidal manner because of the helical structures of the outer wires as shown in Figure 7.80. Similar stress distributions are presented for 2*m*-4*m* wire strands during their analysis in Figure 7.81 through Figure 7.83. When the 4m and 5m wire strands are examined given in Figure 7.83 and Figure 7.84 respectively, it can be seen that wire stresses are increased from one side to the other side stabilized at the end section. This behavior depends on the weight of the wire strand. Both core wire and outer helical wires von-Mises stress distribution shows similar behavior. It can be concluded from the present analysis that, to obtain correct stress distribution over a long wire rope whole model of the problem should be considered. In this way, necessary informations on any part of the wire rope can be obtained with confidence.

Table 7.14: Number of nodes and elements used in 1*m*-5*m* wire strand models.

Length	Total number of nodes	Total number of elements linear hexahedral elements of type C3D8R
1*m*	73,431	57,088
2*m*	120,745	94,016
3*m*	180,851	140,928
4*m*	241,203	188,032
5*m*	301,309	234,944

This analysis scheme gives insight about the behavior of long wire strands under the axial loading conditions. With this analysis, it has been shown that the proposed scheme can be applied to the long wire ropes. In this aspect, it is possible to model and analyze wire ropes without length limitation, which gives opportunity to establish real application models for wire ropes.
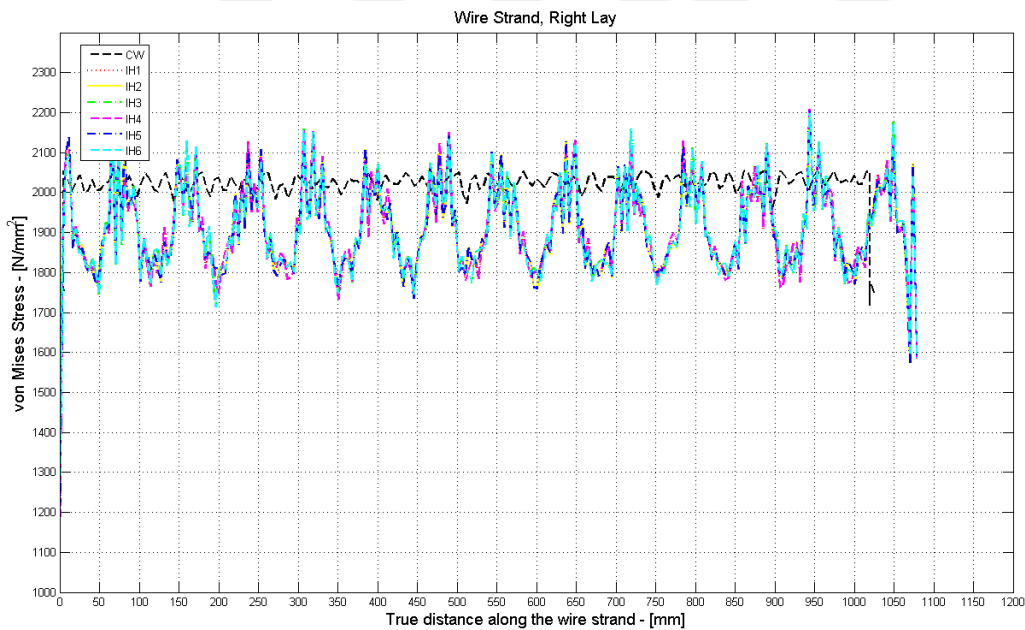
Figure 7.80: von-Mises stress variation with true distance for 1*m* wire strand.
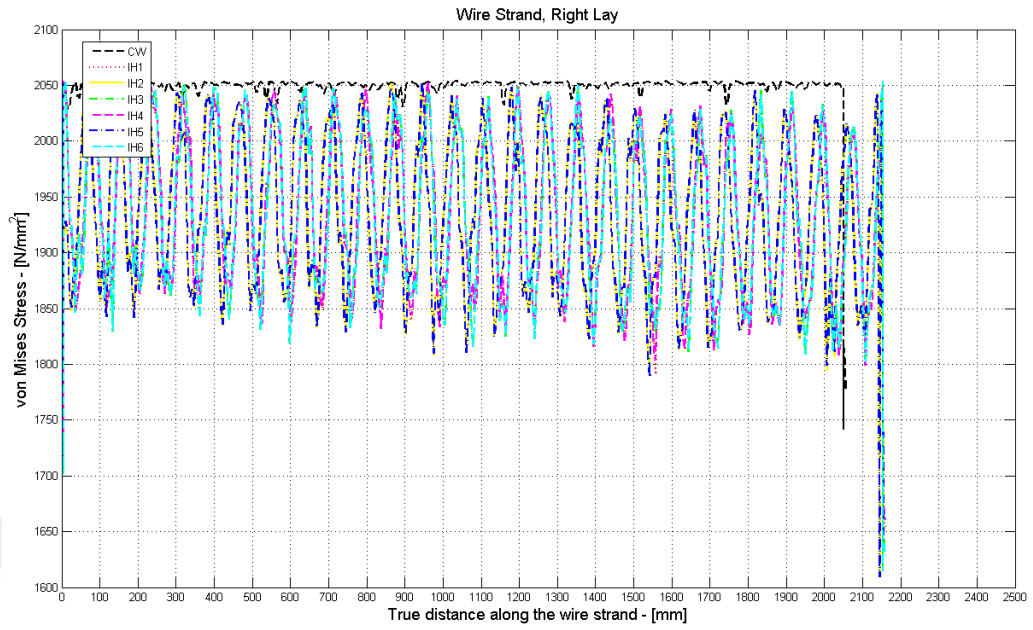
Figure 7.81: von-Mises stress variation with true distance for 2*m* wire strand.
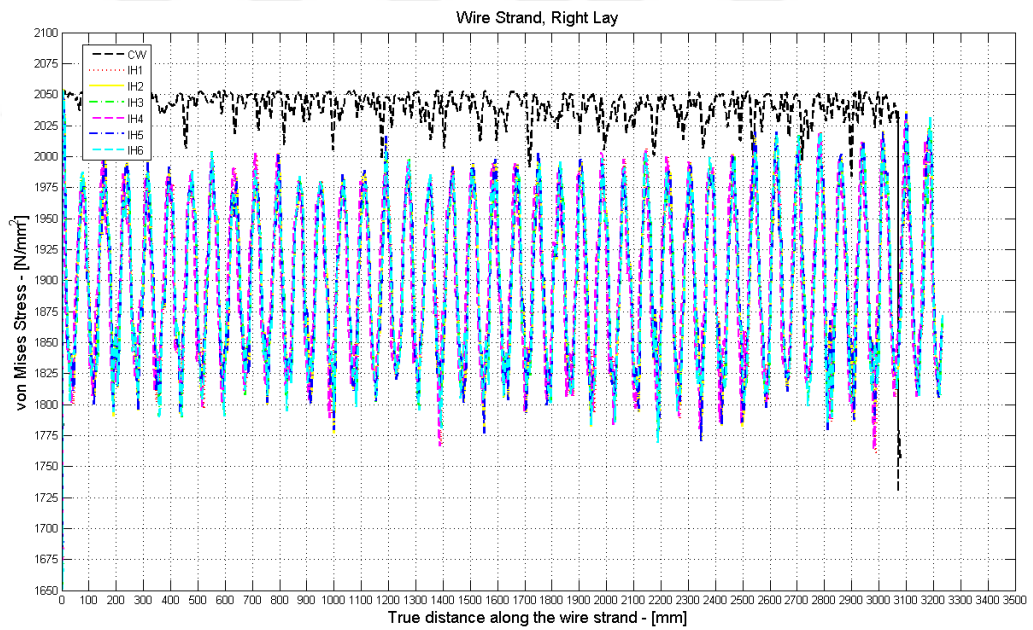
Figure 7.82: von-Mises stress variation with true distance for 3*m* wire strand.

183
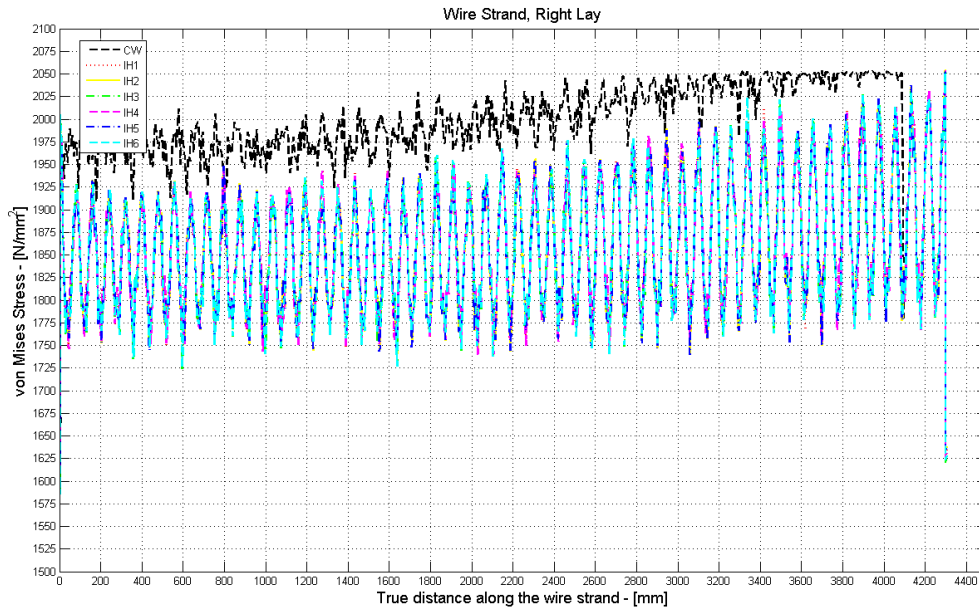
Figure 7.83: von-Mises stress variation with true distance for 4*m* wire strand.
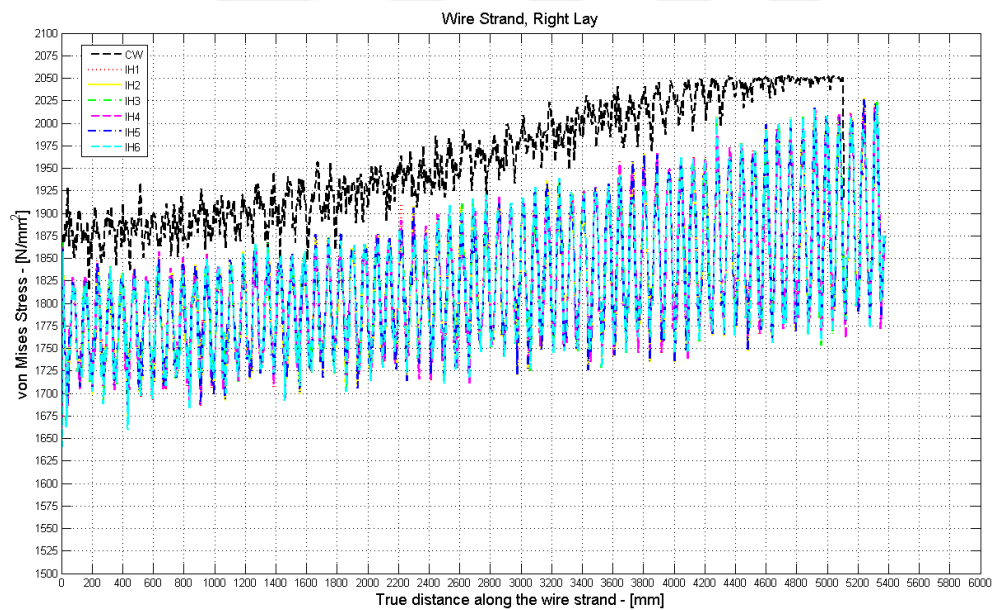
Figure 7.84: von-Mises stress variation with true distance for 5*m* wire strand.

Furthermore, when the stress distributions along 1*m*-5*m* length wire strands are considered, high oscillations are encountered and it is confusing to understand the general behavior of the wire strand clearly. To discard the oscillatory behavior, 1*m* length wire strand is analyzed for different helix pitch lengths and finer mesh sizes defined as in Table 7.15.

Table 7.15: Number of nodes and elements used to construct 1m wire strand.

Helix pitch lengths					
100mm		110mm		115mm	
Num. of Nodes	Num. of Elements	Num. of Nodes	Num. of Elements	Num. of Nodes	Num. of Elements
1,773,273	1,528,594	1,741,257	1,497,610	1,738,329	1,495,090

The analysis of 1m wire strand is conducted with the design parameters of a simple straight strand given in Table 7.1 and wire material properties is defined as in Table 7.3. Encastre boundary condition is applied on one side of the wire strand while the other side is constraint not to rotate in x, y and z directions. Axial strain of $\varepsilon = 0.008$ is applied to the free end of the strand. Variation of von-Mises stress with true distance for 1m Steel wire strand for helix pitch lengths of 100mm, 110mm, and 115mm are presented in Figure 7.85 respectively. To plot the stress distributions along the center and outer wires within strand nodes over the outer surfaces of individual wire is used and a path is generated. Helical path over the wire strand is defined and it is depicted at the bottom of Figure 7.85. These paths are used to probe values along the wire strand. For 1m length wire strand it can be seen from the Figure 7.85 that stress distribution over the center wire is still oscillating but in a much smoother manner while inner helical wire is oscillating with a period. To measure this period distance values belongs to the pick points are noted as in Table 7.16 and distances between consequtive pick points are computed. Average values for the distances of the pick points are listed below each column. From these average values, it can be seen that the oscillations are repeated approximately in every 106.5mm for 100mm pitch length wire strand, 116mm for 110mm pitch length wire strand and 120.14mm for 115mm pitch length wire strand respectively. Values of the oscillations show similar behavior and correlated with the pitch lengths of the wire strands.
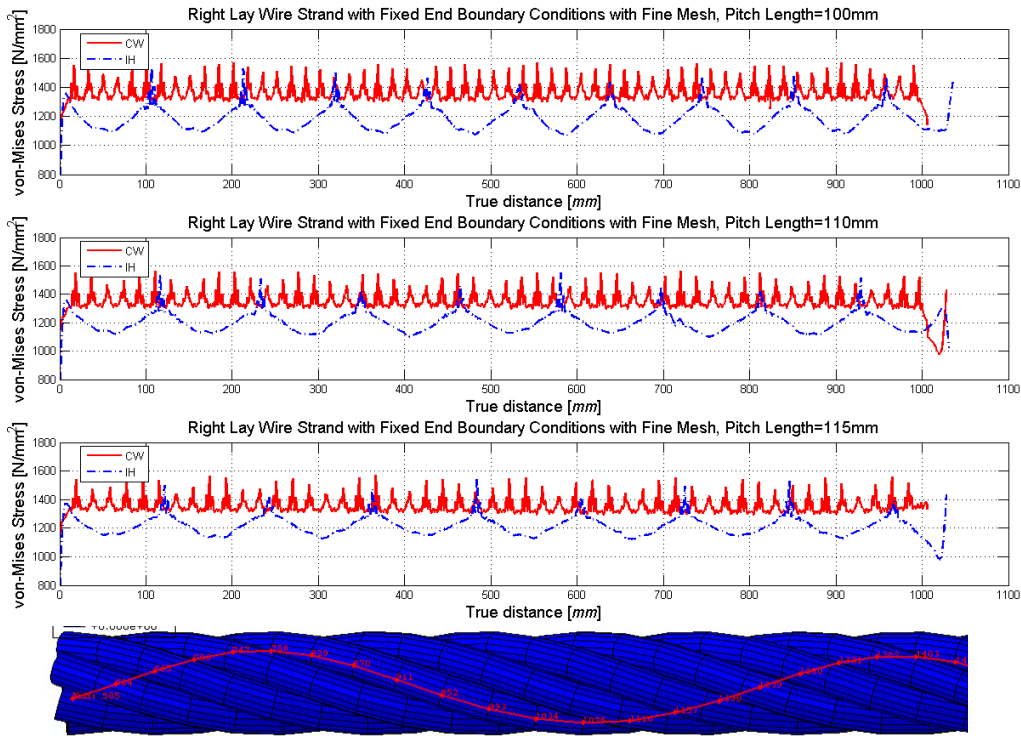
Figure 7.85: Variation of von-Mises stress with distance for 1*m* steel wire strand.

Table 7.16: Oscillation measure for helical wire along 1*m* steel wire strand.

Pick points along 100*mm* WS (*mm*)	Distance between pick points (*mm*)	Pick points along 110*mm* WS (*mm*)	Distance between pick points (*mm*)	Pick points along 115*mm* WS (*mm*)	Distance between pick points (*mm*)
106	—	116	—	124	—
212	106	233	117	242	118
319	107	349	116	361	119
426	107	464	115	483	122
532	106	580	116	604	121
638	106	697	117	724	120
744	106	812	115	846	122
851	107	928	116	965	119
958	107	—	—	—	—
Avarage distance (*mm*)	106.5	—	116.0	—	120.14
Percent (*mm*)	6.5%	—	5.5%	—	4.7%

A similar analysis for 1*m* aluminum wire strand with 115*mm* pitch length is investigated and the obtained results for wire strands with increased mesh sizes are presented in Figure 7.86. Material properties of the aluminum alloy are obtained

186

from [116]; density, elasticity and Poison's ratio are defined as 2.7e-9, 70000 and 0.33 respectively.
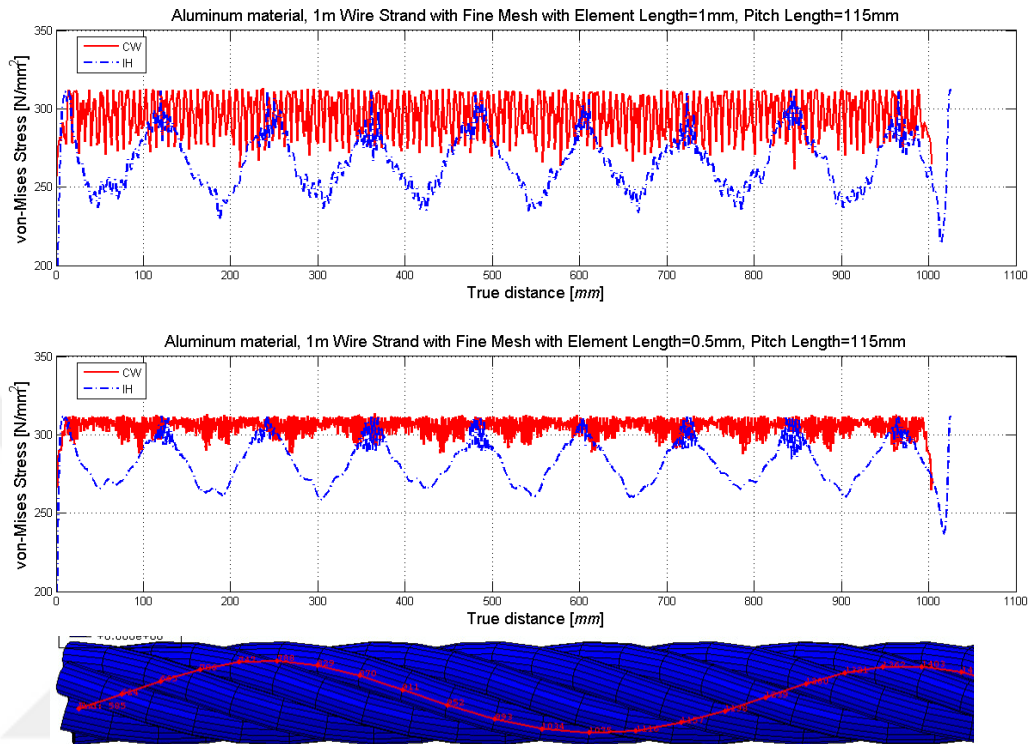
Figure 7.86: Variation of von-Mises stress with distance for 1*m* Aluminum wire strand.

For 1*m* aluminum wire strand with 115*mm* pitch length, it has been obtained that osciallation periods are increased extremely over the center straight wire. Hovewer oscillation over the helical wire is again in periodical manner as in steel wire strand and repeated in every 119.25*mm*. When compared with the steel wire strand with the same pitch length as presented in Figure 7.87, oscillation periods and oscillation distances are seen to be in good agreement for stell and aluminum wire strand models.
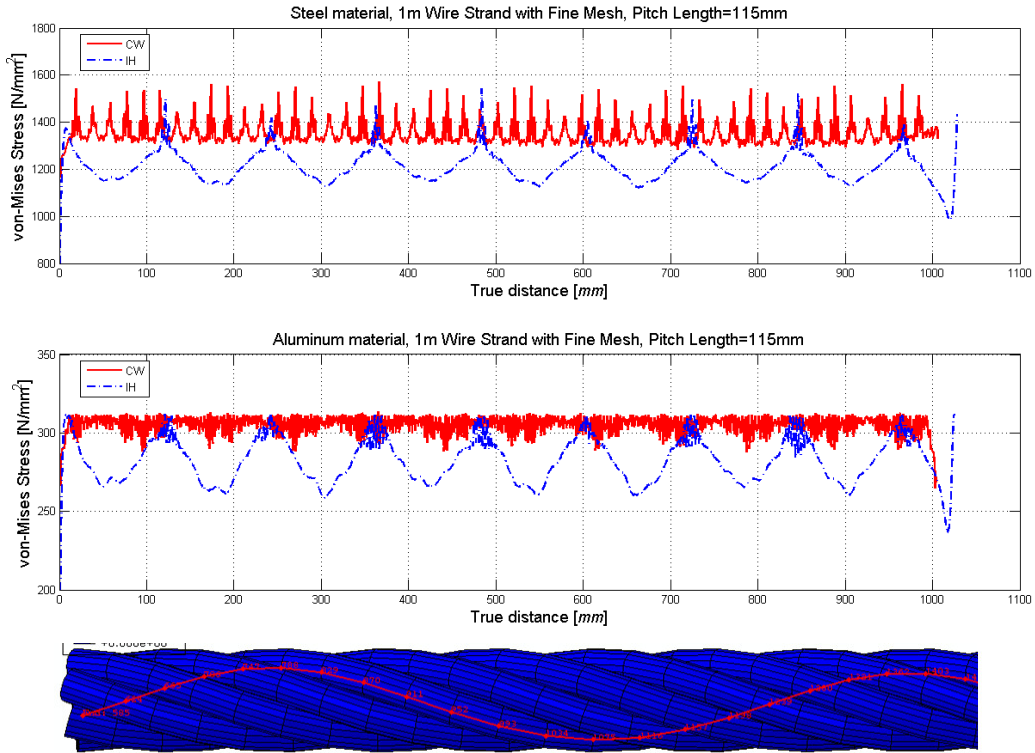
Figure 7.87: Variation of von-Mises stress with distance for 1*m* Steel and Aluminum wire strands.

8. CONCLUSION

In this thesis, a more realistic 3-D solid wire rope model is generated successfully and the finite element analysis is established by means of the generated models. Mainly three solid wire rope models are studied; a simple straight wire strand (WS), an independent wire rope core (IWRC) and a Seale IWRC. The main aims of this study are to model a 3-D solid wire rope without length limitations by using the parametric equations of the nested helical geometry, to analyze reaction force, stress distribution in wire-by-wire basis under different loading conditions, to model, and analyze bending problem defined over the solid wire rope models respectively. In addition, contact behavior of wire ropes are modeled and analyzed. By using the proposed modeling method, analysis of long wire ropes are conducted successfully.

At first using the rod theory deformations over a rod and relations with a helical spring investigated. The angular velocity and curvatures acting over a wire is derived using the loads and moments acting over a thin wire. Using the geometric consideration of a simple straight strand general behavior of a strand is presented. An analytical solution for axial loading problem is proved for the governing equilibrium equations with Mapple in a different way. Afterward, general analytical formulation of a wire rope is established using relation between axial loading and twisting moment.

Equilibrium equations for only bending moment is defined and proved using Mapple. Frictional effects over a strand are defined and static response of an IWRC is investigated. The relation between a sheave and an IWRC diameter is investigated for bending problem analytically. General theoretical formulation of an IWRC using the homogenization method is derived and presented.

Wire rope geometry modeling is a complicated issue because of the complex nature of the wires. (1+6) wire simple straight strand is composed by using a straight core wire, which is wrapped by six outer single helical wires. To construct a more complicated model, which is an IWRC, six strands are wrapped around a simple straight wire strand in helical manner. However, these six strands have a more

complex geometry then the simple straight strand. Core wires of these six strands are single helical shaped solid wires while the outer wires are nested helical shaped solid wires. That is why the outer nested helical wires need to be generated using special treatment. Parametric representations of these outer nested helical wires have to be used during the solid modeling process.

To make a realistic 3-D solid modeling of a complex wire strand/rope, it has been determined that there are problems while modeling single/nested helical solid wires. Definition of the nested helical wire and length limitation are encountered problems at first glance. There is no ready to use tools for defining a nested helical wire centerline in commercial CAD software's. A computer code is written to define control points of the centerline for each single and nested helical wires using Matlab. During the simple straight wire strand generation, a single helical wire wraps a straight wire. However, while an IWRC design, a nested helical wire is wrapped around a single helical wire. The angle of rotation between nested helical wires and single helical wires are in significant importance. This relation is carefully established via the written Matlab code to produce nested helical wires. The code is adapted to CAD software's by using the available macro script languages. At the end of this study, written codes are built to form two GUI codes called WRS and WRMMG respectively.

Length limitation is occurred while CAD software's used, because of the number of control points necessary to define the helical path of the wires. In fact, when the construction is done using the CAD software's such as SolidWorks, it seems that there is no problem with the construction of the wire geometry. When the wire geometry is exported to the analysis software such as Abaqus/CAE, the constructional problems are arised because of the control points used to define splines. When the length of the wire rope is increased, numbers of control points have to be increased also. However, analysis packages cannot capable of handling sweep operation accurately using these increased number of control points. This leads to unwanted and unusable geometrical shapes at the analysis stage. Meshing problems appears and solid model of the wire rope cannot be established at the beginning of the design stage. It has been concluded that the 3-D models constructed by using only the CAD software's capability, such as Solidworks or CATIA, can be used for finite element analysis approximately at a maximum length of 300*mm*.

When the length of wire strand/rope is increased beyond this, aforementioned problems are confronted. To overcome this difficulty two different procedures are tried. First, a pitch length of a helical wire is created by using parametric mathematical functions and splines. Then, number of revolutions has to be computed to construct a wire in its intended length. At the end, numbers of revolutions times pitch length of wires are connected by using tie constraints via the analysis tools. This scheme is conducted to construct such a long wires necessary to build wire ropes for the intended length. However, during the analysis stage it has been seen that there are oscillations in the results at the connection points. For this reason, this scheme is not adequate for the analysis.

Another procedure is investigated to overcome the length limitation problem. The second method is proposed to construct wires long enough at the modeling stage by using CAD software's, such as SolidWorks, and then meshing the solid part by a meshing tool, such as HyperMesh. By the way, using this procedure, wire ropes are built only for limited lengths that can be analyzed correctly. When the wire rope length is increased, meshing and analyzing problems are encountered again. Therefore, this strategy is also failed and abandoned.

At the end, using the generated Matlab code, control nodes are found for the centerline of the wires. Meanwhile three points are generated to construct a plane, which is intended to be perpendicular to the centerline of each wire. This plane is constructed by considering the Frenet-Serret triad. Control nodes for the centerline and three points for defining Frenet-Serret plane are exported to the HyperMesh by an interfacing code. A spline is created using the control nodes for defining the centerline of the wire. In addition, a circle is generated using the three points on the Frenet-Serret plane. This circle is swept along the centerline curve to produce solid mesh of the wire. Furthermore, generated solid meshed wires are exported to a file using Abaqus input file format. Each solid wire is imported in Abaqus/CAE to build the final 3-D wire rope model. The main contribution made here is to construct a solid wire rope model without length limitation and without any meshing problems. Wire rope model produced by using this last scheme generates ready to use meshed models, which can be used in finite element analysis. Using the proposed solid wire rope modeling scheme, an IWRC model for different lay types such as right lang lay, left lang lay, right regular lay and left regular lay can be constructed.

The benefit of the proposed solid wire-modeling scheme enables ones to construct a realistic 3-D solid model of a wire rope. This leads to analyze different types of wire ropes under prescribed conditions by using finite element codes easily. During the proposed modeling strategies, information about each wire within a wire rope can be obtained by means of wire-by-wire basis. As well maximum stress distribution over the wire strand/rope can be probed at the specified point for the specific wires.

In the numerical analysis chapter, finite element analyses are conducted on a simple straight wire strand, an IWRC and a Seale IWRC respectively. First, a simple straight wire strand model is analyzed under axial loading condition. Both frictionless and frictional behaviors are investigated while changing the helix angles between 65° and 84°. Wire strand behaves like parallel rods, for the helix angle higher than 84°. It can be seen that the change of the pitch length of the strand near to helix angle 65° minimizes, while the pitch lengths are dramatically increased after 78°.

An 14mm length, (1+6) wires, simple straight strand is considered under axial loading. Elastic frictionless and elastic-plastic frictional numerical models are developed. An axial strain ε of 0.015, was applied in increments of 0.001 in the analysis. The frictionless behavior of both theory of Costello and FEA results are in good agreement under axial loading conditions. The frictional plastic behavior of the strand is compared with the test results of Utting&Jones [12,13] given in the literature. Plastic behavior of the model is found to be in very good agreement with the test results.

An 18mm length, (6x7) wire IWRC of a three dimensional numerical model is considered. Elastic frictionless and elastic-plastic frictional numerical models are developed for different lay lengths. Axial strain of $\varepsilon = 0.015$ is applied to the free end of the IWRC. Especially for the case of pitch length $p_2 = 70$, very good agreement is obtained between theory and FEA results.

Wire radial contraction is analyzed over an IWRC for Poisson's ratio of v=0 and v=0.3. From the obtained results, it can be concluded that the wire contraction plays a very little role over the whole wire rope model analysis. Tensile forces obtained from the proposed model have a good agreement with Costello's results for both regular lay and lang lay rope constructions. However, twisting moments gives better agreement for regular lay construction than for the lang lay one when compared with

192

Costello's results. These analyses are conducted over a wire rope with the length of 9% pitch length. A wire-by-wire loading is investigated by the analysis of a right lang lay IWRC. The theoretical result of Costello and FEA results shows good agreement in wire-by-wire basis.

Using the same numerical models, forced torque is analyzed over the both simple straight strand and IWRC. Harmonious results are found for both models. In addition, elasto-plastic behaviors of the models are investigated under forced torque conditions.

By using the proposed modeling procedure, a 300*mm* length IWRC is modeled for each lay type and analyzed. In addition, the stress distributions over each lay type and wire-by-wire based reaction forces over fixed end are analyzed. An axial strain of 0.015 is applied to both an 18*mm* length and a 300*mm* length RLL IWRCs and reaction forces are compared in wire-by-wire basis. The proposed model enables one to analyze and see the differences of the reaction forces between small and long length IWRCs.

On the other hand, two different lengths of IWRCs are analyzed for bending problem, a 9*mm* and a 300*mm* lengths respectively. IWRC diameter and cross sectional area are 29.8*mm* and 380.48*mm²* respectively. According to the test standards, sheave diameter should be minimum 30 times the rope diameter. Sheave diameter is computed as 894*mm*. An IWRC is axially loaded in first step and then bent over the sheave with 90*mm* displacement boundary condition. Reaction forces over each strand are increased during the bending process after 72*mm* displacement is applied. Wire-by-wire basis analysis results shows that the core strand of the IWRC holds much more loads while bending over a sheave. Meanwhile the strands located near to the sheave are loaded more than the other strands beyond the wire rope composition. This numerical analysis gives information about the wires and strands, forced to bend over a sheave. In addition, using the benefits of the computer technology, parallelization of the wire rope problem is accomplished, and it has been seen that for a specific bending over a sheave problem, 16 CPUs is enough to conduct analysis for parallel execution.

In this thesis basis of the modeling and numerical analyzes are discussed. A more realistic 3-D solid wire rope model is developed. This study can be used as a guide to

model and analyze wire ropes under different loading conditions. Analytical solutions are available in the literature and can be used for comparison purposes. Numerical analysis scheme is clearly defined and can be modeled easily without any length limitation. Boundary conditions can be defined depending on the requirements, and new problems can be defined for further research purposes. Using the mentioned FEA procedures, simulations of special conditions or specific arrangements can be constructed and analyzed. The proposed scheme is used to model a more complex rope known as Seale IWRC. Numerical results are presented in wire-by-wire basis for each wire of a 6x19 Seale IWRC.

Wire rope modeling scheme defined during this study is used to develop two GUI implementations. First one is called as WRS and it is used to generate control nodes corresponding to the centerline of a specific wire. Using these control nodes, meshed solid wire geometry is constructed by using HyperMesh. Wire rope model generation process is completed by repeating the same procedure for each wire. Second one is called as WRMMG and it is an improved form of the WRS. The main difference is that the new GUI code generates the complete wire rope model automatically with a stand-alone manner. No user interference is needed and meshed wire rope assembly is generated readily with only defining the necessary wire parameters such as radius, pitch lengths and wire rope length. In addition, it has been improved with a tool, which computes wire lengths. This tool makes it easy to compute wire lengths necessary to produce a wire rope and reduces production costs.

Using the benefits of the proposed numerical model, contact interactions are defined and included in FEA analysis. Deformations between wires are obtained and wire radius reduction is computed. During the contact analysis, accuracy of the model is validated by using finer mesh definitions. The response of the problem, depending on the number of elements used, is considered. As a result, it has been obtained that accuracy of FEA results are improved by using finer meshes. It should be considered that while mesh size is increased computational complexity of the problem is also increased. During the dynamic explicit FEA in Abaqus/CAE, job processing time effect is investigated. Job process time is applied to be 1, 3 and 5 seconds. The analysis results are compared with each other and it has been obtained that 1 second is enough to use as job processing time. It should be emphasized that increasing job-processing time also increases the computational cost of the problem.

In addition, a wire rope construction without length limitation is accomplished by modeling and analyzing 1*m*-5*m* wire strands. von-Mises stress variation with true distance is presented in number of figures. It has been seen that there are number of oscillations along wire lengths, which confuses to understand the wire strand behavior correctly. To solve this problem finer mesh sizes are used for the analysis of long wire strands. Increasing the mesh size reduces the oscillations of the von-Mises distribution along the wire to a meaningful size. As a result, it has been obtained that the oscillation period is approximately 4.5%-6.5% larger than the helical wire pitch length. The analysis is repeated using aluminum material on the same wire strand model and the results are compared with steel wire rope. It has been concluded that the wire rope model with both material behaves in a similar manner. Pitch lengths are found to be effective over the stress oscillations along the wire strands. As a result, one of the most important issues of wire rope modeling and analysis without length limitation is accomplished accurately with obtaining detailed understanding of wire strand behavior.

Future studies can be conducted in special applications of wire ropes such as; reverse bending problems, cycling loading problems, fatigue analysis and wire rope fracture condition during bending problems can be studied by using the proposed numerical modeling method. Besides, a proposal for the service life expectancy can be studied with numerical analysis. Wire rope accidents can be modeled by using the damage processes as a future study. Wearing of wire ropes can also be another important application area of the numerical analysis of wire ropes. Non-rotational wire rope configuration can be investigated using finite element analysis as a future study also. In addition, by using the proposed solid modeling scheme, structures including nested helical shapes such as synthetic or nylon fibers can be modeled and analyzed.

REFERENCES

[1] **URL-1** CASAR: Drahtseilwerk Saar Company, *<http://www.casar.de>*, retrieved at 05.05.2006.

[2] **Schroeder, J.**, 1990. *Educational Package and Reference Library Vol 2*, An 1834 Invention, Essential to Our Industry, Elevator World Publication, pp: III-42:44.

[3] **Sayenga, D.,** 2006. Modern History of Wire Rope, *<http://www.atlantic-cable.com/Article/WireRope/Sayenga/wirerope4.htm>*, retrieved at June 11, 2006.

[4] **Costello, G.A., Miller R.E.,** 1979. Lay Effect of Wire Rope, *Journal of Engineering Mechanical Division*, **105** (No.EM4 paper 14753), 597-608.

[5] **Love, A.E.H.,** 1944. *A treatise on the mathematical theory of elasticity*, 4th ed., New York: Dover, 1944 Publications, First American printing 1944, Chapter XVIII-XIX, pp. 381-426.

[6] **Timoshenko, S.,** 1955. *Strength of materials*, New York: Van Nostrand, Vol.2, 292-299.

[7] **Green, A.E., Laws, N.,** 1966. A general theory of rods, *Proceedings of the Royal Society of London*, Series A, Mathematical and Physical Sciences, Vol. **293**, No. 1433, pp. 145-155.

[8] **Hruska, F.H.,** 1951. Calculation of stresses in wire ropes, *Wire and wire products*;**26**(9):766-767.

[9] **Hruska, F.H.,** 1952. Radial forces in wire ropes, *Wire and wire products*;**25**(5):459-463.

[10] **Hruska, F.H.,** 1953. Tangential forces in wire ropes, *Wire and wire products*;**28**(5):455-460.

[11] **Costello, G.A.,** 1990. *Theory of wire rope*. Berlin: Springer.

[12] **Utting, W.S., Jones, N.,** 1987. The response of wire rope strands to axial tensile loads: Part I. *International Journal of Mechanical Science*;**29**(9):605-19.

[13] **Utting, W.S., Jones, N.,** 1987. The response of wire rope strands to axial tensile loads: Part II. *International Journal of Mechanical Science*;**29**(9):621-36.

[14] **Carlson, A.D., Kasper, R.G.,** 1973. A structural analysis of multi-conductor cable. Report No. AD-767 963, *Naval underwater systems center*, distributed by National Technical Information Service.

[15] **Cutchins, M.A. et. al.**, 1987. Initial investigations into the damping characteristics of wire rope vibration isolators, *NASA (non Center*

Specific), NTRS: 2005-10-13, No: 87N20569; ID: 19870011136; NAS 1.26:180698, NASA-CR-180698.

[16] **Cochran, J.E. Jr., Fitz-Coy, N.G., Cutchins, M.A.,** 1987. Finite element models of wire rope for vibration analysis, *NASA Marshall Space Flight Center*, NTRS: 2007-06-26, Number: 87N22748; ID: 19870013315.

[17] **Chiang, Y.J.,** 1996. Characterizing simple stranded wire cables under axial loading. *Finite Elements in Analysis and Design*;**24**:49-66.

[18] **Raoof, M., Huang, Y.P.,** 1992. Free bending characteristics of axially preloaded spiral strands. *Journal of Strain Anal Engng Des*;**27**(4):219-26.

[19] **Velinsky, S.A.**, 1993. A stress based methodology for the design of wire rope systems, *Journal of Mechanical Design*; **115**:69-73.

[20] **Leech, C.M. et.al.,** 1993. Modelling tension and torque properties of fibre ropes and splices, *Proceeding of the Third International Offshore and Polar Engineering Conference Singapore*, 370-376.

[21] **Velinsky, S.A., Lembeck, M.F.,** 1990. Designing wire-rope-based mechanical systems in an expert system environment, *Engineering with Computers*;**6**:167-176.

[22] **Drucker, D.C., Tachau, H.,** 1945. A new design criterion for wire rope, *J. Appl. Mech.*;**67**,A33-A38.

[23] **Cardou, A., Jolicoeur, C.,** 1997. Mechanical models of helical strands, *ASME Reprint No AMR201, Appl Mech Rev,* vol **50**, no 1, 1-14.

[24] **Huang, N.C.,** 1978. Finite extension of an elastic strand with a central core, *Transactions of the ASME, Journal of Applied Mechanics*, Vol. **45**, 852-858.

[25] **Shield, C.K., Costello, G.A.,** 1994. The Effect of Wire Rope Mechanics on the Material Properties of Cord Composites: An Elasticity Approach, *Journal of Applied Mechanics, ASME*, Vol. **61**, 1-8.

[26] **Shield, C.K., Costello, G.A.,** 1994. The Effect of Wire Rope Mechanics on the Mechanical Response of Cord Composite Laminates: An Energy Approach, *Journal of Applied Mechanics, ASME,* Vol. **61**, 9-15.

[27] **Paris, A.J., Lin, C.C., Costello, G.A.,** 1992. Simple cord composites, Journal of the Engineering Mechanical Division, ASCE, Vol **118** (9), 1939-1948.

[28] **Velinsky, S.A.,** 2004. Compressive Loading of Stiffened, Wire-Strand Based Structures, *Mechanics Based Design Of Structures And Machines,* Vol. **32**, No. 1, pp. 101–113.

[29] **Shield, C.K., Costello, G.A.,** 1994. Bending Of Cord Composite Plates, *Journal of Engineering Mechanics,* Vol. **120**, No. 4.

[30] **Costello, G.A., Paris, A.J.,** 2003. Bending of Cord Composite Laminate Cylindrical Shells, *Transactions of the ASME, Journal of Applied Mechanics,* Vol. **70**, 364-373.

[31] **Costello, G.A., Paris, A.J.,** 2000. Bending of Cord Composite Cylindrical Shells, *Transactions of the ASME, Journal of Applied Mechanics,* Vol. **67**, 117-127.

[32] **Kumar, K., Botsis, J.,** 2001. Contact Stresses in Multilayered Strands Under Tension and Torsion, *Transactions of the ASME, Journal of Applied Mechanics,* Vol. **68**, 432-440.

[33] **Jiang, W.G., Yao, M.S., Walton, J.M.,** 1999. A concise finite element model for simple straight wire rope strand. *International Journal of Mechanical Sciences*;**41**:143-61.

[34] **Nawrocki, A., Labrosse, M.,** 2000. A finite element model for simple straight wire rope strands, *Computers and Structures* **77**, 345-359.

[35] **Knapp, R.H.,** 1979. Derivation of a new stiffness matrix for helically armoured cables considering tension and torsion, *International Journal for Numerical Methods in Engineering* **14**, pp. 515–520.

[36] **Velinsky, S.A.,** 1985. Analysis of Fiber-Core Wire Rope, *Transactions of the ASME*, *Journal of Energy Resources Technology*, September, Vol. **107**, 388-393.

[37] **Hoobs, R.E., Raoof, M.,** 1982. Interwire slippage and fatigue prediction in stranded cables for TLP tethers, in *Proc 3rd Int Conf Behavior Offshore Struct*, C Chryssostomidis and JJ Connor (eds), Hemisphere Publ/McGraw-Hill, New York, 77-99.

[38] **Raoof, M., Hobbs, R.E.,** 1984. Bending of spiral strand and armored cables close to terminations, *Journal of Energy Resources Technology*, September Vol. **106**, 349-355.

[39] **Raoof, M., Hobbs, R.E.,** 1988. Analysis of multilayered structural strands, *Journal of engineering Mechanics,* **114**, (7), pp. 1166–1182.

[40] **Raoof, M.,** 1990. Free Bending of Spiral Strands, *Journal of Engineering Mechanics*, Vol. **116**, No. 3, March, pp. 512-530.

[41] **Raoof, M.,** 1991. Method for analyzing large spiral strands, *Journal of Strain Analysis* **26**, (3), pp. 165–174.

[42] **Raoof, M., Kraincanic, I.,** 1995. Analysis of large diameter steel ropes. *Journal of Engineering Mechanics;***121** (6), 667–675.

[43] **Jolicoeur, C., Cardou, A.,** 1996. Semicontinuous mathematical model for bending of multilayered wire strands, *Journal of engineering Mechanics*, **122** (7), 643–650.

[44] **Jolicoeur, C., Cardou, A.,** 1994. Analytical solution for bending of coaxial orthotropic cylinders, *ASCE J. of Eng. Mech.* ;**120**(12):2556-2574.

[45] **Raoof, M.,** 1991. Methods of analysing large spiral strands, *Journal of Strain Analysis*; **26**(3):165-174.

[46] **Raoof, M., Kraincanic, I.,** 1995. Recovery length in multilayered spiral strands, *Journal of engineering mechanics,* Vol **121**, No 7, 795-800.

[47] **Raoof, M., Huang, Y.P.,** 1992. Free bending characteristics of sheathed spiral strands under cyclic loading, *Journal of Strain Analysis*; **27**(4):219-226.

[48] **Raoof, M., Kraincanic, I.,** 1995. Simple Derivation Of The Stiffness Matrix For Axial/Torsional Coupling Of Spiral Strands, *Computers & Structures,* Vol. **55**, No. 4. pp. 589-600.

[49] **Raoof, M., Kraincanic, I.,** 1998. Prediction of coupled axial/torsional stiffness coefficients of locked-coil ropes, *Computers and Structures,* **69**:305-319.

[50] **Raoof, M.,** 1992. Free-bending fatigue life estimation of cables at points of fixity, *Journal of Engineering Mechanics*, Vol. **118**, No. 9, pp. 1747-1764.

[51] **Lanteigne, J.,** 1985. Theoretical Estimation of the Response of Helically Armored Cables to Tension, Torsion, and Bending, *Journal of Applied Mechanics*, Vol. **52**, 423-432.

[52] **Jolicoeur, C.,** 1997. Comparative study of two semicontinuous models for wire strand analysis. *ASCE J. Eng. Mech.*; **123**(8):792-799.

[53] **Ramsey, H.,** 1988. A theory of thin rods with application to helical constituent wires in cables, *International Journal of Mechanical Sciences*. Vol **30**, No. 8, 559-570.

[54] **Phillips, J.W., Costello, G.A.,** 1973. Contact stresses in twisted wire cables, *Journal of engineering mechanics*, *ASCE,* **99** (EM2), 331-341.

[55] **Costello, G.A., Phillips, J.W.,** 1973. Contact Stresses in Thin Twisted Rods, *Journal of Applied Mechanics*;**40**, 629-630.

[56] **Costello, G.A.,** 1977. Large deflections of helical spring due to bending, *Journal of Engineering Mechanics Division, ASCE*, **103** (No.EM3, Proc. Paper 12964), 479-487.

[57] **Costello, G.A.,** 1978. Analytical Investigation of Wire Rope, *Applied Mechanics Reviews*, Vol. **31**, No. 7, pp. 897-900.

[58] **Costello, G.A., Butson, G.J.,** 1982. A simplified bending theory for wire rope, *Journal of the Engineering Mechanical Division*, *ASCE*, **108**, (EM2, Proc. Paper 16984), 219-227.

[59] **Costello, G.A.,** 1983. Stresses in Multilayered Cables, *Journal of energy resources technology*, Vol. **105**, pp. 337-340.

[60] **Velinsky, S.A., Anderson, G.L., Costello, G.A.,** 1984. Wire rope with complex cross sections, *Journal of Engineering Mechanics*, *Trans. ASCE*, **110**(3), 380-391.

[61] **Costello, G.A., Sinha, S.K.,** 1977. Static Behaviour of Wire Rope, *Proceedings ASCE*, *Journal of Engineering Mechanical Division*, **103** (No.EM6), 1011-1022.

[62] **Costello, G.A., Miller, R.E.,** 1980. Static Response of reduced rotation rope, *Proceedings ASCE, Journal of the Engineering Mechanics Division*, Vol **106**(No. EM4), 623-631.

[63] **Costello, G.A., Phillips, J.W.,** 1976. Effective modulus of twisted wire cables, *Proceedings ASCE, Journal of the Engineering Mechanical Division*, Vol **102**(No. EM1), 171-181.

[64] **Costello, G.A., Phillips, J.W.,** 1974. A more exact theory for twisted wire cables, *Journal of the Engineering Mechanics Division*, *ASCE*, **100** (No. EM5, Proc. Paper 10856), 1096-1099.

[65] **Phillips, J.W., Costello, G.A.,** 1977. Axial impact of Twisted Wire Cables, *Journal of Applied Mechanics*, **44**,127-131.

[66] **LeClair, R.A., Costello, G.A.,** 1986. Axial bending and torsional loading of a strand with friction, *Proceedings of the Fifth International OMAE Symposium, ASME*, Vol. **III**, pp. 550-555.

[67] **Conway, T.A., Costello, G.A.,** 1990. Bird-Caging in Wire Rope, *Journal of the Engineering Mechanical Division, ASCE,* Vol **116**, No 4, 822-831.

[68] **Costello, G.A., Sinha, S.K.,** 1977. Torsional stiffness of twisted wire cables, *Proceedings ASCE, Journal of Engineering Mechanical Division*, **103** (No.EM4), 766-770.

[69] **Conway, T.A., Costello, G.A.,** 1993. Viscoelastic response of a strand, *Journal of Applied Mechanics, ASME,* Vol. **60**, 534-540.

[70] **Conway, T.A., Costello, G.A.,** 1993. Viscoelastic response of a simple strand, *Int. J. Solids Structures*, Vol. **30**, No 4. pp. 553-567.

[71] **Chien, C.H., Costello, G.A.,** 1985. Effective length of a fractured wire in wire rope, *Journal of the Engineering Mechanics Division, ASCE*, **III**(7) 952-961.

[72] **Prakash, A., Conway, T.A., Costello, G.A.,** 1992. Compression of a Cord, *Transactions of the ASME*, Vol. **59**, S213-S216.

[73] **Phillips, J.W., Costello, G.A.,** 1985. Analysis of wire ropes with internal-wire-rope cores, *Transactions of the ASME*, Vol. **52**, 510-516.

[74] **Jiang, W.,** 1995. A general formulation of the theory of wire ropes, *Journal of Applied Mechanics*, September, Vol. **62**, 747-755.

[75] **Machida, S., Durelli, A.J.,** 1973. Response of a strand to axial and torsional displacements, *Journal of Mechanical Engineering Science* **15**, pp. 241–251.

[76] **Velinsky, S.A.,** 1981. Analysis of Wire Ropes with Complex Cross Sections, *PhD Thesis*, University of Illinois at Urban-Champaign.

[77] **Velinsky, S.A.,** 1985. General nonlinear theory for complex wire ropes. *International Journal of Mechanical Science*;**27**:497-507.

[78] **Kumar, K., Cochran, J.E. Jr.,** 1987. Closed-form analysis for elastic deformations of multilayered strand, *ASME Journal of Applied Mechanics* **54**, pp. 898–903.

[79] **Velinsky, S.A.,** 1988. Design and Mechanics of Multi-Lay Wire Strands, *Transactions of ASME, Journal of Mechanics, Transmissions, and Automation in Design*, June, Vol. **110**, 152-160.

[80] **Velinsky, S.A.,** 1989. On the design of wire rope, *Transactions of the ASME, Journal of Mechanics, Transmissions, and Automation in Design*, September, Vol. **111**, 382-388.

[81] **Jolicoeur, C., Cardou, A.,** 1991. A numerical Comparison of current mathematical models of Twisted wire cables under axisymmetric loads, *Journal of Energy Resources Technology*, December, Vol. **113**/241-249.

[82] **Sathikh, S., Moorthy, M.B.K., Krishnan, M.,** 1996. A symmetric linear elastic model for helical wire strands under axisymmetric loads, *Journal of Strain Analysis* **31** (5), pp. 389–399.

[83] **Yoo, J.W.,** 1988. Axial and Torsional Analysis of wire ropes, *Master of Science Thesis*, The Ohio State University.

[84] **Yardibi, E.,** 2000. Analysis of wire stresses of axial loaded and bent wire rope, *Master of Science Thesis*, Istanbul Technical University.

[85] **Senturk, O.,** 2007. Modelling and analysis of axial loaded wire rope strand using the finite element method, *Master of Science Thesis*, Istanbul Technical University.

[86] **Durelli, A.J., Machida, S., Parks, V.J.,** 1972. Strains and displacements on a steel wire strand, *Naval engineers journal*, c. **82**, 85-93.

[87] **Utting, W.S., Jones, N.,** 1985. Tensile testing of a wire rope strand, *Journal of Strain Analysis*;**20**(3):151-164.

[88] **Raoof, M., Hobbs, R.E.,** 1988. Torsion tests on large spiral strands, *Journal of Strain Analysis*;**23**(2):97-104.

[89] **Jiang, W.G., Henshall, J.L.,** 1999. The analysis of termination effects in wire strand using finite element method. *Journal of Strain Analysis* **34**:1, 31-38.

[90] **Jiang, W.G., Henshall, J.L., Walton, J.M.,** 2000. A concise finite element model for three-layered straight wire rope strand. *International Journal of Mechanical Sciences* **42**, 63-86.

[91] **Jiang, W.G., Henshall, J.L.,** 1999. The development and applications of the helically symmetric boundary conditions in finite element analysis, *Commun. Numer. Meth. Engng,* **15**, 435-443.

[92] **Elata, D., Eshkenazy, R., Weiss, M.P.,** 2004. The mechanical behavior of a wire rope with an independent wire rope core, *International Journal of Solids and Structures* **41**, 1157–1172.

[93] **Eshkenazy, R., Weiss, M.P., Elata, D.,** 2004. Torsion and bending stresses in wires of non-rotating, tower crane ropes, *Reading Rope Research, Bulletin ISSN 1018-8819,* Vol. **87**:59-81.

[94] **Ghoreishi, S.R., Messager, T., Cartraud, P., et.al.,** 2004. Assessment of cable models for synthetic mooring lines, In: *Proceedings of the Fourteenth International Offshore and Polar Engineering Conference*, Toulon, France., May 23-28.

[95] **Ghoreishi, S.R., Cartraud, P., Davies, P., et.al.,** 2006. Analytical modeling of synthetic fiber ropes subjected to axial loads. Part I: A new continuum

model for multilayered fibrous structures, *International Journal of Solids and Structures* Volume **44**, Issue 9, 1 May 2007, Pages 2924-2942.

[96] **Ghoreishi, S.R., Cartraud, P., Davies, P., Messager, T.,** 2006. Analytical modeling of synthetic fiber ropes. Part II: A linear elastic model for 1 + 6 fibrous structures, *International Journal of Solids and Structures* Volume **44**, Issue 9, 1 May 2007, Pages 2943-2960.

[97] **Seely, F.B., James, O.S.,** 1962. *Advanced mechanics of materials,* Second edition, John Wiley&Sons, New York, pp. 342-378.

[98] **LeClair, R.A., Costello, G.A.,** 1986. Axial, Bending and Torsional Loading of a Strand With Friction, *Proceedings of the Fifth International OMAES symposium, ASME,* **III**:550-555.

[99] **Metzler, R., Dommersnes, P.G.,** 2004. Helical packaging of semiflexible polymers in bacteriophages, *European Biophysics Journal*, Vol.**33**:6,497-505.

[100] **Meng, X., Li, J., Hou, H., et.al.,** 2008. Double helix chain frameworks constructed from bis-benzotriazole building blocks: Syntheses, crystal structures and third-order nonlinear optical properties, *Journal of Molecular Structure* , doi:10.1016/j.molstruc.2008.03.058.

[101] **Luo, F., Che, Y., Zheng, J.,** 2006. Synthesis and description of the first helical chain of Cu–Pb bimetallic atoms and Cu(I)–Cu(II) mixed-valence, *Inorganic Chemistry Communications*, **9**, 848–851.

[102] **Chakraborty, J., Roy, P., Mayer-Figge, H. et.al.,** 2007. Synthesis, crystal structures and magnetic properties of three Ni(II) complexes having NiN4 core with argentocyanide, terephthalate and dicyanamide ions: From discrete molecule to a helical network, *Polyhedron*, **26**, 3609–3616.

[103] **Yin, P.-X., Zhang, J., Li, Z.-J. et.al.,** 2007. Magnetic investigation of two helical frameworks derived from mixed ligands, *Inorganica Chimica Acta*, **360**, 3525–3532.

[104] **Falcón, S., Plaza, A.,** 2008. On the 3-dimensional k-Fibonacci spirals, Chaos, *Solitons and Fractals*, **38**, 993–1003.

[105] **Tsai, W.-W., Li, L.-s., Cui, H. et.al.,** 2008. Self-assembly of amphiphiles with terthiophene and tripeptide segments into helical nanostructures, *Tetrahedron*, **64**, 8504–8514.

[106] **Ren, C., Tarjan, P.P., Popovic, D.B.,** 1995. A Novel Electric Design for Electromagnetic Stimulation - The Slinky Coil, *IEEE Transactions on Biomedical Engineering*, Vol. **42**, No.9.

[107] **Wang, R.C., Miscoe, A.J., McKewan, W.M.,** 1998. Model for the Structure of Round-Strand Wire Ropes, *U.S. Department of Health and Human Services, Public Health Service, Centers for Disease Control and Prevention, National Institute for Occupational Safety and Health, DHHS (NIOSH),* Publication No. 98-148, Report of Investigations 9644:1-19.

[108] **Wang, G., Sun, J., Zhang, H.,** 2002. Geometric Model and Numerical Simulation For the Laying Process of Wire Rope, *Proceedings of the International Conference on Scientific & Engineering Computation [IC-SEC]*, 407-412.

[109] **Eisenhart, L.P.,** 1947**.** *An introduction to differential geometry with use of the tensor calculus*, Chapter I Curves in Space, pp.1-53, Princeton: Princeton University Press.

[110] **Frey, J.P., George, P.-L.,** 2000. *Mesh Generation application to finite elements*, Hermes Science Publishing.

[111] **Lepi, S.M.,** 1998. *Practical guide to finite elements*, Marcel Dekker Inc,Chapter 5.

[112] **Zienkiewicz, O.C.,** 1979. *The finite element method*, third expanded edition, Tata McGraw-Hill Publishing, Chapter 2-6.

[113] **Knight, C.E.,** 1993. *The finite element method in mechanical design*, PWS-KENT Publishing, Chapter 1,5-6.

[114] **Feyrer, K.,** 2007. *Wire Ropes, Tension, Endurance, Reliability,* Springer-Verlag.

[115] **Usabiaga, H., Pagalday, J.M.,** 2008. Analytical procedure for modelling recursively and wire by wire stranded ropes subjected to traction and torsion loads, *Int. Journal of Solids and Structures,*doi: 10.1016/j.ijsolstr.2008.04.009.

[116] **Dassault Sytemes, Simulia,** 2008. Abaqus Version 6.8 Documentation, Abaqus Example Problems Manual (v6.8), Progressive failure analysis of thin-wall aluminum extrusion under quasi-static and dynamic loads, Section 2.1.16

APPENDICES

APPENDIX A: Numerical Examples

A.1   Example 1

Consider a simple straight strand with the parameters given as;

$R_1 = 2.6162 \ mm$, $\quad R_2 = 2.5654 \ mm$, $\quad p_2 = 247.65 \ mm$, $\quad E = 196497.52 \ N/mm^2$,

$v = 0.25$, $m_2 = 6$.

Outside wires are assumed not touching each other. Equation (4.42) yields,

$$r_2 = R_1 + R_2 = 5.1816 \ mm.$$

The helix angle α_2 is determined by equation (4.53); hence,

$$\tan \alpha_2 = \frac{247.65}{2\pi * 5.1816} = 7.606670 \Rightarrow \alpha_2 = 82.510641°.$$

The following values are then computed;

$\sin \alpha_2 = 0.991469$, $\sin^2 \alpha_2 = 0.983011$, $\cos \alpha_2 = 0.130342$, $\cos^2 \alpha_2 = 0.016989$,

$\sin \alpha_2 \cos \alpha_2 = 0.129230$ and $\dfrac{r_2}{R_2} = 2.019802$.

The outside wires are checked to determine if they are touching each other. From the equation (4.52) yields for $m_2 = 6$ that,

$$R_2\sqrt{1 + \frac{\tan^2\left(\dfrac{\pi}{2} - \dfrac{\pi}{m_2}\right)}{\sin^2 \alpha}} = 2.5654\sqrt{1 + \frac{\tan^2\left(\dfrac{\pi}{2} - \dfrac{\pi}{6}\right)}{0.983011}} \quad ,$$

$$= 5.163946 \ mm \ < \ 5.181600 \ mm = R_1 + R_2$$

which shows that the outside wires do not touch each other. Now equations (4.89) and (4.98) are prepared by letting the angle of twist per unit length of the strand $\tau_s = 0$, which means that the strand is not allowed to rotate, and letting $\xi_1 = \varepsilon = 0.003$ as follows,

$$\xi_1 = \xi_2 + \frac{\Delta\alpha_2}{\tan\alpha_2} = \varepsilon \,,$$

$$0.003 = \xi_2 + \frac{\Delta\alpha_2}{7.606670} \,, \tag{A.1}$$

and,

$$\beta_2 = r_2\tau_s = \frac{\xi_2}{\tan\alpha_2} - \Delta\alpha_2 + v\frac{(R_1\xi_1 + R_2\xi_2)}{r_2\tan\alpha_2} \,,$$

$$0 = \frac{\xi_2}{7.606670} - \Delta\alpha_2 + 0.25\frac{(2.6162*0.003 + 2.5654\xi_2)}{2.5654*7.606670} \,. \tag{A.2}$$

If equation (A.1) and (A.2) are solved together for ξ_2 *and* $\Delta\alpha_2$, we found that $\xi_2 = 0.002936$ and $\Delta\alpha_2 = 0.000483596$. From the equations (4.101) and (4.103), the values of $R_2\Delta\kappa_2'$ and $R_2\Delta\tau_2$ can be computed as follows,

$$
\begin{aligned}
R_2\Delta\kappa_2' &= R_2\frac{-2\sin\alpha_2\cos\alpha_2}{r_2}\Delta\alpha_2 + vR_2\frac{(R_1\xi_1 + R_2\xi_2)}{r_2}\frac{\cos^2\alpha_2}{r_2} \\
&= 2.5654\frac{-2(0.99147)(0.13034)}{5.1816}0.00048359 + \\
&\quad 0.25*2.5654\frac{(0.103*0.003 + 0.101*0.002936)}{5.1816}\frac{0.016989}{5.1816} \\
&= -0.00005564,
\end{aligned}
$$

$$
\begin{aligned}
R_2\Delta\tau_2 &= R_2\frac{1 - 2\sin^2\alpha_2}{r_2}\Delta\alpha_2 + vR_2\frac{(R_1\xi_1 + R_2\xi_2)}{r_2}\frac{\sin\alpha_2\cos\alpha_2}{r_2} \\
&= 2.5654\frac{1 - 2*0.98301}{5.1816}*0.00048359 + \\
&\quad 0.25\frac{(0.103*0.003 + 0.101*0.002936)}{5.1816}\frac{(0.99147*0.13034)}{5.1816} \\
&= -0.0001838,
\end{aligned}
$$

Equations (4.104) through (4.116) yields,

$$\frac{G_2'}{ER_2{}^3} = \frac{\pi}{4}R_2\Delta\kappa_2' = \frac{\pi}{4}*(-0.00005564) = \text{-}0.00004370\,,$$

$$\frac{H_2}{ER_2{}^3} = \frac{\pi}{4(1+v)}R_2\Delta\tau_2 = \frac{\pi}{4(1+0.25)}*(-0.0001838) = -0.00011549\,,$$

$$\frac{N_2'}{ER_2{}^2} = R_2\frac{H_2}{ER_2{}^3}\frac{\cos^2\alpha_2}{r_2} - R_2\frac{G_2'}{ER_2{}^3}\frac{\sin\alpha_2\cos\alpha_2}{r_2}$$

$$= 2.5654*(-0.00011549)\frac{0.016989}{5.1816}$$

$$-2.5654*0.00004370\frac{(0.99147*0.13034)}{5.1816} = 0.000001825\,,$$

$$\frac{T_2}{ER_2{}^2} = \pi\xi_2 = \pi*0.002936 = 0.00922505\,,$$

$$\frac{X_2}{ER_2} = R_2\frac{N_2'}{ER_2{}^2}\frac{\sin\alpha_2\cos\alpha_2}{r_2} - R_2\frac{T_2}{ER_2{}^2}\frac{\cos^2\alpha_2}{r_2}$$

$$= 2.5654*0.000001825\frac{(0.99147*0.13034)}{5.1816}$$

$$-2.5654*0.00922505\frac{0.016989}{5.1816} = -0.000077474\,,$$

$$\frac{F_2}{ER_2{}^2} = m_2\left[\frac{T_2}{ER_2{}^2}\sin\alpha_2 + \frac{N_2'}{ER_2{}^2}\cos\alpha_2\right]$$

$$= 6*[0.00922505*0.99147 + 0.000001825*0.13034]$$

$$= 0.054879\,,$$

$$\frac{M_2}{ER_2{}^3} = m_2\left[\frac{H_2}{ER_2{}^3}\sin\alpha_2 + \frac{G_2'}{ER_2{}^3}\cos\alpha_2 + \frac{T_2}{ER_2{}^2}\frac{r_2}{R_2}\cos\alpha_2 - \frac{N_2'}{ER_2{}^2}\frac{r_2}{R_2}\sin\alpha_2\right]$$

$$= 6\begin{bmatrix}-0.00011549*0.99147 + \text{-}0.00004370*0.13034 + \\ 0.00922505*\dfrac{5.1816}{2.5654}*0.13034 - 0.000001825*\dfrac{5.1816}{2.5654}*0.99147\end{bmatrix}$$

$$= 0.013828\,,$$

$$\frac{F_1}{ER_1{}^2} = \pi\xi_1 = \pi*0.003 = 0.00942478\,,$$

$$\frac{M_1}{ER_1^3} = \frac{\pi}{4(1+v)}R_1\tau_s = \frac{\pi}{4(1+0.25)}2.6162*0 = 0,$$

$$F = F_1 + F_2 = ER_1^2*0.00942478 + ER_2^2*0.054879$$
$$= 12675.65 + 70970.48 = 83646.12\ N,$$

$$M_t = M_1 + M_2 = 0 + ER_2^3*0.013828 = 45877.83\ Nmm\ .$$

Since the above equations are linear, a reduction or increase in the axial strain, with $\tau_s = 0$, would correspond to a similar decrease or increase in the loads. For example, with $\varepsilon = 0.0015$ and $\tau_s = 0$, the total axial force would be $41813.3\ N$, and the total axial moment would be $902.989\ Nmm$. This shows that while the strain ε is decreased by half, total axial force and total axial moment also decreased by half of its value.

A.2   Example 2

The same strand used in example 1 is considered again. Let the strand subjected to an axial load of $83646.12\ N$ and not allowed to rotate $(\tau_s = 0)$. Using the results of example 1 and the equations (4.117)-(4.121) gives the following results,

$$_F\sigma_1 = \frac{F_1}{\pi R_1^2} = \frac{12675.65}{\pi*2.6162^2} = 589.49\ N/mm^2,$$

$$_M\sigma_1 = \frac{2M_1}{\pi R_1^3} = 0N/mm^2,\ \text{due to M}_1 = 0\ ,$$

$$_T\sigma_2 = \frac{T_2}{\pi R_2^2} = \frac{11929.88}{\pi*2.5654^2} = 577\ N/mm^2,$$

$$_{G'}\sigma_2 = \frac{4G_2'}{\pi R_2^3} = \frac{4*144.98}{\pi*2.5654^3} = 10.93\ N/mm^2,$$

$$_H\sigma_2 = \frac{2H_2}{\pi R_2^3} = \frac{2*383.15}{\pi*2.5654^3} = 14.44\ N/mm^2.$$

The shearing force can be computed by using equation (4.106) and the result from example 1,

$$\frac{N'_2}{ER_2{}^2} = 0.000001825$$
$$\Rightarrow N'_2 = 0.000001825 * ER_2{}^2$$
$$= 0.000001825 * 1293204.63$$
$$\approx 2.35 \ N.$$

The maximum normal tensile stress can be computed by adding the axial stress caused by the load T_2 and the maximum normal stress due to the bending moment G'_2 such that,

$$_T\sigma_2 + {}_{G'}\sigma_2 = 577 + 10.93 = 587.93 \ N / mm^2,$$

and this stress occurs on the inside of an outer wire (due to the sign of G'_2). These results shows that the center wire is depend on a slightly greater stress than the outer wires as shown in this example.

A.3   Example 3

In this example, the load deformation relation of the given simple straight strand is computed for the strand defined in example 1, and using the computed values from example 2. The constant values of $C_1,...,C_4$ is computed as defined in equations (4.122) and (4.123). The cross sectional area of the given strand is,

$$A = \sum \pi R_i^2 = \pi * 2.6162^2 + 6\pi * 2.5654^2 = 145.5567 \ mm^2,$$

and R can be computed as,

$$R = 2.6162 + 2 * 2.5654 = 7.747 \ mm.$$

Taking $\beta = 0$ and $\varepsilon = \xi_1$, using the results of example 2, equations given in (4.122) and (4.123) can be computed to yield C_1 and C_3 as follows,

$$C_1 = \frac{F}{AE\varepsilon} = 0.975,$$

and

$$C_3 = \frac{M_t}{ER^3 \varepsilon} = 0.167.$$

Now assume that $\xi_1 = \varepsilon = 0$ and $\xi_1 = 0.001$. Using the equation (4.89) we can find,

$$\xi_1 = \xi_2 + \frac{\Delta \alpha_2}{\tan \alpha_2},$$

$$0 = 0.001 + \frac{\Delta \alpha_2}{7.6067}.$$

Solving the equation above yields $\Delta \alpha_2 = -0.0076067$. From the equation (4.98),

$$\beta_2 = r_2 \tau_s = \frac{\xi_2}{\tan \alpha_2} - \Delta \alpha_2 + v \frac{(R_1 \xi_1 + R_2 \xi_2)}{r_2 \tan \alpha_2},$$

$$5.1816 \tau_s = \frac{0.001}{7.6067} + 0.0076067 + 0.25 \frac{2.5654 * 0.001}{5.1816 * 7.6067},$$

which results in $\tau_s = 0.038012$ and from equation (4.125), $\beta = R \tau_s$ which results,

$$\beta = 7.747 * 0.038012 = 0.011593.$$

Now equations (4.101), (4.103) through (4.116) can be solved and the following results are obtained,

$$\begin{aligned}
R_2 \Delta \kappa_2' &= R_2 \frac{-2 \sin \alpha_2 \cos \alpha_2}{r_2} \Delta \alpha_2 + v R_2 \frac{(R_1 \xi_1 + R_2 \xi_2)}{r_2} \frac{\cos^2 \alpha_2}{r_2} \\
&= 2.5654 \frac{-2 * 0.12923 * 0.0076067}{5.1816} * (-0.0076067) \\
&+ 0.25 * 2.5654 \frac{(2.5654 * 0.001)}{5.1816} \frac{0.016989}{5.1816} = 0.00097442, \\
R_2 \Delta \tau_2 &= R_2 \frac{1 - 2 \sin^2 \alpha_2}{r_2} \Delta \alpha_2 + v R_2 \frac{(R_1 \xi_1 + R_2 \xi_2)}{r_2} \frac{\sin \alpha_2 \cos \alpha_2}{r_2} \\
&= 2.5654 \frac{1 - 2 * 0.98301}{5.1816} * (-0.0076067) \\
&+ 0.25 * 2.5654 \frac{(2.5654 * 0.001)}{5.1816} \frac{0.12923 * 0.0076067}{5.1816} \\
&= 0.0036460,
\end{aligned}$$

$$\frac{G_2'}{ER_2^3} = \frac{\pi}{4} R_2 \Delta\kappa_2' = \frac{\pi}{4} * (0.00097442) = 0.0007653,$$

$$\frac{H_2}{ER_2^3} = \frac{\pi}{4(1+v)} R_2 \Delta\tau_2 = \frac{\pi}{4(1+0.25)} * 0.0036460 = 0.0022908,$$

$$\frac{N_2'}{ER_2^2} = R_2 \frac{H_2}{ER_2^3} \frac{\cos^2\alpha_2}{r_2} - R_2 \frac{G_2'}{ER_2^3} \frac{\sin\alpha_2\cos\alpha_2}{r_2}$$
$$= 2.5654 * 0.0022908 * \frac{0.016989}{5.1816}$$
$$- 2.5654 * 0.0007653 * \frac{(0.99147 * 0.13034)}{5.1816} = -0.00002970,$$

$$\frac{T_2}{ER_2^2} = \pi\xi_2 = \pi * 0.001 = 0.0031416,$$

$$\frac{X_2}{ER_2} = R_2 \frac{N_2'}{ER_2^2} \frac{\sin\alpha_2\cos\alpha_2}{r_2} - R_2 \frac{T_2}{ER_2^2} \frac{\cos^2\alpha_2}{r_2}$$
$$= -2.5654 * 0.00002970 * \frac{(0.99147 * 0.13034)}{5.1816}$$
$$- 2.5654 * 0.0031416 * \frac{0.016989}{5.1816} = -0.00002832,$$

$$\frac{F_2}{ER_2^2} = m_2 \left[\frac{T_2}{ER_2^2} \sin\alpha_2 + \frac{N_2'}{ER_2^2} \cos\alpha_2 \right]$$
$$= 6 * [0.0031416 * 0.99147 - 0.00002970 * 0.13034]$$
$$= 0.018665,$$

$$\frac{M_2}{ER_2^3} = m_2 \left[\frac{H_2}{ER_2^3} \sin\alpha_2 + \frac{G_2'}{ER_2^3} \cos\alpha_2 + \frac{T_2}{ER_2^2} \frac{r_2}{R_2} \cos\alpha_2 - \frac{N_2'}{ER_2^2} \frac{r_2}{R_2} \sin\alpha_2 \right]$$
$$= 6 \left[\begin{array}{l} 0.0022908 * 0.99147 + 0.0007653 * 0.13034 + \\ 0.0031416 * \dfrac{5.1816}{2.5654} * 0.13034 + 0.00002970 * \dfrac{5.1816}{2.5654} * 0.99147 \end{array} \right]$$
$$= 0.019546,$$

$$\frac{F_1}{ER_1^2} = \pi\xi_1 = \pi * 0 = 0,$$

$$\frac{M_1}{ER_1^3} = \frac{\pi}{4(1+v)} R_1 \tau_s = \frac{\pi}{4(1+0.25)} * 2.6162 * 0.038012 = 0.00246 \,,$$

$$F = F_1 + F_2 = ER_1^2 * 0 + ER_2^2 * 0.018665 = 24138.34 \; N \,,$$

$$M_t = M_1 + M_2 = 8655.76 + 64844.25 = 73500.01 \; Nmm \,.$$

The general equations of the strand given in (4.122) and (4.123) can be organized to find C_2 and C_4,

$$\frac{F}{AE} = C_1 * 0 + C_2 \beta,$$

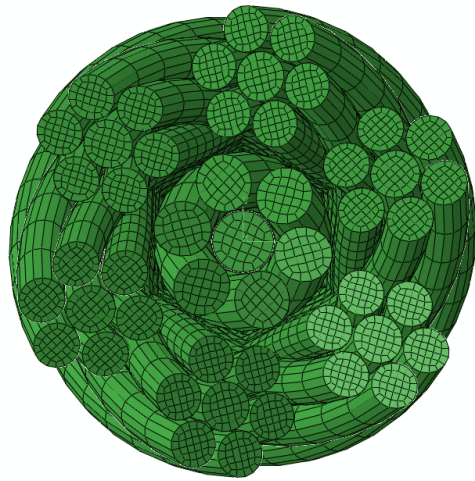$$\Rightarrow C_2 = \frac{F}{AE\beta} = 0.0728,$$

$$\frac{M_t}{ER^3} = C_3 * 0 + C_4 \beta,$$

$$\Rightarrow C_4 = \frac{M_t}{ER^3 \beta} = 0.0694.$$

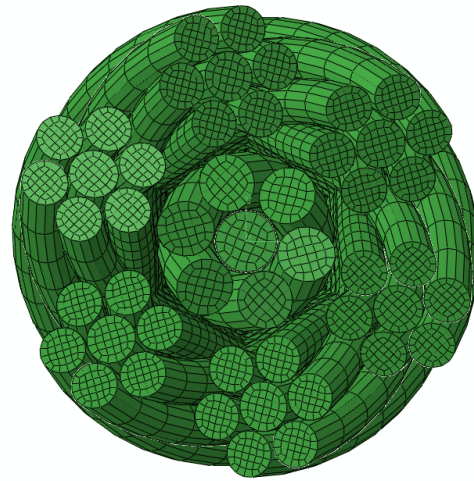Finally, equations of the strand can be written as,

$$\frac{F}{AE} = 0.975 * \varepsilon + 0.0728 * \beta \,,$$

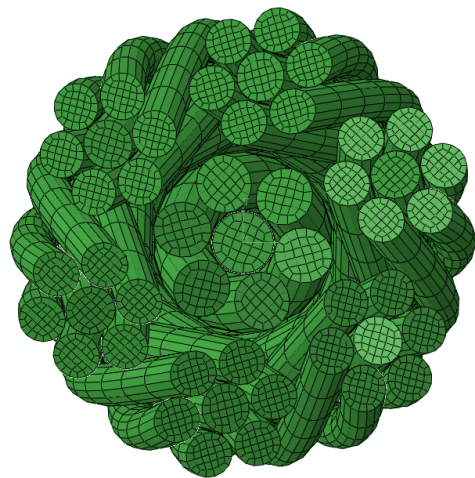$$\frac{M_t}{ER^3} = 0.167 * \varepsilon + 0.0694 * \beta \,.$$

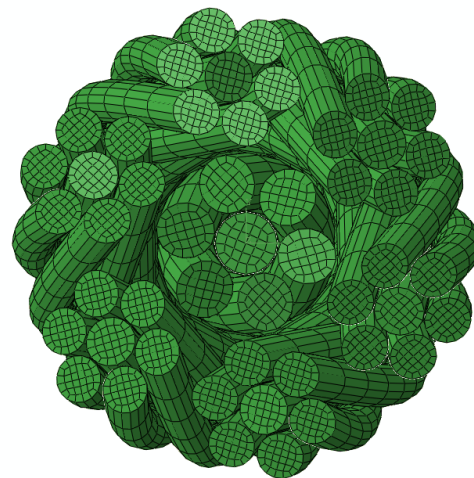**APPENDIX B: IWRC cross-sections for different lay types**

(a) Right Lang Lay (RLL)
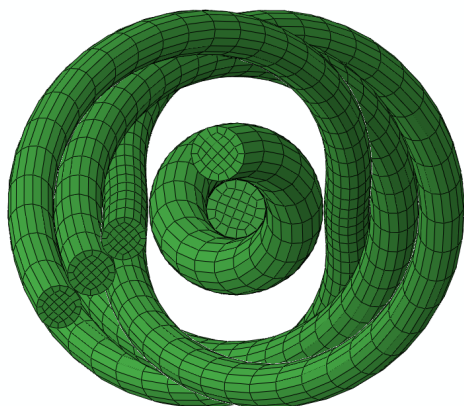
(b) Left Lang Lay (LLL)

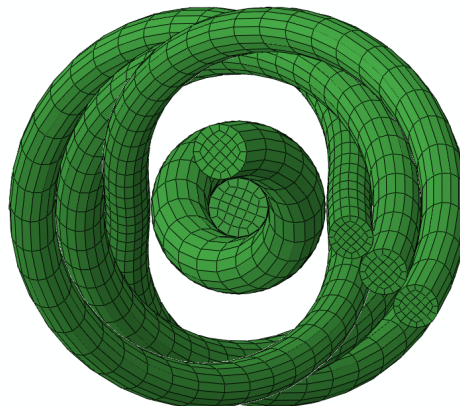(c) Right Regular Lay (RRL)

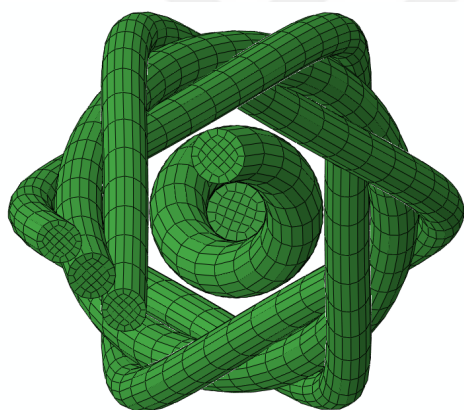(d) Left Regular Lay (LRL)

Figure B.1: Cross-sectional view of IWRCs for different lay types.
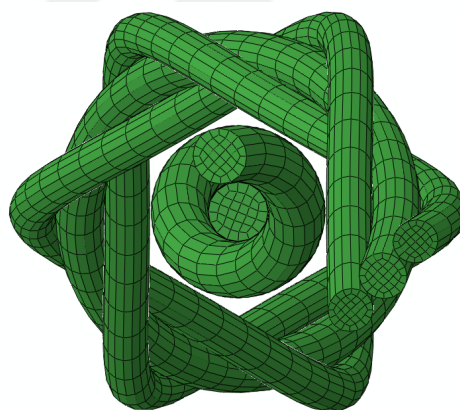
(a) Right Lang Lay (RLL)

(b) Left Lang Lay (LLL)

(c) Right Regular Lay (RRL)

(d) Left Regular Lay (LRL)

Figure B.2: Wrapping nested helical wires; (a,b) without indentations, (c,d) with indentations over a simple straight core strand.

APPENDIX C: Matlab code to construct a nested helical wire

```
% This code creates the nested helix to construct an IWRC and three points perpendicular to the wire
centerline.
% All nodes are written in a text file.
clear all
format long
    telyaricaplari(1) = 1.970 ;   %'R1
    telyaricaplari(2) = 1.865 ;   %'R2
    telyaricaplari(3) = 1.600 ;   %'R3
    telyaricaplari(4) = 1.500 ;   %'R4
% Right Lang Lay IWRC
%    oshw_sign=1; odhw_sign=1;
% Left Lang Lay IWRC
%    oshw_sign=1; odhw_sign=-1;
% Right Regular Lay IWRC
%    oshw_sign=-1; odhw_sign=-1;
% Left Regular Lay IWRC
    oshw_sign=-1; odhw_sign=1;
    bosluk1 = 0.05;
    bosluk2 = 0.05;
    nokta = 30;
    p2 = 193; %                              ' pitch lengt
    uzunluk = 300; %                         ' wire length
    wirenumber= 6;
    j = wirenumber-1;
    % ' j=0,1,2,3,4,5 nested helix numbers
    rs = telyaricaplari(1) + bosluk1 + 2 * telyaricaplari(2) + bosluk2 + 2 * telyaricaplari(4) + bosluk2 +
telyaricaplari(3);
    %' rs = R1+2*R2+2*R4+R3
    tw0 = 0 * pi / 3;%                         ' 0 * PI/3 to 5*PI/3
    rw = telyaricaplari(4) + bosluk2 + telyaricaplari(3); %      ' rw = R4+R3
%'  *****************************
    alfas = atan(p2 / (2 * pi * rs));%          ' radian
%'  ************************************************************
%'  array length of nPtData is computed
%'  ************************************************************
%'   rev = uzunluk / (2 * PI * rs * Tan(alfas))
    rev = uzunluk/p2;
    i = 0;
    for ts=0:pi/nokta:(2 * rev * pi)
      i = i + 1;
    end
    rev = i / (2 * nokta);
    i = 0;
    for ts=0:pi/nokta:(2 * rev * pi)
      i = i + 1;
    end
    indis = 3 * i - 1;
%'  ************************************************************
    m = 1;
    i = 1;
    for ts=0:pi/nokta:(2 * rev * pi)
      xyz(i) = oshw_sign*rs * cos(ts);
      xyz(i + 1) = rs * sin(ts);
```

```
    xyz(i + 2) = rs * ts * tan(alfas);
    i = i + 3
  end
%'  rw = 0.025815 * 25.4 + 0.1 + 0.027725 * 25.4
%'  tw0 = 0 * PI / 3                          ' 0 * PI/3 to 5*PI/3
  for k=j:j
  tw0 = k * pi / 3;%                          ' 0 * PI/3 to 5*PI/3
  i = 1;
  for ts=0:pi/nokta:(2 * rev * pi)
    tw = m * ts + tw0;
    % - sign show regular lay otherwise it is lang lay
%       nPtData(i) = (oshw_sign*xyz(i) + odhw_sign*( rw * cos(tw) * cos(ts) - rw * sin(tw) * sin(ts) *
sin(alfas))) / 1000;
      nPtData(i) = odhw_sign*(xyz(i) + ( rw * cos(tw) * cos(ts) - rw * sin(tw) * sin(ts) * sin(alfas))) /
1000;
%       nPtData(i) = (xyz(i) + rw * cos(tw) * cos(ts) - rw * sin(tw) * sin(ts) * sin(alfas)) / 1000;
      nPtData(i + 1) = (xyz(i + 1) + rw * cos(tw) * sin(ts) + rw * sin(tw) * cos(ts) * sin(alfas)) / 1000;
      nPtData(i + 2) = (xyz(i + 2) - rw * sin(tw) * cos(alfas)) / 1000;
    i = i + 3;
  end
  i = i - 3;
    P3=[nPtData(i) nPtData(i+1) nPtData(i+2)];
  end
n=max(size(nPtData));
j=1;
for i=1:3:n
  xw(j)=nPtData(i);
  yw(j)=nPtData(i+1);
  zw(j)=nPtData(i+2);
  j=j+1;
end
plot3(xw,yw,zw,'k','linewidth',2);
hold on
maxelsay=max(size(xw));
sirano=1:1:maxelsay;
xyz=[sirano' xw' yw' zw'];
% file name for writing the nodes
fid = fopen('helixpoint.inp','w');
fprintf(fid,'*NODE\n');
for i=1:maxelsay
  fprintf(fid,'%3d, %15.10f, %15.10f, %15.10f\n',sirano(i),xw(i),yw(i),zw(i));
end
% *****************************************************************************
%  three points which are perpendicular to wire centerline
% *****************************************************************************
syms x y
twyedek=tw;
syms t tw
%helix=[-(xyz(i) + rw * cos(tw) * cos(ts) - rw * sin(tw) * sin(ts) * sin(alfas))/1000,(xyz(i + 1) + rw *
cos(tw) * sin(ts) + rw * sin(tw) * cos(ts) * sin(alfas))/1000,(xyz(i + 2) - rw * sin(tw) *
cos(alfas))/1000]
helix=[(oshw_sign*xyz(i) + odhw_sign*(rw * cos(tw) * cos(ts) - rw * sin(tw) * sin(ts) *
sin(alfas)))/1000,(xyz(i + 1) + rw * cos(tw) * sin(ts) + rw * sin(tw) * cos(ts) * sin(alfas))/1000,(xyz(i
+ 2) - rw * sin(tw) * cos(alfas))/1000]
dhelix = diff(helix)
ddhelix =diff(dhelix)
realdot = @(u, v) u*transpose(v)
veclength = @(v) sqrt(realdot(v,v))
binormal = cross(dhelix,ddhelix)/veclength(cross(dhelix,ddhelix))
normalvect= cross(binormal,dhelix)/veclength(cross(binormal,dhelix))
```

```
tw=twyedek
bval=eval(binormal)
hval=eval(helix)
hval=P3
tval=eval(dhelix)
nval=eval(normalvect)
% ********************************************************************
% normal binormal and tangent lines
grid on;
xlabel('x'); ylabel('y'); zlabel('z')
k=-5:0.1:5;
plot3(hval(1)+k*tval(1),hval(2)+k*tval(2),hval(3)+k*tval(3),'m'); % tangent line
tanpoints=[(hval(1)+k*tval(1))' (hval(2)+k*tval(2))' (hval(3)+k*tval(3))'];
k=-0.01:0.001:0.01;
plot3(hval(1)+k*bval(1),hval(2)+k*bval(2),hval(3)+k*bval(3)); % binormal line
binormalpoints=[(hval(1)+k*bval(1))' (hval(2)+k*bval(2))' (hval(3)+k*bval(3))'];
k=-0.01:0.001:0.005;
plot3(hval(1)+k*nval(1),hval(2)+k*nval(2),hval(3)+k*nval(3),'g'); % normal line
normalpoints=[(hval(1)+k*nval(1))' (hval(2)+k*nval(2))' (hval(3)+k*nval(3))'];
% **********************************************************************
k=0.01;
P0=[hval(1)+k*tval(1),hval(2)+k*tval(2),hval(3)+k*tval(3)]
P1=[hval(1)+k*bval(1),hval(2)+k*bval(2),hval(3)+k*bval(3)]
P2=[hval(1)+k*nval(1),hval(2)+k*nval(2),hval(3)+k*nval(3)]
P0=tanpoints(5,:);
P=[P0;P2;P3]
plot3(P1(1),P1(2),P1(3),'ro','linewidth',1.5)
plot3(P2(1),P2(2),P2(3),'ys','linewidth',1.5)
plot3(P3(1),P3(2),P3(3),'g*','linewidth',1.5)
sirano=[maxelsay+1;maxelsay+2;maxelsay+3];
xyz=[sirano P];
for i=1:3
    fprintf(fid,'%3d, %15.10f, %15.10f, %15.10f\n',sirano(i),P(i,1),P(i,2),P(i,3));
end
fprintf(fid,'*****\n');
fclose(fid)
max(zw)*1000
return
```

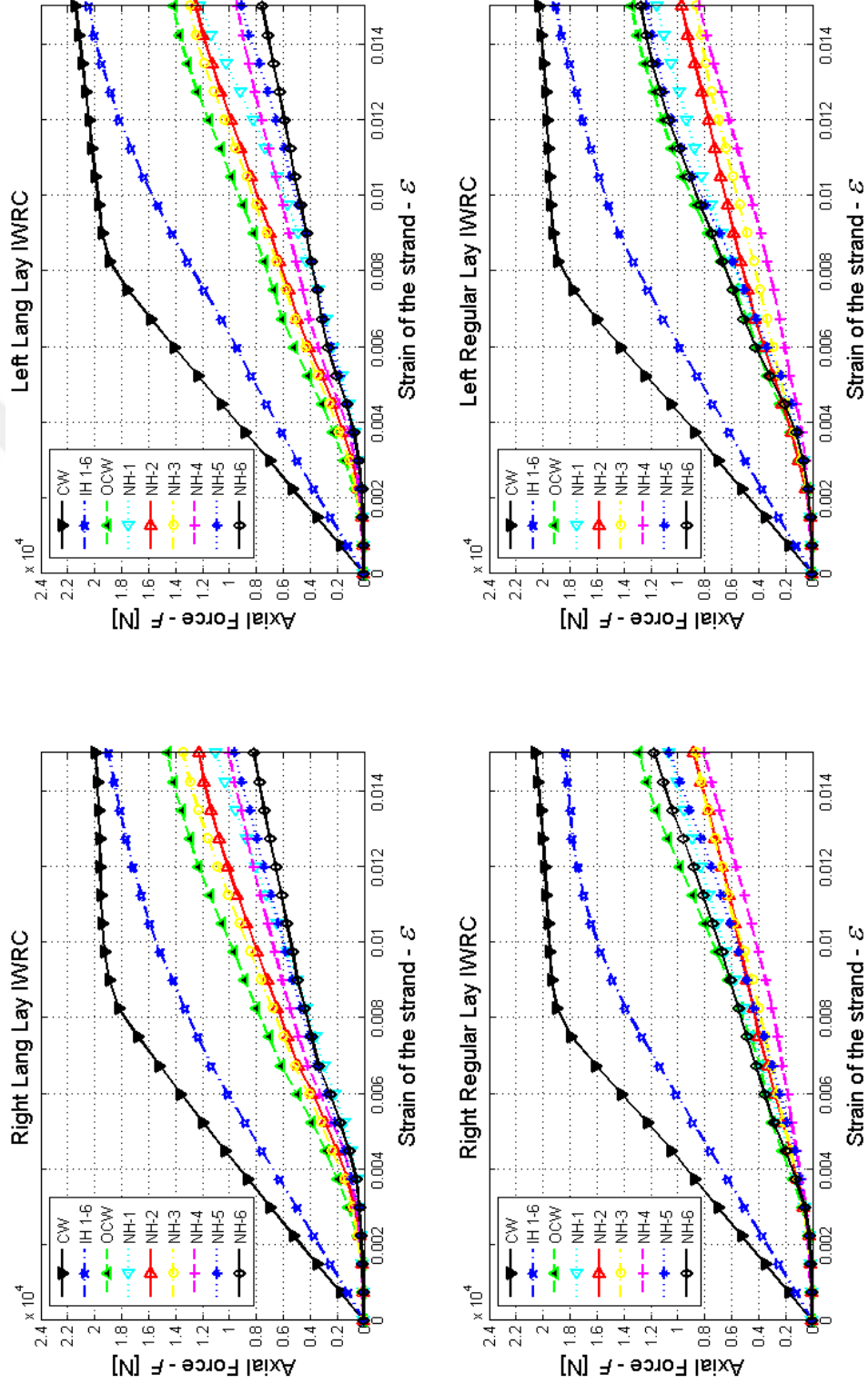# APPENDIX D: Numerical analysis results for IWRC

Figure D.1: *A 300mm non-rotating end, reaction force variation with strain for RLL, LLL, RRL and LRL type IWRCs.*
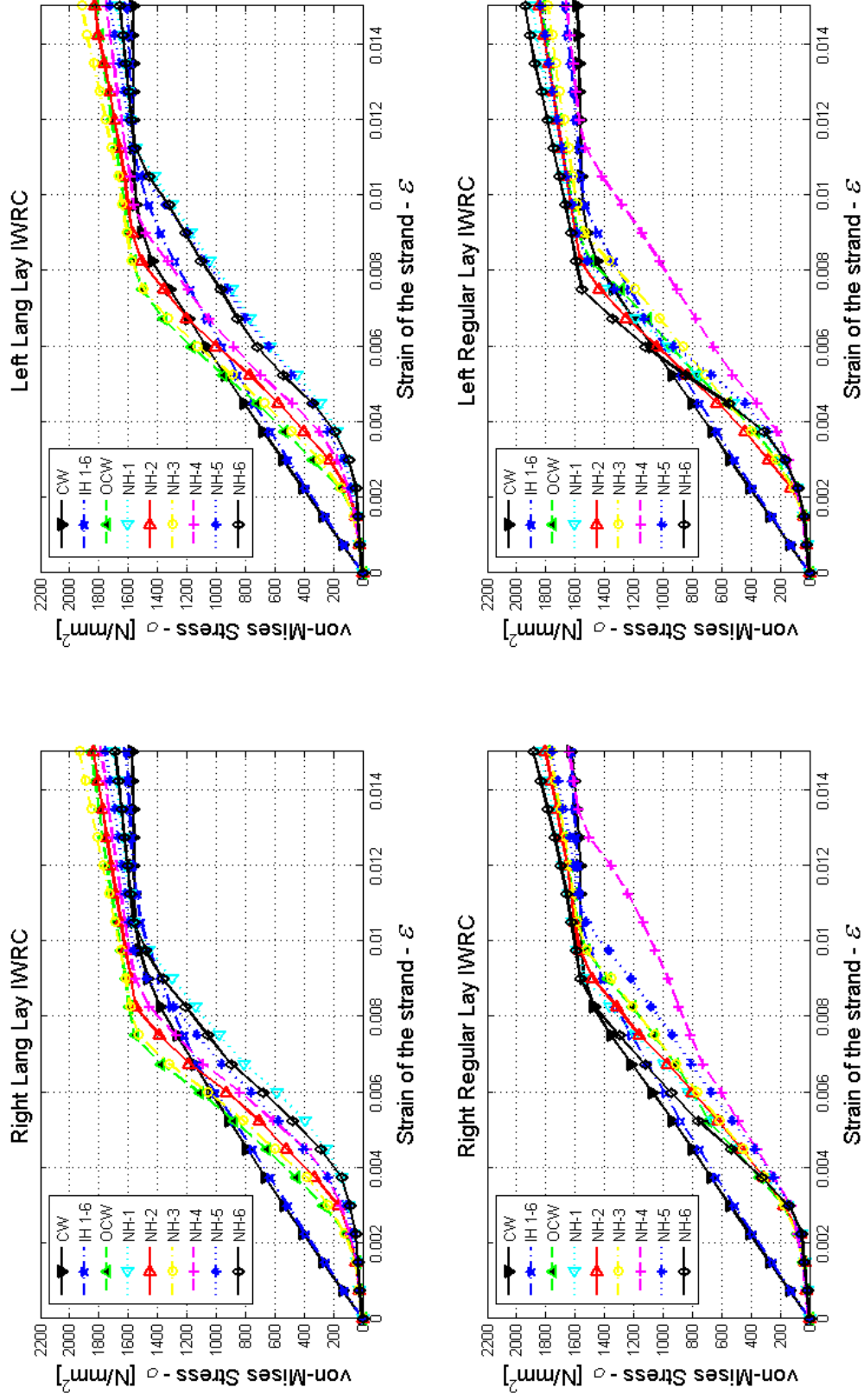
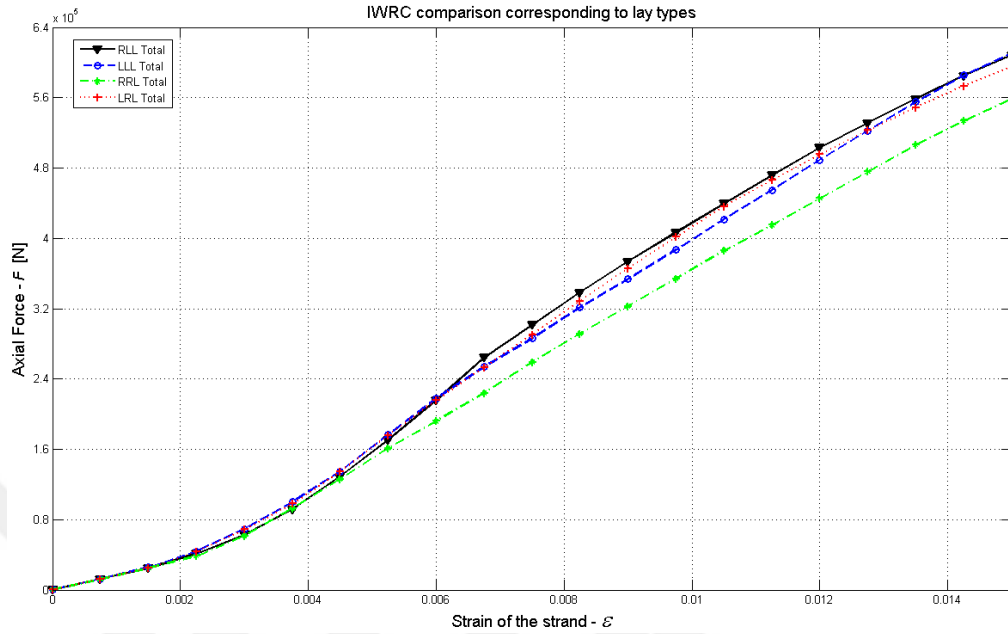**Figure D.2:** A 300*mm* non-rotating end, von-Mises Stress variation with strain for RLL, LLL, RRL and LRL type IWRCs.

220

Figure D.3: A 300*mm* non-rotating end, total reaction force variation with strain for RLL, LLL, RRL and LRL type IWRCs.
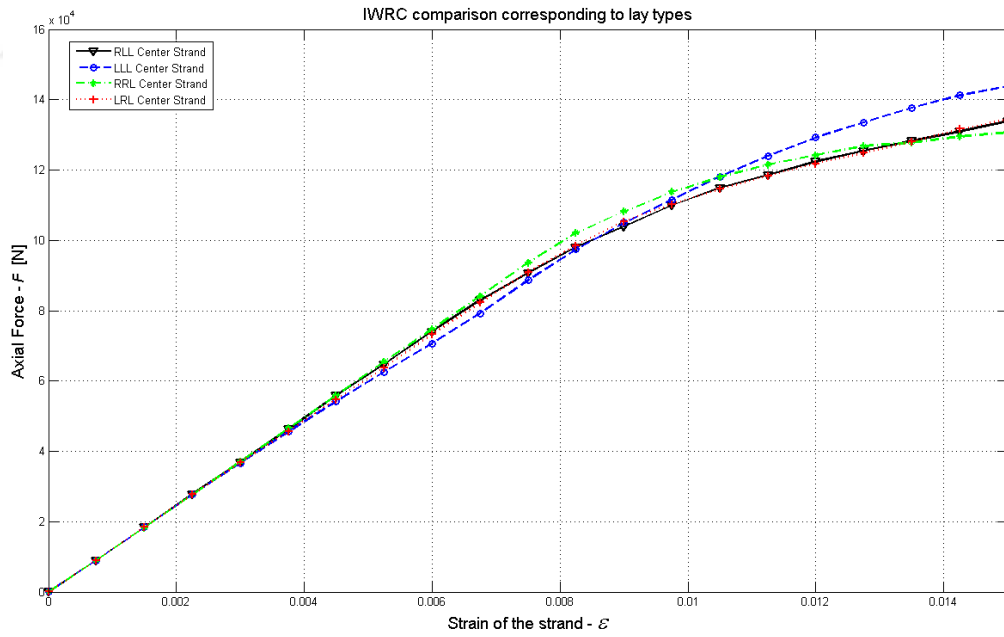

Figure D.4: A 300*mm* non-rotating end, center strand reaction force variation with strain for RLL, LLL, RRL and LRL type IWRCs.
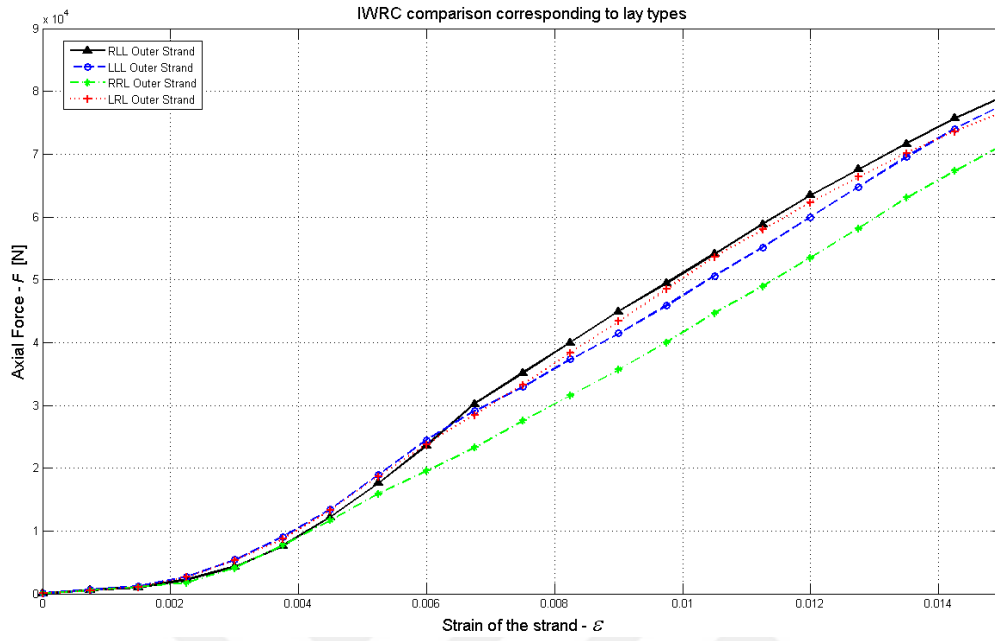
221

Figure D.5: A 300*mm* non-rotating end, outer strand, reaction force variation with strain for RLL, LLL, RRL and LRL type IWRCs.

CURRICULUM VITAE

Candidate's full name : Cengiz ERDÖNMEZ

Place and date of birth : Ankara, 1973

Universities and
Colleges attended :
- Ankara University, B.Sc. degree from the Faculty of Science, department of Mathematics, 1998.
- Middle East Technical University (METU), M.Sc. degree from the Natural and Applied Sciences Institute, Department of Mathematics, 2001.
- Ph.D. candidate at the Computational Science and Engineering programme, Institute of Informatics, ITU.

Publications :

Papers accepted and published in journals:

- **İmrak, C.E., Erdönmez, C.,** 2010. On the problem of wire rope model generation with axial loading, *Mathematical and Computational Applications*, **15**(2):259-268.
- **Erdönmez, C., İmrak, C.E.,** 2009. Modeling and numerical analysis of the wire strand, *Journal of Naval Science and Engineering,* **5(1):**30-38.

Conference attendances :

- **Erdönmez, C., İmrak, C.E.,** 2008. Mathematical Modeling and Static Stress Analysis of Steel Wire Rope Strand using Finite Element Method, *12'th International Research/Expert Conference "Trends in the Development of Machinery and Associated Technology" (TMT 2008),* Bahcesehir University Istanbul, 26-30 August.
- **Erdönmez, C., İmrak, C.E.,** 2008. Finite Element Modeling and Static Stress Analysis of Axial Loaded Wire Ropes, *Mechanics of Slender Structures (Moss 2008),* University of Maryland Baltimore County, U.S.A., 22-25 July.
- **Erdönmez, C., İmrak, C.E.,** 2008. Modeling and Solution of the Bending Problem over the Helical Wire Strand, *5th. European Congress on Computational Methods in Applied Sciences and Engineering (ECCOMAS 2008),* Lido Island in Venice, Italy on 30 June - 4 July.
- **Erdönmez C., İmrak C.E.,** 2007. General Nonlinear Equilibrium Equation Solution of the Straight Wire Strand, *Numerical Analysis and Applied Mathematics: International Conference of Numerical Analysis and Applied Mathematics. AIP Conference Proceedings,* Volume **936**, pp. 174-177.